

Dimensional measurements with X-ray Computed Tomography and application to Cultural Heritage

Original

Dimensional measurements with X-ray Computed Tomography and application to Cultural Heritage / Vigorelli, Luisa. - (2023 Jul 12), pp. 1-189.

Availability:

This version is available at: 11583/2981490 since: 2023-08-31T14:46:30Z

Publisher:

Politecnico di Torino

Published

DOI:

Terms of use:

Altro tipo di accesso

This article is made available under terms and conditions as specified in the corresponding bibliographic description in the repository

Publisher copyright

(Article begins on next page)



**Politecnico
di Torino**

ScuDo

Scuola di Dottorato ~ Doctoral School

WHAT YOU ARE, TAKES YOU FAR

Doctoral Dissertation
Doctoral Program in Metrology (35th Cycle)

Dimensional measurements with X-ray Computed Tomography and application to Cultural Heritage

By

Luisa Vigorelli

Supervisors:

Prof. Alessandro Re, Supervisor
Prof. Sabrina Grassini, Co-Supervisor

Doctoral Examination Committee:

Prof. Daniela Di Martino, Referee, Università di Milano-Bicocca, Italy
Prof. Roberto Sacchi, Referee, Università di Torino, Italy
Prof. Guido Perrone, Politecnico di Torino, Italy
Prof. Carlo Trigona, Università di Catania, Italy
Prof. Jean-Marc Tulliani, Politecnico di Torino, Italy

Politecnico di Torino

2023

Declaration

I hereby declare that the contents and organization of this dissertation constitute my own original work and do not compromise in any way the rights of third parties, including those relating to the security of personal data.

Luisa Vigorelli

2023

* This dissertation is presented in partial fulfillment of the requirements for **Ph.D. degree** in the Graduate School of Politecnico di Torino (ScuDo).

To my loving family, especially those who are no longer here and watching me from there. I hope that I have made you proud of me.

Acknowledgment

Generally, I would like to express my sincere gratitude to all those who contributed to the successful completion of this thesis. Your support and guidance were crucial to achieving my academic goals, and I will always be grateful for your contributions.

First and foremost, I want to thank my thesis supervisors, prof. Alessandro Re and Sabrina Grassini for the opportunity they gave me three years ago when I started my PhD and their guidance, support, and encouragement throughout this project. Their expertise and mentorship helped me to navigate the complex challenges of this research and achieve my goals. I've learned much from both, and I hope to continue our collaboration in the future.

I would like to express my gratitude to prof. Alessandro Lo Giudice and the entire Solid State Physics group from the Physics Department of the University of Torino for the continuous and helpful collaboration and for their insightful comments and suggestions.

I would like also to acknowledge the Centro Conservazione e Restauro "La Venaria Reale" for the support related to the research carried out in the frame of my Ph.D. activity, in particular Dr. Paola Buscaglia and all the LaboS staff, together with all the master's degree students in Conservation and Restoration of Cultural Heritage.

I am also very grateful to Prof. Maurizio Galetto and Dr. Giacomo Maculotti for helping me with measurements of some samples with the ATOS Scanbox machine available at the Department of Management and Production Engineering (DIGEP) of the Politecnico of Torino.

I would like to acknowledge also Dr. Sara Aicardi, Dr. Paolo del Vesco, Dr Federica Facchetti and Dr Valentina Turina from the Museo Egizio di Torino, and

Matilde Borla, from the Soprintendenza Archeologia, Belle Arti e Paesaggio per la Città Metropolitana di Torino, for allowing me to perform the CT analyses on the wooden and bronze artefacts of the museum collection. I would like to extend my sincere thanks to the BeArchaeo project and Dr Roberta Zanini (in the framework of an OpenAIAR call) for allowing me to carry out part of my Ph.D. activity on archaeological samples.

I want also to acknowledge all the INFN CHNet-NICHE project collaborators, thanks to which I had the opportunity to learn more about neutrons and relative imaging techniques (not only science and measurement shifts, but also some board games to learn in the free time).

My gratitude extends to the Associazione Italiana di Archeometria, which awarded me with the "Sportello Giovani" grant, that allows me to participate and to present the results of my work to an international conference.

I am deeply grateful to prof. Marco Parvis, and prof. Emma Angelini and to all my colleagues from the COMETA (Corrosion Measurement Tools for Artefacts) group of the Politecnico of Torino and the Cultural Heritage people in the Solid State Physics group at the Physics Department of the University of Torino for their encouragement, assistance, and constructive feedback throughout this project. Their support and encouragement were invaluable in helping me to overcome any obstacles that arose during the course of this research. Thanks also to all the bachelor and master students which I had the opportunity to follow in these years and whose work I am proud of.

Lastly, I would like to express a special and sincere thanks to my family, my friends and Vincenzo for their unwavering support, understanding, and love during my studies. Their constant encouragement and motivation helped me to stay focused and determined to achieve my academic goals.

Thank you to all the people that made this journey possible.

Abstract

Computed Tomography (CT) is a non-invasive X-ray technique that makes it possible to obtain information about the internal structure of the object under study without taking samples. CT is now used in many applications for the study of different types of samples (industrial workpieces or archaeological artefacts). Since the data from CT contains complete volumetric information about the measured part, after reconstructing the two-dimensional projection images, it is possible to perform dimensional measurements of the external and internal structures and provide accurate dimensional and geometric information. For this reason, CT is often used for quality control in industrial applications, to detect defects in manufacturing and to perform measurements on parts with difficult-to-access internal microstructures. To achieve this goal, it is necessary to evaluate and analyse different aspects of a tomographic measurement, also using standard reference objects. This methodological approach is increasingly used in industry, but rarely in the field of cultural heritage; however, in some applications, a quantitative assessment of some features through dimensional CT measurements is of great importance. This is the case for wind instruments to obtain playable 3D printed replicas with acceptable tolerances compared to the originals. In this work, a woodwind instrument from the end of the 18th century, a “Piccolo”, is studied.

For the reasons described above, the principles of the analysis of industrial dimensional CT were adopted for the characterisation of the parameters during the acquisition and reconstruction phases. To this end, two reference objects for the performance characterisation of CT systems were developed as part of this work: a “ball bar” and a “ball plate”, which were used to identify, characterise and correct measurement errors in the CT volume and to evaluate the dimensional reproducibility of measurements. Their application seemed to be suitable for this task, especially the use of the ball plate, with which several CT tests were performed to analyse different CT parameters such as source voltage, magnification and sample orientation. Since the two objects are realised with ruby spheres and carbon fibres, volume segmentation of the spheres is easier for

evaluating sphere-to-sphere distances, which is a robust quantity for determining a correction factor for CT dimensions. Using this quantity, a scale error correction method was implemented to correct the original reconstructed volume datasets by correcting the voxel size when the distance between sphere centres measured by CT is compared to calibrated measures (in this case, the reference distances were measured using a non-contact structured light 3D volume scanner).

Once determined which factors affect dimensional CT measurements, the developed correction method was first applied to a LEGO brick, to test it on a regularly shaped object, and then to the musical instrument using the calibration objects scanned before and after the sample and together with it; a third test on the LEGO brick was performed using a calibrated feature of the sample itself. These tests were conducted to determine the best correction method.

At the same time, X-ray tomography has also been used to investigate and analyse different types of archeological artefacts from archaeological excavations and museum collections. These projects provided more important knowledge of the CT technique applied to different materials and with different aims, and different strategies have been implemented and used to achieve optimal results. During the PhD work, imaging analysis was also conducted using neutrons, which can provide complementary information with respect to X-rays for certain types of investigated material. In the framework of the INFN-CHNet NICHE project, a neutron imaging beamline was developed and characterised at the LENA centre in Pavia.

Contents

1. Introduction.....	13
1.1 Aim and context of the work	13
1.1.1 CT for Cultural Heritage: the case of historical musical instruments	15
1.2 Thesis overview	17
2. X-ray Computed Tomography	19
2.1 Theory of X-ray physics	19
2.1.1 Discovery and production	19
2.1.2 Radiation-matter interaction	21
2.2 Principle of X-ray Imaging techniques.....	24
2.2.1 Instrumentation	25
2.2.2 Measurements parameters.....	29
2.2.3 Image data acquisition	33
2.2.4 Data elaboration and reconstruction	34
2.2.5 Volume segmentation and surface model	35
3. Dimensional CT measurements	38
3.1 Introduction	38
3.2 Reference guidelines.....	39
3.3 Calibration objects.....	41
3.4 Experimental equipment.....	44
3.5 CT correction methodology.....	48

4. Results and Discussion	52
4.1 Ball bar tests	52
4.2 Ball plate tests.....	55
4.2.1 Number of projections	59
4.2.2 Sample orientation	61
4.2.3 Source focal spot size	65
4.2.4 Source voltage.....	67
4.2.5 Magnification.....	69
4.2.6 CT measurements over time	73
4.2.7 Discussion.....	75
4.3 Correction methodology application on samples	80
4.3.1 Preliminary tests	80
4.3.1.1 Ball plate + ball bar corrections (1-2).....	81
4.3.1.2 Ball plate corrected with ball plate before + after (3).....	83
4.3.2 LEGO brick.....	84
4.3.3 Piccolo Flute	88
4.3.4 Discussion.....	94
5. Case studies.....	100
5.1 CT investigation on wooden artefacts from the Museo Egizio of Torino	100
5.1.1 Bearers statuettes	102
5.1.2 Taweret statuettes	105
5.2 Microtomography analysis on different small artefact typologies	109
5.2.1 Pottery sherds.....	110
5.2.2 Roman glass fragments	114
5.3 CHNet_NICHE project: Neutron Imaging for Cultural HERitage.....	123
5.3.1 Neutron imaging	124
5.3.2 NICHE facility development	126

6. Conclusions.....	135
7. References.....	139
Appendix A: Instrumentation alignment	150
Appendix B: CT reconstruction and data analysis on Dragonfly	152
Appendix C: Center-to-center spheres distances of the Ball plate	157
Appendix D: Lego brick and Piccolo Flute measures	174
Appendix E: Visible light and radiographic images of <i>BeArcheo</i> pottery samples	176

List of Figures

Figure 1.1: Piccolo Flute; A: head, B: body, C: foot. Dimensions: h 33.9 × w 2.2 cm.....	17
Figure 2.1: Electromagnetic spectrum (from https://www.britannica.com/science/electromagnetic-spectrum).....	20
Figure 2.2: Schematic representation of an X-ray tube on the left and an X-ray spectrum with the Bremsstrahlung and Characteristic radiation formation phenomena on the right (Berger et al., 2018).	21
Figure 2.3: Emitted and transmitted X-ray photons with dependences	22
Figure 2.4: Schematic representation of X-rays-matter interactions (Guntoro et al., 2019)	23
Figure 2.5: (left) Attenuation coefficients of lead as function of incident X-rays energy (Schäfers et al., 2014); (right) effects of X-rays-matter interaction as function of energy (Singh, 2016).....	24
Figure 2.6: Typical CT process chain: from scanning of the object through acquisition of the projection images at defined angular positions, their reconstruction using proper software to a visualization of the 3D volume model.	25
Figure 2.7: Effect of radiation filtering (left) and effect of voltage and current (right) on X-ray tube spectrum (Amiri et al., 2021; Chhem & Brothwell, 2008)..	27
Figure 2.8: Schematic of X-ray CMOS detector (left) and principle of X-ray detection (right) (adapted from http://www.spring8.or.jp/en/).....	28
Figure 2.9: Schematic representation of a typical geometry of CT (top view). f is the focus size and p the detector pixel size.	30
Figure 2.10: Magnification (left) and penumbra (right) dependance on distances and source focal spot (X-RAY WorX GmbH, 2014).....	31

Figure 2.11: Schematic explanation of spatial resolution with resolved or not resolved closed points (left) and example of spatial target for x-ray imaging (right) (Castellano et al., 2007).	31
Figure 2.12: Contrast scale varying X-ray tube voltage (left); optical density as function of energy logarithm (right).....	32
Figure 2.13: 2D projection of the analysed object and an example of CT reconstruction with the software Dragonfly	35
Figure 2.14: Grey level histogram (logarithmic scale) used for volume segmentation; example of extracted ROI, where all voxels belonging to material (value 1) are segmented in purple.....	36
Figure 2.15: Determination of the object's surface from the extracted ROI...37	
Figure 3.1: Some of the main factors influencing the CT measurements grouped in five main categories (Ishikawa diagram) (Villarraga-Gómez et al., 2018).....	40
Figure 3.2: Some reference workpieces used for CT dimensional analysis and other CT tests (Kruth et al., 2011).	42
Figure 3.3: The ball bar and ball plate developed and used in this work as calibration objects; for the ball plate letters from A to Y are given to the 25 sphere as in the shown scheme, with the reference near the sphere A.....	43
Figure 3.4: Atos ScanBox and a detail of the projected narrow-band blue light from the instrument head on the ball plate positioned on the rotating stage.	44
Figure 3.5: CT setup at the Physics department (University of Torino) used in this work	45
Figure 3.6: LabVIEW program for CT acquisition (main window for setting CT acquisition parameters and minor window for setting of integration time)....	48
Figure 3.7: X-ray CT measurements of the calibration object (L_{CT}) plotted against reference dimensions (L_{ref}); the slope of the fit equation represents the correction factor f , while the intercept is close to 0. If f is less than one, it means that the CT measurements are larger than the real measurements and vice versa.	50
Figure 3.8: Schematic CT workflow for dimensional correction.....	51
Figure 4.1: Ball bar orientation during CT scan: horizontal, vertical and 45° tilted.	53
Figure 4.3: Standard deviations obtained from repeated measurements.....	56

Figure 4.4: Repeated ball plate SD before the correction (left) and linear regression fit (right).	57
Figure 4.5: Repeated ball plate SD after the correction (left) with a comparison example of the second measurement (right).	58
Figure 4.6: Repeated ball plate E_n values calculated between the three measurements before the correction (left) and between data before and after the correction for the three measurements (right).....	58
Figure 4.7: Repeated ball plate E_n values calculated between the CT and reference lengths before (left) and after (right) the correction.	59
Figure 4.8: SD data for datasets with different projection numbers before and after the correction (top) and E_n values before the correction (bottom).	60
Figure 4.9: Ball plate orientation during CT scan: projection examples of horizontal, vertical and 45° tilted position.....	61
Figure 4.10: Linear regression fit (top) and SD values before and after correction for the three-ball plate orientations (bottom).....	62
Figure 4.11: Ball plate E_n values calculated between the three orientations before the correction (left) and between reference and uncorrected CT distances (right).	63
Figure 4.12: CT slices of ball plate in the three tested positions.	63
Figure 4.13: CT slice of the ball plate in horizontal position with changed LUT, where reconstruction edges unsharpness, artefacts and x-ray absorption differences are visible (top) and the comparison with the same CT reconstructed slices of tilted and vertical datasets (bottom).....	64
Figure 4.14: Linear regression fit (top) and SD values before and after correction for the three focal spot size (bottom).....	66
Figure 4.15: Ball plate E_n values calculated between the three focal spot sizes before the correction (left) and then between reference and uncorrected CT distances (right).....	67
Figure 4.16: Linear regression fit (top) and SD values before and after correction for the two-source voltage (bottom).	68
Figure 4.17: Ball plate E_n values calculated between the two voltage datasets before the correction (left) and compared with reference values after the correction (right).	69

Figure 4.18: Ball plate magnification during CT scan (1.1×, 2.0× and 4.1×).	70
Figure 4.19: Ball plate SD before the correction (top left), linear regression fit (top right) and SD values after the correction for the three magnification datasets (bottom).	71
Figure 4.20: False colors CT slice with considered central spheres for the magnification tests, where for the 4× magnification image artefacts are visible near the edge spheres.	72
Figure 4.21: Ball plate E_n values calculated between the datasets after the correction (left) and with respect to the reference lengths (right).	73
Figure 4.22: Ball plate SD values before (left) and after the correction (right) for the three times.	74
Figure 4.23: Ball plate E_n values calculated between the datasets before (left) and after the correction (right).	74
Figure 4.24: Ball plate false colors CT slice for the magnification 2× dataset, where the difference between central spheres and close to the image edge is highlighted.	76
Figure 4.25: SNR evaluation for the different CT tests	78
Figure 4.26: SNR evaluation for the horizontal position CT tests.	79
Figure 4.27: SNR comparison between the vertical and horizontal position CT tests.	79
Figure 4.28: Ball plate SD values (left) and ball bar values (right) before and after the applied corrections.	82
Figure 4.29: Ball plate E_n values calculated between reference and CT distances (left) and between the three datasets (the one non corrected and the two corrected, right).	83
Figure 4.30: Ball plate SD values before and after the applied correction (top) and E_n values calculated for both non corrected and corrected data and between the three datasets (bottom).	84
Figure 4.31: LEGO brick used for CT correction tests, with indication of the measured quantities.	85
Figure 4.32: Sequence of CT acquisition for LEGO brick sample correction.	85

Figure 4.33: SD values of uncorrected CT scan.....	86
Figure 4.34: SD values of lengths and diameters of the different correction methods.....	87
Figure 4.35: SD values of c-c distances of the different correction methods.	87
Figure 4.36: SD values of c-c distances of the different correction methods.	88
Figure 4.37: CT projection of the Piccolo Flute components (from left: body, head and foot) with the ball bar. The objects are positioned vertically with the help of wooden sticks; the darker parts on the head and foot (more attenuating) represent the ivory rings decorations.	89
Figure 4.38: Piccolo Flute scheme of the three components with indication of the measured features.....	90
Figure 4.39: SD values of the uncorrected CT datasets, divided on the left based on the three flute parts (head, body and foot) and on the right based on the considered measured feature (diameters, lengths and holes diameters).	91
Figure 4.40: SD values of the non-corrected and corrected CT datasets, divided based on the considered measurand (top left: diameters; top right: lengths; bottom: holes).	92
Figure 4.41: Deviation color map of the corrected BB head dataset with respect to the uncorrected one.	93
Figure 4.42: Deviation color map of the corrected BB body dataset with respect to the uncorrected one.	93
Figure 4.43: Deviation color map of the corrected BB foot dataset with respect to the uncorrected one.	94
Figure 4.44: En values obtained for the LEGO brick comparing CT corrected data with each other (left) and with reference distances (right).	95
Figure 4.45: En values obtained for the flute comparing CT corrected data with reference distances for all the three components (left) and for the foot (right).	96
Figure 4.46: SD values divided by flute parts (top left: head; top right: body; bottom: foot), with indication of considered tolerance of ± 0.1 mm (legend: d= diameters; l= lengths; h=holes).....	97
Figure 5.2: The analyzed Bearers statuettes, frontal and lateral views (left: statuette A, n° inv. S. 08795, 60×13×26 cm; right: statuette B, n° inv. S. 8796,	

45×15×21 cm), with the details of the heads' radiographs where a different basket-head junction is visible. 102

Figure 5.3: CT horizontal and vertical slices of the two statuettes (a-e: statuette B; e-f: statuette A), where the use of wooden dowels is visible (a: central pith highlighted in the yellow square; b-c: basket; d-e: junction of the arms; f-g: basket and shoulders respectively). Green arrow: defect; orange arrows: cracks; blue arrows: thicker preparation layer; yellow arrows: wooden dowels with filling material; red arrow: wood pith, also visible in the entire figure on the right. (Vigorelli et al., 2022). 104

Figure 5.4: CT slices of the two statuettes (a: statuette B; b: statuette A) in which the preparation layer is visible (pink arrow: lack of material; blue arrow: thicker preparation layer; green arrow: defects); c: difference in the junction legs-base (up: statuette B; down: statuette A). (Vigorelli et al., 2022) 105

Figure 5.5: The analyzed Taweret statuette (Cat. 528), frontal (a) and lateral (b) views. (Vigorelli et al., 2021) 107

Figure 5.6: CT slices of the statuette: (a,b) horizontal sections; (c–e) longitudinal slices. In all the sections the wood structure (vessels and growing rings) is visible (green arrows: preparation layer in the face area; blue arrows: fractures inside the preparation layer; orange arrows: thin preparation material for the gold leaf adhesion). (Vigorelli et al., 2021) 108

Figure 5.7: Profile plots along A and B (green arrow: preparation layer; orange arrow: preparation material for the gold leaf adhesion; pink arrow: material layer above the gold leaf). (Vigorelli et al., 2021) 108

Figure 5.8: Backscattering image by means of SEM, the gold layer is in light gray (a); (c) profile plot along A line shown in (b), only wood; (d) profile plot along B line shown in (b), gold on thin preparation layer. (Vigorelli et al., 2021) 109

Figure 5.9: Experimental setup for the local-CT and scheme of analyzed volume. 111

Figure 5.10: TT2 sherd sample and CT vertical slice reconstruction, in which ring artefacts are removed with appropriate filters; voids (black areas) and different minerals with different radiopacity are visible inside the reconstructed volume (green and purple circles). 112

Figure 5.11: Segmented parts of the selected volume for TT2 sample, with the indication of the “cutting” planes in the object (blue: porosity; red: inclusions; purple: ceramic matrix).....	113
Figure 5.12: Comparison between a reconstructed CT slice (upper figure) with a SEM image of sample SH_1 (lower figure).....	114
Figure 5.13: The analyzed glass fragments. Top line: altered samples; bottom line: decorated samples.	115
Figure 5.14: CT reconstruction and analysis of sample 581755, where fractures (orange, ~10% of the entire volume) and filled minerals (blue and yellow) are segmented.	117
Figure 5.15: CT reconstruction and analysis of sample 591639, where the fractures (blue areas, ~7.3% of the entire volume) are segmented. Detail of an optical microscope image is also shown for comparison.	117
Figure 5.16: CT reconstruction and analysis of sample 591554, where the corrosion pits (purple area) are segmented and a detail of a hole depth.....	118
Figure 5.17: CT reconstruction of sample 581681, where the corroded patina and holes are segmented (orange area). A detail of the different corrosion layers that follow the glass surface and the concentric layers in one of the holes are also shown.	119
Figure 5.18: CT reconstruction and analysis of sample 591748, with details of the decorative stripes are shown. Precipitated crystals are found only in the colored layers (segmented in red).....	120
Figure 5.19: CT reconstruction and analysis of sample 591612, with details of the gold leaf, for which the average thickness was calculated.	121
Figure 5.20: CT reconstruction and analysis of sample 2.2243, where the colored rods used for the decoration and their orientation are clearly visible.	121
Figure 5.21: CT reconstruction of samples 2.2269-70-71, where porosity, precipitated crystals and alteration were highlighted from the analysis of slices and volume segmentation.	122
Figure 5.22: CT reconstruction and analysis of sample 2.2048, with details of the decorative drops and their segmentation based on gray levels are shown.	123
Figure 5.23: Interaction of matter with X-rays (top left) and neutrons (bottom left); mass attenuation coefficients for thermal neutrons and 100 keV x-rays for the different chemical elements (right) (Strobl et al., 2009).....	124

Figure 5.24: Greyscale attenuation maps the different interaction behaviour of thermal neutron (left) and X-Rays (right) with 1cm thickness of given materials. The darker the color, the stronger the attenuation, and vice versa (Oriol Sans Planell, 2022).	125
Figure 5.26: The LENA reactor (PV) and the installed NICHE setup in the shielded room. Neutron channel with pinhole and custom-made camera box for imaging analysis is shown.	127
Figure 5.27: Some of the bronze testing samples analyzed and the corresponding neutron radiography. The green samples are the ones treated with different chemical solution to realized artificial corrosion patinas.	129
Figure 5.28: Mass attenuation coefficient results from the analyzed bronze samples; it is possible to notice the difference between the Cu-Sn alloys, where Sn% doesn't influence the results, and the Cu-Sn-Pb where if Pb% increase, Σ/ρ decrease.	130
Figure 5.29: Mass attenuation coefficient results obtained for the patinated samples; in this case, no difference respect to the non-altered sample could be highlighted because of the low thickness of the corrosion layer.	131
Figure 5.30: CT slice obtained for sample C.0887 (cat); the mummy is visible inside the coffin (red arrow: bones), together with filling bundles. Blue arrows indicate the metal pins, while purple arrow indicates the casting core in the whole head.	133
Figure 5.31: CT slice obtained for sample C.2381 (crowned hawk); the mummy is visible inside the bronze box, together with many bundles (red arrows: bones; orange arrow: detail of textile). Green arrows indicate bronze porosity, visible also in the X-ray CT.	133
Figure 5.32: CT slice obtained for sample C.0893 (cat head); casting core with metals contaminants is visible inside. The green arrow indicates bronze porosity in the left ear, while the red arrow indicates the presumably gold material inside the right ear hole.	134
Figure 5.33: CT slice obtained for sample C.5220 (hawk); casting core remains are visible inside the two broken legs (purple arrows), together with bronze porosity (green arrows). Yellow arrows indicate lead filling, visible with different radiopacity in neutron CT (left) and x-ray radiography (right). Blue arrow indicates a metal pin.	134

Figure A.1: Ball bar orientation during CT scan: horizontal, vertical and 45° tilted.	151
Figure A.2: Ball bar orientation during CT scan: horizontal, vertical and 45° tilted.	151
Figure B.1: Ball bar orientation during CT scan: horizontal, vertical and 45° tilted.	153
Figure B.2: Ball bar orientation during CT scan: horizontal, vertical and 45° tilted.	154
Figure B.3: Ball bar orientation during CT scan: horizontal, vertical and 45° tilted.	154
Figure B.4: Ball bar orientation during CT scan: horizontal, vertical and 45° tilted.	155
Figure E.1: Visible light and radiographic images of <i>BeArchaeo</i> pottery samples.....	176

List of Tables

Table 3.1: Distance between spheres centers of the ball bar	44
Table 3.2: Specific of X-ray source.....	46
Table 3.3: Specific of X-ray detector	46
Table 3.4: Specific of rotation stage.....	47
Table 3.5: Performed measurements to investigate influence factors.	51
Table 4.1: Ball bar CT acquisition parameters.....	53
Table 4.2: Ball bar CT measurements before and after correction	53
Table 4.3: Ball bar E_n values before and after correction	54
Table 4.4: Ball bar E_n values between orientations.....	54
Table 4.5: Repeated ball plate CT acquisition parameters.....	55
Table 4.6: Repeated ball plate CT values after application of correction factors.....	57
Table 4.7: Ball plate CT acquisition parameters	59
Table 4.8: Ball plate CT acquisition parameters for orientation test.....	61
Table 4.9: Ball plate CT values after application of correction factors	62
Table 4.10: Ball plate CT acquisition parameters	65
Table 4.11: Ball plate CT values after application of correction factors	66
Table 4.12: Ball plate CT acquisition parameters	67
Table 4.13: Ball plate CT values after application of correction factors	69
Table 4.14: Ball plate CT acquisition parameters	70
Table 4.15: Ball plate CT values after application of correction factors	71

Table 4.16: Ball plate CT values after application of correction factors	74
Table 4.17: SD minimum and maximum values before and after correction	77
Table 4.18: Ball plate + ball bar CT acquisition parameters.....	81
Table 4.19: CT parameter and voxel size after application of correction factors.....	81
Table 4.20: Ball bar En values calculated before and after the correction.....	82
Table 4.21: CT values after application of correction factors.....	86
Table 4.23: CT values after application of correction factors.....	90
Table 5.1: CT acquisition parameters for the artefacts of the Museo Egizio	101
Table 5.2: CT parameters for pottery analysis	111
Table 5.3: Percentage estimation of the three segmented features.....	113
Table 5.4: μ -CT acquisition parameters for glass fragments.....	115
Table 5.5: Technical specification of the NICHE set-up	128
Table 5.7: Technical specification of TU-Delft reactor and neutron CT acquisition parameters	132
Table 1: Reference c-c spheres distances measured by ATOS Scanbox (± 0.002 mm)	157
Table 2: CT c-c spheres distances of 150kV measurements, rep.1 before and after correction (± 0.06 mm).....	158
Table 3: CT c-c spheres distances of 150kV measurements, rep.2 before and after correction (± 0.06 mm).....	159
Table 4: CT c-c spheres distances of 150kV measurements, rep.3 before and after correction (± 0.06 mm).....	160
Table 5: CT c-c spheres distances of orientation measurements, horizontal before and after correction (± 0.05 mm)	161
Table 6: CT c-c spheres distances of orientation measurements, vertical and spot S before and after correction (± 0.05 mm) Table 7: CT c-c spheres distances of orientation measurements, tilted before and after correction (± 0.05 mm).....	162
Table 8: CT c-c spheres distances of focal spot size measurements, spot M before and after correction (± 0.05 mm)	164

Table 9: CT c-c spheres distances of focal spot size measurements, spot L before and after correction (± 0.05 mm)	165
Table 10: CT c-c spheres distances of n° of proj. measurements, no binning before and after correction (± 0.05 mm)	166
Table 11: CT c-c spheres distances of n° of proj. measurements, binning 2x and 90 kV before and after correction (± 0.05 mm).....	167
Table 12: CT c-c spheres distances of n° of proj. measurements, binning 3x before and after correction (± 0.05 mm)	168
Table 13: CT c-c spheres distances of voltages measurements, 150 kV before and after correction (± 0.05 mm/ ± 0.04).....	169
Table 14: CT c-c spheres distances of magnification measurements, M1 before and after correction (± 0.06 mm)	170
Table 15: CT c-c spheres distances of magnification measurements, M2 before and after correction (± 0.06 mm)	170
Table 16: CT c-c spheres distances of magnification measurements, M4 before and after correction (± 0.04 mm)	170
Table 17: CT c-c spheres distances of measurements at different time, time 0 before and after correction (± 0.06 mm)	171
Table 18: CT c-c spheres distances of measurements at different time, after 3 months before and after correction (± 0.06 mm).....	172
Table 19: CT c-c spheres distances of measurements at different time, after 4 months before and after correction (± 0.06 mm).....	173
Table 20: Lego brick reference measures of lengths (A,B, and C), knobs diameter and knobs' center distances obtained with ATOS Scanbox (mm).	174
Table 21: Piccolo Flute reference measures of diameters, lengths and holes obtained with a centesimal caliper (instrumental error ± 0.01 mm). Diameters uncertainty = ± 0.03 mm; lengths uncertainty = ± 0.07 mm; holes diameters uncertainty = ± 0.04 mm.....	175

Chapter 1

Introduction

1.1 Aim and context of the work

This thesis concerns the application of X-ray tomography in the field of cultural heritage research; this measurement technique is used for the study of objects of historical interest, especially woodwind musical instruments from the end of the 18th century. The research aims to create sounding physical copies of these objects, made with modern additive manufacturing techniques. To achieve this goal, it is necessary to evaluate and analyse various aspects of a tomographic measurement, also using standard reference objects.

Computed Tomography (CT) is a non-destructive technique based on X-rays that allows to obtain information on the internal structure of the analysed object without the need to take samples (Greg Michael, 2001; Kak et al., 2002; Withers et al., 2021). Originally developed for medical purposes, CT is now widely used in many other fields of application, such as industry (Carmignato et al., 2017), materials science (Wevers et al., 2012) and cultural heritage (Casali, 2006; Morigi et al., 2010), thanks to the non-invasiveness and the strong penetrating power of the radiation. This technique allows the visualisation and the study of the internal parts of the human body in the case of medical purposes, where low X-ray energy is required to avoid problems for patients, and for inner characteristics of different types of objects depending on the field of application; in industry, CT is often used for quality control (i.e. inspection of large castings and mechanical samples), in order to reveal defects in the manufacturing and also measurements

of components containing hard-to-access internal micro structures, like components produced by additive manufacturing, as well as measurements of assemblies (Villarraga-Gómez et al., 2019). CT is nowadays also very common in the cultural heritage field, since a non-invasive technique is required for the investigation of archaeological and historical artefacts to preserve their integrity; imaging analysis allow researchers to obtain valuable information about the nature of materials, manufacturing techniques and state of conservation of the objects (Albertin et al., 2019; Otte et al., 2013; Re et al., 2016; Wilson et al., 2017).

Using CT, a complete three-dimensional model of the scanned part can be produced in a relatively short time, thanks to the interaction of the X-ray beam with the object; data analysis results in tomographic slices of the artefact in the three spatial directions, representing a “virtual section” through the entire volume. The images obtained are a representation of the X-ray attenuation coefficient distribution of the different materials present, usually represented as greyscale images. Thanks to the improved technology of both hardware and software, laboratory instruments for CT analysis are now widespread and easily accessible, although synchrotron radiation is sometimes required to gain a more detailed insight into objects. Industrial CT is now being developed into a quantitative inspection technique: since CT data contain complete volumetric information about the measured part, it is possible to perform dimensional measurements of external and internal structures and provide accurate dimensional and geometrical information with micrometric accuracy (Kruth et al., 2011; Trent Neel et al., 1998; Villarraga-Gómez, 2016; Villarraga-Gómez et al., 2014). This type of analysis approach is increasingly used in industry and in metrology laboratories generally using commercial equipment (e.g., Nikon, Skyscan etc...). Measurement tasks focus on the determination of geometric features such as thickness, diameters and lengths, often in comparison with reference data (CAD model or reference objects, Brunke et al., 2010). This type of CT analysis is rarely applied to cultural heritage, as in most cases, a qualitative study of artefacts is usually performed. However, to obtain playable 3D printed replicas of historic wind musical instruments, a quantitative assessment of some features through dimensional CT measurements is a very important issue.

For these reasons, the principles of industrial dimensional CT analysis are applied in this work: the characterisation of CT parameters during the acquisition and the reconstruction phases is carried out using calibration objects, like ball bars (often used for metrological purposes), to evaluate the reproducibility of CT measurements in terms of dimensions, to finally obtain 3D copies that meet the

required tolerance with respect to the original artefacts. Tolerances in the manufacture of instruments are not precisely defined by experts in the field, as there are different opinions on the subject. Some publications state tolerances between 0.1 mm and 0.2 mm, which vary depending on the instrument part (Forrester et al., 2018; Ignesti, 2007). Other authors discuss the problem of tolerances for the measurements of the internal parts and give a maximum deviation of ± 0.1 mm (Karp, 1978).

1.1.1 CT for Cultural Heritage: the case of historical musical instruments

The initial problem in this case is conservation: historical wind instruments belonging to museums and private collections are usually unplayable because the moisture produced by the musician's breath during a performance is absorbed by the instrument itself. As old instruments are usually made of wood, variations in humidity and temperature can cause irreversible damage and permanent deformation that would irrevocably alter the sound of the instrument; the conservation strategy chosen thus robs the community of its original sound (Barclay, 1996; Hunt, 2012). The need to preserve historical musical instruments also stems from the fact that a piece of historical music may sound different on modern instruments than on those used at the time the piece was written. In the past, this problem was partly solved by asking expert craftsmen to make replicas based on manual measurements of the originals. However, the degree of precision and thus compatibility between the original and the copy is not yet high enough, as both taking the accurate measurements and making the copy are difficult. The possibility of using non-invasive analysis techniques and digital technologies for measurements and subsequent modelling offers new opportunities for the reproduction of historical wind instruments and thus for the restoration of their forgotten sound (Howe et al., 2014).

In recent years, the process of recording CT musical instruments has been addressed in previous projects and detailed technical guidelines have been published (Bär, 2018). However, in some cases, photogrammetry was used as a method to first create a digital model of the object (Katz, 2017), but this technique has the limitation that it only reproduces the external surface and not the internal features; in other cases, the use of CT was limited to a qualitative inspection (Lehmann et al., 2018; Van den Bulcke et al., 2017), and no particular attention was paid to dimensional measurements when 3D printing was carried out (Bellia, 2019), so further metrological and practical specifications are needed. With

modern technologies, such as X-ray tomography and additive manufacturing, it is possible to reproduce these artefacts first virtually and then physically; however, the dimensions of certain features in the copies (e.g., lengths, hole diameters, etc.) need to be very accurate. In fact, the sound of low-pressure wind instruments is largely determined by the shape and dimensions of the vibrating inner cavity, with very limited influence from the material the instrument is made of (Boutin et al., 2017; Coltman, 2005). This aspect gives us the opportunity to use 3D printing to produce copies (Damodaran et al., 2021), using in this case a non-toxic polymer material with a density like wood.

The analysis protocol developed for this work follows different steps:

1. Evaluation and choice of CT scan parameter (setup geometry, X-rays energy, object position, etc...) and instrumentation alignment
2. CT scan of calibration reference objects (before and after the sample scan)
3. CT scan of the sample together with a reference object
4. CT reconstruction and dimensional evaluations
5. CT correction and 3D digital model extraction
6. 3D printing of the copy and dimensional evaluations
7. Evaluation of sound (acoustic measurements)

For this work, steps 1 to 5 were performed and further developed together with other measurements previously performed on the calibration objects to: (i) identify all relevant influencing factors and potential sources of error in the tomographic process, (ii) provide a quantitative result about the effects of the influencing factors on the measured quantities, and (iii) finally optimize and test the measurement procedures. Prior to these tests, a preliminary CT analysis and 3D printed copies of some musical instruments were also carried out to get a preliminary evaluation of the accuracy level of the 3D printing process. The results of a single woodwind instrument, with which further tests were carried out, are presented in chapter 4. The novelty of the analysis presented here lies in the aim of the study: the application of metrology in the field of cultural heritage, in particular the use of CT dimensional measurements and additive manufacturing to achieve a high level of compatibility between the original instruments and their replica, both in terms of shape and sound.

From an initial set of three woodwind instruments belonging to a private collection (Tansella et al., 2022), including a modern copy of a Renaissance flute, a historical “Piccolo” (Figure 1.1) was considered for this study because the

dimensions of its components allow the entire object to be acquired in a single CT scan, avoiding a later stitching operation for this initial test; the maker is unknown, but it is probably an English or American production. This flute is made of boxwood and is distinguished by the presence of three ivory rings. Unlike many European historical piccolos, which consist of two or four parts (<https://mimo-international.com/MIMO/>) this one consists of three parts: the head, the middle part and the foot with a brass key. This observation also helps in dating the instrument, as all three-piece instruments are dated between the last years of the 18th century and the beginning of the 19th century.

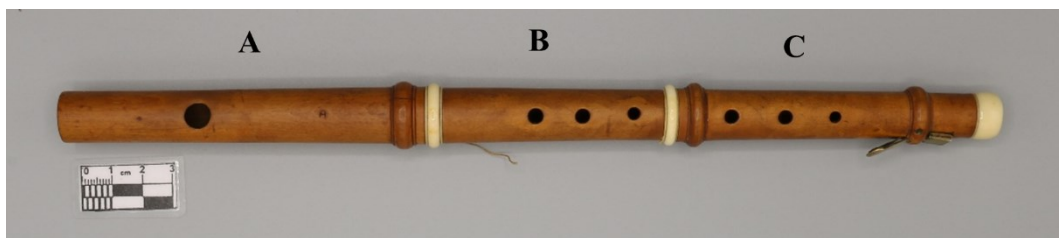


Figure 1.1: Piccolo Flute; A: head, B: body, C: foot. Dimensions: h 33.9 × w 2.2 cm

1.2 Thesis overview

The structure of the Ph.D. thesis is schematically described as follow:

- **Chapter 2** describes basic theory about X-ray physics and the main principle of Imaging techniques (i.e., CT); the main instrumentation (hardware and software) needed for analysis is presented, too.
- **Chapter 3** discusses the basic principles of dimensional CT analysis and presents the calibration objects developed and used for the aim of the work; a description of the applied correction methodology is also reported.
- **Chapter 4** gives a complete overview of the obtained results, both on calibration objects and the application of the analytical procedures on the Piccolo flute; also, a further test and relative results on a more regular item (a LEGO brick) is presented.
- **Chapter 5** reports CT analysis applied on different kinds of artefacts realized during the PhD period.

- **Chapter 6** summarizes the findings and achievements of this work. Suggestions for future work based on this Ph.D. project are provided, too.

All the work that will be illustrated was performed by the PhD candidate, with the support and suggestions of the supervisors, from the bibliographic research to the elaboration of methods, CT scan execution and data analysis strategies.

Chapter 2

X-ray Computed Tomography

2.1 Theory of X-ray physics

X-rays are electromagnetic waves with the same basic physical properties as the other components of the electromagnetic spectrum (visible light, IR, UV, etc., Figure 2.1). The wavelength range of X-rays is between about 10^{-8} and 10^{-12} m, which corresponds to photon energies between about 10^2 and 10^5 eV. Their energy is much larger than visible radiation, more precisely their wavelength is of the order of atoms, and this is the reason why they can penetrate materials opaque to visible light and be absorbed by atoms. Due to the nature of electromagnetic radiation (quantum mechanical theory), X-rays can be described as photons carrying discrete amounts of energy and momentum. The properties of X-rays (high penetrating power and high energy) lead to a wide range of applications, from medicine to industry and material analysis.

2.1.1 Discovery and production

X-rays were discovered in 1895 by the physicist Wilhelm Conrad Röntgen when, while researching the passage of cathode rays in a vacuum tube, he noticed that some strips of paper covered with fluorescent material lit up when brought close to the tube. On this occasion, in 1895, Röntgen took the famous first photograph of his wife's hand, creating the first X-ray image in history. This discovery earned him the Nobel Prize in Physics in 1901 (Rossi & Kellerer, 1995).

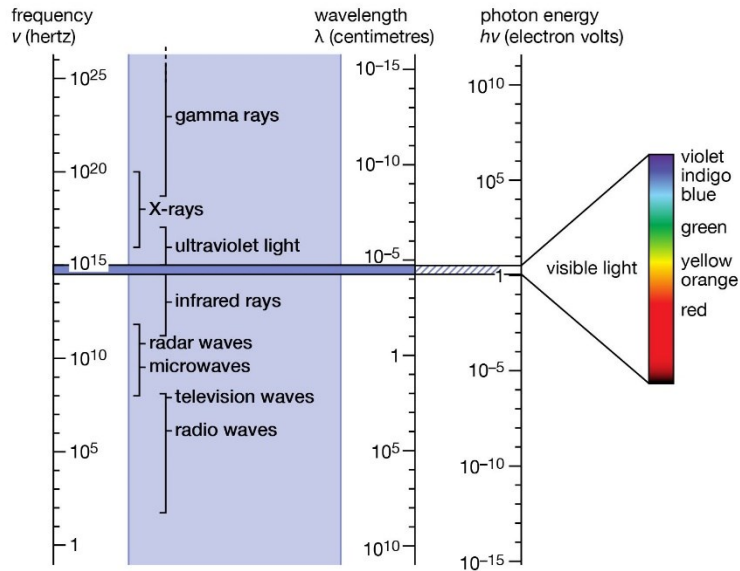


Figure 2.1: Electromagnetic spectrum (from <https://www.britannica.com/science/electromagnetic-spectrum>)

The most common apparatus for producing X-rays is the X-ray tube (Figure 2.2), in which high vacuum is created (10^{-2} – 10^{-6} Pa) for radiation production. The emission of X-rays takes place through an unshielded emission window, generally in beryllium. Inside the tube are the cathode, usually a tungsten filament through which a current flow that causes the emission of electrons through the thermionic effect, and the metal anode (usually W, Cu, Mo) onto which the electrons strike thanks to a high potential difference (Seibert, 2004). The production of X-rays is due to the loss of energy from electrons that interact with the anode material. The voltages applied between the two poles vary according to the type of use, normally in the medical field from 40 to 130 kV, while in the industrial one goes from 90 kV to 450 kV, even reaching 600 kV in some cases.

The production of X-rays is based on two different processes: first, as the colliding electrons pass the nucleus of an anode atom, they can be deflected and slowed down by the anode material, producing photons of different energy and thus a continuous radiation called Bremsstrahlung (“bremsen” is the German verb for “slowing down”); the amount of kinetic energy lost in this way can vary from zero to the total incident energy. Secondly, the incident electron can also interact with an electron of the inner shell of the target, which is thereby removed, leaving a gap in the atomic shells that can be filled with an electron of the outer shell; this

transition produces the emission of an X-ray photon with an energy corresponding to the difference in the binding energies of the orbital electrons involved. This leads to a series of characteristic peaks at certain energies and is material-dependent (Characteristic radiation). The total emission spectrum is thus characterised by a series of peaks that are due to the emission of characteristic X-ray radiation, as well as by a continuous distribution of radiation that can vary in intensity. The energy maximum corresponds to the energy of the electrons hitting the anode: the higher the accelerating voltage, the stronger the interactions with the sample and the stronger the X-ray emission. The X-ray energy spectrum (Figure 2.2), defining the penetrative power of the radiation, as well as its relative attenuation passing through materials of different densities, is affected by: tube current, tube voltage, filtration, and target material (see section 2.2.1).

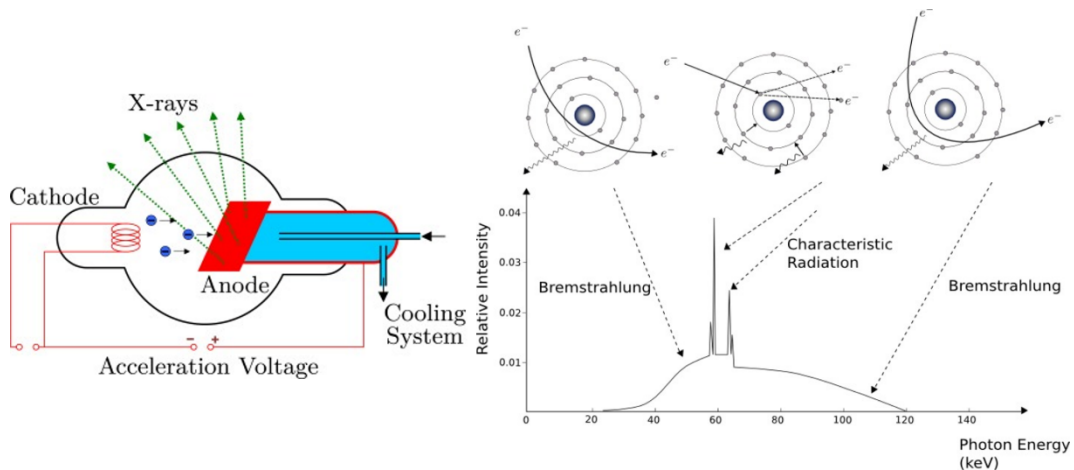


Figure 2.2: Schematic representation of an X-ray tube on the left and an X-ray spectrum with the Bremsstrahlung and Characteristic radiation formation phenomena on the right (Berger et al., 2018).

2.1.2 Radiation-matter interaction

X-rays have a high penetrating power into matter, and the thickness of the material they can penetrate depends mainly on three factors: the energy of the X-rays (determined by the voltage of the X-ray tube, section 2.2.1), the atomic number Z and the density of the material under investigation (Seibert & Boone, 2005). The intensity of the transmitted X-rays after interaction with the object is given by the Lambert-Beer exponential law:

$$I = I_0 e^{-\mu x} \quad (2.1)$$

If I_0 is the initial X-ray intensity, after a material thickness x , a radiation intensity equal to I is transmitted. The intensity of the transmitted beam decreases exponentially with increasing thickness x and the attenuation coefficient μ of the traversed material (Figure 2.3). The attenuation coefficient μ indicates the probability that a photon is absorbed or scattered by the atoms of the material per unit distance crossed. It depends on the atomic density, the atomic number Z and the photon energy. Equation (2.1) refers to a specific X-ray energy and to an absorber type. Therefore, it must be adapted for inhomogeneous materials and polychromatic X-rays:

$$I = \int I_0(E) e^{-\int \mu(x,E) dx} dE \quad (2.2)$$

where the exponential integral is a line integral taken along the direction of propagation.

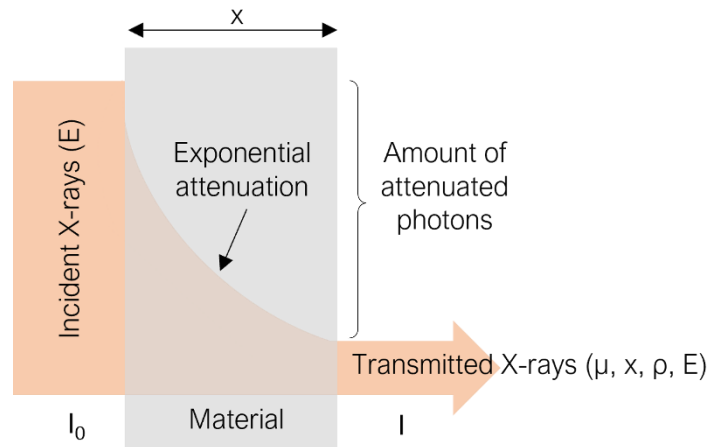


Figure 2.3: Emitted and transmitted X-ray photons with dependences

Among X-rays-matter interaction processes, those that contribute to the attenuation of X-rays as a function of the thickness of the material traversed and are therefore important for imaging include absorption and scattering, i.e., the photoelectric effect and the Compton effect (Seibert & Boone, 2005). In the former, the incident photon is absorbed by an atom, transferring its energy to one of the bound electrons, which is ejected from the shell. The resulting gap is occupied by one of the outermost electrons to stabilise the atom, and this process can lead to a characteristic X-photon emission (fluorescence) or Auger emission (energy is transferred to a bound electron that is ejected from the atom, Figure 2.4). In the Compton effect, incident X-rays interact with loosely bound electrons

in the outermost shells of the atom; the incident photon is deflected from its original direction by transferring energy to the electron, which is ejected from the atom. The result of the Compton effect is thus the output photon with a lower energy (Figure 2.4).

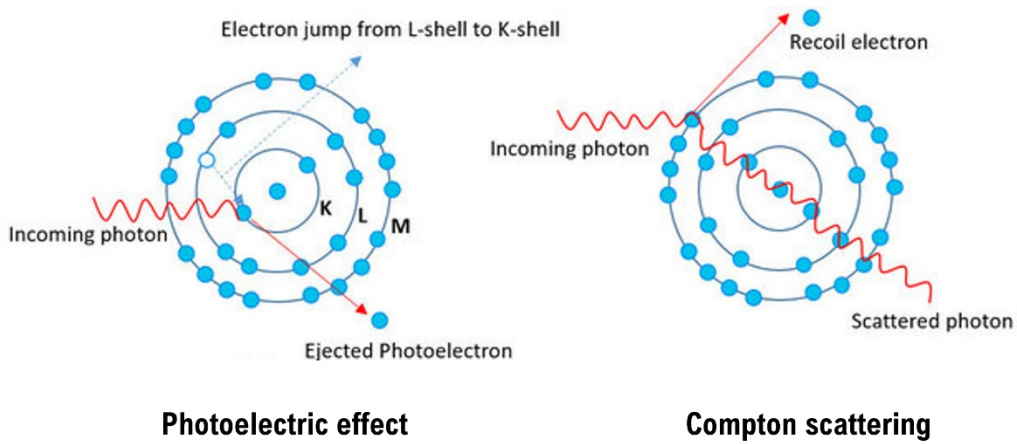


Figure 2.4: Schematic representation of X-rays-matter interactions (Guntoro et al., 2019)

From Figure 2.5, the prevalence of the photoelectric effect at low energies can be observed; the Compton effect dominates in the intermediate energy range, but the amplitude of this region decreases as the atomic number Z increases. Another important interaction phenomenon is electron-positron pairs production (Seibert & Boone, 2005); this phenomenon becomes relevant at higher energies which do not fall within the working range of the X-ray tube used. Since the value of the attenuation coefficient generally considers the number of atoms/cm³ and the probability that a photon is absorbed or scattered by a nucleus or an electron of one of these atoms, the linear attenuation coefficient can be written as:

$$\mu_{tot} = \mu_{ph} + \mu_{sc} + \mu_{pp} \quad (2.3)$$

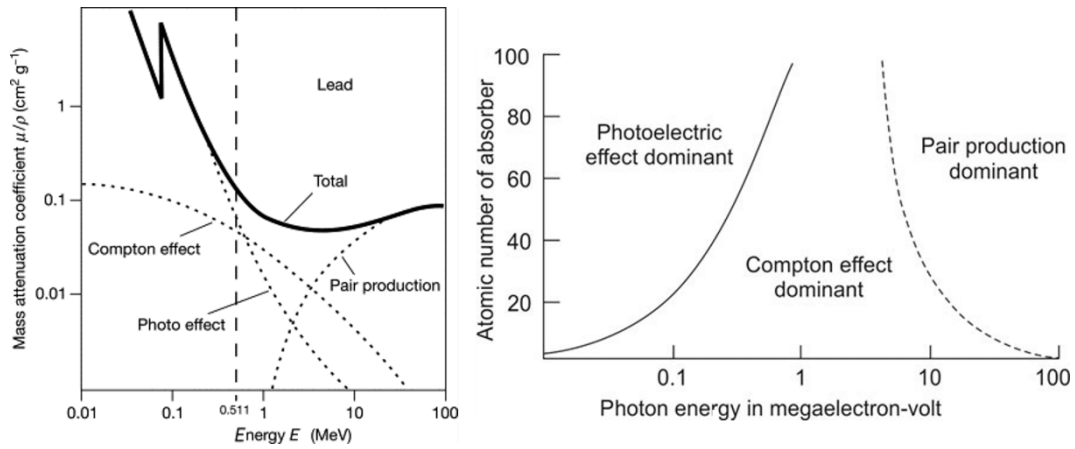


Figure 2.5: (left) Attenuation coefficients of lead as function of incident X-rays energy (Schäfers et al., 2014); (right) effects of X-rays-matter interaction as function of energy (Singh, 2016)

2.2 Principle of X-ray Imaging techniques

Imaging techniques are based on the transmitted radiation captured by a detector resulting from the interaction of the beam with the object under investigation, placed in between the source and the detector. An X-ray image can therefore be defined as a two-dimensional view of the different components of the sample that attenuate the incident beam. Since it is a two-dimensional projection of a three-dimensional object, it is necessary to take X-ray images of the sample from several angles to obtain depth information, thus performing computed tomography (CT). By recombining the two-dimensional information with suitable mathematical algorithms, the cross-sections of the object (slices) are reconstructed, resulting in a three-dimensional model that allows a complete visualisation of the sample morphology. The reconstructed 3D object consists of voxels (volumetric pixels), where each voxel represents the local attenuation coefficient and a point-by-point map of the μ -value of the entire volume is obtained from each slice. A schematic representation of the CT process chain, including the actual scanning of the object, the acquisition of the projection images, the reconstruction and the final visualisation of the volumetric model, can be seen in Figure 2.6. The CT was introduced in 1972 with the development of the first scanner by Godfrey Newbold Hounsfield (Nobel Prize 1979). Microtomography is an investigation technique that makes it possible to obtain images of significantly higher quality and resolution compared to simple

tomography. The distinction is based on the pixel size of the detector: if this is in the order of micrometres, the technique is called microtomography. In this thesis, we work with a detector whose pixels have micrometric dimensions, which leads to better analysis accuracy.

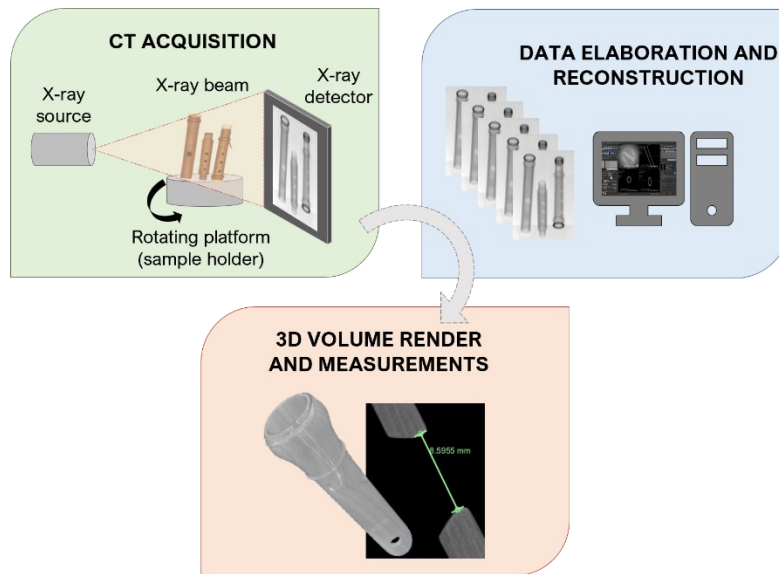


Figure 2.6: Typical CT process chain: from scanning of the object through acquisition of the projection images at defined angular positions, their reconstruction using proper software to a visualization of the 3D volume model.

2.2.1 Instrumentation

The instruments required for radiographic and tomographic analysis are an X-ray source, a rotating platform for moving the sample and a detector. The movement of the detector, the platform and the acquisition of the images are controlled by a PC. The obtained data is finally analysed by dedicated software.

X-ray source

Generation of X-rays from X-ray tube has been described in section 2.1.1; generally, only 1 % of the energy of the electrons hitting the anode is available to produce X-rays, the rest is converted into heat, which can lead to degradation or even melting of the anode. For this reason, tubes with rotating anodes are usually used to distribute the heat over a larger area. In addition, X-ray radiation sources with an innovative liquid anode technology have recently been developed to avoid

deterioration problems and to achieve high brilliance. The radiation produced emerges in an area of the anode called focal spot, whose size contributes to the resolution of the X-ray image (section 2.2.2., equation 2.7.) Good focusing of the electron beam is required, resulting in a small focal spot, to obtain images with good spatial resolution. For this reason, the size of the focal spot together with the intensity of the emitted X-rays must be carefully selected to produce a good X-ray image.

Since the X-rays produced are emitted in an isotropic way and must be addressed on the sample, the emission angle of the radiation is limited by a lead shield. A filter can be placed in front of the exit window, generally made of a suitable thickness of aluminium or copper, which serves to harden the X-ray spectrum produced by the tube and to filter out low-energy photons that are not useful for radiographic and tomographic purposes. The average energy of the emission spectrum increases (Figure 2.7), which leads to an improvement in image quality and reduce possible image artefacts (e.g., beam hardening artefacts, Barrett & Keat, 2004). However, when the low-energy photons are filtered out, the number of X-rays is reduced, resulting in a lower signal-to-noise ratio (SNR).

The formation of the image on the detector is influenced by the energy, the number and the scattering of the X-rays inside the object: if the energy of the X-rays is too low, they cannot reach the sample or are completely absorbed, so that the object is underexposed; if it is too high, they reach the sample but most of them don't interact with the atoms, so that the object is overexposed. The energy of the emitted X-rays must be sufficient for the interaction with the sample and the transmitted radiation to reach the detector.

Working with X-ray tubes, three parameters can be set: the voltage (in kV) and the current (generally in mA or μA) between the anode and the cathode, which determine the energy interval and the number of X-rays emitted, as well as the size of the focal spot, if the equipment allows it. Finally, another important parameter is the power of the tube (W), which depends on the voltage and current set and varies up to a maximum value that must not be exceeded, otherwise there is a risk of anode damage. These parameters affect the emission spectrum of the tube (Figure 2.7), so it is advisable to find the right setting based on the analysis to be performed.

Generally, the X-rays energy is chosen based on the thickness and the material of which the investigated object is made of (a thicker object needs higher

radiation energy than a thinner one with the same composition, while, with equal thickness, materials with higher Z require higher photons energy). The choice could be made using tabulated values of the attenuation coefficients for different materials, but in most cases the operator experience is fundamental. Once the tube voltage is set, the tube current is regulated based on the maximum power value that depends also on the focal spot size.

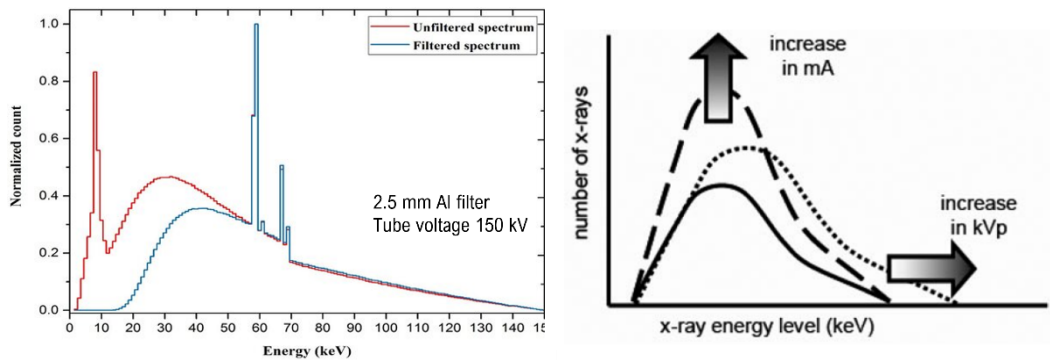


Figure 2.7: Effect of radiation filtering (left) and effect of voltage and current (right) on X-ray tube spectrum (Amiri et al., 2021; Chhem & Brothwell, 2008)

Detector

There are different ways of making the transmitted X-rays visible: (i) by analog plates impressed by radiation and subsequently developed (rarely used today), (ii) by reusable digital X-ray plates impressed and read by a special scanner, and (iii) via active digital detectors, which are widely used nowadays, i.e. electronic devices that display an image in real time directly on the computer by measuring the intensity of the incident radiation. The latter generally use active pixel sensor (APS) technology to detect and record the incident radiation (Figure 2.8). A detector using APS technology consists of a matrix of pixels, each consisting of a photodiode and one or more active transistors for charge detection and amplification (using CCD or CMOS technology). When the transmitted radiation reaches the scintillator layer on the detector surface, the X-ray photons are converted into visible light, which creates electron-hole pairs in the photodiodes that generate a current. This current is proportional to the intensity of the incident radiation, and the generated charge is stored, amplified and digitised (AD converter) and passed on to the computer. It is therefore necessary to evaluate the exposure time of the detector appropriately to avoid the acquired image being overexposed or underexposed. The integration time must be chosen

in such a way that the largest possible range of available greyscales (2^n levels, where n is the number of bits of the AD converter) is used to avoid saturation. However, this aspect is not the only one to consider, because increasing the integration time will increase the acquisition time for a complete tomography. It is therefore necessary to carefully evaluate these aspects when performing a CT depending on the purpose of the analysis.

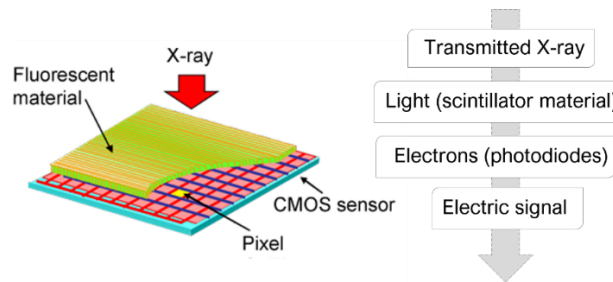


Figure 2.8: Schematic of X-ray CMOS detector (left) and principle of X-ray detection (right) (adapted from <http://www.spring8.or.jp/en/>)

Digital detectors can also be divided into linear detectors, in which one or more rows of active pixels are generally arranged along the main axis of the device and which are generally suitable for image analysis of large objects, even if image acquisition takes longer because it requires moving scanning, and area detectors (flat panel detectors), in which a matrix of pixels is arranged in a square or rectangle, which are generally keep fixed during image acquisition and in which the reading and transmission of the image is extremely fast.

Rotating platform

Unlike medical CT, where the patient is static during the analysis and the source and detector rotate around him, in the industrial and cultural heritage field, the source and detector are in a fixed position and the analysed object rotates around an axis of rotation. Since tomographic analysis is based on the acquisition of multiple radiographs of the sample from different angles, which are then reassembled, a precise rotating platform is required that can perform a complete rotation (360°) with a sufficiently small and precise rotation angle step to obtain the required number of X-ray projections. In addition, the platform must be able to support the weight of the sample and nothing must make rotation difficult.

2.2.2 Measurements parameters

Before scanning the object, some considerations must be made: several parameters (e.g., tube voltage and current, orientation of the object in the measurement volume, integration time of the detector, distances, etc.) have to be carefully selected to obtain a high-resolution CT scan that provides the best possible accuracy. These also depend on the size of the object, the complexity of the geometry, the material composition, the properties of the CT system, etc. (Kruth et al., 2011).

Geometric factors that influence a tomographic reconstruction are:

- X-ray source focal spot size
- Relative source-object-detector distances (Figure 2.9)

These factors determine the magnification and the geometric blurring, i.e., the lack of sharpness, also called penumbra. Magnification is related to the size of the projected object on the detector and depends on how close the sample is to the source or how far apart the source and detector are; it is calculated as the ratio between the distance between the source and the detector (SDD) and the distance between the source and the object (SOD):

$$M = \frac{SDD}{SOD} \quad (2.4)$$

The size of a voxel v is then determined by the detector pixel size p :

$$v = \frac{p}{M} \quad (2.5)$$

The closer the object is positioned to the source, the higher the magnification and the smaller the voxel size (Figure 2.9). To obtain an accurate reconstruction of the entire volume, the sample must remain within the field of view of the cone beam during rotation. The maximum magnification is limited by the ratio between the effective detector width D and the sample diameter d and can be expressed as follows:

$$M_{max} = \frac{D}{d} \quad (2.6)$$

Measurement accuracy can be improved by scanning a selected region of interest (ROI) as the object is moved closer to the source. Choosing to scan a smaller area of a sample can be suitable when measuring small features in large parts to increase resolution (local tomography, see section 5.2.1).

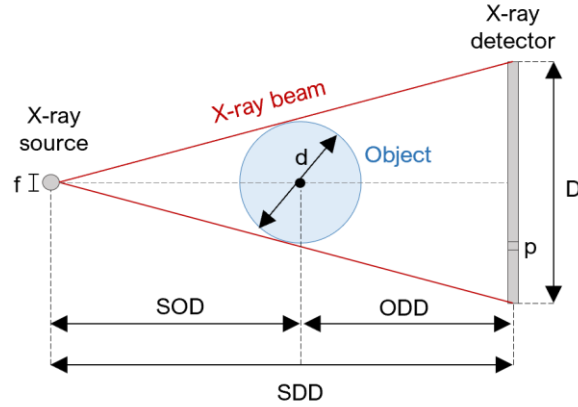


Figure 2.9: Schematic representation of a typical geometry of CT (top view). f is the focus size and p the detector pixel size.

Penumbra (P) is defined as the inability to clearly reproduce the edges of a given object (Figure 2.10). If the source focal spot is not point-like, the image is degraded by blurring, which degrades resolution (Kruth et al., 2011). In addition, the penumbra area tends to increase as the object moves away from the detector and tends to decrease as it moves away from the source. It is calculated as the ratio between object-detector distance (ODD) and source-object distance (SOD) multiplied by the focal spot:

$$P = f * \frac{ODD}{SOD} \quad (2.7)$$

This penumbra effect can also be caused by Compton scattering: the deflected X-rays interact with the detector in a different point than expected, making the image less sharp and blurred (visible especially at the edges).

The relative distances between source, object and detector must be evaluated and selected based on the spatial resolution required for the specific analysis. In this work, SDD and SOD have been measured with a measuring tape and repeated three times to obtain the standard deviation. The total uncertainty is calculated from the quadratic sum of standard deviation and instrumental error (± 1 mm).

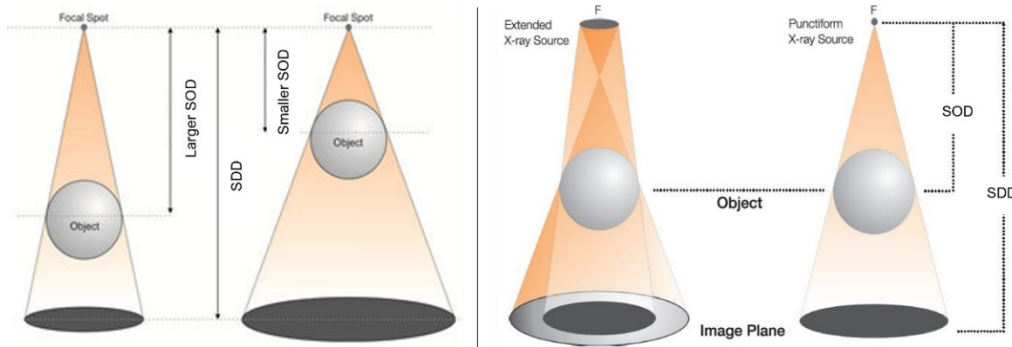


Figure 2.10: Magnification (left) and penumbra (right) dependence on distances and source focal spot (X-RAY WorX GmbH, 2014).

Spatial resolution is defined as the smallest distance between two points that the detector can distinguish as separate objects. It is also defined as the ability of a given system to reproduce image details. If the image is blurred, the resolution is low (presence of penumbra). The spatial resolution of an X-ray image is generally expressed in line pairs per millimetre (lp/mm), i.e., how many line pairs, black and white, can be distinguished as separate objects. To determine the spatial resolution a specific target can be used (Figure 2.11), i.e., a radiopaque object consisting of a series of vertical and parallel lines whose density per millimetre is associated with a certain resolution, or by an edge analysis using a thin metal plate that in the X-ray image has a sharp edge with respect to the surrounding air (Rueckel et al., 2014).

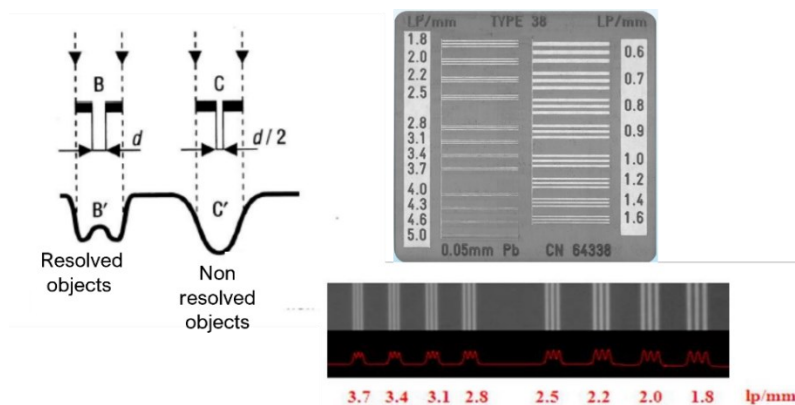


Figure 2.11: Schematic explanation of spatial resolution with resolved or not resolved closed points (left) and example of spatial target for x-ray imaging (right) (Castellano et al., 2007).

Contrast is instead defined as the minimum difference in optical density between two different components of the object under examination that can be detected by the system; it depends on the sensitivity of the detector and on some physical parameters. Contrast can be defined with the following formula:

$$C = \frac{\Phi_1 - \Phi_0}{\Phi_0} \quad (2.8)$$

where Φ_1 and Φ_0 are respectively the photon flux in two generic adjacent points of the sample projected on the detector. Contrast depends mainly on three factors: X-ray energy, sample attenuation and detector properties. At a higher source voltage, the X-rays are more energetic, and a more uniform grey scale distribution is observed, resulting in lower contrast (long scale). Lower voltage values, on the other hand, produce higher contrast images (short scale) because it is more difficult for the X-rays to penetrate higher density objects and only the presence or absence of attenuation can be observed. The current has no influence on the contrast. In addition, the sample components have different attenuation coefficients, which lead to variations in the contrast. Finally, it also depends on the sensitometric curve of the detector, which describes the blackening of the image on the detector, i.e., the optical density, as a function of the logarithm of the exposure, i.e., the measurement of the X-ray intensity. The best contrast is obtained in the linear region of the sensitometric curve (Figure 2.12), an interval called latitude. The left area of the curve would give an overexposed image, the right area an underexposed image. While with analog detectors this property is fixed, with digital ones it is possible to modify the images contrast during the post-processing if details visualization is needed.

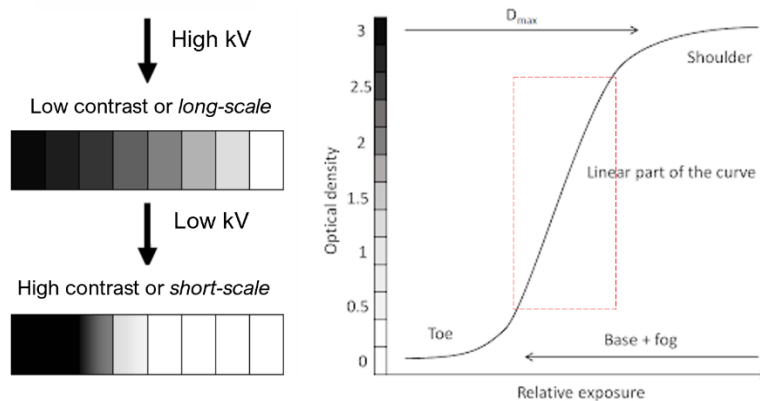


Figure 2.12: Contrast scale varying X-ray tube voltage (left); optical density as function of energy logarithm (right).

To conclude, the dynamic range indicates the ability of the detector to detect variations in X-ray intensity. The greater the dynamic range, the greater the differences in X-ray intensity that can be detected. The dynamic range is the actual number of grey levels available and can be calculated by SNR ratio analysis (Bettuzzi et al., 2007).

2.2.3 Image data acquisition

Once all geometric (distances) and hardware parameters (voltage, current, integration time) are set, projection images are acquired at each rotation step of the object set by the operator. The angular step determines the number of projection images and thus the quality of the resulting volumetric model as well as the required measurement time. To perform a CT scan, a proper compromise between all the variables described must be found to improve the quality of the resulting data set. Before scanning, the alignment of the instruments (source, rotating platform and detector) has to be performed. The alignment between the focal point of the source, the centre of rotation of the sample and the centre of the active area of the detector is crucial for the subsequent CT scan; a wrong alignment could lead to an incorrect CT volume reconstruction, resulting in the loss of important information for data analysis. The alignment protocol used is described in Appendix A. The specimen is then positioned on the platform, supported with a low absorbent material such as ethafoam (expanded polystyrene) to avoid interference from the specimen holder and inadvertent movement of the specimen during the scan. The position of the sample must also be considered, as the uniform length of the X-ray beam represented by the sample thickness should be preferred if possible. Analysis of sample orientation (horizontal, vertical, and tilted position) was carried out during the PhD and the results are presented in Chapter 4. Together with the sample projections, “white” and “dark” images are also collected for subsequent data processing (flat-field correction, Seibert et al., 1998). The former are projections acquired with the radiation source switched on, but without the object, to record the intensity of the X-rays used (not attenuated). From these X-ray images, information can be obtained about any radiation inhomogeneities and different pixel reactions. Dark images, on the other hand, are taken with the source switched off and provide information about the electronic noise of the detector.

2.2.4 Data elaboration and reconstruction

After scanning and obtaining a series of 2D projection images, the volume is reconstructed using specific software. For this work we use Dragonfly, version 2022.2 (Figure 2.13), developed and distributed by ORS Inc. (Montréal, Québec) with a free licence for academics (Object Research Systems (ORS) Inc., 2022). This software, developed in Python, is optimized for image processing; it was decided to use it since the short time required for CT reconstruction with respect to the other software available in that moment (used for example for some data analysis reported in Chapter 5). Moreover, it allows all the subsequent steps for CT slices processing and analysis. The CT reconstruction engine used in this work is based on the FDK algorithm (Feldkamp, Davis and Kress), which is normally used for cone beam imaging configurations (Feldkamp et al., 1984). In the latter, the X-ray beam has a cone shape and the detectors used are generally two-dimensional, since the entire sample projection must be contained in its active area. In this case, it is sufficient to rotate the sample at a fixed height without moving the source and the detector. Another possible beam geometry is the fan beam, where the X-rays are collimated and approximated to a sheet crossing the sample at a certain height; in this case, linear detectors are usually used because the output radiation reaches the detector along a horizontal line of pixels. In this case, the filtered back projection (FBP) reconstruction algorithm is used to reconstruct the samples acquired with this geometry (Kak et al., 2002). Before reconstruction, the software performs flat-field correction on the raw projections using white (W) and dark (D) images, which corrects and normalises them from background noise and intensity emanating from the source (Seibert et al., 1998):

$$I' = -\ln \frac{I-D}{W-D} \quad (2.9)$$

where I' is the normalized image and I is the acquired projection. The natural logarithm is linked to the Lambert Beer law (equations 2.1 and 2.2) to obtain the attenuation coefficient distribution in the whole reconstructed object volume. Once the centre of rotation is found, a fundamental step for a correct reconstruction, it is also possible to apply some correction techniques to the 2D projection images to minimise some possible physical effects, e.g., noise, beam hardening, ring artefacts, etc... using appropriate filtering tools (Barrett & Keat, 2004; Mallat, 1999; Pal et al., 2013; Villarraga-Gómez et al., 2019). The final reconstructed volume is modelled as a 3D greyscale matrix of voxels representing

a map of the attenuation coefficients of the materials in the sample visualized as slices in the three spatial directions XY, XZ, YZ and as a 3D model in render window. The obtained slices are saved as 32-bit tiff images. The reconstruction process using Dragonfly is described in Appendix B.

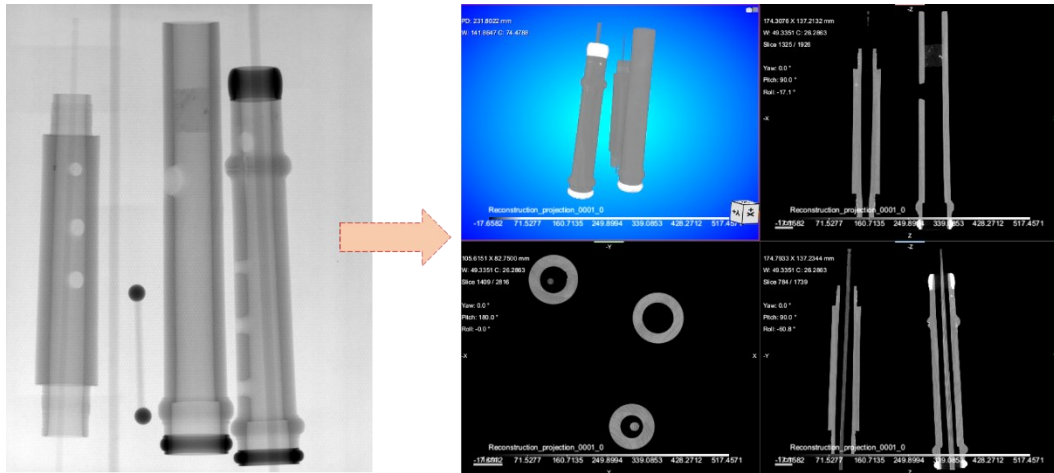


Figure 2.13: 2D projection of the analysed object and an example of CT reconstruction with the software Dragonfly

2.2.5 Volume segmentation and surface model

Once the reconstructed slices are obtained, segmentation of the volume is required to make dimensional measurements, applying a threshold that has to be carefully determined for accurate surface data. A typical method is based on the histogram showing the grey values distribution of the scan volume, i.e., frequency (number of voxels) on the y-axis and grey values on the x-axis (Figure 2.14). The method initially uses an iso-50% value determined as the ratio between the air (background) and the material (object), where 50% is assigned to the air and 50% to the material. In Dragonfly, this initial volume segmentation could be calculated by the Otsu method (Otsu, 1979), which performs automatic image thresholding. In its simplest form, the algorithm provides a single intensity threshold that divides the pixels into two classes: foreground and background. This threshold is determined by minimising the intensity variance within the class or maximising the variance between the classes. Ideally, i.e., when scanning a homogeneous object (only one material) and assuming no artefacts in the reconstructed volume,

this method would work well. However, this is not the case for most real CT scans, where objects made of several materials are often examined (especially in the field of cultural heritage), which is associated with the possible presence of image artefacts (Barrett & Keat, 2004). Therefore, after an initial estimation, the threshold could be changed directly on the histogram to create one or more region of interest (ROI). A ROI is a binary three-dimensional matrix (0/1) whose value is 1 if a voxel belongs to the object and 0 if it does not. It is possible to create an initial ROI with histogram-based segmentation and then refine it during subsequent processing, using other algorithms if necessary.

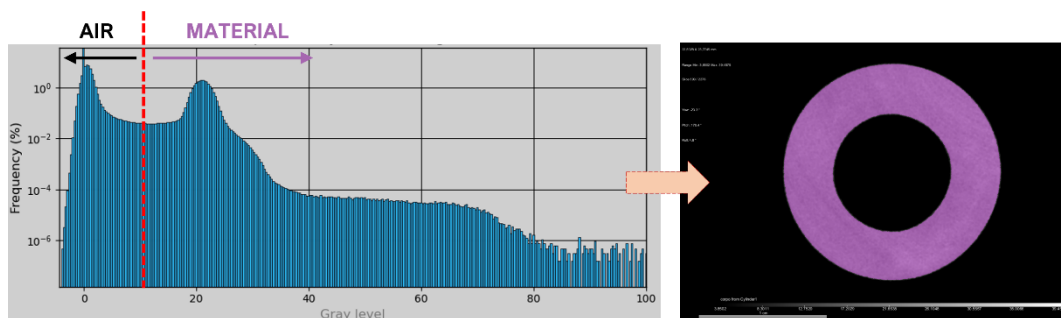


Figure 2.14: Grey level histogram (logarithmic scale) used for volume segmentation; example of extracted ROI, where all voxels belonging to material (value 1) are segmented in purple.

Once the definition of ROI is complete, the surface of the object is extracted as a ROI mesh (Figure 2.15). Points are positioned at the edge between regions "1" or "0", possibly averaged or interpolated. A region of interest can also be extracted by other image segmentation methods, such as region-based and AI or deep learning techniques (Badran et al., 2020; Enríquez-León et al., 2022). In this work, the described thresholding method is used for the segmentation of the samples (calibration objects and real artefacts). For the calibration objects (ball bar and ball plate), in contrast to the measurement of the diameter, the threshold method has almost no influence and is very robust, as we and other authors have experienced since the centre-to-centre sphere distances are considered.

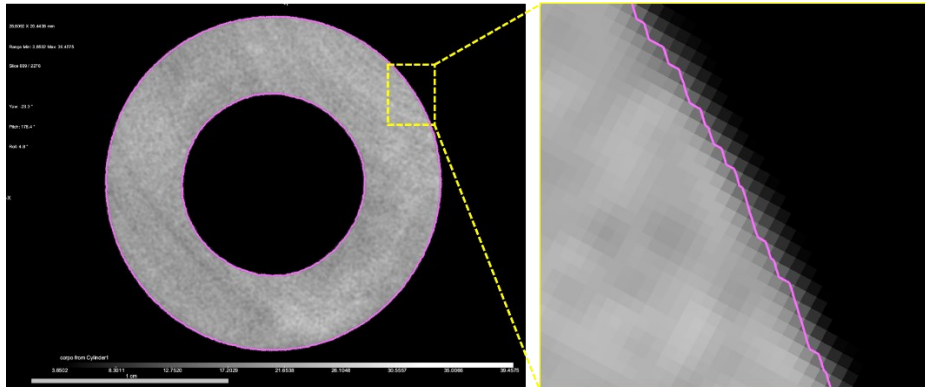


Figure 2.15: Determination of the object's surface from the extracted ROI.

Once the pattern surface has been defined, the mesh can be exported so that it can be easily edited by other software tools, preferably as an STL model characterised by polygons in the form of triangles (e.g., MeshLab). This is a discrete description whose accuracy depends on the number of points/triangles used: a very dense mesh is necessary to describe fine details of the objects, but this results in very large files (up to several GB). However, some errors could occur when evaluating the STL model, as the data is very sensitive to image noise. The STL file could therefore be refined and then used for 3D printing.

Chapter 3

Dimensional CT measurements

3.1 Introduction

The first attempts to adapt medical CT technology to industrial non-destructive testing began in the 1980s. Soon after, in the early 1990s, the concept of extracting dimensional features from CT data emerged, with technology and measurement techniques continually evolving. In 2005, the first dedicated measuring CT device was exhibited at the Control International Trade Fair for quality assurance in Germany. From then on, several powerful other industrial CT devices were developed over the years (Villarraga-Gómez et al., 2019).

In industry, X-ray CT is one of several non-destructive techniques used for quality tests and structural integrity assessment of manufactured components and assembled devices, as it is the best method for non-invasively inspecting complex structures and geometries within a volume, with resolution ranging from millimetres to nanometres. The potential of X-ray CT for reliable dimensional measurements, especially for objects or components with internal features inaccessible to conventional measuring machines (e.g., coordinate measuring machines (CMMs) or laser scanners), has attracted the attention of the metrology community as a tool for non-destructive dimensional quality control, i.e., traceable measurements and geometric tolerance verification (Villarraga-Gómez et al., 2018). These are the reasons why this technology is so widely used nowadays not only in industry but also in different application areas, including cultural heritage. However, in this field, CT technology is mainly used for the

qualitative investigation and study of materials and components, but rarely for the quantitative analysis of dimensions in the study of ancient and historical artefacts.

Although the physical principles are the same for the various fields of application, the equipment and procedures differ significantly depending on the requirements and purposes of analysis. While in medical applications the power of the X-ray source must be limited, and the accuracy and spatial resolution requirements are usually relatively low, dimensional CT often requires a wider range of penetration power and higher spatial resolution as it is used to measure workpieces with very different sizes, thicknesses and absorbing materials. Although CT has been developed and used for several decades, its application to dimensional metrology is far from trivial and still requires significant development.

3.2 Reference guidelines

Unlike some measurement methods that are now established and used in the field of metrology (e.g., CMM), there are currently no international standards defining procedures and guidelines for uncertainty analysis in CT measurements, although some pre-normative work has started (Bartscher et al., 2014; Carmignato et al., 2017). The reason for this lack of standardisation for X-rays CT is mainly due to its relatively recent application in the industrial field and its complexity in terms of physical processes and influences. In fact, the estimation of measurement uncertainties of CT depends on several influencing factors (Figure 3.1), such as the measurement environment, the object to be measured, the operator, the measurement strategy or data processing and variations in the operation of the CT system (power, resolution, magnification, focal spot size, etc.).

Currently, some uncertainty assessment initiatives are based on comparisons with calibrated objects and other methods, including simulation approaches (i.e., Monte Carlo) (Hiller & Reindl, 2012; Schmitt & Niggemann, 2010). Furthermore, although several standard guidelines for CT users have been developed by various institutions (e.g., ASTM International, EN normatives) (EN 16016-2, 2011; Müller, 2013; Villarraga-Gómez et al., 2019), these do not include references to dimensional measurement issues. Currently, the only reference document with procedures for dimensional system testing CT is Guideline 2630-1.3 published by VDI/VDE in 2011, which applies the approaches used for CMM testing to CT.

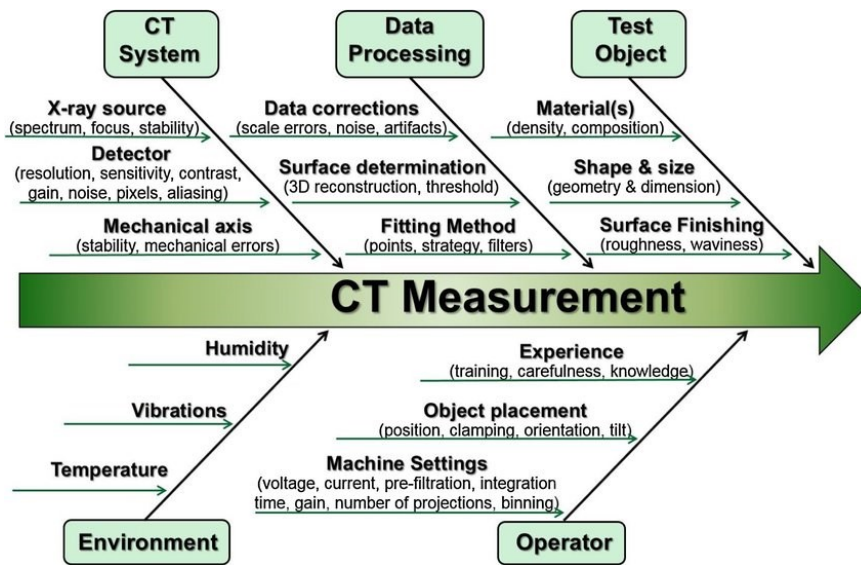


Figure 3.1: Some of the main factors influencing the CT measurements grouped in five main categories (Ishikawa diagram) (Villarraga-Gómez et al., 2018)

However, some authors point out that the procedures described are not exhaustive: there is no clear interpretation, so any test sample could be used, as there are no standard specifications or limitations. This is a contentious issue as the operation of CT is very different from that of CMMs and it is not easy to adapt the test procedures of CT to those of CMMs. Furthermore, a standardisation guideline should take into account the use of the measuring instrument and all known potential sources of error, of which there are several in the case of X-rays CT. For this reason, efforts to create international standards for acceptance testing in dimensional CT metrology have recently intensified, leading to new ideas that are currently being discussed in various committees (e.g., a possible future part of ISO 10360). In 2015, an update of the former VDI/VDE document containing procedures for the determination of measurement uncertainty was published (VDI/VDE 2630-2.1) (Müller, 2013), but there are still no guidelines or recommended standard procedures for the calibration of CT systems, although there are methods to compensate for some geometric errors in dimensional measurements by rescaling the voxel data, which will be the focus of this study.

As previously anticipated, there are many acquisition parameters and factors that influence the measurement accuracy of a CT system. The image quality of the collected projections for CT analysis has a direct influence on the performance of

the dimensional measurement. This quality depends on the resolution (size of the source focal spot, magnification, blur), greyscale contrast and signal-to-noise ratio produced by the X-ray imaging device, which typically depends on operating parameters such as X-ray tube voltage and current, integration time, filtering and dimensions, density and shape of the object under examination. In addition, processing methods for 3D reconstruction of the volume, such as reconstruction algorithms and the choice of filters for correction of artefacts, can also influence the quality of the images and thus the dimensional measurements.

Several investigations have been conducted to study systematic variations of selected influencing factors that contribute to the inaccuracies in dimensional measurements from CT data, most of which make quantitative comparisons with CMM data (Pierobon, 2012; Lifton, 2015; Tan, 2015). The results show that the CT technique can deliver measurement accuracies comparable to conventional CMM systems, with typical uncertainties in the range 5–20 μm . This range of values has been achieved and is valid for industrial applications where commercial imaging systems have been used in most cases. In our study, we want to test and find the best measurement accuracy achievable with our customised CT setup (see section 3.4), which consists of separate and independent instruments (X-ray source, rotation stage, flat panel detector and relative handling systems), as for cultural heritage the systems used should be versatile and transportable, if possible, depending on the type of analysis to be performed. But also, in our field of application and with our setup, the measurement accuracy depends very much on the use of optimal or best possible settings for CT scanning. For this reason, in this work we decided to investigate some of the presented influencing factors for a CT scan, also using some calibration objects, to investigate the effects on scale errors, which will be described in the next section.

3.3 Calibration objects

Determination of scale errors and influencing factors in CT is done by using calibrated reference objects, like those used in classical coordinate metrology (Figure 3.2). There are many different reference objects developed for different purposes and applications related to CT, some of them for the same or similar applications (Brunke & Suppes, 2010; Kiekens et al., 2011; Müller, 2010; Müller et al., 2012; Weckenmann & Krämer, 2009). Commonly used reference objects are spheres made of different materials (preferably ruby, alumina, zirconia and steel) that allow point-to-point distance measurements. In most cases, these objects are attached to carbon fibre supports, all of which are used for scale

corrections in the CT volume. In this case, the centres of the spheres are usually used for distance measurements, as their evaluation is independent of the chosen threshold for volume segmentation. In this work, two of these reference objects have been realised and used for dimensional tests: a spherical rod and a spherical plate, the latter as described by Hiller et al.(Müller et al., 2012).

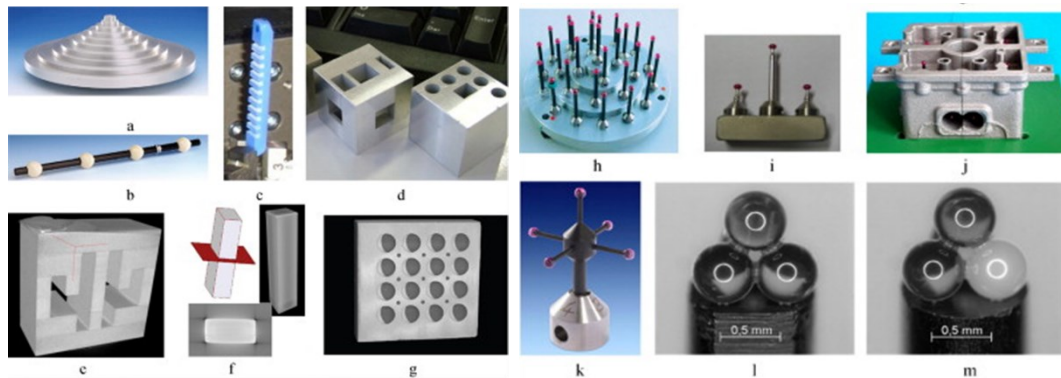


Figure 3.2: Some reference workpieces used for CT dimensional analysis and other CT tests (Kruth et al., 2011).

The ball bar consists of a carbon fibre rod with two alumina spheres at the ends, while the CT ball plate consists of a regular 5×5 array of the same alumina spheres glued to a carbon fibre plate (Figure 3.3). Carbon fibre is a low attenuation material for X-rays, allowing clear visibility of the spheres, which in this case are made of a denser material such as aluminium oxide (Al_2O_3). Furthermore, although they are multi-material objects, the carbon fibre does not create image artefacts in the reconstructed volume. Since the spheres are glued on by hand, concave housings were implemented in the plate to allow for easier attachment and more precise distribution of the spheres on the plate. The nominal distance between the ball centres is 10 mm, while the ball diameter is 5 mm. A small copper wire was fixed in one corner of the plate to identify ball A (Figure 3.3, right). The general concept of the CT ball plate is similar to the conventional ball plates and hole plates used in classical coordinate measuring technology.

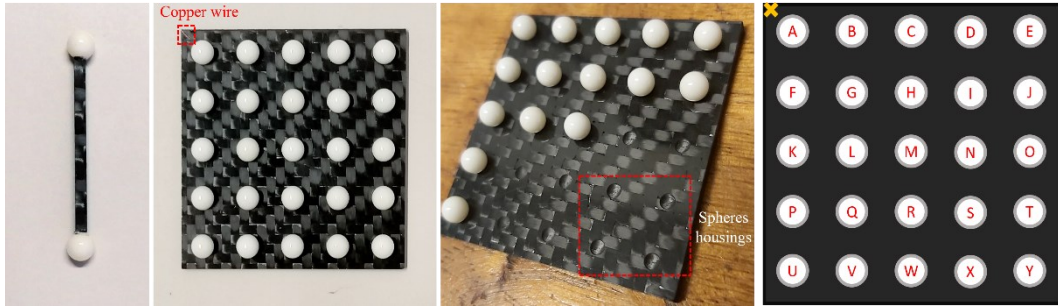


Figure 3.3: The ball bar and ball plate developed and used in this work as calibration objects; for the ball plate letters from A to Y are given to the 25 sphere as in the shown scheme, with the reference near the sphere A.

These calibration objects can be considered as a multi-purpose reference samples with different type of applications, such as:

- Performance characterization of CT scanner.
- Determination of measuring errors in the CT volume.
- Geometrical correction of CT data, e.g., scale errors.

For all tests performed, length measurements are considered as unidirectional distances, in particular the sphere centre distances (C-C) are evaluated as they are independent of the thresholding in the CT analysis. While only one measurement can be evaluated with the ball bar, the ball plate allows the simultaneous measurement of 300 sphere distances (distance of each sphere from all others), increasing the statistics and being closer to a real object. To determine the C-C sphere distances, a 3D optical measurement system was used, specifically the ATOS ScanBox machine from the J-Tech laboratory of the Politecnico of Turin (DIGEP department), which uses structured light to measure the three-dimensional shape of an object using projected light patterns and a camera system (Figure 3.4). When the projected light hits the surface of the object, the patterns are distorted, the cameras capture these images and send them to the 3D scanning software for processing. The object is positioned on a rotating stage, so that this process is repeated at different angles. From the 3D model created, (x,y,z) spatial coordinates are extracted for each fitted sphere, from which the distances can be calculated. The measurement uncertainty was calculated starting from the maximum deviation from the machine calibration certificate, considering $\sigma=2 \times (\max_dev/\sqrt{3})$ and obtaining $\sigma=(\pm 0.002 \text{ mm})$. The C-C distance for the ball bar is given in Table 3.1. All measured distances for the ball plate are given in Appendix C.

Table 3.1: Distance between spheres centers of the ball bar


C-C distance ball bar	
	$35.040 \pm 0.002 \text{ mm}$



Figure 3.4: Atos ScanBox and a detail of the projected narrow-band blue light from the instrument head on the ball plate positioned on the rotating stage.

3.4 Experimental equipment

As previously mentioned, the experimental setup used for CT analysis is not a commercially available one, but a fully customised setup that can be adapted to the requirements of the analysis. The tested imaging setup (Figure 3.5) was developed in the framework of the project "neu_ ART", born from the collaboration between the University of Turin, the National Institute of Nuclear Physics (INFN) and the Centro Conservazione e Restauro (CCR) "La Venaria Reale", Venaria Reale (Turin), and funded by Regione Piemonte (Italy) from 2010 to 2013 (Nervo, 2013; Re et al., 2012). The instruments, installed in a shielded laboratory at the Department of Physics of the University of Turin, were designed for "ad hoc" analyses required in the study of artworks of different sizes, shapes and material compositions. Some recent instrumental upgrades to the

systems (a new detector acquired thanks to the NEXTO project funded by the Compagnia di San Paolo in 2017) make it possible to improve results on small objects, increase resolution and reduce acquisition time.

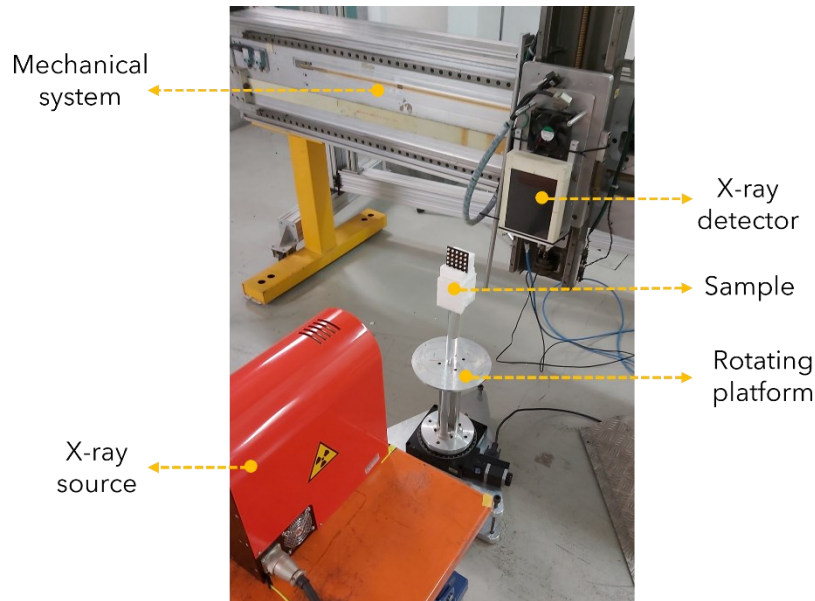


Figure 3.5: CT setup at the Physics department (University of Torino) used in this work


The setup consists of a Microfocus L8121-03 X-ray source from Hamamatsu, connected to a digital control unit for setting and controlling the operating parameters from the control room. This source features a tungsten anode and a 200 μm thick beryllium window; it is also equipped with an air-cooling system (technical data in Table 3.2).

The source has three selectable focal points of different sizes:

- Small spot mode (S): 7 μm (10 W, 5 μm at 4W)
- Medium spot mode (M): 20 μm (30 W)
- Large spot mode (L): 50 μm (75 W)


For each focal spot, maximum current values can be set based on the maximum power; if exceeded, a risk of melting the anode can occur.

Table 3.2: Specific of X-ray source

Hamamatsu Microfocus L8121-03 X-ray Source		
	Voltage	40-150 kV
	Current	10-500 μ A
	Max. power	75 W
	Focal spot size	5-50 μ m
	Target material	W
	Cone beam angle	43°
	Min. focus-object distance	17 mm

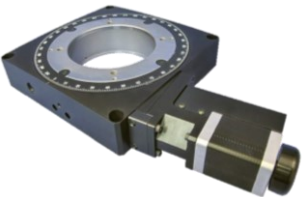
The X-ray detector used is a flat panel Shad-o-Box 6K HS from Teledyne Dalsa, consisting of a 2304×2940 pixel matrix, corresponding to an active area of 11.4×14.6 cm², with an individual pixel size of 49.5 μ m; the active area is protected by a thin carbon fibre cover. Image reading and transfer is fast with a reading speed of up to 9 fps. Each pixel consists of a direct contact scintillator (caesium iodide), a photodiode and a CMOS transistor. The scintillator converts X-ray photons into visible light, which is detected by the photodiode and converted into electrical charges; thus, a current proportional to the intensity of the incident radiation is generated and detected by the CMOS chain, amplified and digitised (14 bits) and sent to the computer (Table 3.3).

Table 3.3: Specific of X-ray detector

Shad-O-Box 6K HS Flat Panel Detector		
	Pixel number	2304×2940
	Active area	11.4×14.6 cm ²
	Pixel size	49.5 μ m
	A/D converter	14 bits
	Energy range	15-225 keV
	Scintillator	CsI
	Data transfer	Gigabit Ethernet

The rotating platform is the Newport URS150BPP model (Table 3.4), mounted on a triangular metal support to move it and to adjust its inclination for levelling during the alignment phase (Figure 3.5). To perform the CT scan of the object, an additional support is mounted on the platform to align the sample with the focal point of the X-ray source. The rotation speed of the sample and the angular step are adjusted with a programme developed in LabVIEW that controls the movements of the platform.

Table 3.4: Specific of rotation stage

Newport URS150BPP Rotation Stage		
	Travel range	360° continuous
	Min. incremental motion	0.0002°
	Accuracy	±0.015°
	Max. speed	40°/s

In this configuration, the X-ray source is placed on a table that allows the positioning at the selected distance from the detector and vertical movement to achieve the correct height of the focal point. The detector is installed on a mechanical X-Y scanning system that allows optimal alignment in relation to the X-ray source. The programme for acquiring the CT projections was developed in the LabVIEW environment and can control the rotating stage and the detector (Figure 3.6). In particular, the operator can specify directly in the programme the integration time, the angular step and the rotation speed; it is also necessary to specify the name of the image files and the PC path where the projections will be stored. When everything is ready for the CT scan, after a 20-minute warm-up period of the source for signal stabilisation, the programme can be launched and automatically starts projection recording until the full 360° rotation is reached and the last image is stored. The projections are saved as 16-bit images in tiff format. After scanning the sample CT, the same procedure is used to acquire the white and dark images needed for the subsequent reconstruction steps.



Figure 3.6: LabVIEW program for CT acquisition (main window for setting CT acquisition parameters and minor window for setting of integration time)

3.5 CT correction methodology

As described in section 3.2, an important factor directly affecting the dimensional measurements of CT is the size of the reconstructed voxel, which depends on the pixel size of the detector and the magnification (equation 2.5), which in turn is a function of the source-detector distance and the source-object distance (equation 2.4). Possible sources of error in determining the voxel size could therefore be: (i) the pixel size, which in our case is given by the detector manufacturer without uncertainty, even though local defects on the scintillator crystals have been detected in some works, leading to possible deviations in the dimensional measurements depending on which part of the detector was used (larger deviations at the edges); (ii) SDD and SOD distances, i.e. axis position errors, radial deviations of the centre of rotation from its mean position and unwanted sample movements. In addition, a possible drift of the X-ray focal spot and the tilt of the detector could also cause dimensional errors, apart from all other possible influencing factors presented in section 3.2. This means that the measurements from CT can be wrong and influenced by deviations from the real object dimensions.

A robust method for determining voxel size and subsequent correction is to scan a reference workpiece under the same conditions as the sample to be analysed, in our case evaluating the centre-to-centre distance between calibrated spheres (Blažek et al., 2019; Zemek et al., 2020). Considering the reference dimension L_{ref} determined with an accurate measuring instrument as the distance between the centres of two spheres and the same dimension determined in the volume CT, L_{CT} , the new corrected voxel can be calculated by multiplying the ratio between L_{ref} and L_{CT} , which gives a voxel scaling factor f_c , by the original voxel size:

$$voxel_{corr} = voxel_{orig} \times f_c \quad (3.1)$$

where $f_c = \frac{L_{ref}}{L_{CT}}$. Evaluating corrected voxel size in this way considers all errors present in the CT measurement procedure and data processing steps (reconstruction and volume segmentation through thresholding).

Several authors (Carmignato et al., 2009; Kiekens et al., 2011; Müller et al., 2017) have discussed the use of equation 3.1 and proposed different reference workpieces for voxel size correction; however, few have shown the application of this method and how it can be used to measure a real sample; this is one of the aims of the present work.

This correction method is applied to both the ball bar and ball plate tests. However, while the correction factor for the ball bar is simply given by $f_c = \frac{L_{ref}}{L_{CT}}$ since only one dimension is evaluated, f_c for the ball plate is determined using the method described in (Lifton et al., 2013.): instead of calculating different voxel correction factors for each of the reference dimensions (according to equation 3.1), a single "best-fit" voxel scaling factor is derived, which takes into account all reference dimensions simultaneously and thus a larger part of the volume CT. In this sense, we can assume that $L_{ref} = f_c \times L_{CT}$ derived from equation 3.1 is a linear regression model; the left term is the dependent variable, the right term is the independent variable, and the correction factor is the unknown coefficient, thus derived from the "best-fit" voxel scaling factor (Figure 3.7). Other authors use a comparable correction method (Lifton et al., 2013), that similarly uses a linear regression model to calculate a voxel scaling factor that results in a different formula, but with the same results.

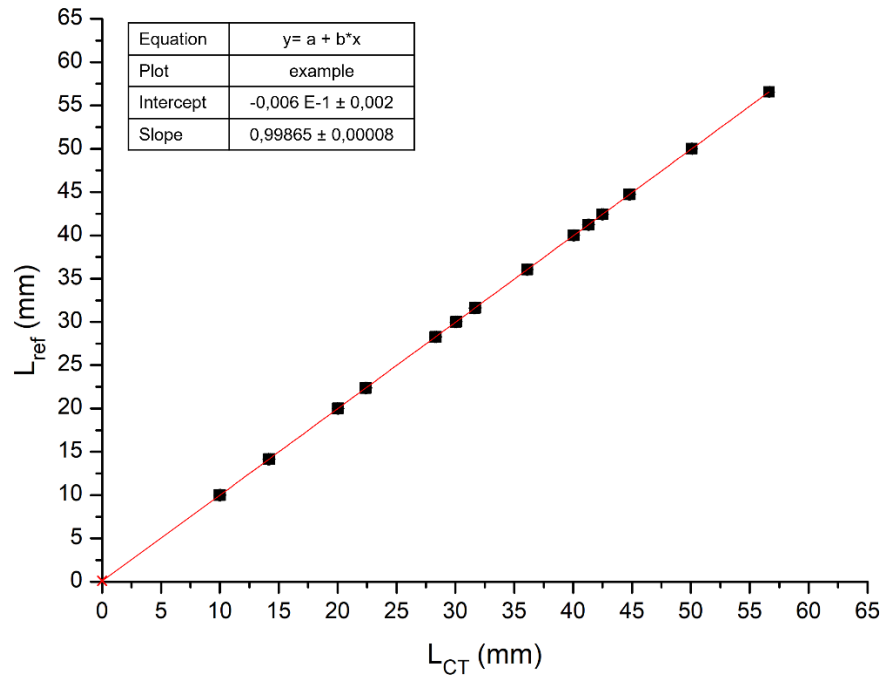


Figure 3.7: X-ray CT measurements of the calibration object (L_{CT}) plotted against reference dimensions (L_{ref}); the slope of the fit equation represents the correction factor f , while the intercept is close to 0. If f is less than one, it means that the CT measurements are larger than the real measurements and vice versa.

Once the correction factor is determined, it is applied to the original voxel to obtain the correct voxel size, which is used to rescale the distance SOD, obtaining a corrected magnification, too. The calculated values are used for a new reconstruction of the original CT data to check the effectiveness of the correction.

To demonstrate the application of voxel size correction to the measurement of a real sample, this methodology is applied to two real objects: a LEGO brick and the piccolo flute already described in Chapter 1. The plastic brick was chosen to have a more regular object with different dimensional features to better evaluate the correction compared to a real historical artefact. Once the scanning parameters were set, the following measurement procedure was applied: (i) CT scan of the calibration objects (ball bar + ball plate); (ii) scan of the sample under examination together with the ball bar (not the ball plate because of its dimensions in relation to the field of view of the detector); (iii) another CT scan of the calibration objects (Figure 3.8). This procedure is used to evaluate the results of the two different types of correction, e.g., by scanning the calibration objects

before and after or by scanning the calibration object with the sample under study, and to determine the best correction method for our objectives. The same scanning conditions are maintained for both the calibration and the real objects.

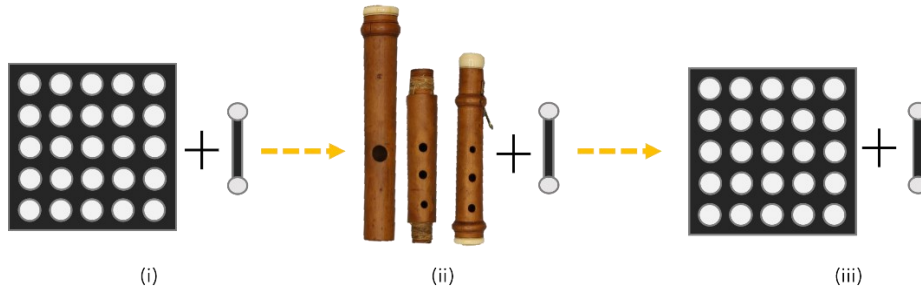


Figure 3.8: Schematic CT workflow for dimensional correction

The calibration objects are not only used for the correction of the voxel size, but also in other CT tests to investigate some of the influencing factors mentioned in section 3.2, especially regarding sample positioning, X-ray source parameters (voltage, focal spot size) and geometric magnification. All measurements performed are summarised in Table 3.5.

Table 3.5: Performed measurements to investigate influence factors.

CT TESTS		
Measurements	Ball plate	Ball bar
Object position	Vertical, horizontal, tilted	Vertical, horizontal, tilted
Source voltage	90kV, 150kV	-
N° projection	2400, 1200, 800	-
Focal spot size	7 μ m (S), 20 μ m (M), 50 μ m (L)	-
Magnification	1 \times , 2 \times , 4 \times	-
Repetition (same scan conditions)	3 @150kV	-

Chapter 4

Results and Discussion

4.1 Ball bar tests

The ball bar described in section 3.3 is used for the initial tests on the dependence of orientation during the CT scan and to check whether the correction method works, as the correction factor is easier to determine this way. Three positions of the ball bar are examined: horizontal, vertical and tilted at 45° (Figure 4.1). The aim is to investigate whether the position of the sample in the X-ray cone beam could have an influence on the dimensional measurements (Weckenmann & Krämer, 2009). The method used is the one already described in section 3.5: The reference length is the centre-to-centre distance between the two spheres of the ball bar. Since the reference value is known, we can evaluate the deviations from the reference length and finally apply a voxel correction to the CT reconstruction. The acquisition parameters were chosen to remain constant for all tomographic acquisitions (Table 4.1).

The sphere centre distances of the three orientations determined from the reconstructed volume are summarised in Table 4.2. From the results, there is a slight deviation from the nominal value in the three measurements, but they are compatible with each other, so we can confirm that the different sample orientations have no influence on the deviations. From these results, using equation 3.1, the correction factors are calculated and applied to obtain the new

corrected voxel size. The readings from CT are equal to the reference value after correction.

Table 4.1: Ball bar CT acquisition parameters

Voltage	90 kV
Current	111 μ A
Integration time	3.2 s
Focal spot size	7 μ m (S)
¹ SDD	654.8 \pm 1.6 mm
SOD	260.0 \pm 1.4 mm
Magnification	2.5 \times
Voxel size	19.7 \pm 0.1 μ m
Angular step	0.25 $^\circ$

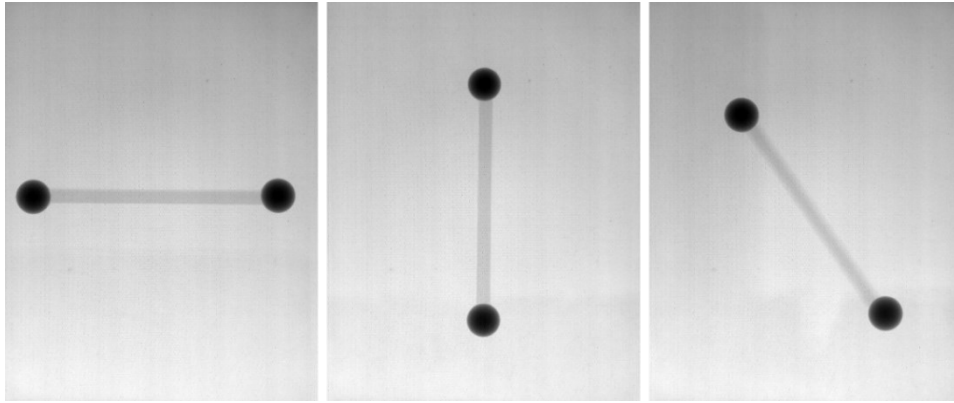


Figure 4.1: Ball bar orientation during CT scan: horizontal, vertical and 45 $^\circ$ tilted.

²**Table 4.2:** Ball bar CT measurements before and after correction

Position	L_{CT} (mm)	f_c	$voxel_{corr}$ (μ m)	SOD_{corr} (mm)	L_{CT_corr} (mm)
Horizontal	35.51 \pm 0.02	0.9868 \pm 0.0005	19.40 \pm 0.12	256.6 \pm 1.7	35.04 \pm 0.02
Vertical	35.46 \pm 0.02	0.9881 \pm 0.0005	19.42 \pm 0.12	256.9 \pm 1.7	35.04 \pm 0.02
Tilted 45 $^\circ$	35.49 \pm 0.02	0.9873 \pm 0.0005	19.41 \pm 0.12	256.7 \pm 1.7	35.04 \pm 0.02

¹ Uncertainty of SDD and SOD values results from the quadratic sum of instrumental error (measuring tape) and standard deviation (calculated from repeated measures).

² The uncertainty associated to L_{CT} is equivalent to one voxel in mm; the other reported uncertainties are derived with error propagation (see also Appendix B).

To evaluate the agreement between the measurements of CT and the reference values, a statistical parameter E_n (called “normalised error”) can be calculated between the data before and after correction (Steele & Douglas, 2006; Villarraga-Gómez et al., 2018):

$$E_n = \frac{\bar{x}_1 - \bar{x}_2}{\sqrt{U_1^2 + U_2^2}} \quad (4.1)$$

where x_1 and x_2 can be both the value obtained from a CT and its reference and two different CT scans and U_1 and U_2 are the corresponding uncertainty.

If the absolute value obtained is $|E_n| \leq 1$, the result is acceptable, otherwise it is considered unsatisfactory. From the obtained results (Table 4.3), we can see that the dimension data before correction is unacceptable, while the values after correction go towards 0. If we make the same evaluation between the results obtained from the three positions before correction, we can see that one value is greater than 1, which corresponds to the horizontal-vertical comparison.

Table 4.3: Ball bar E_n values before and after correction

Position	Before	After
Horizontal	23.8	0.005
Vertical	21.3	0.01
Tilted 45°	22.8	0.01

Table 4.4: Ball bar E_n values between orientations

Comparison	horizontal vs. vertical	vertical vs. tilted	horizontal vs. tilted
E_n	1.8	1	0.7

From this we can conclude that the position of the sample has no significant influence on the measured dimensions, especially not after correction. However, to obtain a more accurate result, the same tests were carried out with the spherical plate as described in the next section.

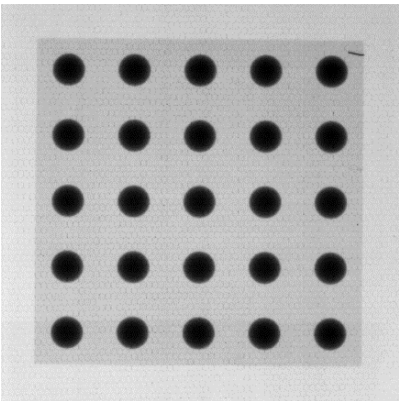
4.2 Ball plate tests

In order to obtain more statistical data and a better approximation of a more complex object than a real object analysis, the realised ball plate (section 3.3) is used for different types of tests to check the influence of different factors and parameters on the CT dimensional analysis:

- projections number;
- sample positioning in the X-ray beam: horizontal, vertical and 45° tilted (the same tests performed for the ball bar);
- focal spot size (7, 20, 50 μm)
- tube voltage (90 and 150 kV);
- magnification (1 \times , 2 \times , 4 \times);

To determine the precision of the method, an additional test was carried out in which the CT scan of the sample was repeated three times under the same conditions on the same day to check the repeatability of the process and thus the compatibility of the dimensional results obtained from the reconstructions. The measurement conditions are summarised in Table 4.4. From this analysis, statistical uncertainty could be determined.

Table 4.5: Repeated ball plate CT acquisition parameters

	Voltage	150 kV
	Current	66 μA
	Integration time	1.75 s
	Focal spot size	7 μm (S)
	SDD*	653.8 \pm 1.6 mm
	SOD	595.0 \pm 1.4 mm
	Magnification	1.1 \times
	Voxel size	45.1 \pm 0.2 μm
	Angular step	0.25°

The standard deviation has been computed for the three set of data, and the maximum standard deviation among all the C-C distances is considered the

statistical error that is quadratically added to the uncertainty of distances measured in the CT reconstruction (one voxel, see Appendix B) to obtain the total error. The standard deviation values distribution is visible in Figure 4.3; the considered value is 0.04 mm.

$$U_{L_{CT}} = \sqrt{voxel_{size}^2 + std^2} \quad (4.2)$$

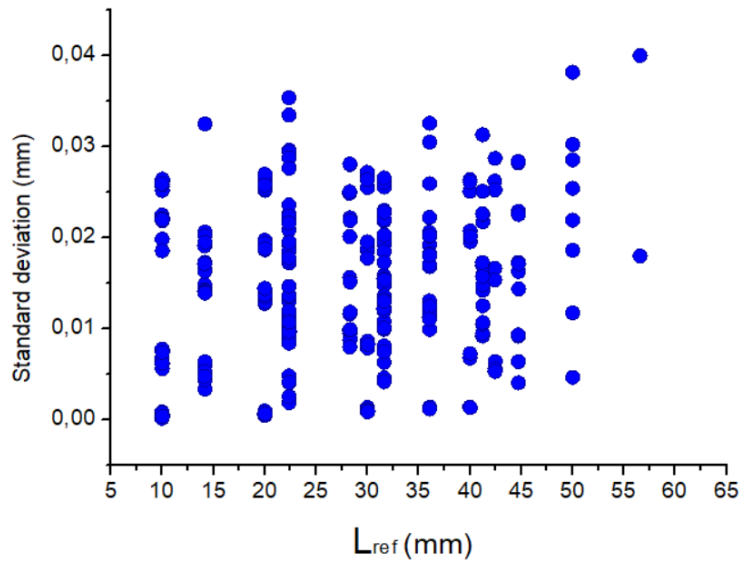


Figure 4.3: Standard deviations obtained from repeated measurements.

It could be determined that the standard deviations are evenly distributed and that there is no dependence on the spheres distances.

For all three measurements, an evaluation of the deviations from the reference values could be observed; in particular, the difference between the displayed value L_{CT} (test length) and the reference value (calibrated C-C ball distances) L_{ref} is the ball distance error SD, expressed as (Müller et al., 2017):

$$SD = L_{CT} - L_{ref} \quad (4.3)$$

This parameter is used in most cases in the results shown. The deviations of the measured quantity are shown graphically, as in Figure 4.4, where SD is plotted as a function of the reference values. In this case, the deviations agree for the three measurements and increase with the length value. If we apply the correction

method described in section 3.5, we can obtain three correction factors from the linear fits, which are used for rescaling the voxels, performed separately for the three CTs (Table 4.5).

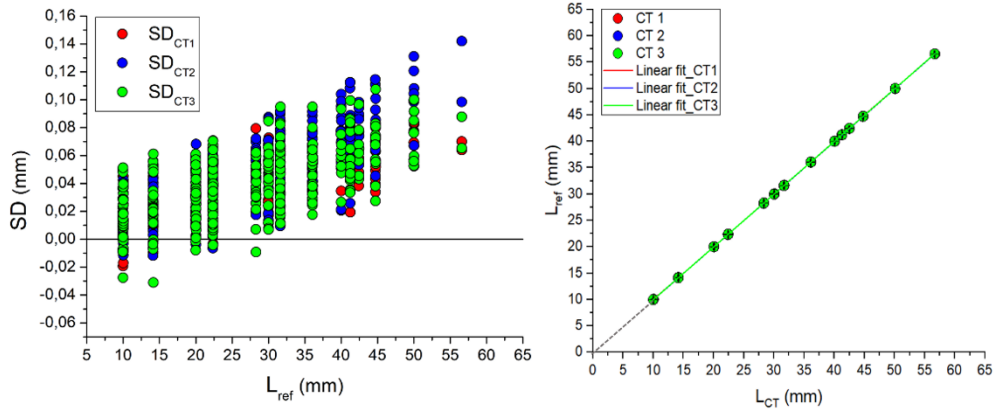


Figure 4.4: Repeated ball plate SD before the correction (left) and linear regression fit (right).

Table 4.6: Repeated ball plate CT values after application of correction factors

Measure	f_c	$\text{voxel}_{\text{corr}} (\mu\text{m})$	$\text{SOD}_{\text{corr}}(\text{mm})$
CT 1	0.9986 ± 0.0003	44.99 ± 0.15	594.2 ± 2.5
CT 2	0.9981 ± 0.0003	44.96 ± 0.15	593.9 ± 2.5
CT 3	0.9986 ± 0.0003	44.99 ± 0.15	594.1 ± 2.5

Looking at the deviations after the application of the correction, one can see its effectiveness, as all values are distributed around 0 and no specific trends are discernible (Figure 4.5).

However, residual deviations ranging between ± 0.05 mm are observed for all the three datasets.

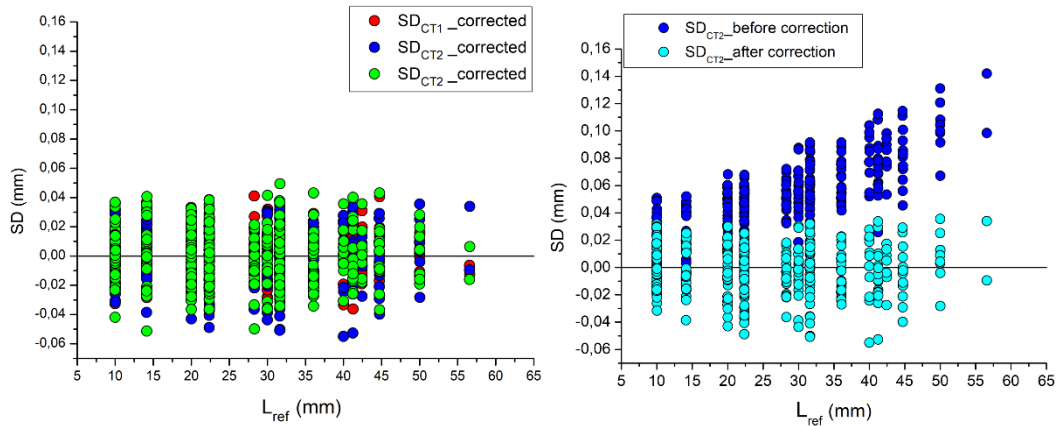


Figure 4.5: Repeated ball plate SD after the correction (left) with a comparison example of the second measurement (right).

When calculating the parameter E_n for comparing the three measurements with each other before correction, all the values result minor than 1 and randomly distributed, thus the three initial datasets agree with each other (Figure 4.6 left). Comparing CT data before and after correction, an increasing linear trend can be seen, e.g., the E_n values grow for longer distances (Figure 4.6 right). In addition, comparing E_n values between CT and reference lengths both before and after correction, the improvement of the results, especially of larger distances, can be noticed, thus correction method works properly (Figure 4.7). The observed trend is consistent with the results of the evaluation of SD.

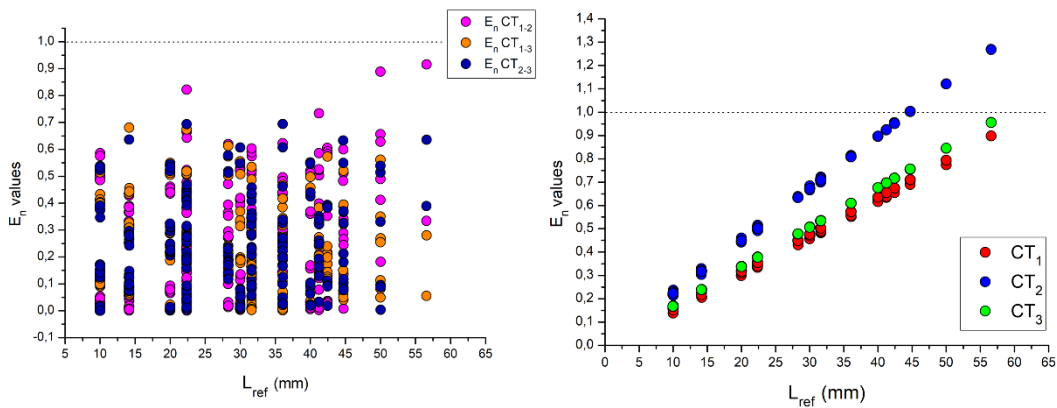


Figure 4.6: Repeated ball plate E_n values calculated between the three measurements before the correction (left) and between data before and after the correction for the three measurements (right).

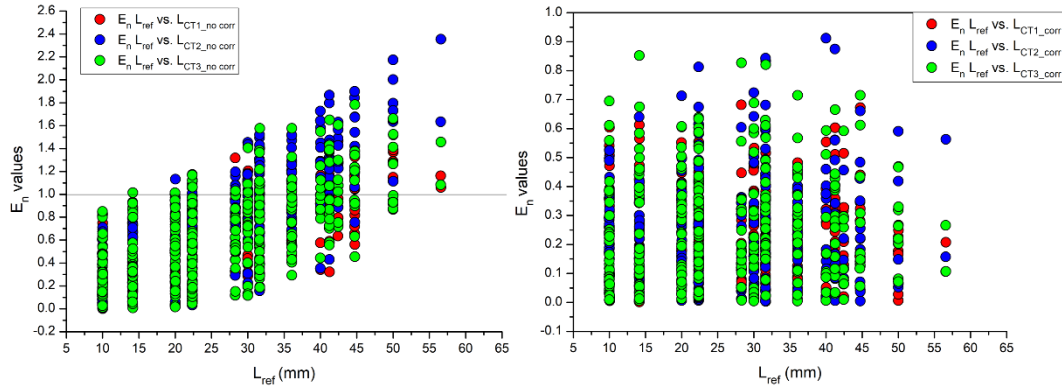


Figure 4.7: Repeated ball plate E_n values calculated between the CT and reference lengths before (left) and after (right) the correction.

4.2.1 Number of projections

A first test to check whether the number of acquired projections in a CT scan could have an influence on the dimensional analysis was performed on a dataset that was also used for other tests (magnification and voltage evaluations, see sections 4.2.4 and 4.2.5). The working conditions are listed in Table 4.7.

Table 4.7: Ball plate CT acquisition parameters

Voltage	90 kV
Current	111 μ A
Integration time	3.2 s
Focal spot size	7 μ m (S)
SDD*	653.8 \pm 1.6 mm
SOD	320.0 \pm 1.4 mm
Magnification	2 \times
Voxel size	24.23 \pm 0.12 μ m
Angular step	0.15 $^\circ$

The whole dataset consists of 2400 projections to which image selection was applied in terms of number of projections, keeping one image every two and three

ones, thus obtaining two more datasets with 1200 and 800 projections respectively, where the pixel and consequently the voxel dimension remains unchanged. For each data set, a CT reconstruction and correction was performed.

As can be seen from the results obtained, the dimensional deviations agree for the three datasets, so that the number of projections does not have a significant impact on the dimensional analysis (Figure 4.8). This aspect could bring some advantages in terms of saving time in the acquisition of CT if the number of projections has to be reduced. However, as this means a loss of spatial resolution, a trade-off between image quality and acquisition time has to be found based on the CT analysis objectives. From now on, it was decided to record 1440 projections (angular step = 0.25°) for the other CT tests to obtain good image quality in a relatively short time.

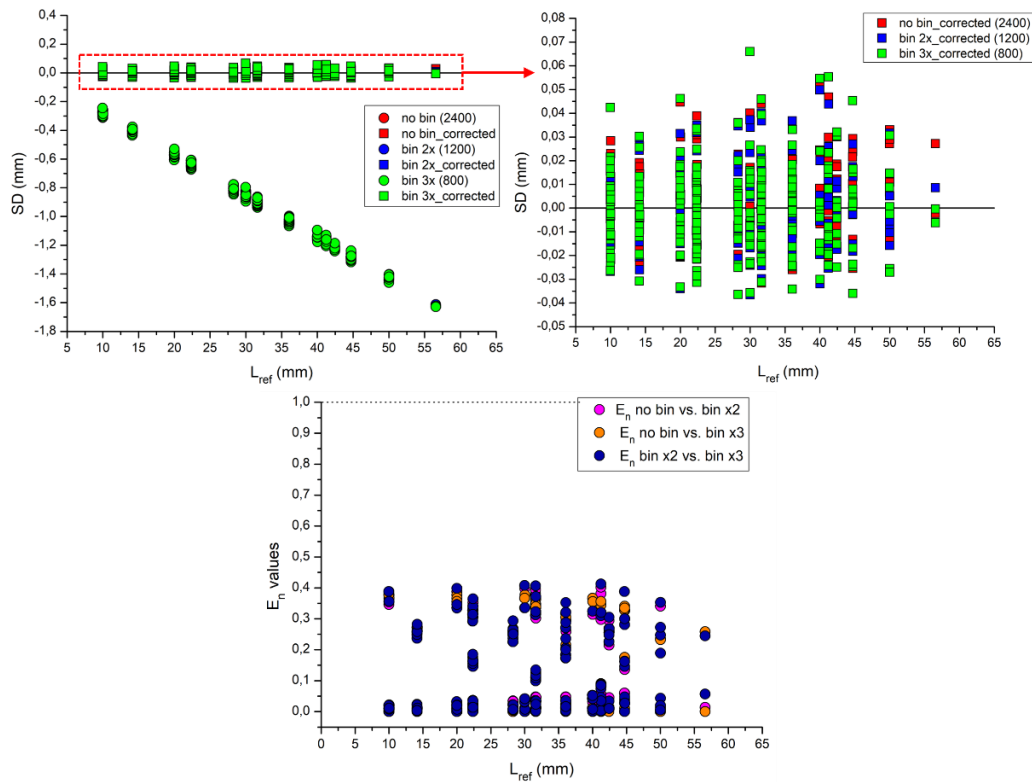


Figure 4.8: SD data for datasets with different projection numbers before and after the correction (top) and E_n values before the correction (bottom).

4.2.2 Sample orientation

As with the ball bar, the same specimen alignment tests were performed with the ball plate (horizontal, vertical and tilted positions, Figure 4.9). The same parameters and geometries were used for the three CT scans (Table 4.8).

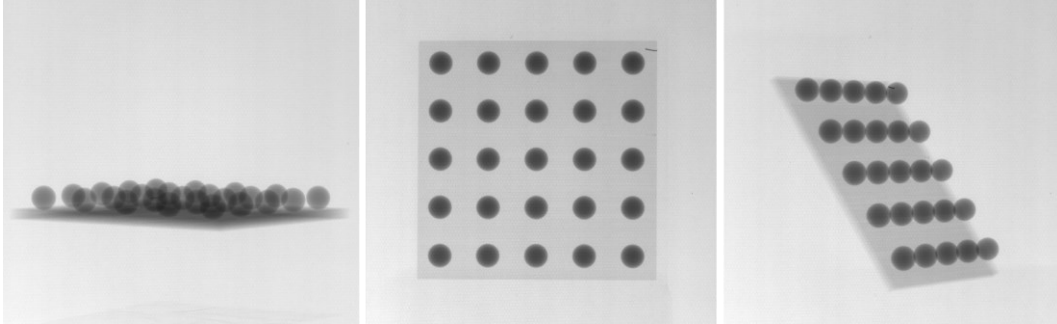


Figure 4.9: Ball plate orientation during CT scan: projection examples of horizontal, vertical and 45° tilted position.

As in the previous case, the deviations of the CT data from the reference lengths can be observed and the agreement between the three data sets in terms of values and increasing trend is highlighted (Figure 4.10). The calculation of the correction factors by regression fitting and the reconstruction of CT with the correct parameters (Table 4.10) shows that all the new deviations are evenly distributed around 0. However, as in the previous case, there is still a small residual difference (± 0.04 mm).

Table 4.8: Ball plate CT acquisition parameters for orientation test

Voltage	150 kV
Current	66 μ A
Integration time	1.75 s
Focal spot size	7 μ m (S)
SDD*	654.8 \pm 1.6 mm
SOD	450.0 \pm 1.4 mm
Magnification	1.5 \times
Voxel size	34.1 \pm 0.2 μ m
Angular step	0.25°

From the calculation of the parameter En, it appears that all values are smaller than 1 when the three orientation samples are compared both before and after voxel correction, with no evident trend; the same applies to the comparison between the reference and the uncorrected CT distances, except for a few values; the maximum En value calculated in the comparison with the corrected CT distances is 0.8. This means that in this case a correction for these specific measurements might not be necessary (Figure 4.11); this aspect could be convenient in terms of saving time and space for data analysis and files storage.

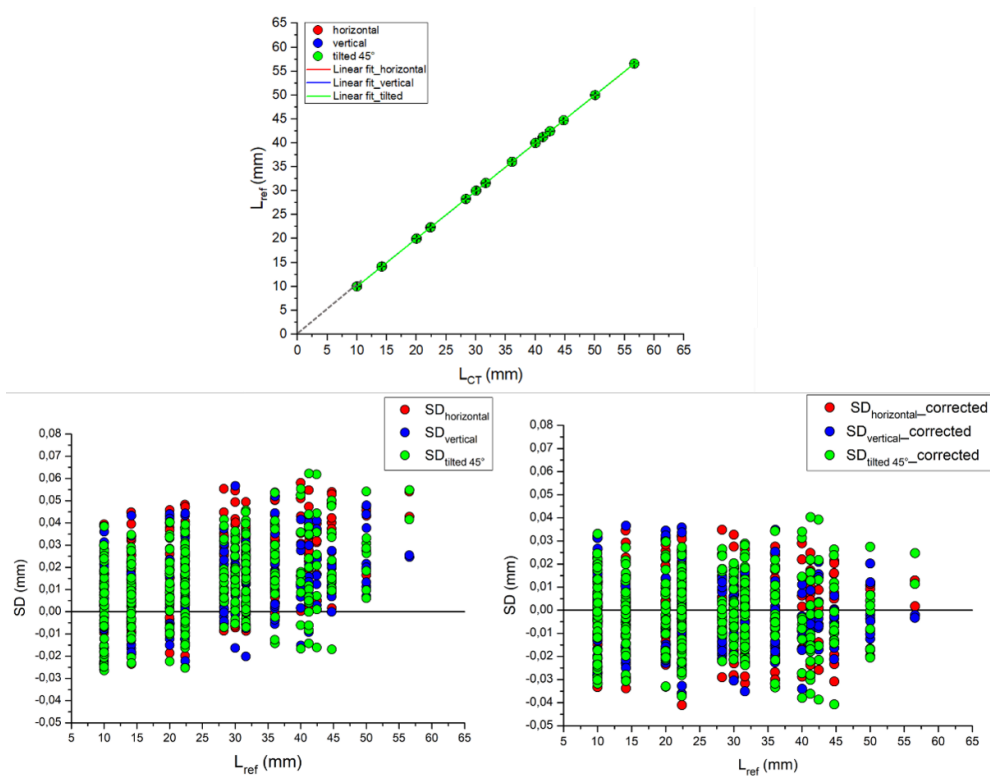


Figure 4.10: Linear regression fit (top) and SD values before and after correction for the three-ball plate orientations (bottom).

Table 4.9: Ball plate CT values after application of correction factors

Position	f_c	voxel _{corr} (μm)	SOD _{corr} (mm)
Horizontal	0.9993 ± 0.0003	34.00 ± 0.14	449.7 ± 2.1
Vertical	0.9996 ± 0.0003	34.00 ± 0.14	449.8 ± 2.1
Tilted 45°	0.9995 ± 0.0003	34.00 ± 0.14	449.8 ± 2.1

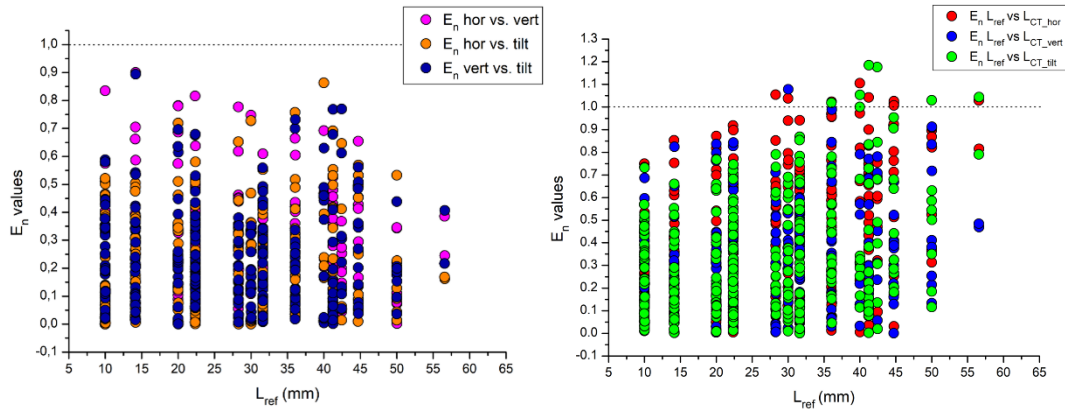


Figure 4.11: Ball plate E_n values calculated between the three orientations before the correction (left) and between reference and uncorrected CT distances (right).

However, looking at the CT reconstructed slices of the ball plate in horizontal orientation, one can notice a different quality of the images, such as the sharpness of the edges and some reconstruction artefacts that affected the data set (Figure 4.12). In addition, a different X-ray absorption of the central sphere compared to the peripheral ones can be observed here, highlighted using a different look-up table (LUT) for the example slice (Figure 4.13). The observed artefacts can derive from the different X-rays path and thus attenuation through the object volume during the rotation when positioned horizontally; in particular, the central sphere is the one mainly affected by a beam hardening effect, where the central area results in a lower signal respect to the edge.

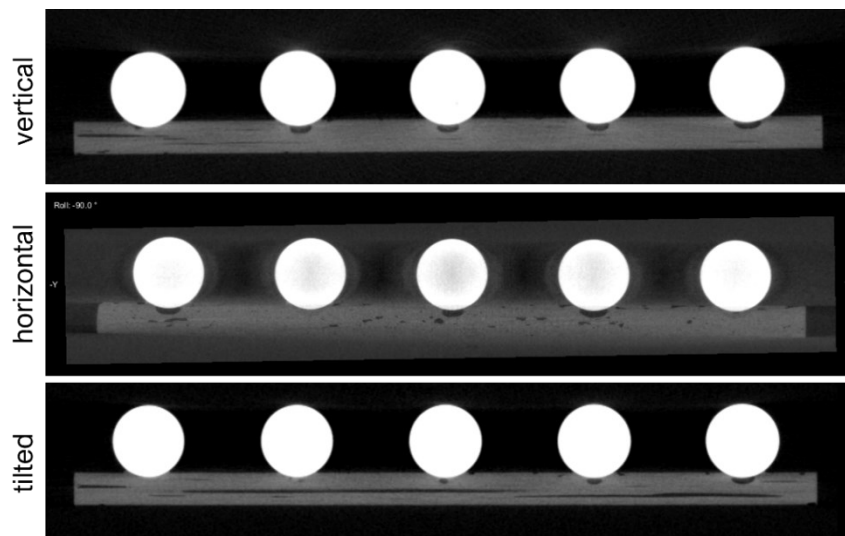


Figure 4.12: CT slices of ball plate in the three tested positions.

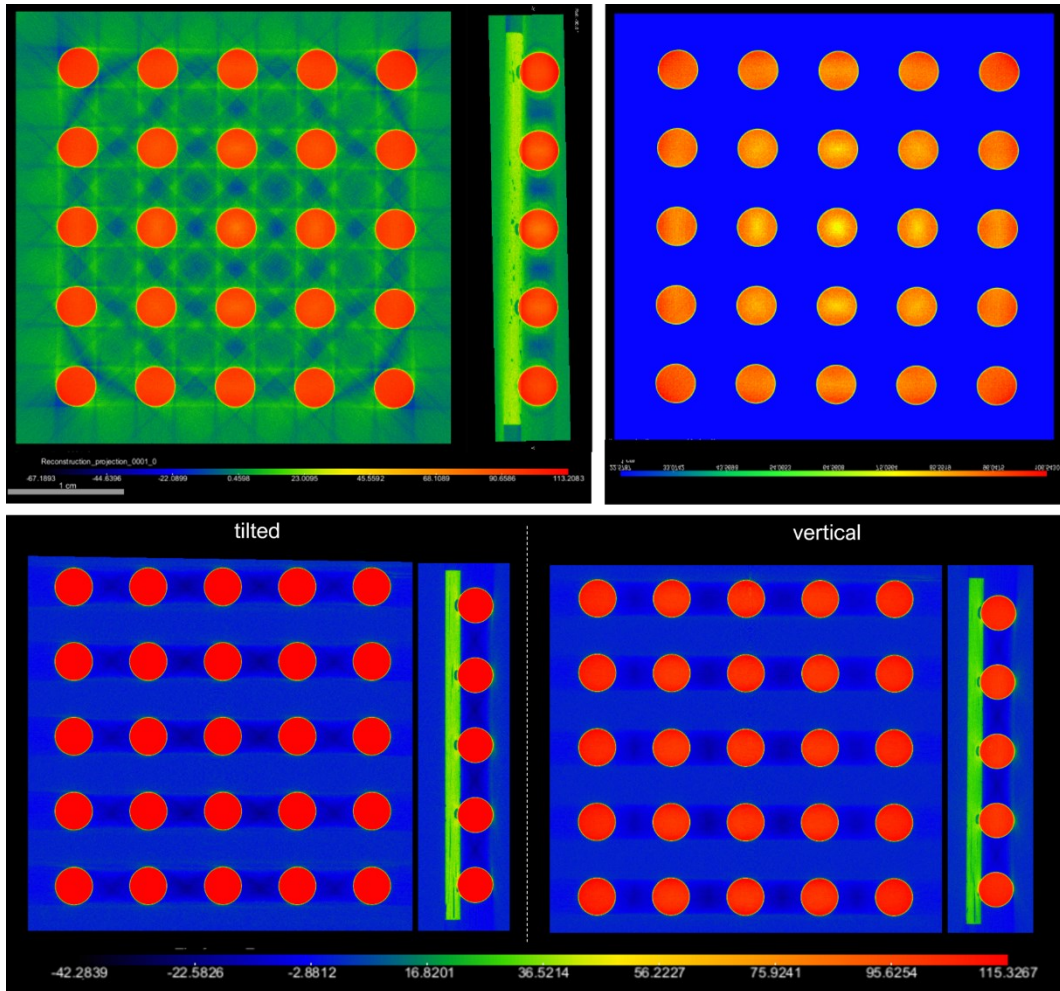


Figure 4.13: CT slice of the ball plate in horizontal position with changed LUT, where reconstruction edges unsharpness, artefacts and x-ray absorption differences are visible (top) and the comparison with the same CT reconstructed slices of tilted and vertical datasets (bottom).

Nevertheless, reconstruction artefacts do not affect significantly dimensional analysis results, since in this specific case the measured quantity (c-c distances) is not influenced by surface determination. However, since this is not applicable in most cases, positions in which object thickness is too irregular during rotation, that means different thicknesses crossed by X-rays at different angles, should be avoided if possible.

4.2.3 Source focal spot size

Another important parameter in the CT analysis is the size of the focal spot of the X-ray source, since it contributes to the spatial resolution of the CT reconstruction, as explained in section 3.2. Since the X-ray tube used in this work has three different focal spot sizes, tests were performed to determine their influence on the CT dimensional analysis. During the acquisition, the voltage was kept constant while the current intensity and integration time were varied depending on the focal spot. In addition, the geometry of the three scans remained unchanged (as in the orientation test) and the sample was positioned vertically (Table 4.10).

Table 4.10: Ball plate CT acquisition parameters

Focal spot size	S (7 μm)	M (20 μm)	L (50 μm)
Voltage		150 kV	
Current	66 μA	200 μA	500 μA
Integration time	1.75 s	850 ms	165 ms
SDD		654.8 \pm 1.6 mm	
SOD		450.0 \pm 1.4 mm	
Magnification		1.5 \times	
Voxel size		34.02 \pm 0.14 μm	
Angular step		0.25 $^\circ$	
Geometric penumbra	3.2 μm	9.1 μm	22.8 μm

As in the previous cases, the CT data agrees both before and after dimensional correction (Table 4.11 and Figure 4.14), and lower than 1 E_n values can be observed for the initial uncorrected data (Figure 4.15). As in the previous test, comparison between reference and uncorrected CT distances results in values lower than 1, thus also in this case, correction might not be applied if necessary. We can conclude that the size of the focal spot does not affect the dimensional analysis.

Table 4.11: Ball plate CT values after application of correction factors

Spot size	f_c	voxel _{corr} (μm)	SOD _{corr} (mm)
S (7 μm)	0.9995 ± 0.0003	34.00 ± 0.14	449.8 ± 2.1
M (20 μm)	0.9995 ± 0.0003	34.00 ± 0.14	449.8 ± 2.1
L (50 μm)	0.9994 ± 0.0003	34.00 ± 0.14	449.7 ± 2.1

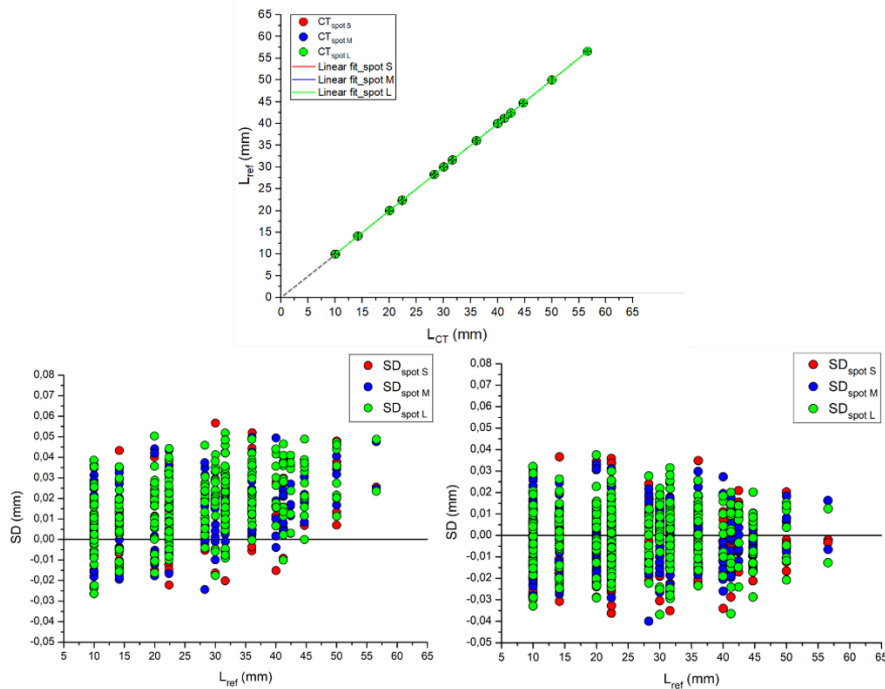


Figure 4.14: Linear regression fit (top) and SD values before and after correction for the three focal spot size (bottom).

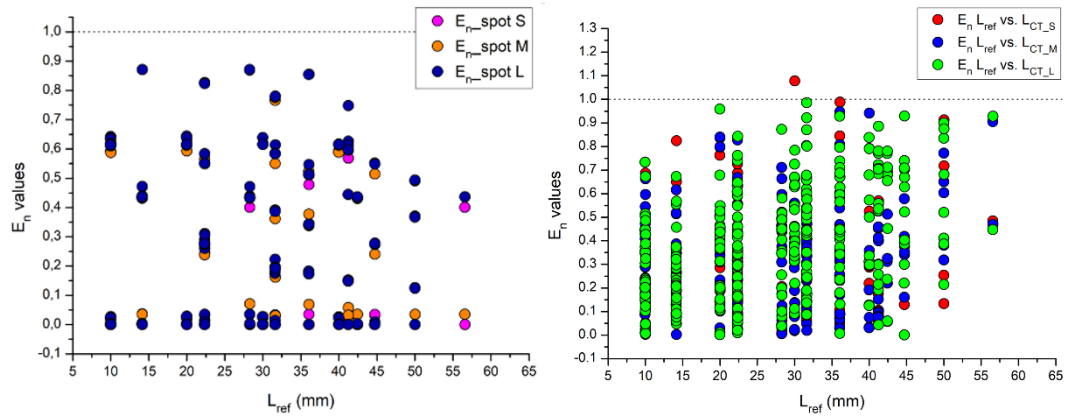


Figure 4.15: Ball plate E_n values calculated between the three focal spot sizes before the correction (left) and then between reference and uncorrected CT distances (right).

4.2.4 Source voltage

Two CT scans were performed with different source voltages (90 and 150 kV), varying the other CT parameters while keeping the geometry constant (Table 4.12). The sample was positioned vertically.

Table 4.12: Ball plate CT acquisition parameters

Voltage	90 kV	150 kV
Current	111 μ A	66 μ A
Integration time	3.2 s	1.75 s
Focal spot size	7 μ m (S)	
SDD	653.8 \pm 1.6 mm	
SOD	320.0 \pm 1.4 mm	
Magnification	2 \times	
Voxel size	24.23 \pm 0.12 μ m	
Angular step	0.15 $^\circ$	

In this case, 2400 projections were taken, as this is the dataset used for the test of the number of projections; since this parameter did not affect the dimensional analysis, one image every two was considered for the voltage tests (the number of projections is reduced, 1200, the pixel dimensions remain unchanged), to have a smaller dataset to work with. Also, unlike the previous analysis, a higher magnification ($2\times$) was used for the CT scan, as the same data set is also used for the magnification tests (see next section).

From data analysis, larger deviations were observed compared to the previous cases, with a negative trend down to a minimum value of -1.63 mm (Figure 4.16). The calculated correction factors are both larger than 1, i.e., the CT dimensions are smaller than the real ones; also, the recalculated SOD used for the corrected CT reconstructions increases by slightly less than 1 cm (Table 4.13).

After correction, the new SD values are within ± 0.05 mm, as observed in the previous analysis.

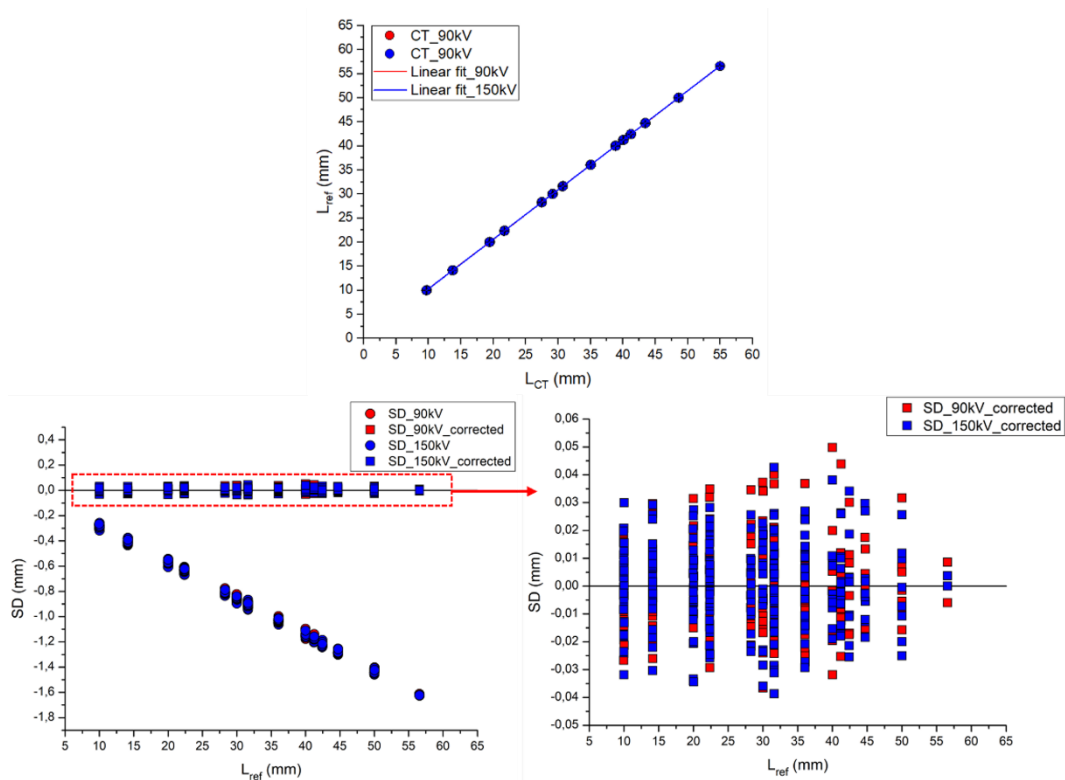


Figure 4.16: Linear regression fit (top) and SD values before and after correction for the two-source voltage (bottom).

Table 4.13: Ball plate CT values after application of correction factors

Voltage	f_c	voxel _{corr} (μm)	SOD _{corr} (mm)
90 kV	1.0295 ± 0.0003	24.94 ± 0.13	329.4 ± 1.8
150 kV	1.0296 ± 0.0003	24.95 ± 0.13	329.5 ± 1.8

The calculated E_n values between the two uncorrected dataset show that they agree and thus voltage parameter does not have a significant influence on dimensional analysis. After correction, all the value result from the comparison of reference and CT distances are lower than 1, thus the correction method works properly. The fact that in this time initial deviations are larger than the previous case could be linked to the different magnification factor, and thus geometry, adopted for the measurements, since a source voltage of 150 kV was already used.

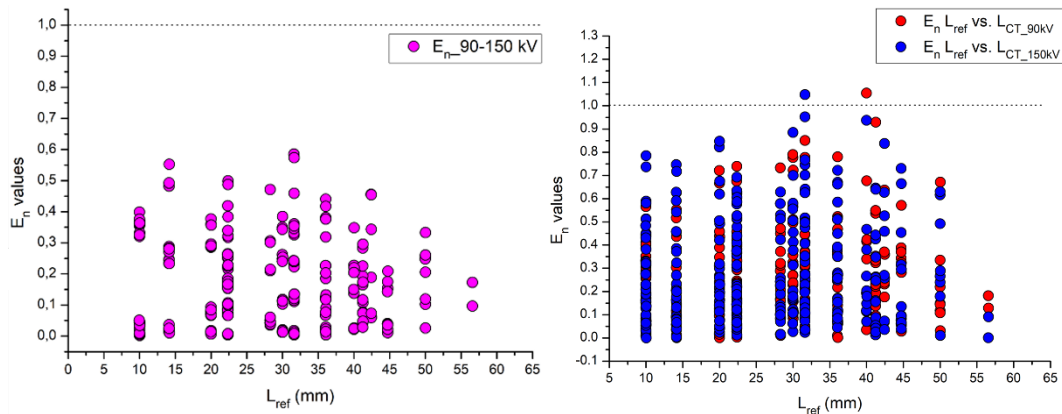


Figure 4.17: Ball plate E_n values calculated between the two voltage datasets before the correction (left) and compared with reference values after the correction (right).

4.2.5 Magnification

To investigate the influence of magnification (M) on the dimensional CT analysis, three scans were made with three different geometries (only SOD was varied), thus testing magnification levels $1.1\times$, $2.0\times$ and $4.1\times$ (Figure 4.18). For simplicity, the three measurements will be indicated as M1, M2 and M4 respectively in the following. Since the dimensions of the flat panel detector allow the entire ball plate to be scanned with a maximum magnification of $2\times$, only 3×3

central spheres are considered in all three tests to achieve the higher magnification. As mentioned in section 4.2.2, the M2 data set is the same used for the 90 kV voltage tests (Table 4.14).

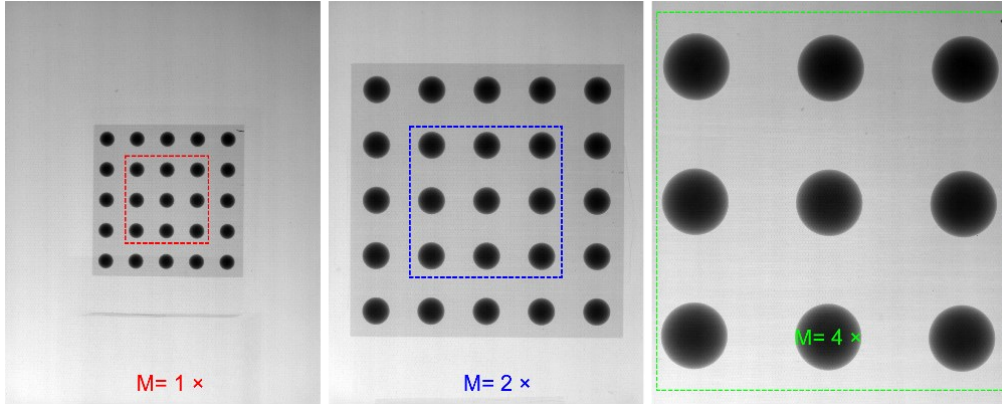


Figure 4.18: Ball plate magnification during CT scan (1.1 \times , 2.0 \times and 4.1 \times)

Table 4.14: Ball plate CT acquisition parameters

Magnification	1.1\times	2.0\times	4.1\times
Voltage		90 kV	
Current		111 μ A	
Integration time		3.2 s	
SDD		653.8 \pm 1.6 mm	
SOD (\pm 1.4 mm)	595.0	320.0	160.0
Voxel size	45.05 \pm 0.15 μ m	24.23 \pm 0.12 μ m	12.10 \pm 0.11 μ m
Angular step	0.25 $^\circ$	0.15 $^\circ$	0.25 $^\circ$
Focal spot size		7 μ m (S)	
Penumbra	0.7 μ m	7.3 μ m	21.6 μ m

As observed in the previous section, deviations are larger for the data sets with higher magnification M2 and M4, while the values for M1 range between -0.02 mm and 0.07 mm, thus showing a slightly positive trend (Figure 4.19). It could also be observed that M2 and M4 show opposite trends in the same absolute value range. This behaviour is also reflected in the correction factors and the recalculated SOD (Table 4.15). However, since in this case changing the

magnification implies varying SOD, it would be difficult to evaluate the effect of the magnification from the reconstructions obtained before the correction, given that their discrepancy with the reference distances is also influenced by the difference in the accuracy of the SOD measure.

Table 4.15: Ball plate CT values after application of correction factors

Magnification	f_c	$\text{voxel}_{\text{corr}} (\mu\text{m})$	$\text{SOD}_{\text{corr}}(\text{mm})$
1.1 \times	0.9982 ± 0.0003	44.97 ± 0.15	593.9 ± 2.4
2.0 \times	1.0295 ± 0.0003	24.94 ± 0.13	329.4 ± 1.8
4.1 \times	0.9695 ± 0.0011	11.73 ± 0.11	155.1 ± 1.5

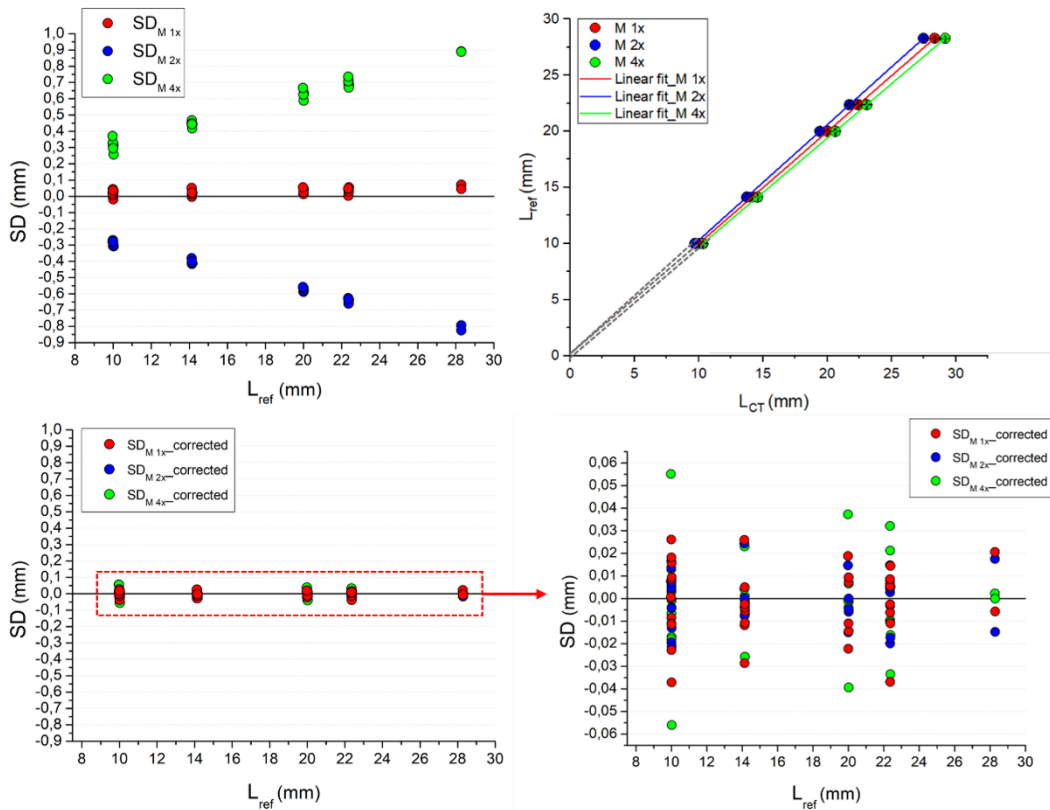


Figure 4.19: Ball plate SD before the correction (top left), linear regression fit (top right) and SD values after the correction for the three magnification datasets (bottom).

After applying the correction, the new data for the three scans are distributed around 0, with a generally larger residual deviation for M4, as indicated in (Müller et al., 2017) for high magnification, even though larger values could be obtained in this case (7×) working with industrial commercial CT equipment. Various reasons are given by the authors, but for their experience they cite the Feldkamp effect as the main one (Xue et al., 2015), that could cause image artefacts when an object is scanned at large opening angles, especially in the image edge parts. To have a validation of this on our data, CT reconstructed slices of the 9 central scanned spheres were elaborated changing color and contrast, obtaining for M4 a similar effect than the one reported by Müller et al., but we cannot affirm that these artefacts lead to higher residual deviations (Figure 4.20).

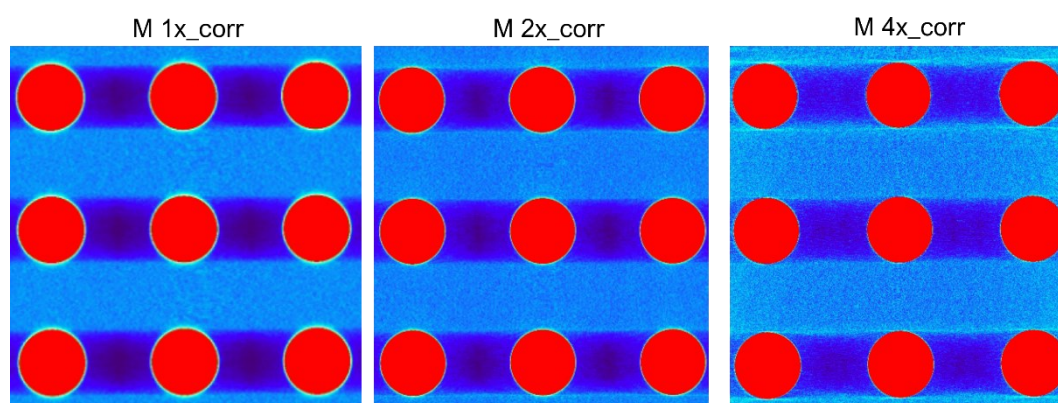


Figure 4.20: False colors CT slice with considered central spheres for the magnification tests, where for the 4× magnification image artefacts are visible near the edge spheres.

Looking at the E_n values, after the correction all the values result lower than 1 for the M1, M2 and M4 comparison between each other and also with respect to the reference distances, indicating that the correction procedure has produced the expected results in these cases as well, showing the effectiveness of the method both when the original reconstruction is magnified or not (Figure 4.21).

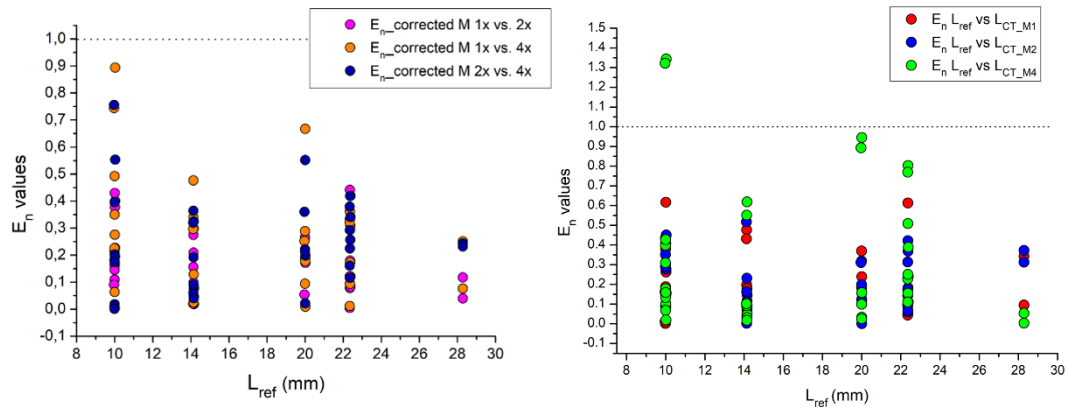


Figure 4.21: Ball plate E_n values calculated between the datasets after the correction (left) and with respect to the reference lengths (right).

4.2.6 CT measurements over time

A comparison was also made between CT scans with the same geometry and the same acquisition parameters but on different days. The measurement conditions are the same as in Table 4.12, trying to position the source and the rotating platform as evenly as possible. The other two analyses were carried out after 3 and 4 months, the first being considered as "time 0". The aim was to check the repeatability of the CT scan in terms of dimensional analysis over the time of the equipment used.

Based on the reported results, differences in the deviations of the three uncorrected data sets could be identified (Figure 4.22). Especially in the last measurement (Figure 4.22, green dots), an increasing behaviour with respect to time 0 can be observed; this is also reflected in the calculated correction factors (Table 4.16). In this case, apart from a few data, there is no compatibility with the E_n values. If the dimensional correction is applied, the deviations agree and are around 0, as in the other cases. Looking at the E_n values after correction, almost all data are smaller than 1 (Figure 4.23). The same applies to the comparison between the reference and the corrected CT distances.

Table 4.16: Ball plate CT values after application of correction factors

Magnification	f_c	$\text{voxel}_{\text{corr}} (\mu\text{m})$	$\text{SOD}_{\text{corr}}(\text{mm})$
#1 (time 0)	1.0003 ± 0.0003	45.06 ± 0.15	595.2 ± 2.5
#2 (after 3 mth)	0.9982 ± 0.0003	44.97 ± 0.15	593.9 ± 2.4
#3 (after 4 mth)	0.9931 ± 0.0003	44.75 ± 0.15	591.9 ± 2.5

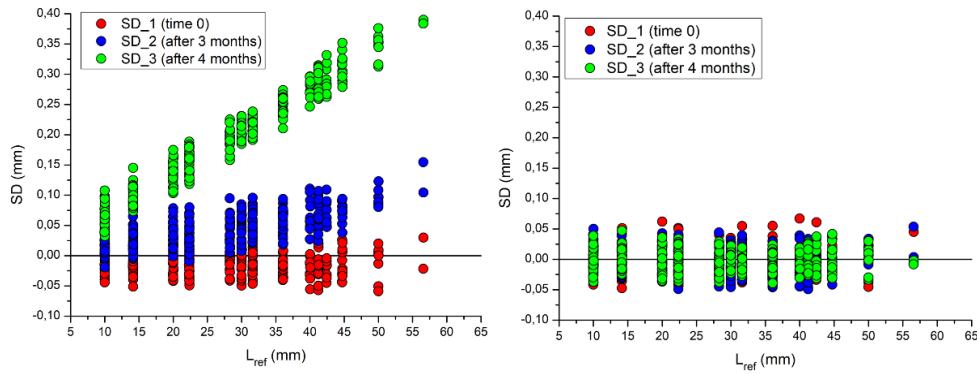


Figure 4.22: Ball plate SD values before (left) and after the correction (right) for the three times.

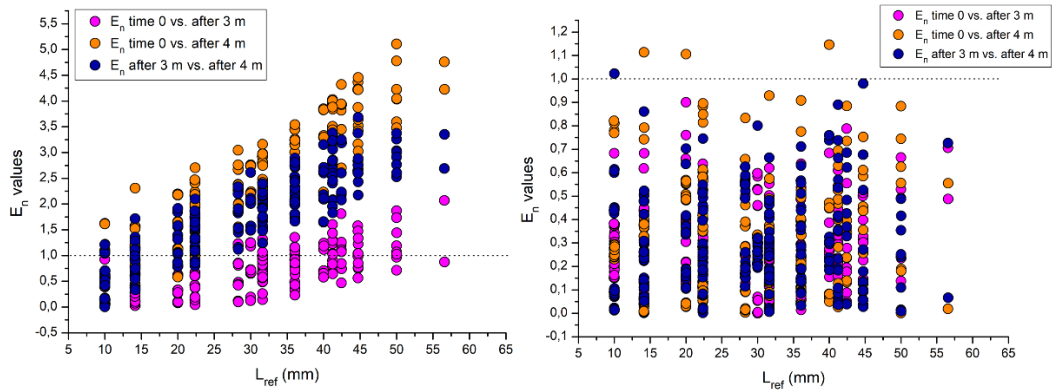


Figure 4.23: Ball plate E_n values calculated between the datasets before (left) and after the correction (right).

In general, it could be affirmed that, even if initial data are not compatible, dimensional correction methodology works properly and it could be then possible to obtain correct measurements.

4.2.7 Discussion

From the obtained results of the illustrated tests, it can be confirmed that the investigated parameters do not have a significant influence on the dimensional analysis, as the data from CT agree in most cases, even if the deviations of the measured quantities from the reference values are present in all analysed cases. Most tests show that the CT reconstructed volume is larger in terms of dimensions, except in the M2 case, where the data showed a negative trend before correction.

In most cases, the values of SD from uncorrected CT reconstruction range from a minimum of -0.03 mm to a maximum of 0.15 mm, except for the measurement at 90kV after 4 months, where the maximum value of SD is 0.4 mm. Moreover, the deviations are larger when higher magnification was used (2× and 4×) and range from -1.6 mm to 0.9 mm (Table 4.17). This is probably due to the accuracy in the measurement of SOD, considered the most influencing parameter in a CT scan with the instrumentation used. Nevertheless, the tested correction method shows its effectiveness in the situations studied, even if residual deviations from the reference values after correction are observed, that lead to think to a systematic effect. Analysing data falling outside the SD range of ± 0.04 mm, we can observe that 93 % of these data concern distances between spheres of which at least one is on the edge, and of which slightly more than half concern both spheres on the edge. In particular, the last sphere line of the sphere plate is most affected (U-Y spheres). As some authors reported, this could be due to some artefacts caused from the reconstruction algorithm FDK used, which is known to affect mainly the upper and lower edges of the images (Figure 4.24), as also observed in Müller et al., 2017. This aspect is not observed instead for the ball plate CT placed horizontally: even if the reconstructed slices show many artefacts, also due probably to a beam hardening effect (section 4.2.2, Figure 4.13), max deviations after correction remain in the range ± 0.04 mm.

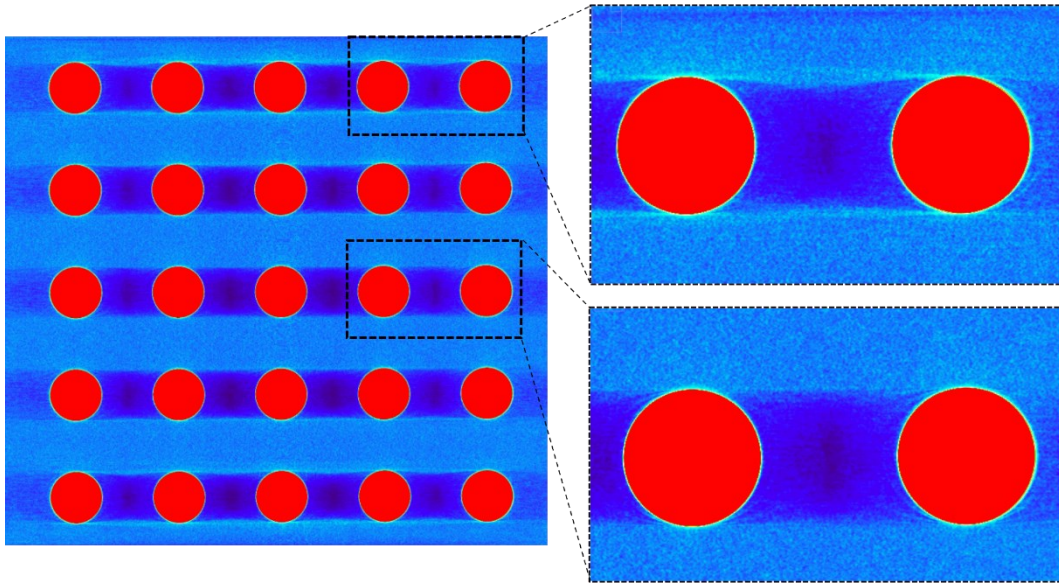


Figure 4.24: Ball plate false colors CT slice for the magnification $2\times$ dataset, where the difference between central spheres and close to the image edge is highlighted.

In addition, some authors (Müller et al., 2017) investigated the influence of image quality, particularly in relation to SNR (signal-to-noise ratio), which is determined as the ratio between the average grey values (signal) and the associated standard deviation (noise) (Goldman, 2007). An evaluation of the SNR values of the conducted CT tests was carried out with both uncorrected and corrected data sets (Figure 4.25). It is immediately evident that the applied correction has no effect on the results and in most cases the values between the parameters in the different data sets are compatible. The two exceptions relate to the orientation test, where SNR values for horizontal position decrease (this is to be expected given the reconstructed images shown in section 4.2.2), and the magnification tests, where low SNR was measured on reconstructed CT images at higher magnification; this is also to be expected as generally CT scans taken at higher spatial resolution lead to an increased noise, since a smaller voxel size means a decreased average number of photons per voxel (Ghani et al., 2017; Müller et al., 2017).

Table 4.17: SD minimum and maximum values before and after correction

Measure	SD_before (mm)		SD_after (mm)	
	min	max	min	max
150 kV_rep.1	-0.019	0.10	-0.04	0.04
150 kV_rep.2	-0.012	0.14	-0.05	0.04
150 kV_rep.3	-0.03	0.11	-0.05	0.05
no bin	-1.6	0.3	-0.03	0.05
bin 2x	-1.6	0.3	-0.04	0.05
bin 3x	-1.6	0.2	-0.04	0.07
horizontal pos.	-0.03	0.06	-0.04	0.03
vertical pos.	-0.02	0.06	-0.04	0.04
tilted pos.	-0.03	0.06	-0.04	0.04
spot size S	-0.02	0.06	-0.04	0.04
spot size M	-0.02	0.05	-0.04	0.03
spot size L	-0.03	0.05	-0.04	0.04
voltage_90kV	-1.6	-0.3	-0.04	0.05
voltage_150kV	-1.6	-0.3	-0.04	0.04
M1	-0.019	0.07	-0.04	0.03
M2	-0.8	-0.3	-0.02	0.02
M4	0.3	0.9	-0.06	0.06
90kV_time 0	-0.06	0.06	-0.05	0.07
90kV_after 3 m	-0.019	0.15	-0.05	0.05
90kV_after 4 m	0.03	0.4	-0.04	0.05

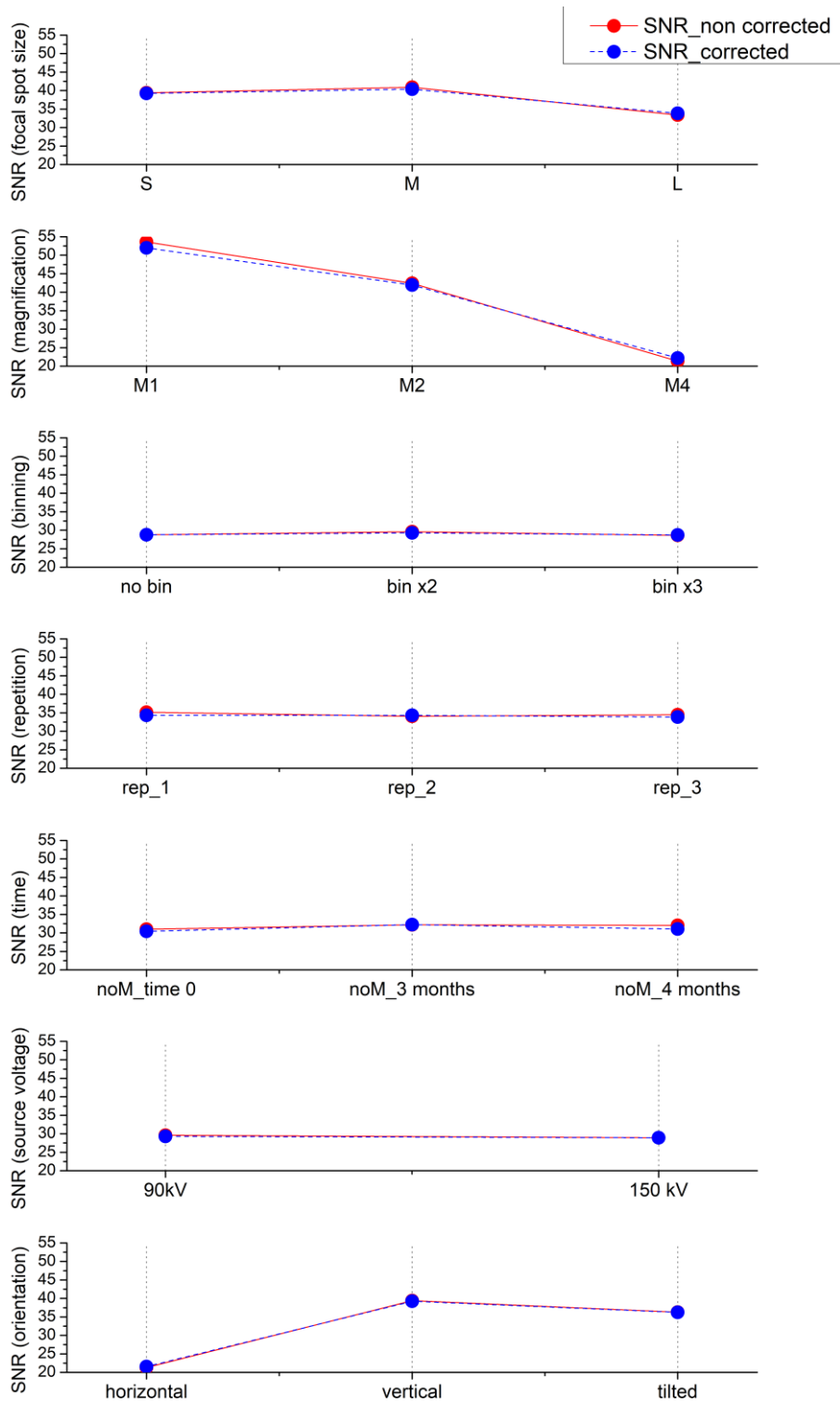


Figure 4.25: SNR evaluation for the different CT tests

Looking at the SNR values for each sphere in the horizontal position dataset, a decreasing trend from the edges to the central sphere is evident (Figure 4.26), following the intensity maps in Figure 4.12. Comparing for example the SNR value of the vertical position dataset with the horizontal one, as shown in Figure 4.27 where the spheres are presented following the rows, differences in SNR are smaller, although the more central spheres (green and blues spheres in Figure 4.26) always result in smaller SNR values.

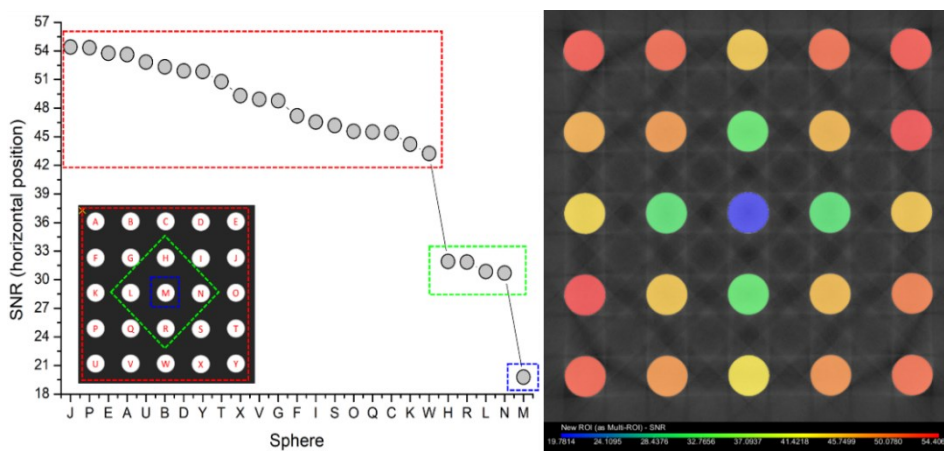


Figure 4.26: SNR evaluation for the horizontal position CT tests.

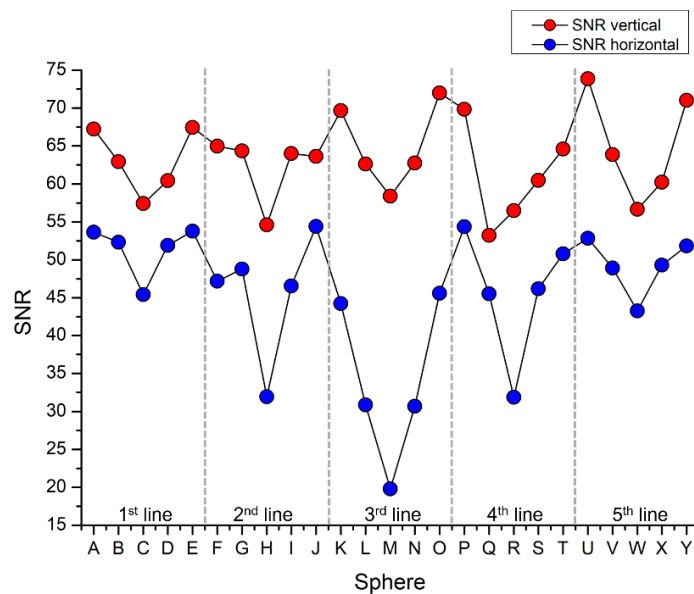


Figure 4.27: SNR comparison between the vertical and horizontal position CT tests.

4.3 Correction methodology application on samples

The methodology tested for voxel size correction to obtain a more precise and accurate dimensional CT results was applied to different type of samples, which is one of the final goals of this work. First, the analysis was performed on a LEGO brick as an example, since it has a regular geometry; then, the same method was applied for the CT correction of the piccolo flute described in Chapter 1. In both cases, a CT scan of the two tested calibration objects (ball bar and ball plate) was performed before and after the CT scan of the sample, as described in section 3.5; together with the sample, the ball bar was also scanned. In this way, two types of corrections could be performed: (i) using the average correction factor derived from the CT scans of the ball plate (before and after), and (ii) using the correction factors derived from the ball bar scanned with the real sample. A third type of test, applied only on the Lego brick, consists in the use of a sample's calibrated feature (e.g., the centre-to-centre distances of the LEGO knobs), was also performed. In this last case, the brick was measured with the ATOS Scanbox machine (Figure 3.4) to obtain reference values for the considered parameter; however, this method could not always be applied to the samples studied and thus calibration objects were needed anyway.

The described correction strategy could lead to the definition of the best correction method to be applied to different kinds of sample, like historic artefacts.

4.3.1 Preliminary tests

Before applying the correction methodology to the samples, some preliminary tests have been performed on the calibration objects. Three analyses have been conducted:

- using the data from CT of ball plate + ball bar acquired before of the LEGO brick one, corrections have been made on the ball plate using the correction factor derived from the ball bar (1) and vice versa (2);
- using the 150 kV repeated measurements datasets (section 4.2), correction of the second ball plate CT scan has been made with the average correction factor derived from the first and the third CT measurements (3).

The aim was to try to have an initial idea of correction effectiveness with the first two illustrated methods, that will be applied to our samples.

4.3.1.1 Ball plate + ball bar corrections (1-2)

The test has been performed on the ball plate + ball bar CT scan acquired before the LEGO brick, whose set parameters are listed in Table 4.18. Two correction factors with the already used methodology have been calculated, and the results are summarized in Table 4.19.

Table 4.18: Ball plate + ball bar CT acquisition parameters

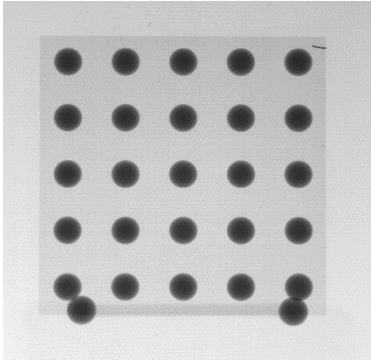
	Voltage	90 kV
	Current	111 μ A
	Integration time	3.2 s
	Focal spot size	7 μ m (S)
	SDD	654.8 \pm 1.6 mm
	SOD	450.0 \pm 1.4 mm
	Magnification	1.5 \times
	Voxel size	34.02 \pm 0.14 μ m
	Angular step	0.25 $^\circ$

Table 4.19: CT parameter and voxel size after application of correction factors

Object	f_c	voxel _{corr} (μ m)	SOD _{corr} (mm)
Ball plate	0.9997 \pm 0.0003	34.01 \pm 0.14	449.9 \pm 2.1
Ball bar	0.9989 \pm 0.0013	33.98 \pm 0.14	449.5 \pm 2.1

Different correction factors were obtained for the two calibration objects, with a larger uncertainty obtained for the ball bar, probably due to the method used for calculation of correction factors, i.e., for the ball one single distance is considered against the 300 lengths considered for the ball plate. When the ball plate is corrected using the ball bar, the obtained SD (green point in Figure 4.28 left) seems to have an opposite trend with respect to the non-corrected one (red points

in the same figure), going forward negative values; the correction works properly if the ball plate is corrected with its own correction factor (blue points). The same occurs when the ball bar is corrected with the ball plate correction factor, that is, the obtained L_{CT} value tends to improve but does not reach the accuracy of the correction with the own f_c . If we look at the relative E_n test (Table 4.20), all values are lower than 1, where the minor one results when its own f_c is used.

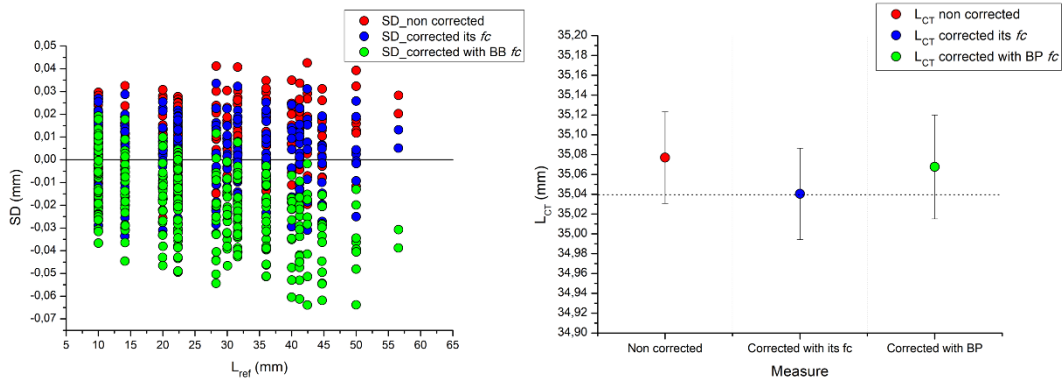


Figure 4.28: Ball plate SD values (left) and ball bar values (right) before and after the applied corrections.

Table 4.20: Ball bar E_n values calculated before and after the correction.

Measure	L_{CT} (± 0.05)	E_n
no_corr. (mm)	35.08	0.8
corr. its f_c (mm)	35.04	0.009
corr. BP (mm)	35.07	0.5

If we perform the E_n test between the reference distances and the ones obtained from CT for the ball plate, we can observe that values obtained with the ball bar correction are higher than the other, with some of them larger than 1 (Figure 4.29). An increasing trend could be observed if we compare the two corrections to each other and with the non-corrected L_{CT} , as expected for higher distances; all the reported values are lower than 1, even if the correction with itself correction factor shows the lower values.

From the obtained results, we can conclude that the most suitable correction method in this case is to use the correction factor derived from the object itself.

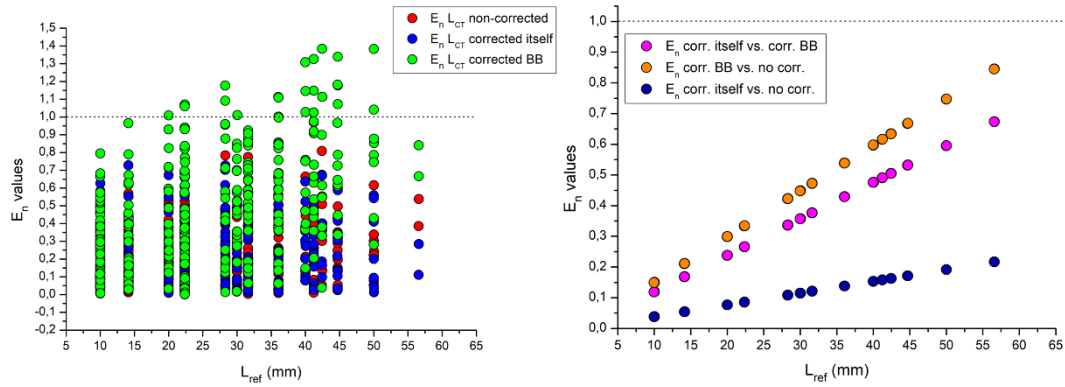


Figure 4.29: Ball plate E_n values calculated between reference and CT distances (left) and between the three datasets (the one non corrected and the two corrected, right).

4.3.1.2 Ball plate corrected with ball plate before + after (3)

The datasets used for this type of test were the 150 kV repeated CT scans, illustrated in section 4.2; the first and the third ball plate CT were used in this case to correct the second CT scan, whose correction factor differs from the other two (Table 4.6). Correction factors for the first and third scans were compatible but differed in the last three significant digits (CT1= 0.998649; CT3=0.998562), and this resulted in different SOD-corrected values from the fifth significant digit (549.19 and 549.14 mm). Because the software considers all numbers after the comma for the reconstruction, it was decided to use an average SOD value (549.17 mm) as the corrected parameter.

In this case, if we compare the two corrected SD values (in blue, the one derived from the own correction factor; in green, the one from the average of CT1 and CT3), better results with respect to the correction with the BB explained previously can be highlighted (Figure 4.30). In addition, the E_n values calculated by comparing the reference distances with the corrected CT values were smaller than 1. From the comparison of the E_n values between the two performed corrections (purple points in Figure 4.30 right), all are much lower than one, which means that the two methods are completely compatible in this case.

Comparing these results with those obtained from the previous analysis (ball plate corrected with the ball bar), it can be noticed that in this case, the correction was more effective.

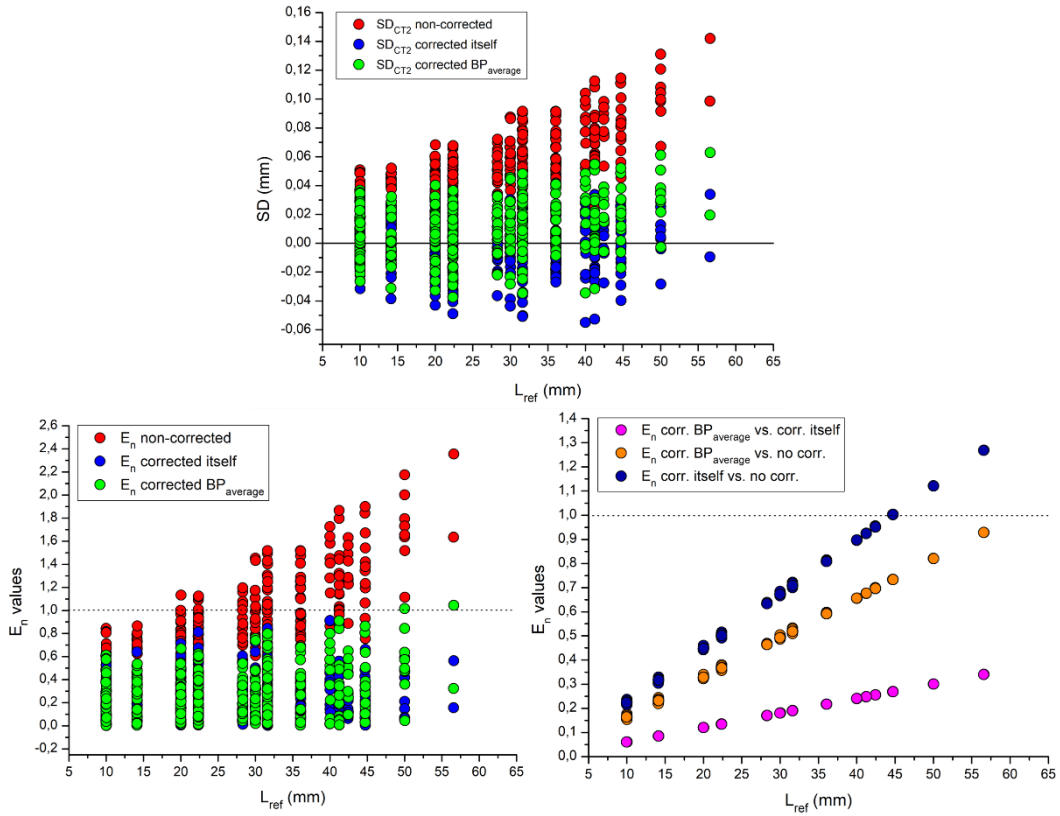


Figure 4.30: Ball plate SD values before and after the applied correction (top) and E_n values calculated for both non corrected and corrected data and between the three datasets (bottom).

4.3.2 LEGO brick

The measured quantities considered for the 4×2 LEGO brick are knobs diameters and centre distances, total length (A), width (B) and height (C). A thin metal rod was placed between knobs 1 and 2 to have a spatial reference (Figure 4.31). All measured values are listed in Table 20 in Appendix D. The measurements of the CT parameters are listed in Table 4.18.

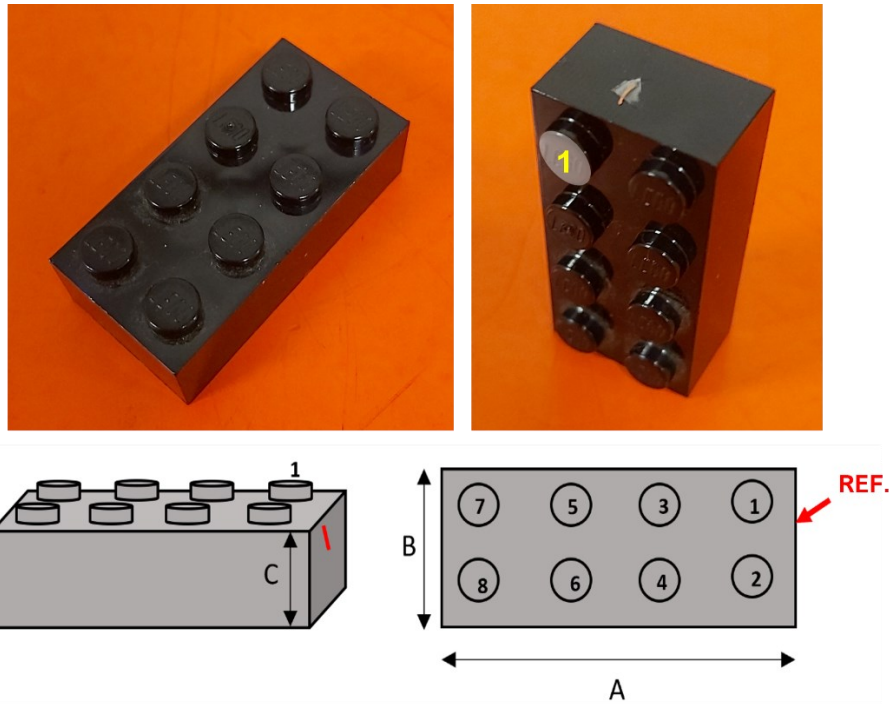


Figure 4.31: LEGO brick used for CT correction tests, with indication of the measured quantities.

As anticipated, in addition to the two correction tests with the calibration objects (Figure 4.32), a third correction attempt was made using a calibrated features measured by the ATOS Scanbox (in this case, the knobs center distance of the brick itself was chosen). The same approach as the already tested correction method is applied, i.e., The correction factor was derived by the linear regression fit, fixing the intercept to 0 in this case because it was not compatible with it, as was the case for the ball plate fits. The results obtained from the three correction tests are presented in Table 4.21.

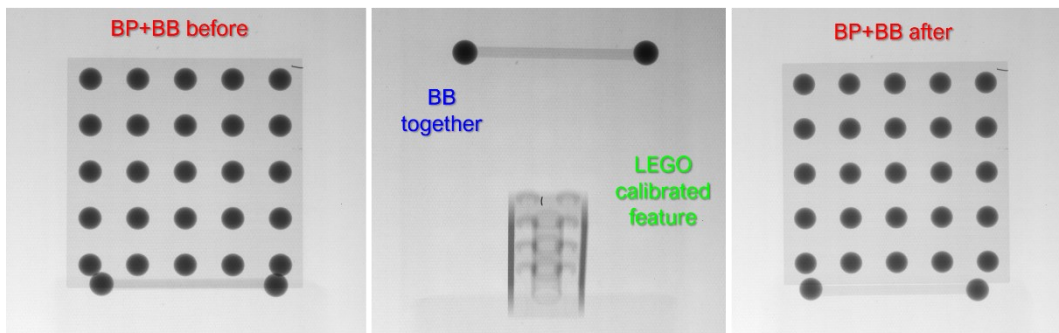


Figure 4.32: Sequence of CT acquisition for LEGO brick sample correction.

Table 4.21: CT values after application of correction factors

Measure	f_c	$\text{voxel}_{\text{corr}} (\mu\text{m})$	$\text{SOD}_{\text{corr}}(\text{mm})$
BP before	0.9997 ± 0.0003	34.01 ± 0.14	449.9 ± 2.1
BP after	0.9995 ± 0.0003	34.00 ± 0.14	449.8 ± 2.1
BP average	0.9996 ± 0.0004	34.01 ± 0.14	449.8 ± 2.1
BB together	0.9994 ± 0.0009	34.00 ± 0.14	449.7 ± 2.1
LEGO calibrated feature	1.008 ± 0.002	34.28 ± 0.16	453.4 ± 2.4

Differences in the values of calculated correction factors from the calibration objects and from the LEGO brick chosen feature can be noticed. Looking at the SD values obtained from the uncorrected dataset (Figure 4.33), different behaviours between the measured quantities were observed; in particular, the A, B, and C lengths and knobs diameters showed negative and positive SD, respectively, while c-c distances show both negative and positive values. This could lead to the assumption that a single correction factor will not be able to correct the sample uniformly.

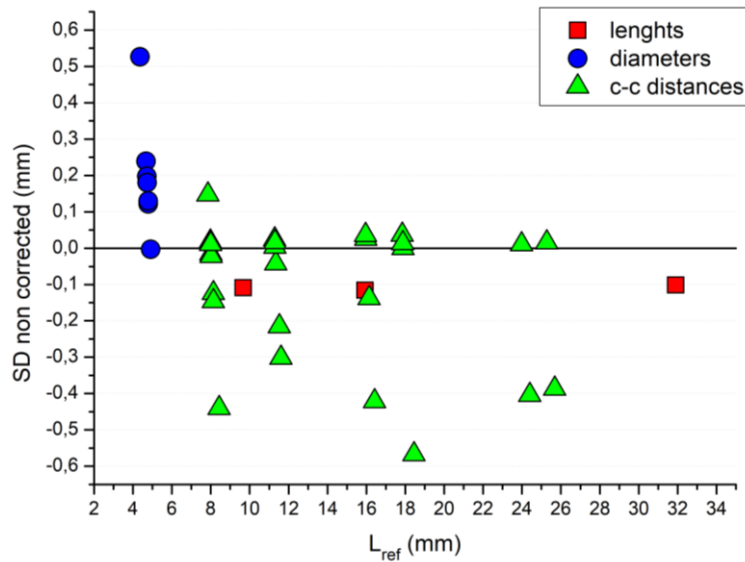


Figure 4.33: SD values of uncorrected CT scan.

After the application of corrections, there were no significant differences between the starting dataset and the ones corrected with the calibration objects, while using the calibrated feature correction, some values improved while others worsened in terms of SD (Figure 4.34 and 4.35), as expected from the evaluation of the initial SD. This aspect is also evident from the colour deviation maps of the LEGO 3D model between the datasets (Figure 4.36), where the scale bar is set between ± 1 voxel (0.035 mm) for the BB and BP corrected datasets and in the range ± 0.2 mm for the other correction.

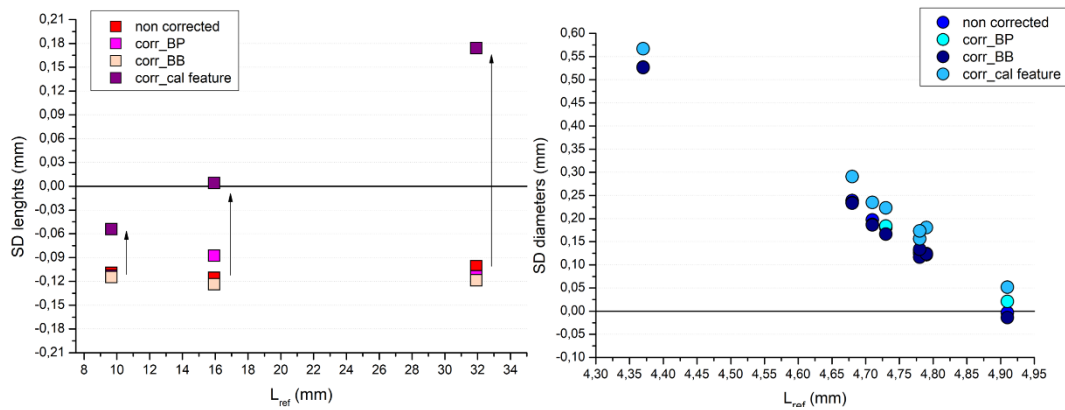


Figure 4.34: SD values of lengths and diameters of the different correction methods.

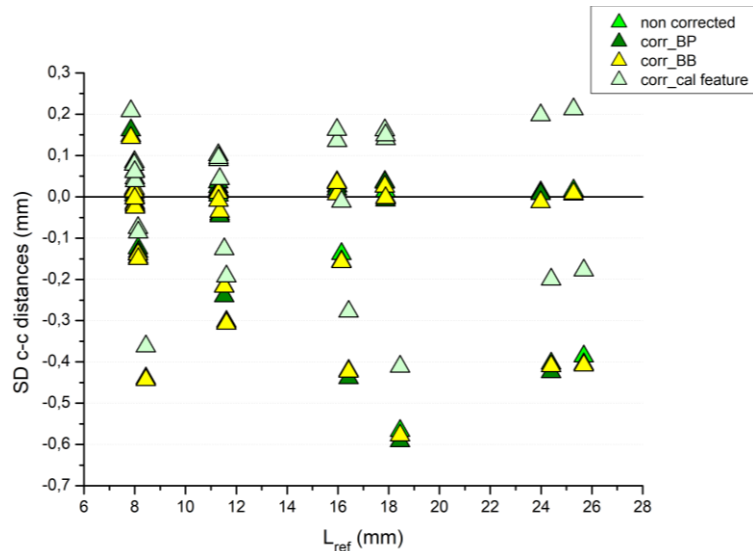


Figure 4.35: SD values of c-c distances of the different correction methods.

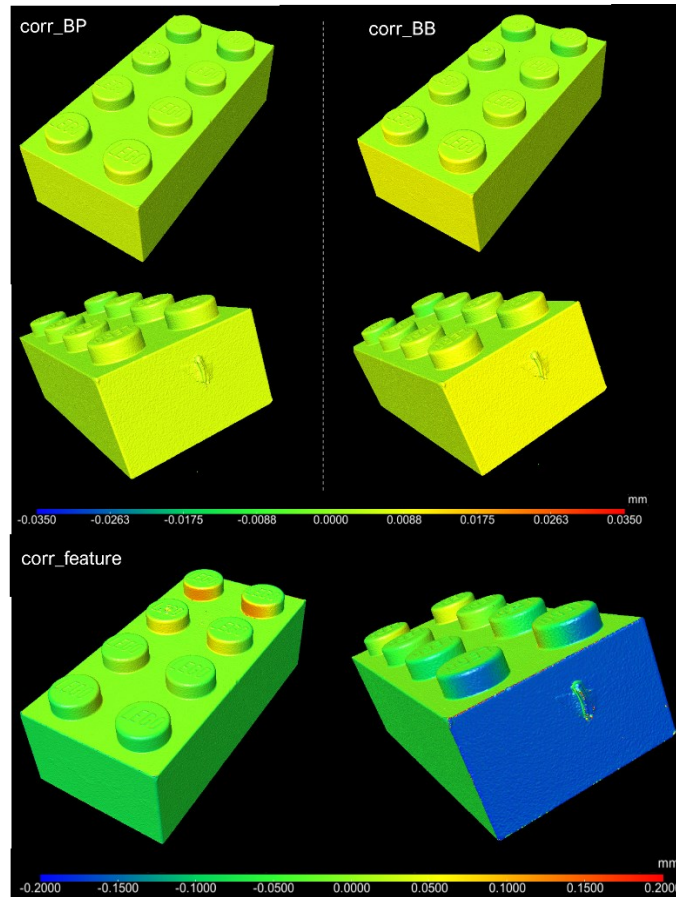


Figure 4.36: SD values of c-c distances of the different correction methods.

4.3.3 Piccolo Flute

The same correction methodology was applied to the woodwind instrument presented in Section 1 (Figure 1.1): a first test with the ball bar scanned together with the flute (whose components were separated for the analysis and positioned vertically, Figure 4.37), and the second using the average correction factor derived from the ball plate scanned before and after the flute.

In Tables 4.22 and 4.23 are summarized the CT parameters adopted for the analysis (based also on the previously performed tests and obtained results), correction factors, and recalculated values. The final factors used were those obtained from the BP average and BB together.

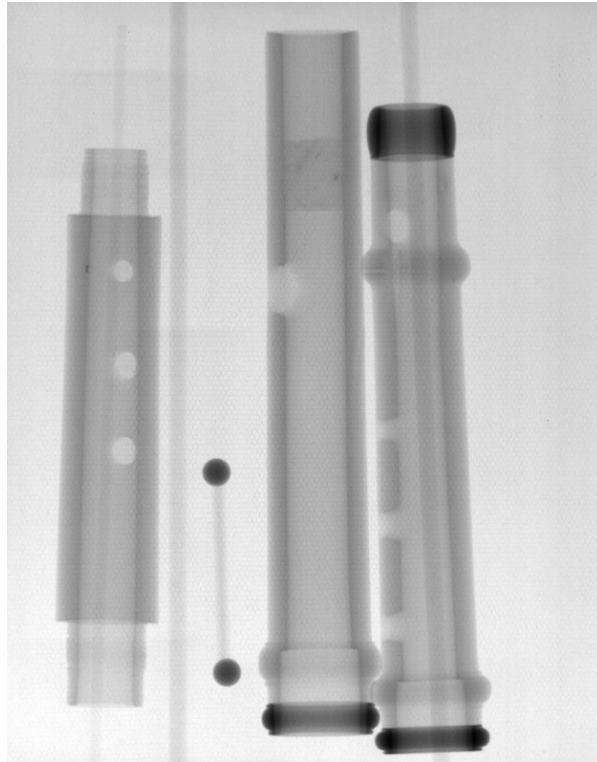


Figure 4.37: CT projection of the Piccolo Flute components (from left: body, head and foot) with the ball bar. The objects are positioned vertically with the help of wooden sticks; the darker parts on the head and foot (more attenuating) represent the ivory rings decorations.

Table 4.22: CT acquisition parameters

Voltage	90 kV
Current	500 μ A
Integration time	4 s
Focal spot size	50 μ m (L)
SDD	1403.8 \pm 1.6 mm
SOD	1300.0 \pm 1.4 mm
Magnification	2 \times
Voxel size	45.84 \pm 0.07 μ m
Angular step	0.25 $^\circ$

Table 4.23: CT values after application of correction factors

Measure	f_c	voxel _{corr} (μm)	SOD _{corr} (mm)
BP before	1.0020 ± 0.0003	45.93 ± 0.07	1302.7 ± 2.6
BP after	1.0018 ± 0.0003	45.92 ± 0.07	1302.3 ± 2.6
BP average	1.0019 ± 0.0002	45.93 ± 0.07	1302.5 ± 2.5
BB together	1.0009 ± 0.0017	45.88 ± 0.11	1301.1 ± 3.4

In this case, the features considered for the measurements were the inner and outer terminal diameters, lengths, and horizontal and vertical hole diameters for all three parts of the flute, as illustrated in Figure 4.38. These measures are some of the typical ones that specialized craftsmen use for manufacturing wind musical instruments and are important for the realization of copies. Measurements on the three parts were performed using a digital calliper (± 0.01 instrumental error), repeating one representative measure for the three chosen features (A'_{ext} , D' and hole 1 in the body) ten times to calculate the standard deviations, that were quadratically added to instrumental error to obtain the final uncertainties (all the results are reported in Appendix D).

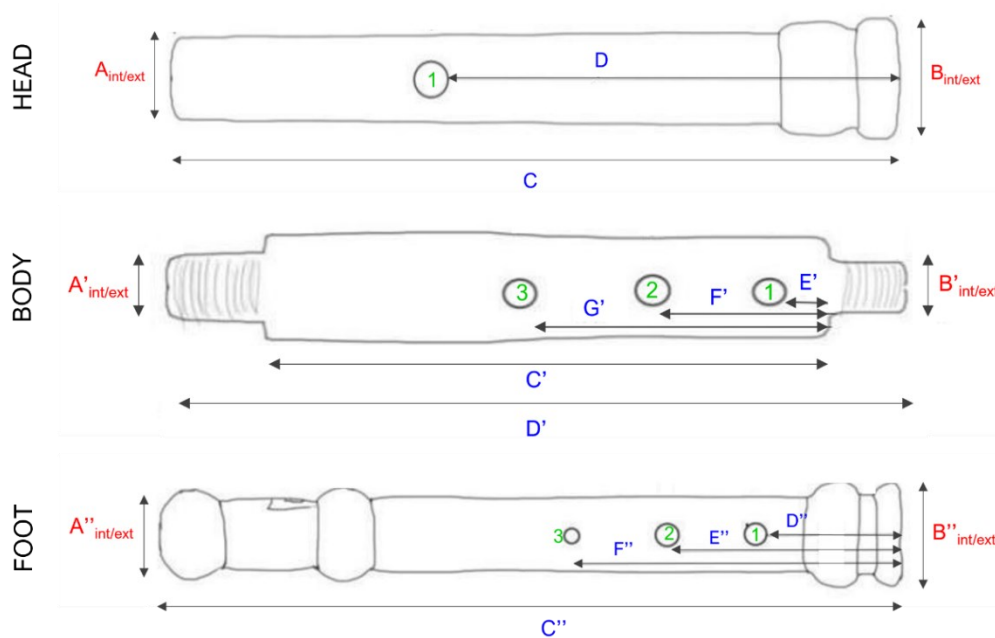


Figure 4.38: Piccolo Flute scheme of the three components with indication of the measured features.

As for the Lego brick, the SD values obtained from the uncorrected CT data demonstrate that the three components have both positive and negative deviations from the reference, with deviations ranging from 0.20 to -0.35 mm (Figure 4.39). Examining the adjusted SD values (Figure 4.40), the correction generally increases the values of the measurands, which is consistent with the correction factor being greater than 1, although there are some exceptions, which may be due to the software measurements. Additionally, it has been established that the measurements of the lengths and diameters are usually contingent on the threshold used for surface determination, as discussed in Section 3.3.

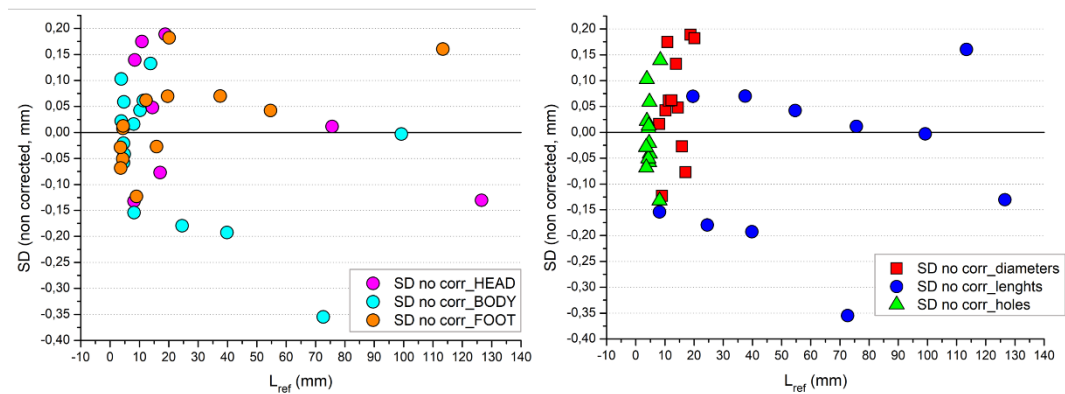


Figure 4.39: SD values of the uncorrected CT datasets, divided on the left based on the three flute parts (head, body and foot) and on the right based on the considered measured feature (diameters, lengths and holes diameters).

As for the LEGO brick, a comparison between the mesh obtained from the uncorrected CT datasets and the two corrected ones for each flute components have been done, highlighting differences through a color deviation maps (Figure 4.41-42-43). For the flute head CT corrected with the ball bar (BB), deviations in lengths and in the hole's diameters are visible up to ± 0.1 mm; the latter, in particular, show a higher deviation in the range ± 0.05 mm (voxel size), while at the opposite side (where the ivory ring is inserted), little differences could be seen. Regarding deviation with the CT corrected with ball plate (BP) deviations are already visible in the range ± 0.25 mm for length and ± 0.13 mm for the hole. In the body of the flute, with respect to the CT corrected with BB data, deviations are visible from ± 0.08 mm, while in the dataset corrected with BP, differences are highlighted from ± 0.2 mm, equivalent to about four time the voxel size. The

flute's foot show deviation from the range ± 0.1 mm with respect to the BB corrected dataset, and the maximum values increase for the BP corrected dataset, as highlighted for the holes' diameters in Figure 4.42.

The fact that the deviations of the corrected BP dataset with respect to the uncorrected dataset are higher is in line with the higher value of the obtained correction factor (Table 4.23).

The third correction test using calibrated feature of the object itself was not performed since it was not possible to use the ATOS Scanbox for the reference measurements.

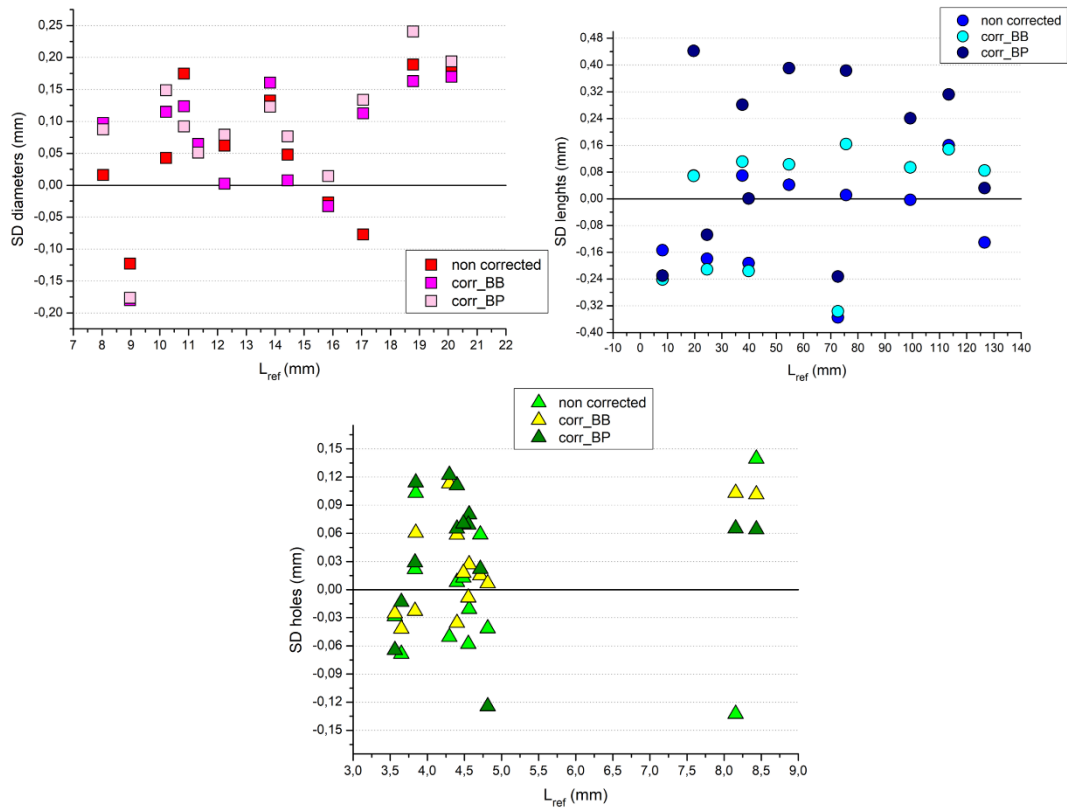


Figure 4.40: SD values of the non-corrected and corrected CT datasets, divided based on the considered measurand (top left: diameters; top right: lengths; bottom: holes).

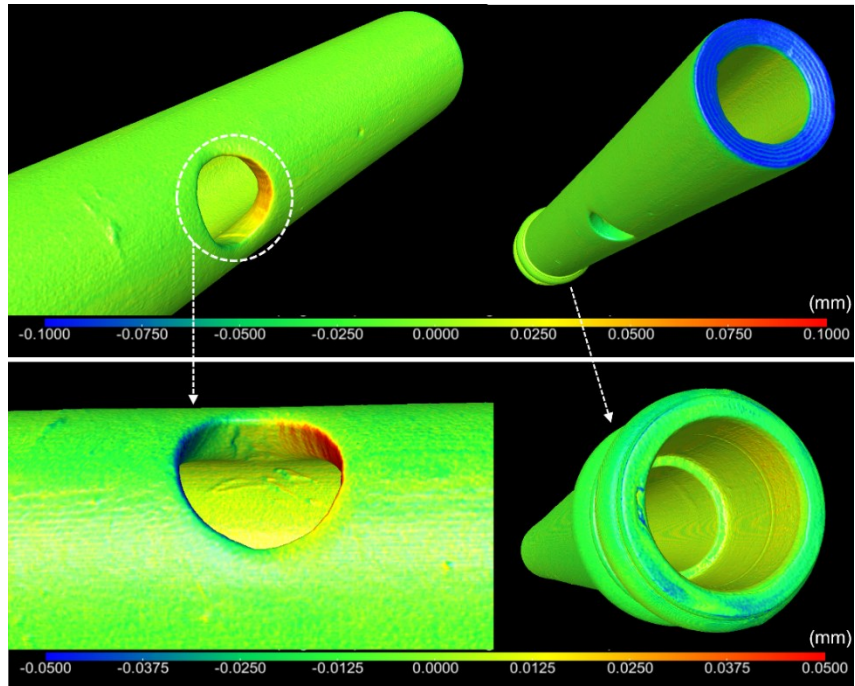


Figure 4.41: Deviation color map of the corrected BB head dataset with respect to the uncorrected one.

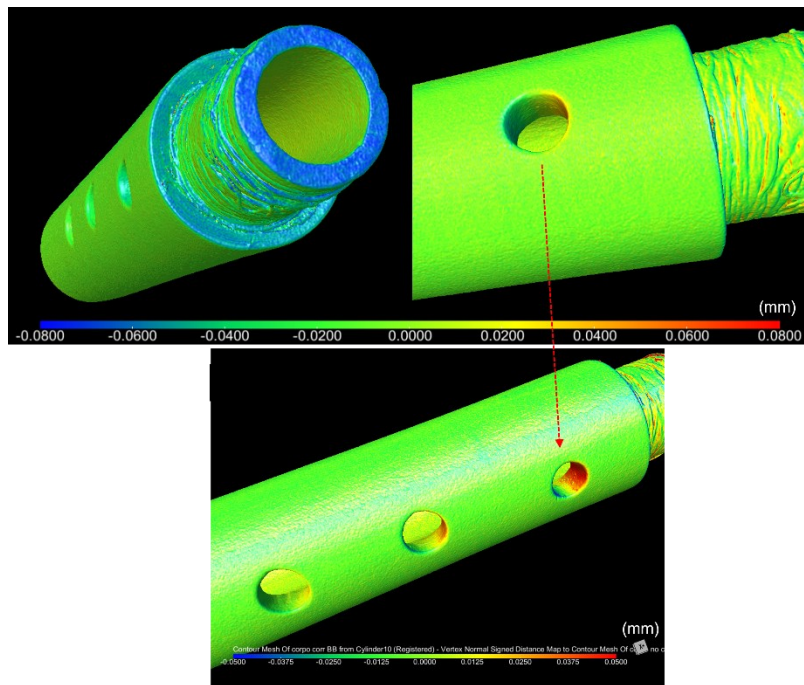


Figure 4.42: Deviation color map of the corrected BB body dataset with respect to the uncorrected one.

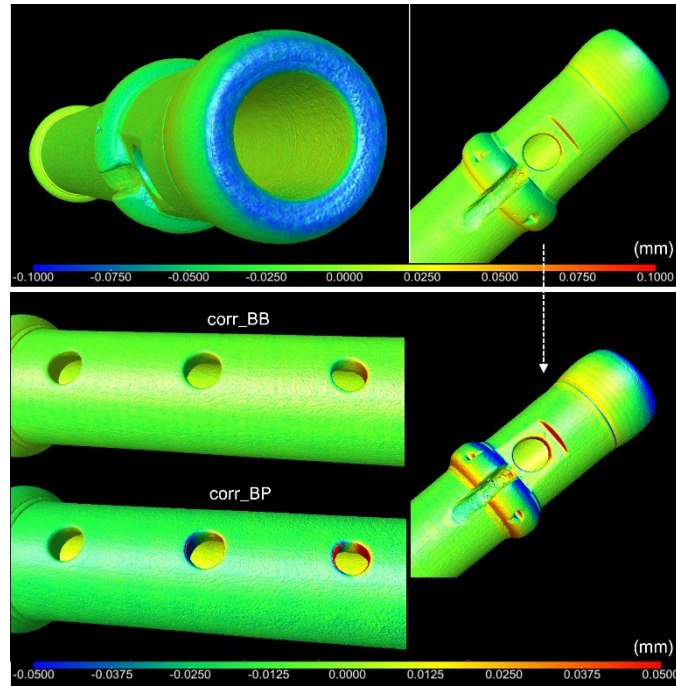


Figure 4.43: Deviation color map of the corrected BB foot dataset with respect to the uncorrected one.

4.3.4 Discussion

When the correction methodology was tested on samples, different issues emerged with respect to the previous analysis performed on calibration objects. In fact, while for the latter deviations with respect to the reference values initially follow a positive or negative trend for the uncorrected CT data, in the case of the LEGO brick and the flute, different SD values (both positive and negative) were obtained for the quantities taken into consideration. The main difference compared with the calibration objects is the evaluated features, that are the sphere centre-to-centre distances for the ball plate and the ball bar and the diameters and lengths for the samples, except for the brick knobs centre distances, for which a difference in the SD values was obtained using the calibrated features correction (Figure 4.35). As explained, the centre-to-centre distance is a more robust parameter in terms of dimensional analysis because it is independent of the threshold used for segmentation and surface determination, unlike, for example, diameters. This could be one of the reasons why we encountered more difficulties with our samples. Another thing to consider is the software used, in this case

Dragonfly, which is not born specifically for metrological aims like some of the ones used, for example, in the industrial field (e.g., VGStudioMax with specific tools or Avizo), but in most cases they required a very expensive licence. The method followed for the measurements in Dragonfly is to segment the interested part of the sample and generate the surface mesh with histogram thresholding (with Otsu algorithm); then the software calculates the distance from the surface mesh to the centroid of the segmented part, so the final measure is obtained from the sum of the two distances. This is a more automated method for distance calculation with respect to the use of the “ruler” function also available in the software: indeed, the ruler has to be “placed” between two points manually by the operator, which implies a certain user dependence and fewer reference points for the measurements. Moreover, reference measures of the LEGO brick and flute were obtained with two different instruments (with the ATOS scanbox for the first and the callipers for the second), which have different instrumental uncertainty and measurement accuracy. In addition, more difficulties in the measurement and calculation of the Piccolo Flute were verified, especially for the holes, because of the lower regularity of the shapes with respect to the brick.

Looking at E_n parameter values obtained for the LEGO brick and the flute analysis, it can be observed as in both cases the two applied correction with BB and BP are compatible with each other (values lower than 1, Figure 4.44). Comparing the corrected CT data with the reference distances, is evident as E_n values results to be much larger than 1 for almost all the measured quantities (Figure 4.45). Concerning the flute, only the foot shows the lower E_n values when reference and CT corrected data are compared, while for the other parts most of the values are incompatible.

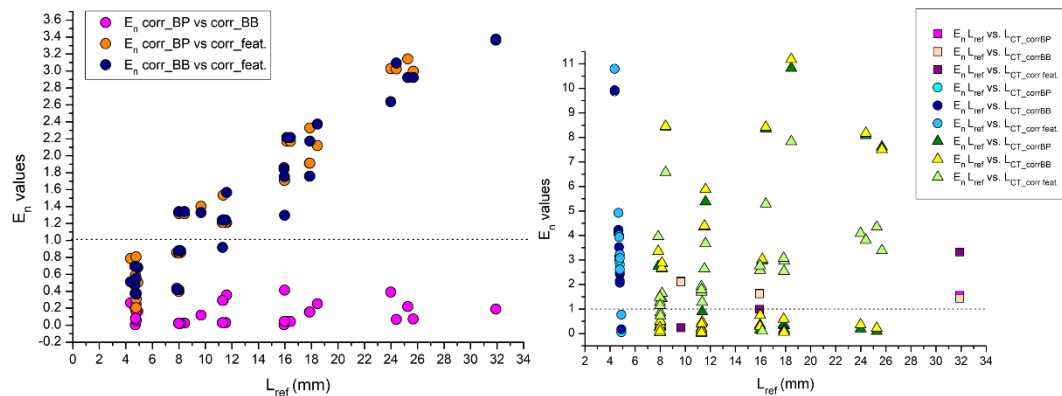


Figure 4.44: E_n values obtained for the LEGO brick comparing CT corrected data with each other (left) and with reference distances (right).

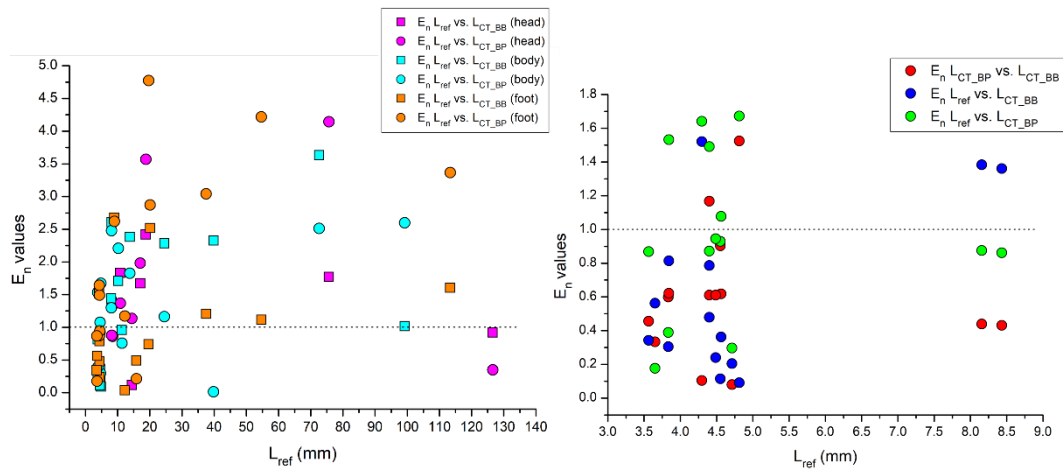


Figure 4.45: E_n values obtained for the flute comparing CT corrected data with reference distances for all the three components (left) and for the foot (right).

Regarding the instrument, bibliographic research has been conducted to determine the maximum deviations for copy realisation. As mentioned in section 1.1, instrument manufacturing tolerances are more craftsmen's opinions rather than scientific issues; in most cases, musical instruments are optimised manually to compensate for any errors afterwards. In addition, it is reasonable to expect different tolerances for different parts of an object (Myers 1994). In some publications, tolerances between 0.1 mm and 0.2 mm are indicated, differentiating them based on the instrument parts (Forrester et al., 2018; Ignesti, 2007), while other authors indicated a maximum deviation of ± 0.1 mm for the inner part of the instruments (Karp, 1978). Considering this last value, some of the obtained data are outside the maximum suggested deviation, as can be seen in Figure 4.40. To better visualise and compare our data with the suggested tolerance, the SD values divided by flute components and measurands are shown in Figure 4.46. It is evident from the graphs that some values fall out of the range, especially the lengths in the case of the body and foot, while hole diameter measurements are inside the considered tolerance in most cases. This could be due to their higher values in general, which could lead to larger deviations, as also observed for the higher sphere c-c distances in the ball plate. As already mentioned, some uncorrected values worsened with the applied correction, especially with BP correction.

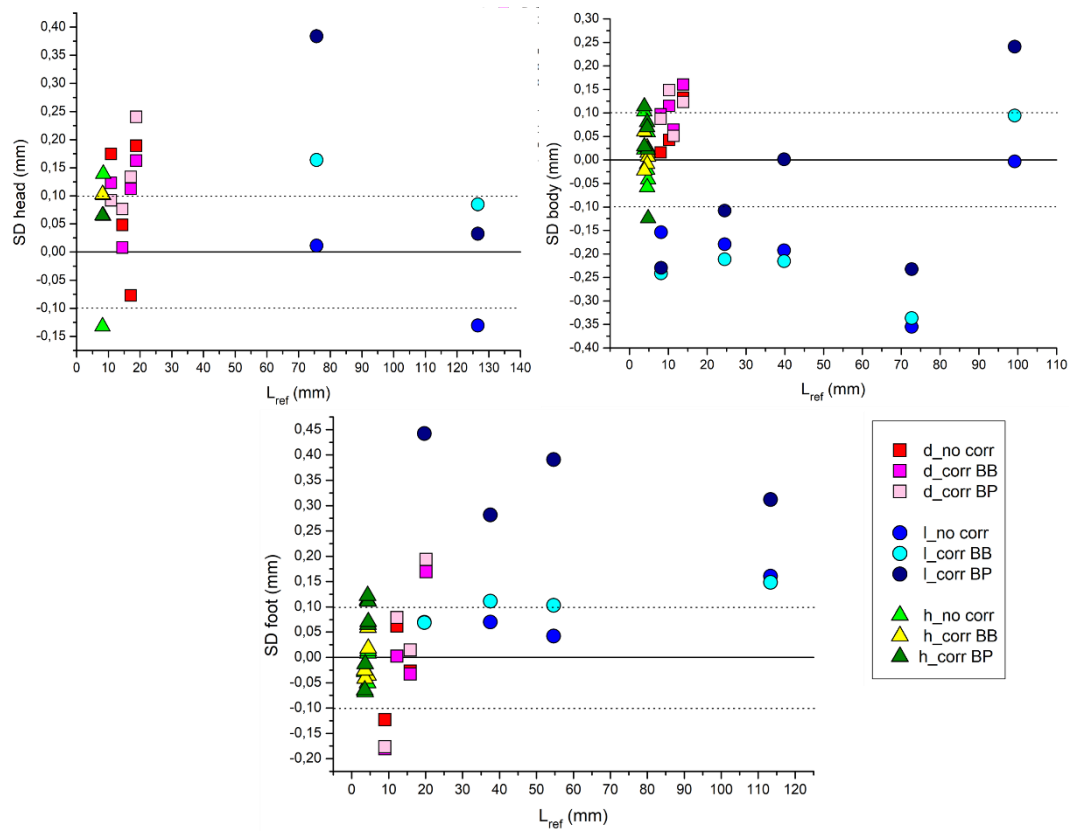


Figure 4.46: SD values divided by flute parts (top left: head; top right: body; bottom: foot), with indication of considered tolerance of ± 0.1 mm (legend: d= diameters; l= lengths; h=holes).

A preliminary CT test on this object was conducted before this thesis work, in order to qualitatively investigate the inner structure of the flute (also to assess the state of conservation, Tansella et al., 2022) and from the digital model, a 3D printed copy of the instruments was realised (together with the other two samples mentioned in section 1.1), in order to have an initial idea of the procedure to follow and the accuracy level of the 3D printing process. The copies were printed with a nontoxic polymer (polyamide-12) through Selective Laser Sintering methodology by the company *Materialise NV*. It is interesting to see the SD results obtained for the CT scan (realised some months before the one illustrated in this work), whose general distribution looks like the last obtained with some differences (Figure 4.45).

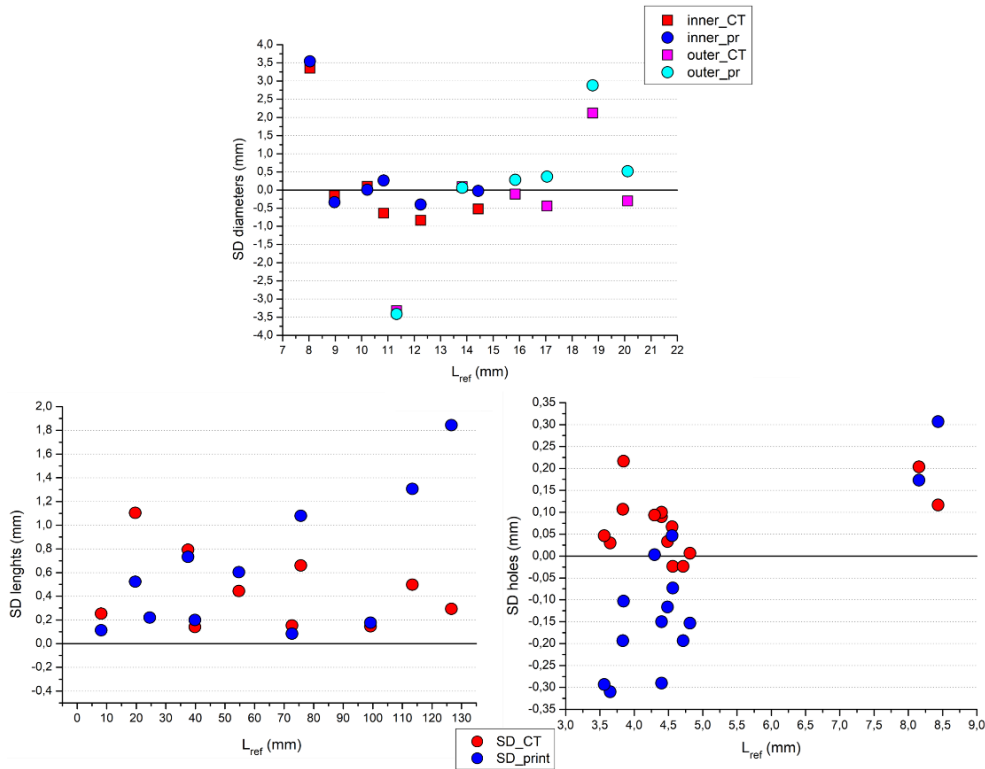


Figure 4.45: SD values divided by measured feature between CT and 3D printed copies.

If we look at the SD values of the 3D printed instrument in Figure 4.45, positive and negative deviations of lengths and hole diameters could be observed, probably due to the deposition of more material during the printing process (the company that produced the copy indicated a standard accuracy of $\pm 0.3\%$, with a lower limit of ± 0.3 mm, which is in line with some of the SD values obtained). It should be pointed out that instrument copies follow a process of refinement through polishing and painting operations of all the surfaces, which could lead to some dimensional differences with respect to the original data taken on the rough object.



Figure 4.46: Original (top) and 3D printed (bottom) Piccolo Flute.

Anyway, before creating other printed copies, a deeper investigation on dimensional CT analysis with other tests is necessary to reduce deviations with respect to the reference value and to limit the uncertainty contribution of the CT scan.

Chapter 5

Case studies

In this chapter, some case studies are presented in which X-ray tomography was applied with different purposes based on the analyzed artefact, in some cases as support to multi-analytical diagnostic campaigns. Moreover, projects that involved neutron imaging techniques are also presented.

Some of the work described in this chapter has been previously published in (Vigorelli et al., 2021, 2022).

5.1 CT investigation on wooden artefacts from the Museo Egizio of Torino

In this section the results of the X-ray CT analysis performed at the Centro Conservazione e Restauro “La Venaria Reale” (CCR) on Ancient Egyptian wooden statuettes are presented. The artefacts (two offering bearers and the goodness “Taweret”) belong to the collection of Museo Egizio of Torino, and the measurements have been conducted before the conservation treatment in order to provide useful information to plan it. The measurements were conducted with the imaging setup present in the CCR laboratory (Figure 5.1)(Nervo, 2013) but employing the X-ray flat panel detector used for the main thesis work (see section 3.4), to obtain a higher spatial resolution with respect to the installed setup. In this case, a better resolution was more advantageous to obtain high quality images and thus better interpretation of data. “The reconstruction of the CT sections in both cases was made using a filtered backprojection algorithm (Brancaccio et al., 2011;

Kak et al., 2002) by means of two non-commercial software developed by the University of Bologna (Parrec and ImgreC, Martz et al., 2016) and by Dan Schneberk of the Lawrence Livermore National Laboratory (USA).” (Vigorelli et al., 2022). CT acquisition parameters are summarized in Table 5.1.

Table 5.1: CT acquisition parameters for the artefacts of the Museo Egizio

	Bearer A	Bearer B	Taweret
SDD		3.75 m	
SOD		3.51 m	
Magnification		1.07	
Voxel dimension		46 μm	
Tube voltage		80 kV	
Tube current		10 mA	
Integration time	1.75 s	1.65 s	1.75 s
Scan phases (portions)	3	5	1
Projections/portion		1440	
Angular step		0.25°	

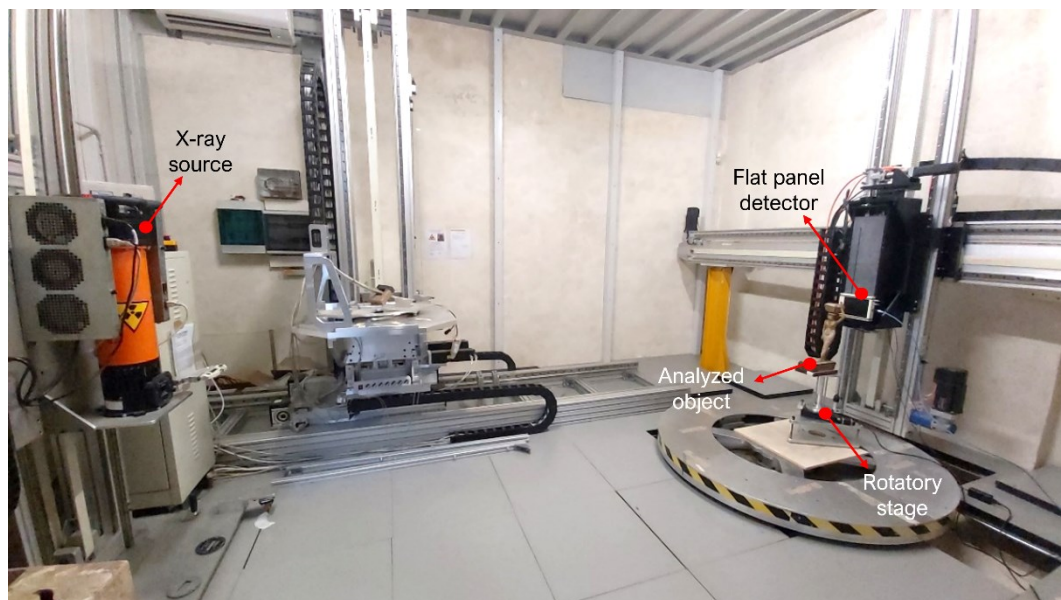


Figure 5.1: The CCR X-ray imaging laboratory, during the CT analysis of Bearer B.

5.1.1 Bearers statuettes

In the framework of the mentioned set-up upgrade, a comparison between the results of the CT analysis on two painted wooden statuettes representing offering Bearers, is illustrated. The statuettes “were found during the 1908 excavation season of the Italian Archaeological Mission, directed by Ernesto Schiaparelli, in the Asyut necropolis (Egypt)(Del Vesco & Moiso, 2017). They were part of the rich funerary assemblage found in the tomb of Minhotep which included”(Vigorelli et al., 2022) many other artifacts “most of which came from specialized workshops operating during the early Middle Kingdom, XII Dynasty (ca. 1980–1900 BCE)”(Vigorelli et al., 2022). The two statuettes appear very similar (Figure 5.2), since they belong to the same iconographic typology (features, position, pictorial treatment etc.), apart from their state of preservation (lack of the arms in the statuette A and of the feet and the animals, generally present in both the artefacts) and the wooden bases and anchoring system (thicker base and visible “footprints” in statuette B and different basket-head junction).



Figure 5.2: The analyzed Bearers statuettes, frontal and lateral views (left: statuette A, n° inv. S. 08795, 60×13×26 cm; right: statuette B, n° inv. S. 8796, 45×15×21 cm), with the details of the heads' radiographs where a different basket-head junction is visible.

From the CT analysis “the characteristic wood growth rings and vessels are very well distinguishable in the different tomographic slices (vertical and horizontal).”(Vigorelli et al., 2022). For statuette B “the presence of the central pith, extended through almost the entire height of the statuette (Figure 5.3a) (a detail emerging from the CT vertical sections of bearer B) suggests the use of a single wooden block for the realization, confirming the same hypothesis based on the absence of dowels junctions. As regards the assembly between the basket and the head, starting from the upper portion, the tomographic reconstructions of the statuette B confirm the absence of wooden dowels, used instead in the statuette A (Figure 5.3f). Some wooden dowels in bearer B can be instead observed for the junction of the left hand with the basket and of both arms with the body (Figure 5.3b-e), together with a material (possibly the same used for preparation) applied to ensure a better hold of the pieces; this is not found instead in correspondence of the different dowels used in statuette A (Figure 5.3g), probably due to the perfect adherence of the inner elements in their place.”(Vigorelli et al., 2022) “As for the insertion of the legs into the base, from the radiographic results of the statuette A (the tomographic analysis was performed only from the top to the hips of the figure) it is possible to distinguish two holes made to accommodate the end portions of the legs, fixed by means of a filler material with a higher radiopacity than the wooden material (Fig. 5.4c), applied in occasion of a previous intervention.”(Vigorelli et al., 2022) “The tomographic analysis of the same part of statuette B shows very clearly the insertion of the right leg in the base via its hole, fixed with the application of a radiopaque material, clearly distinguishable from wood. Concerning the left leg, missing of the last part, the CT analyses evidently show the insertion of a wooden element, applied in a previous intervention to support the leg, in the still existing original hole functional to the assembly and, during this treatment, filled with a radiopaque material.” (Vigorelli et al., 2022).

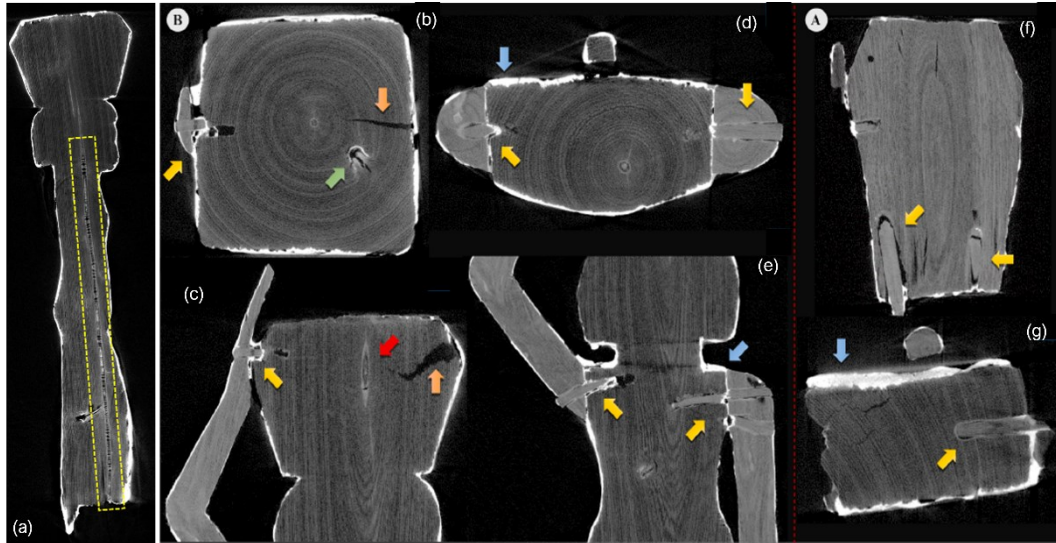


Figure 5.3: CT horizontal and vertical slices of the two statuettes (a-e: statuette B; e-f: statuette A), where the use of wooden dowels is visible (a: central pith highlighted in the yellow square; b-c: basket; d-e: junction of the arms; f-g: basket and shoulders respectively). Green arrow: defect; orange arrows: cracks; blue arrows: thicker preparation layer; yellow arrows: wooden dowels with filling material; red arrow: wood pith, also visible in the entire figure on the right. (Vigorelli et al., 2022).

“Unlike what was observed for the statuette A, the preparatory layer of bearer B shows in general a homogeneous thickness (0.7–1 mm), except in a few points where it reaches 2.3 mm (Fig.5.4a-b). This might be caused by the presence of a less homogeneous wood material and structure underneath. This feature, different from what was seen on the statuette A, where in many parts volumes were modelled with this material, is to be considered: in combination with other slight differences emerged, extremely significant for the study of the artistic technique, it can be a clue of the technical approach of the sculptor. From the evaluation of the resulting attenuation coefficient’s values, it can be supposed that the type of material is the same used for the statuette A, a feature that will be further investigated through other diagnostic methods”(Vigorelli et al., 2022)“In conclusion, the importance of underlining similar and different features in terms of assembly, modelling technique and materials used could suggest possible different hands in the realization of the objects.”(Vigorelli et al., 2022)“In the future, if it will be possible to apply the same investigation strategy to the other wooden artefacts and statuettes belonging to the same framework, analogies and differences in terms of materials, manufacturing techniques and state of preservation will support the Egyptological study aiming at the possible

reconstruction of different workshops active in Asyut in the early Second Millennium BCE.” (Vigorelli et al., 2022)

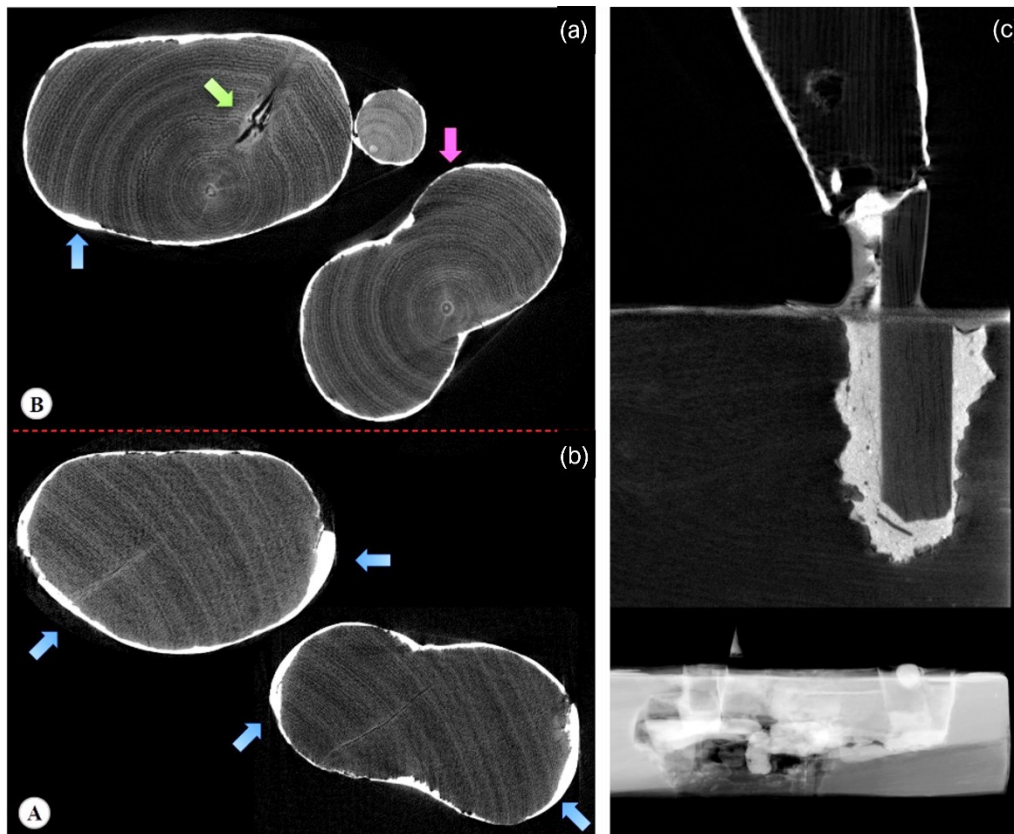


Figure 5.4: CT slices of the two statuettes (a: statuette B; b: statuette A) in which the preparation layer is visible (pink arrow: lack of material; blue arrow: thicker preparation layer; green arrow: defects); c: difference in the junction legs-base (up: statuette B; down: statuette A).(Vigorelli et al., 2022)

5.1.2 Taweret statuettes

The other sculpture analyzed is a “representation of the ancient Egyptian goddess Taweret, represented as a hippopotamus with human pendulous breasts, standing erect on its hind legs, the right one being slightly advanced. She has the tail of a crocodile and the legs of a lioness.”(Vigorelli et al., 2021)“In this statuette, the original wig, probably inlaid on the carved wood, is not preserved as it is for the crown and for any other symbol she could handle. The forward part of the muzzle being truncated, we cannot appreciate her fearsome appearance, with an open

mouth exposing her tusks and tongue. The find is missing the feet and it shows evidence of fracture at the height of the ankles. Furthermore, the original base is lost, replaced by a modern one set up for exhibition functions. Being a purchased item (probably acquired with the Drovetti Collection in 1824), and giving the lack of any inscription, only some generic hypothesis about provenance, date, and function of the statuette Cat. 528 could be drawn”(Vigorelli et al., 2021)“Despite the difference in material, the sculpture object of this study could be instead stylistically compared with some statues of Taweret dated from the Third Intermediate to the Ptolemaic Period”(Vigorelli et al., 2021)“In relation to the manufacture, the sculpture is carved on wood and gilded with some colored details, features visible despite its fragmentary state of preservation (Figure 5.5).”(Vigorelli et al., 2021)“After researching the literature on specific studies dedicated to gilding materials and techniques in Ancient Egypt and finding little information about the topic (Hatchfield & Newman, 1991), it was decided to investigate the technique used for the decoration of this specific artifact through targeted scientific studies, among which was X-ray imaging.”(Vigorelli et al., 2021)

“The evaluation of the horizontal (in which the vessels of the wood are clearly visible, see Figure 5.6a-b) and longitudinal slices (Figure 5.6c-e) obtained from the CT analysis confirm the first visual observation and allow us to hypothesize the use of a sub tangential cut taking into account the position of the growth rings”(Vigorelli et al., 2021). The preparatory layer directly applied to the wooden support “was functional to the application of the metal leaf and presumably also useful for definitive modeling, taking into account the greater thickness”(Vigorelli et al., 2021)“in some parts of the body, which are visible also to the naked eye. The thicknesses of the preparation layer in those areas, beneath the gilding, can be observed in the horizontal slices of the CT scan (Figure 5.7)”(Vigorelli et al., 2021) “In some places, it is also possible to observe micro-fractures inside the preparation layer itself (Figure 5.7). On the surface, it is possible to visualize limited areas with high radiopacity, above the preparation, presumably identifiable with the applied gold leaf, and in some places, with another layer of lower radiopacity material placed above (similar to that of the preparatory layer, but slightly less radiopaque), attributable to a blackish-brown material visible to the naked eye.”(Vigorelli et al., 2021)

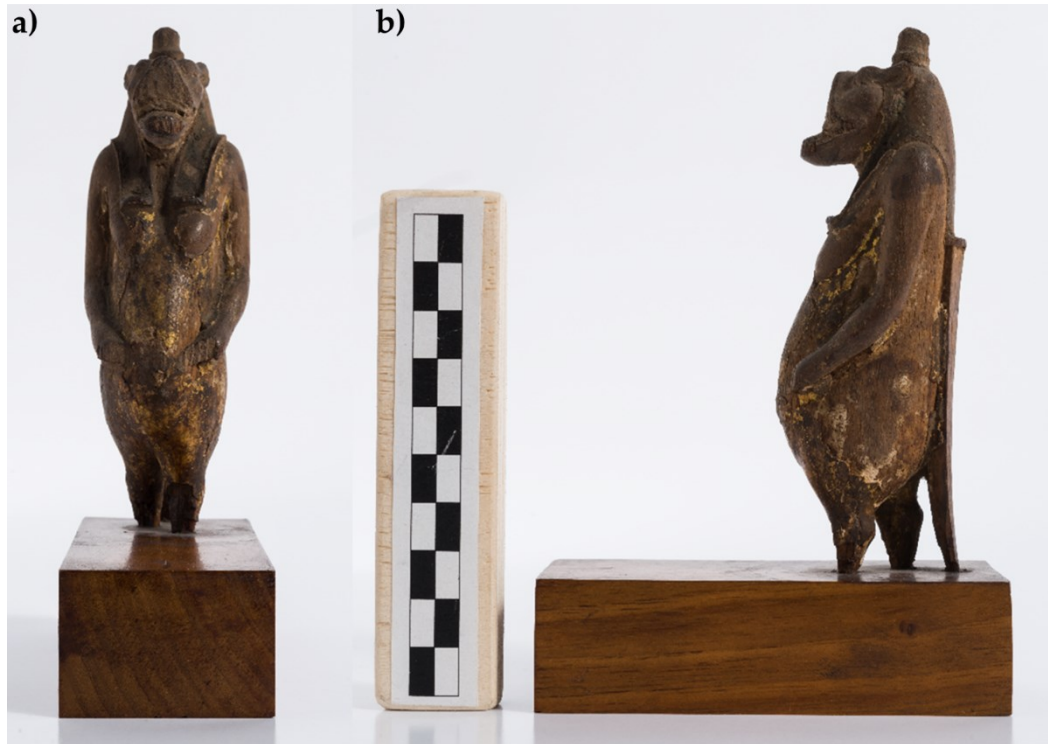


Figure 5.5: The analyzed Taweret statuette (Cat. 528), frontal (a) and lateral (b) views.(Vigorelli et al., 2021)

In Figure 5.7, “the profile plots in two regions of interest are shown. It is possible to better observe the different thicknesses of the preparation layers in the two parts of the object (thicker in part B than in part A), the peak due to the gold layer, and the contribution of the blackish-brown material (present only in part A)”(Vigorelli et al., 2021)“The slices corresponding to the body confirm a rather homogeneous distribution and thin thickness of the preparatory layer, confirming, in this case, the application of this material for the metal leaf adhesion and not for modeling the object.”(Vigorelli et al., 2021)“Despite the gold layer being clearly observable by means of CT, the thickness is smaller than the voxel size ($46\ \mu\text{m}$) and the penumbra due to the measurement geometry ($205\ \mu\text{m}$). In any case, an attempt to extrapolate some information about the thickness of the gold leaf was made, in order to test the methodology used and to verify the maximum resolution obtainable in such experimental conditions.”(Vigorelli et al., 2021)

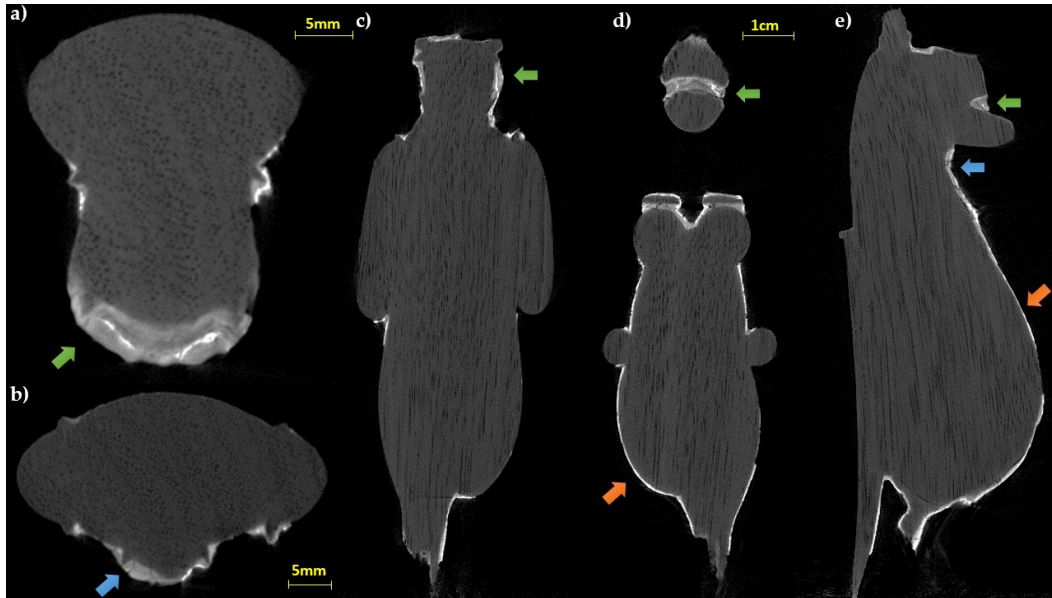


Figure 5.6: CT slices of the statuette: (a,b) horizontal sections; (c–e) longitudinal slices. In all the sections the wood structure (vessels and growing rings) is visible (green arrows: preparation layer in the face area; blue arrows: fractures inside the preparation layer; orange arrows: thin preparation material for the gold leaf adhesion).(Vigorelli et al., 2021)

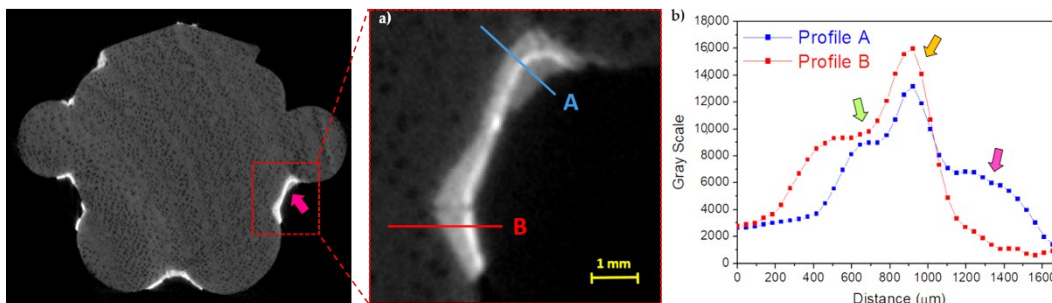


Figure 5.7: Profile plots along A and B (green arrow: preparation layer; orange arrow: preparation material for the gold leaf adhesion; pink arrow: material layer above the gold leaf).(Vigorelli et al., 2021)

The area visible in Fig.5.8 “was selected because there are parts with gold on a very thin preparation layer and parts without any surface layer, i.e., the wood is exposed. A first fit using a sigmoidal curve was made on this last part and the results”(Vigorelli et al., 2021)“were used as starting parameters for the wooden part of the profile shown in Figure 5.8 and related to the gold layer. In this second profile, the contribution from the preparation layer is negligible and it produces only a very small band on the right of the gold peak. In this way, using a first approximation gaussian fit for the gold layer, a value of $2\sigma = 216 \pm 7 \mu\text{m}$ was

obtained that confirms the limits due to the geometrical conditions used.” (Vigorelli et al., 2021)

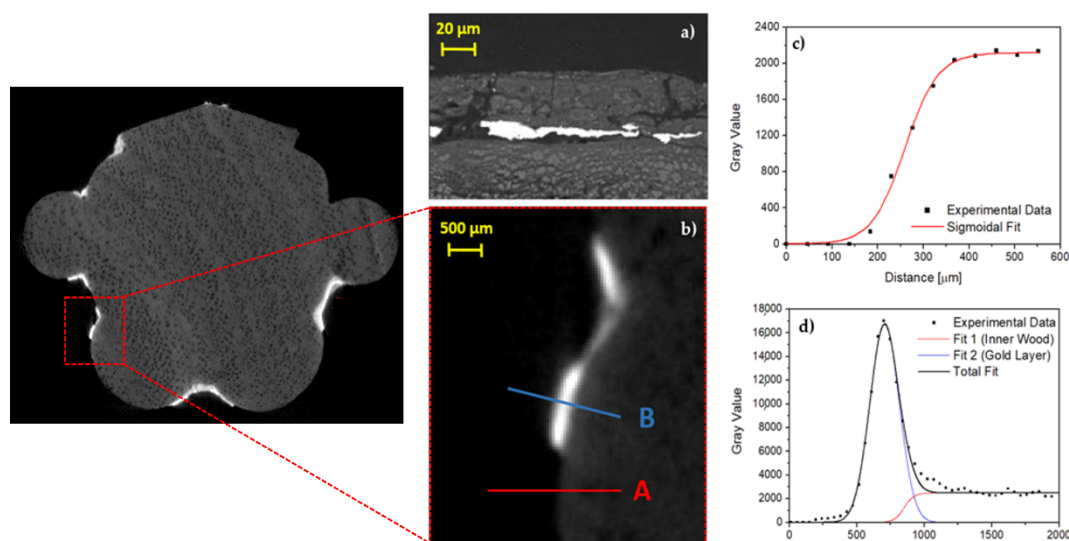


Figure 5.8: Backscattering image by means of SEM, the gold layer is in light gray (a); (c) profile plot along A line shown in (b), only wood; (d) profile plot along B line shown in (b), gold on thin preparation layer.(Vigorelli et al., 2021)

In order to obtain better results always in a non-invasive way, further CT analysis should be conducted, e.g., a local tomography (a scan of only a small object portion at high magnification) to increase the spatial resolution. The performed work could help the Egyptologist to improve the knowledge about this kind of artifacts, in terms of manufacturing and eventual conservation treatments.

5.2 Microtomography analysis on different small artefact typologies

In this section, micro-CT analysis performed on different types of ancient artefacts and their results are discussed. All the analysed samples are smaller than the statuettes presented in Section 5.1, and the main difference is the material of which they are made of, in particular, some pottery sherds and Roman glass fragments. Even if the final purposes of the CT measurements were different (they will be illustrated in the following sections), a high spatial resolution for all the samples (voxel size in the order of a few micrometers) was necessary for the

analysis. In this sense, microtomography (μ CT) was performed using the instrumentation described in section 3.5, i.e., the microfocus X-ray source with the smaller focal spot size (S mode, 7 μ m) and the flat panel detector with a pixel size of 49.5 μ m, setting then the proper CT geometry and measurements parameters. For pottery sherds, tomographic acquisition of only the central part of every sample was performed (local tomography) to reach the maximum possible spatial resolution in the final CT reconstruction.

5.2.1 Pottery sherds

X-ray imaging investigations were conducted on some pottery fragments from the Shimane and Okayama prefectures, in Japan, in the framework of the ‘Be-Archaeo’ project (<https://www.bearchaeo.com/>). 2D radiographs were performed on all 17 available samples, while 3D local CT measurements were conducted on a limited number of samples due to the required time for the whole analysis and to test the developed methodology. From this analysis, it is possible to visualise the internal porosity of the material (void size and directionality) and principal mineral components, which can provide valuable information on the manufacturing and execution techniques of the artefact. Based on the radiographs, CT analysis was performed on selected ceramic fragments with the main purpose of understanding whether this non-invasive methodology can give results comparable to those derived from a Scanning Electron Microscope (SEM), which generally reaches high magnifications to distinguish the different characteristics of the sample (e.g., minerals, porosity, etc.) with a good spatial resolution. For this purpose, it was decided to perform a local tomography, that is, a tomography not of the entire object, but only a part of it, to reach high magnification and be able to visualise the smallest details. In this case, an appropriate acquisition geometry was set to reach the maximum possible resolution in the final CT reconstruction (voxel size \sim 7 μ m, Figure 5.9). The final acquisition parameters adopted for the tomographic measurements are listed in Table 5.2.

To obtain the best results, a methodology for processing the tomographic data was developed and tested, which involves several steps of correction and processing of raw and intermediate images to remove some artefacts (especially ring artefacts) that could afflict CT reconstructed slices, which are more visible when working at high magnifications (Fig.5.10). It is important to remove these artefacts through a specific software filter because they can compromise the correct interpretation of reconstructed images and consequently the 3D volume segmentation process (Erika Fissore, 2021).

Table 5.2: CT parameters for pottery analysis

Sample position	Vertical
SOD	90 mm
ODD	560 mm
SDD	650 mm
Voltage	150 kV
Current	66 μ A
Integration time	2 s
Angular step	0.15°

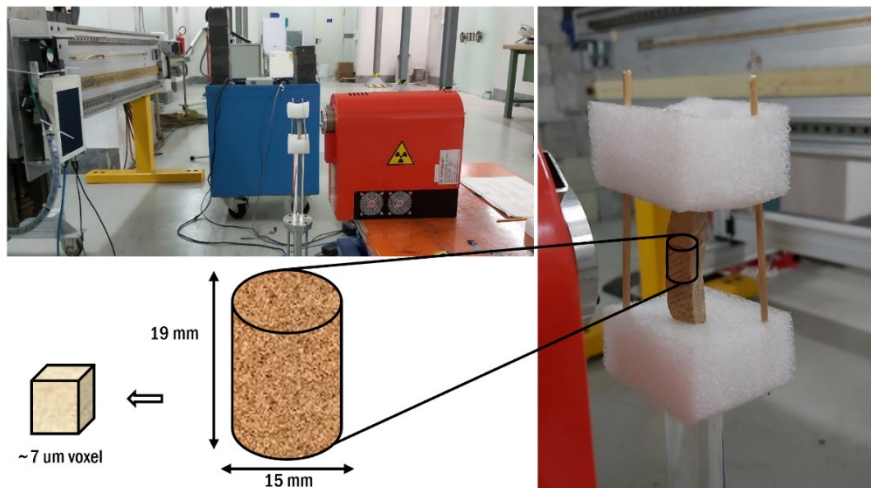


Figure 5.9: Experimental setup for the local-CT and scheme of analyzed volume.

In this section, CT results of two pottery fragments (TT2 and TT10) are presented.

In the reconstructed tomographic images, different ceramic components (voids and minerals) were clearly visible with different gray levels according to the material density (Figure 5.10). Higher-density areas, composed of more heavy chemical elements, such as ferrous minerals, are visible as brighter areas, while dark areas indicate the presence of voids and porosity that extend over the entire investigated volume. Areas with intermediate gray levels represent medium-density materials, such as other types of minerals or inclusions, and the ceramic matrix.

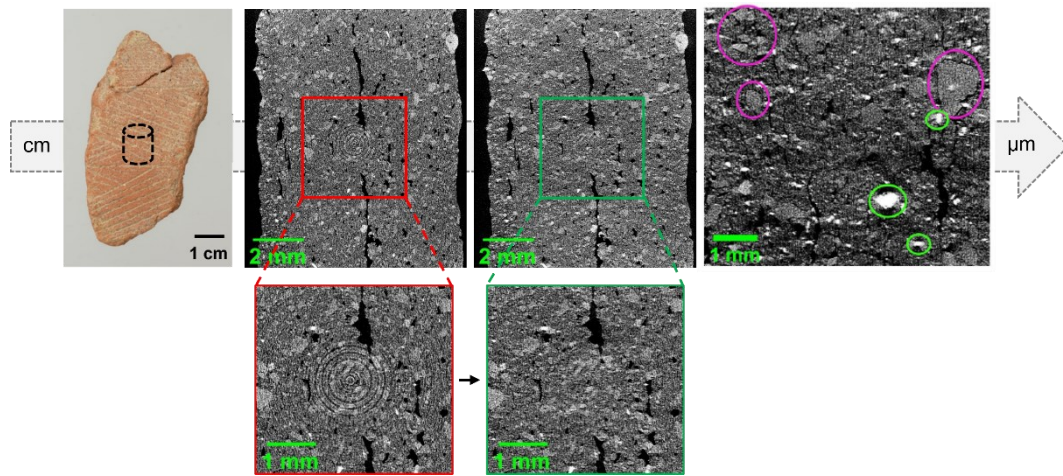


Figure 5.10: TT2 sherd sample and CT vertical slice reconstruction, in which ring artefacts are removed with appropriate filters; voids (black areas) and different minerals with different radiopacity are visible inside the reconstructed volume (green and purple circles).

The 3D rendering phase of the two samples and volume segmentation were carried out using the software Dragonfly. In the segmentation phase, the ROIs of elements with different radiopacities, such as porosity, highly absorbent mineral inclusions, and ceramic matrix, were isolated. For an initial evaluation of the segmentation parameters and better data manipulation (the size of a reconstructed volume is in the order of gigabytes), a central sub-volume of the sample was analysed (Figure 5.11). For this work, the threshold-based method was used (different gray levels corresponding to the different materials present were separated, and the single volumes were segmented). The total analyzed volume corresponds to 235.51 mm³ for both samples. In Table 5.3, the percentage estimation of the extracted features is reported. The sum of the values does not correspond to 100% as a small difference of gray levels equal to 0.01 between the ROIs was left to better highlight (from a qualitative point of view) the distinction between porosity, ceramic matrix, and inclusions. The next step will be to analyse all the scanned volumes and attempt to extract more precise quantitative data.

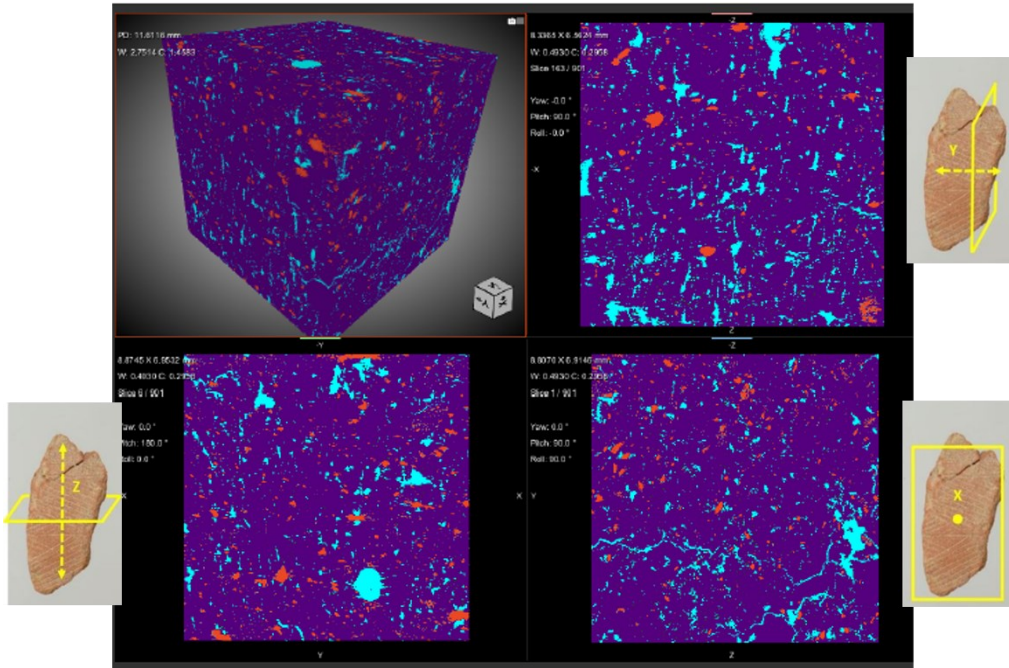


Figure 5.11: Segmented parts of the selected volume for TT2 sample, with the indication of the “cutting” planes in the object (blue: porosity; red: inclusions; purple: ceramic matrix).

Table 5.3: Percentage estimation of the three segmented features

SAMPLE	POROSITY	CERAMIC BODY	INCLUSIONS
TT2	~8 %	~87 %	~2 %
TT10	~6 %	~90 %	~1 %

An attempt to compare the details of the tomographic image with a SEM image (of sample SH_1 in this case, see Appendix E) was made, and although the spatial resolution is different, it can be seen that these initial results are very promising (Figure 5.12). In this direction, the next step will be to study a methodology to identify the mineral species present directly from tomographic reconstructions by carrying out calibration of gray levels in the image.

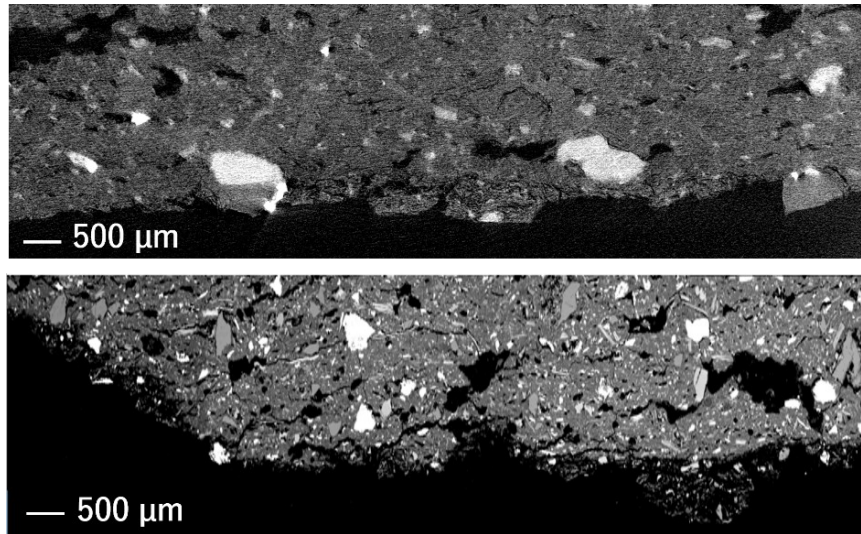


Figure 5.12: Comparison between a reconstructed CT slice (upper figure) with a SEM image of sample SH_1 (lower figure).

5.2.2 Roman glass fragments

The aim of the CT analysis conducted on 12 Roman glass fragments (from an archaeological excavation in Aquileia, UD, Figure 5.13) was to validate a non-invasive analytical procedure to achieve a better understanding of the degradation mechanisms of ancient glass (Alloteau et al., 2020). In this project, the 3D material density of ancient glass was investigated using X-ray μ CT. To this effect, different types of degraded glass have been analysed: glass with diffused 3D cracking, glass with pitting, and iridescent glass with multilayered patina on the surface. In addition, non-altered glass samples were studied by μ CT to obtain useful information to better understand the decorative and manufacturing techniques. The CT analysis was conducted in the framework of an Open AIAR project (initiative of the Associazione Italiana di Archeometria dedicated to young members designed to allow free access to the scientific laboratories of researchers belonging to the association) in collaboration with a PhD student from Ca' Foscari University (Venice).

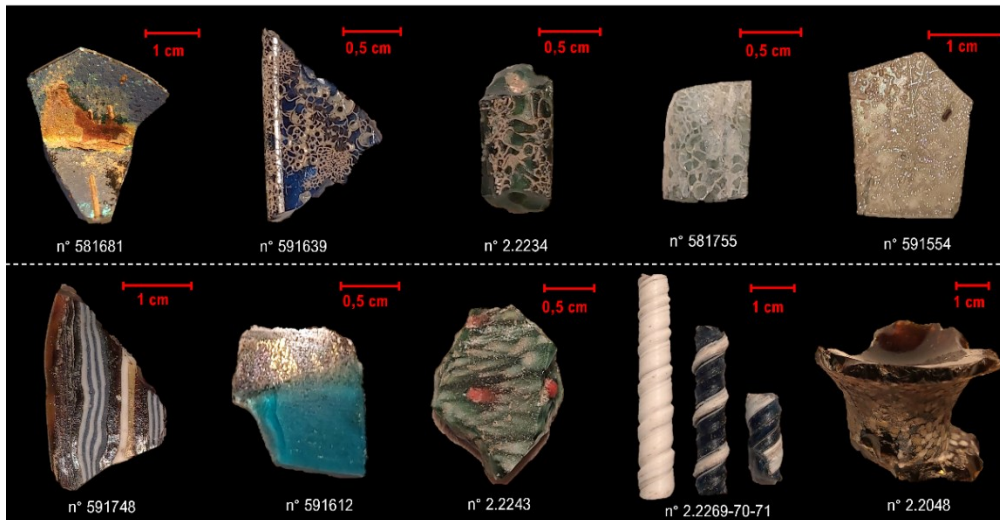


Figure 5.13: The analyzed glass fragments. Top line: altered samples; bottom line: decorated samples.

As in the previous case study, a high spatial resolution was required for the visualisation and investigation of the inner microstructure of the sample. The CT setup is the same used for the main work of this thesis; geometry and acquisition parameters set for the analysis are reported in Table 5.4. In this case, the acquired projections are processed with the non-commercial software for CT reconstruction Parrec, which was also used in the previous case studies, with the same pre-filtering operations for ring artefact removal, using an FDK algorithm. Then, the reconstructions obtained were analysed using the software Dragonfly for 3D rendering to extract the necessary information for each sample.

Table 5.4: μ -CT acquisition parameters for glass fragments

Voltage	90 - 150 kV
Current	111 - 66 μ A
Integration time	3 – 1.75 s
Focal spot size	7 μ m
Angular step	0.15°
SOD	min. 100 mm, max. 320 mm
Magnification	min. 2, max. 6.5
Voxel	min. 8 μ m, max. 24 μ m

In the following, results obtained on some representative samples are presented.

Altered samples

Figure 5.14 shows several images obtained from the reconstruction of the slices of sample 581755, a blue-green Roman glass bead. The images highlight the dense network of fractures that covers the surface of the sample and affects its entire volume and how the cracks are interconnected and propagate very deep into the sample until they reach the central hole, which appears to be filled with material originating from the soil in which the glass fragments have been buried. From the volume segmentation, it is possible to say that fractures occupy more than 10% of the glass volume, with a width approximately of 0.1-0.3 mm, arriving at ~ 0.8 mm in some wider areas. From CT slices, it is also possible to recognise an area at the interface between the crack's void and the glass volume that appears visually of a different grey level, suggesting the presence of a material with a density different from that of the glassy matrix. The same material also seems to cover the external glass surface; one possible explanation may be the formation of a layer of hydrated silica because of the glass alteration process, as described in (Lenting, 2019).

CT images collected for sample 591639 revealed a different geometry of the cracking propagation with fractures partially or totally filled with mineralised material, possibly coming from the burial soil. Crack segmentation in the CT volume enables the reconstruction of the 3D geometry of their network (Figure 5.15). In this case, the cracks appear to be less wide than those in the previous sample, occupying a smaller volume of glass (approximately 7.3%). In the slice reported in Figure 5.15, it is possible to show larger areas where mineralised material is present and appears with a leopard-like texture. Looking at the surface of the sample (Figure 5.15), it is possible to note that these areas correspond to whitish areas visible on the surface of the glass fragment. It is also possible to see how the fractures connect under the surface of the glass and are welded by soil acting as cement, which is important information in the case of a restoration action because it entails that an excessively deep cleaning of the sample could result in the removal of soil in the cracks and the consequent loss of cohesion.

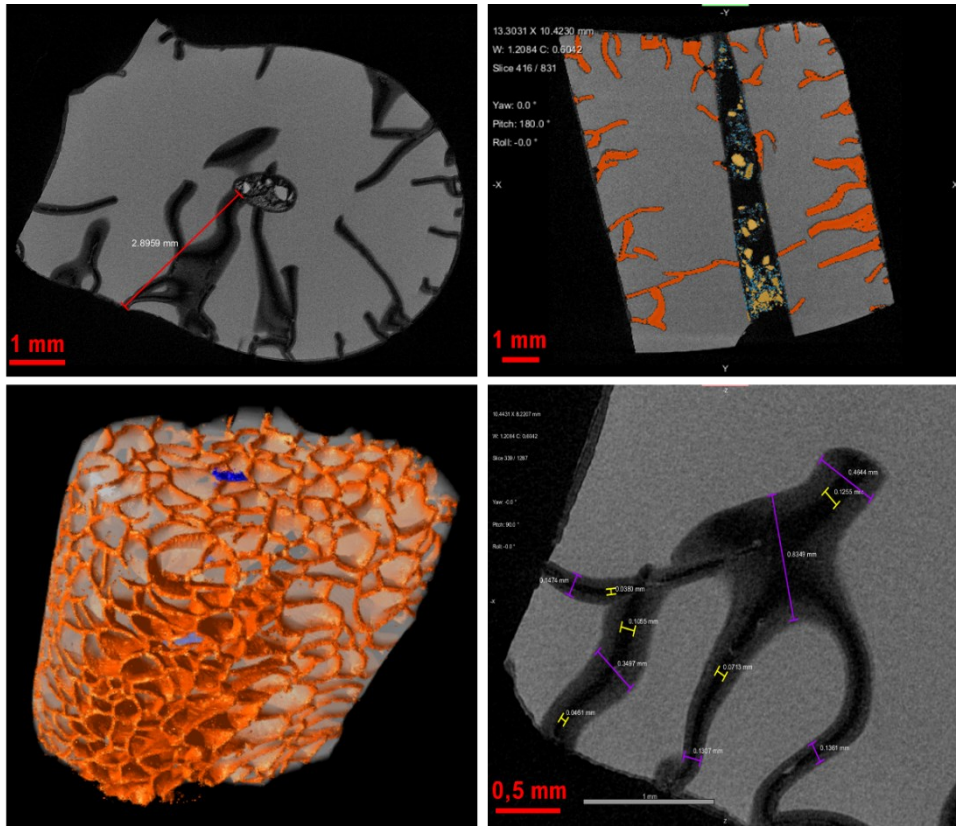


Figure 5.14: CT reconstruction and analysis of sample 581755, where fractures (orange, ~10% of the entire volume) and filled minerals (blue and yellow) are segmented.

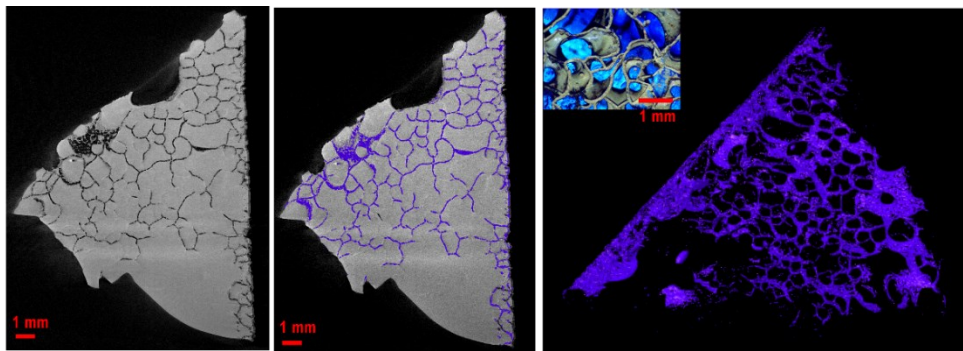


Figure 5.15: CT reconstruction and analysis of sample 591639, where the fractures (blue areas, ~7.3% of the entire volume) are segmented. Detail of an optical microscope image is also shown for comparison.

In contrast to the other samples analysed, sample 591554 showed the formation of pits as a corrosion phenomenon on the surface, with no evidence of patina formation. From the slices in Figure 5.16, one can see the perfectly concave

profile of these alteration marks. Some of them dissolved the siliceous matrix to a depth of approximately 0.3 mm. The total volume of the glass dissolved by the formation of pits was approximately 12%.

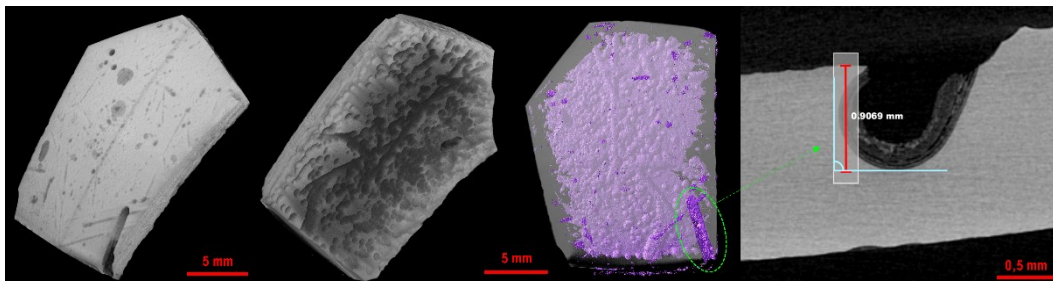


Figure 5.16: CT reconstruction and analysis of sample 591554, where the corrosion pits (purple area) are segmented and a detail of a hole depth.

For sample 581681, μ CT and additional local CT performed on the central part allowed the characterisation of the thickness, shape, and separation of each layer comprising the surface iridescent patina. The various layers that constitute the patina are organised in packets of different thicknesses separated by the zone of air (darker areas in the images). Each packet was composed of a different number of microlayers, as reported in the literature (Lombardo et al., 2013; Schalm et al., 2021). Observing the images reported in Figure 5.17, the profile of the patina follows that of the glass, just as it detached from the bulk of the glass. According to the researchers involved in the project, this structure could be the result of glass alteration governed by dissolution and re-precipitation processes (Schalm et al., 2021). The images also show the presence of two pits on the vertical side of the sample, one of which runs through the wall of the glass fragment. These pits also had an ordered structure of concentric layers, which can be classified as U-grooves, as reported by (Krauss & Whymark, 2021). A further CT investigation conducted at Elettra Sincrotrone in Trieste by the other researchers involved in the project allowed us to observe the presence of a heterogeneous distribution of microcrystals within the pit, which reinforces the alteration hypothesis in (Lenting, 2019). However, for this case, as the corrosion mechanism is not yet clear, further investigation is necessary to understand the kinetics of the formation mechanism of these marks of glass corrosion.

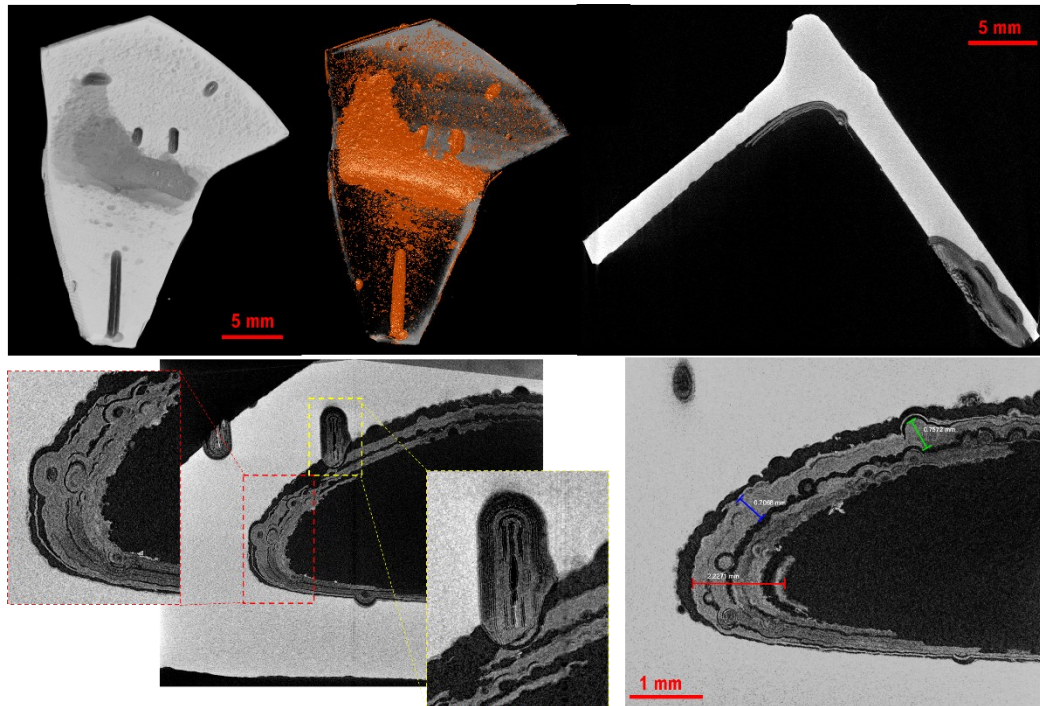


Figure 5.17: CT reconstruction of sample 581681, where the corroded patina and holes are segmented (orange area). A detail of the different corrosion layers that follow the glass surface and the concentric layers in one of the holes are also shown.

Decorated samples

The unaltered glass samples (Figure 5.13, below) instead showed different types of decorations, and the aim of the tomographic analysis in this case was to obtain information on the manufacturing techniques of these artefacts. In general, from the data analysis, information on the porosity (mainly air bubbles) and the observation of more radiopaque material within the glassy bulk were obtained; the latter is probably due to crystal precipitation linked to the colouring or opacifying compounds used. In addition, specific aspects of the individual cases were investigated.

For samples 591748 (inner porosity $\sim 0.1\%$), it is possible to notice that the coloured stripes (the white stripes in particular) are well distinguishable from the amber glass base because of the higher attenuation coefficient, going from one side to the other passing through the whole sample (Figure 5.18). In these areas, some more radiopaque precipitated crystals are visible, and owing to segmentation, it is possible to confirm their presence only in the coloured bands.

From tomographic analysis, no distinction between the different coloured stripes arises; nevertheless, for the white-blue band, a different thickness inside the glass bulk could be noticed, with a peculiar “waveform”; this detail indicated that this stripe decoration was applied on the glass body after its realisation, unlike the central white stripe. At a specific point, air bubbles filled with other materials can be seen (Figure 5.18); since this area is close to the surface, it is possible to associate it with the burial ground.

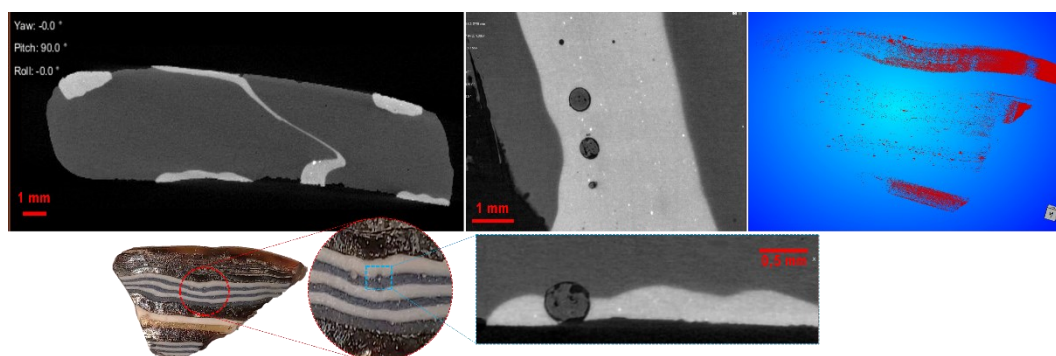


Figure 5.18: CT reconstruction and analysis of sample 591748, with details of the decorative stripes are shown. Precipitated crystals are found only in the colored layers (segmented in red)

In sample 591612 (inner porosity $\sim 0.1\%$, especially concentrated at the leaf-glass interface), the CT analysis was concentrated on the gold leaf inside the glass body, which appeared highly fragmented (Figure 5.19). In particular, it is placed between two layers of transparent glass and not in the blue area, as shown in the CT slice; this manufacturing technique could be attributable to the one for mosaic tesserae, even if in this case the sample could be a fragment of a roman *pisside*. With volume segmentation, the gold leaf was isolated and its average thickness was estimated to be ~ 0.05 mm. However, to have a more precise indication, some other analysis could be performed (e.g., SEM investigation), to have a comparison with the data obtained from CT, for which we have some limitation due to the geometric penumbra (see section 2.2.2). In contrast to the other samples, no precipitated crystals were found, but a peculiar, more radiopaque area was visible on one side of the sample (Figure 5.19), for which further investigation should be performed.

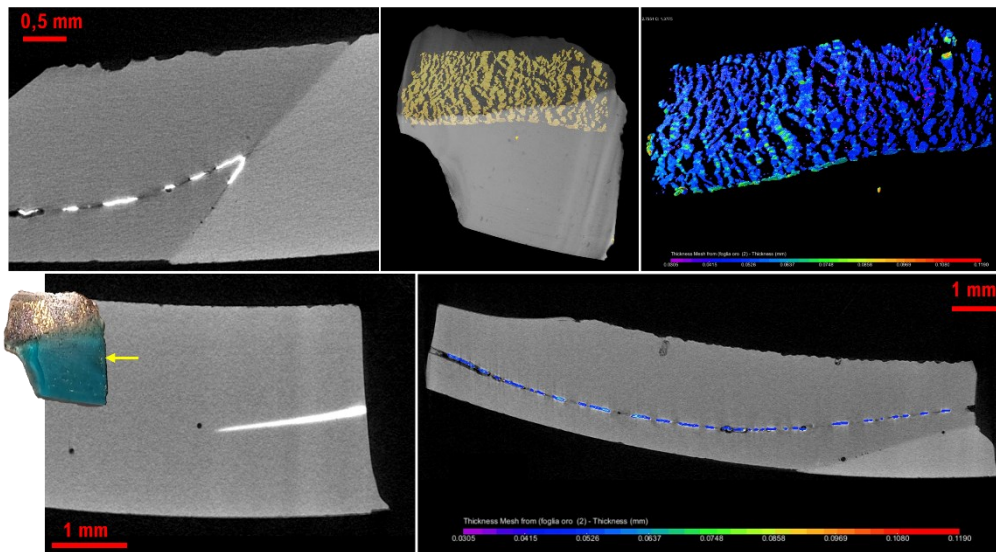


Figure 5.19: CT reconstruction and analysis of sample 591612, with details of the gold leaf, for which the average thickness was calculated.

Sample 2.2243 (inner porosity $\sim 0.3\%$) is a fragment of a glass object realized probably with the mosaic technique, which is expected to use colored glass rods to realize some patterns, such as flowers, as in this sample. From the CT slices, it is possible to appreciate the used glass sticks and their orientation inside the volume (Figure 5.20); however, no difference in gray level between the different colors could be noticed. Even in this case, it is possible to see some very bright precipitated crystals inside the green glass (Figure 5.20).

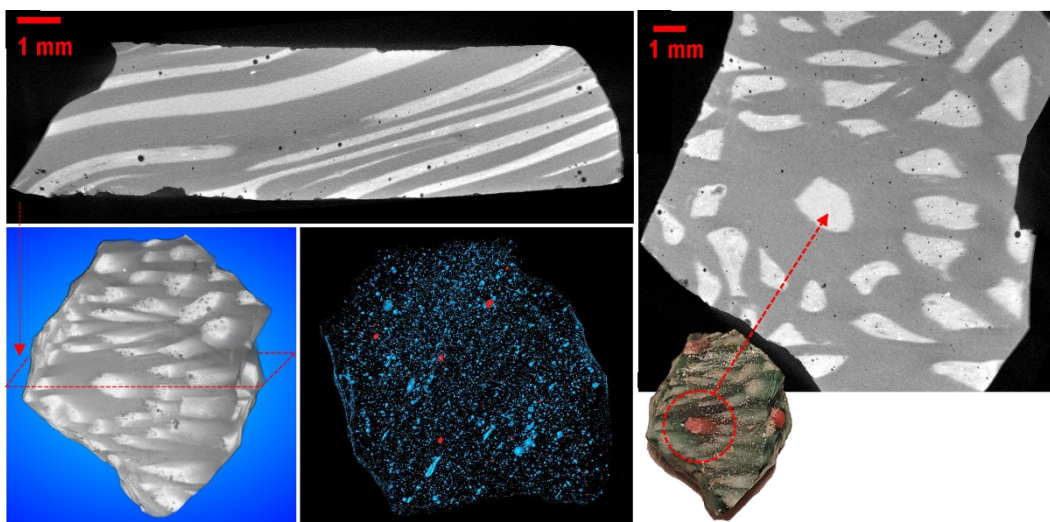


Figure 5.20: CT reconstruction and analysis of sample 2.2243, where the colored rods used for the decoration and their orientation are clearly visible.

The three blue and white twisted sticks (samples 2.2269-70-71), probably used for decorative mosaics inside the ancient thermal bath, presented higher inner porosities (~1.5%, 2.2%, and 1%, respectively), which follows the twirled motif (Figure 5.21). In the white sample, it is possible to notice from the CT slice that it was realized from a unique piece of glass and then twisted, unlike the two blue samples, for which one of the hypotheses is that the white glass decoration was placed on the blue rods and then twisted together. In addition, many bright crystals were distinguishable in all volumes of the white stick and only in the white decoration of the blue ones. For sample 2.2271, the small one, some alterations in both the blue glass and white decoration emerge from CT, especially in the terminal parts (Figure 5.21).

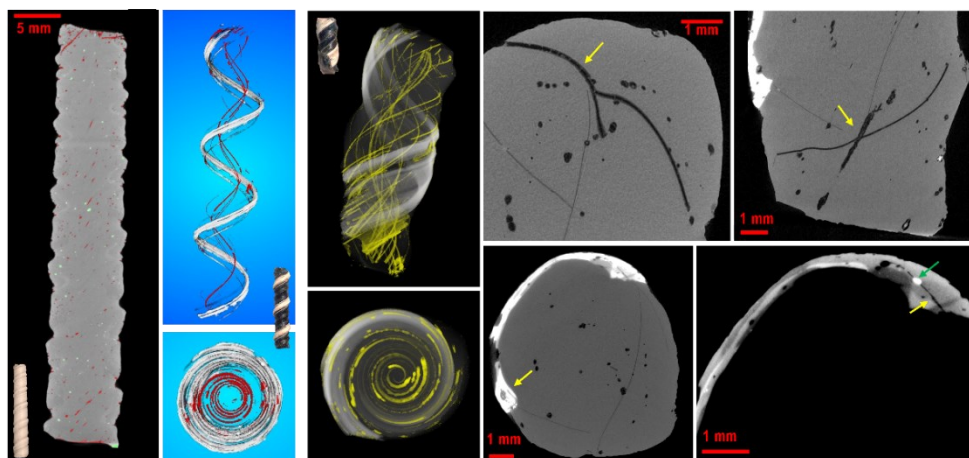


Figure 5.21: CT reconstruction of samples 2.2269-70-71, where porosity, precipitated crystals and alteration were highlighted from the analysis of slices and volume segmentation.

The larger sample (2.2048), probably a fragment of a roman *carchesium*, shows a “spray” decoration, with many colored glass drops on the surface. CT analysis has pointed out that the glass volume is uniform (no porosity is highlighted, a part in the decoration drops) and that the decoration is also present at the base-body interface (Figure 5.22), which demonstrates that the two parts were probably manufactured separately and then joined together. From the CT analysis, colored drops show different gray levels based on their composition; through segmentation, it is possible to separate them, analyzing radiopacity, thickness, and overlapping. An example is shown in figure 5.22, where a segmentation based on the different attenuations was performed and a specific area was investigated to associate the different drop of colors with the segmented ones. It can be noticed that the more radiopaque particles are yellow, which are

distinguishable from the blue ones; however, no distinction between the white- and red-colored drops could be highlighted. Moreover, at some points, it is possible to see a partial overlap between the brighter particles and others; this could indicate that the yellow drops may have been added after.

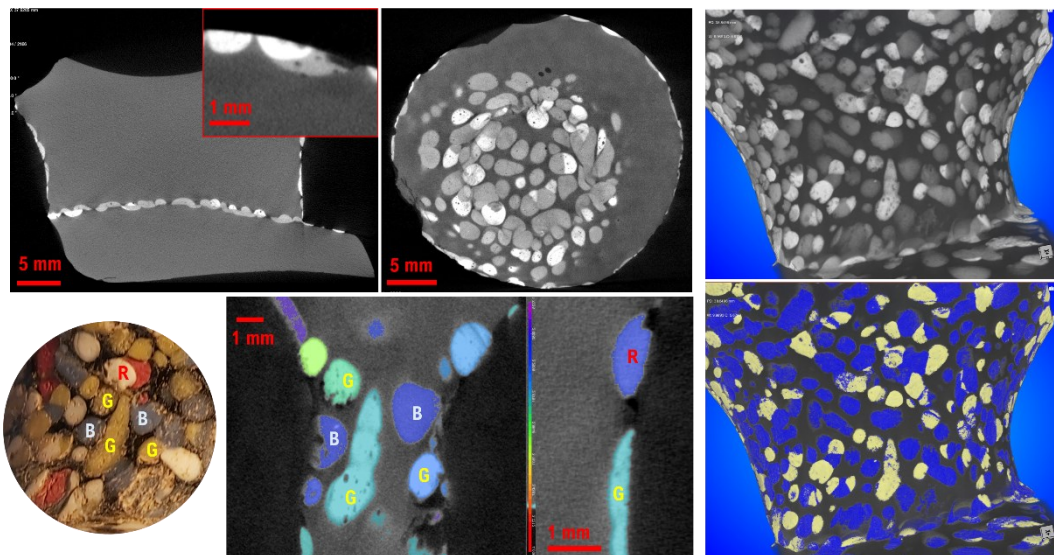


Figure 5.22: CT reconstruction and analysis of sample 2.2048, with details of the decorative drops and their segmentation based on gray levels are shown.

5.3 CHNet_NICHE project: Neutron Imaging for Cultural HEritage

In this section, a research activity involving imaging techniques using neutrons instead of X-rays is presented. Neutron imaging is a powerful method for morphological analysis and characterization of several categories of materials (Watkins & Payzant, 2013). The method is fully complementary to X-ray Imaging, allowing us to obtain a different contrast for metal or light elements, even if the use of neutron techniques is linked to nuclear reactors or spallation source facilities, with respect to X-rays for which laboratory instrumentation is available. Nevertheless, the range of application of neutron imaging to morphological diagnostics in cultural heritage artifacts is quite wide because it is a noninvasive technique that allows the identification of different materials and their relative spatial distribution with a reasonable level of contrast and resolution (Kardjilov & Festa, 2017).

5.3.1 Neutron imaging

Neutrons are electrically neutral subatomic particles, located in the atomic nucleus together with protons. Atoms of the same chemical elements can differ in the neutrons number (thus in mass number), generating different isotope, some of which are unstable (e.g., ^{12}C , ^{13}C and ^{14}C , which is radioactive) (Nico & Snow, 2005).

Together with X-rays, are one of the most used beams for imaging analysis; the two radiation approaches are complementary to each other, as different information from the same sample can be obtained (Triolo et al., 2010). The principal difference between X-rays and neutrons depends on the different interaction with the investigated sample: the former interacts with matter through photoelectric effect, Compton effect and pair production, as illustrated in section 2.1.2, while the latter interact through nuclear reactions, elastic and inelastic scattering, which depend on the internal structure of the nucleus (Figure 5.23) (Kardjilov & Festa, 2017; Strobl et al., 2009).

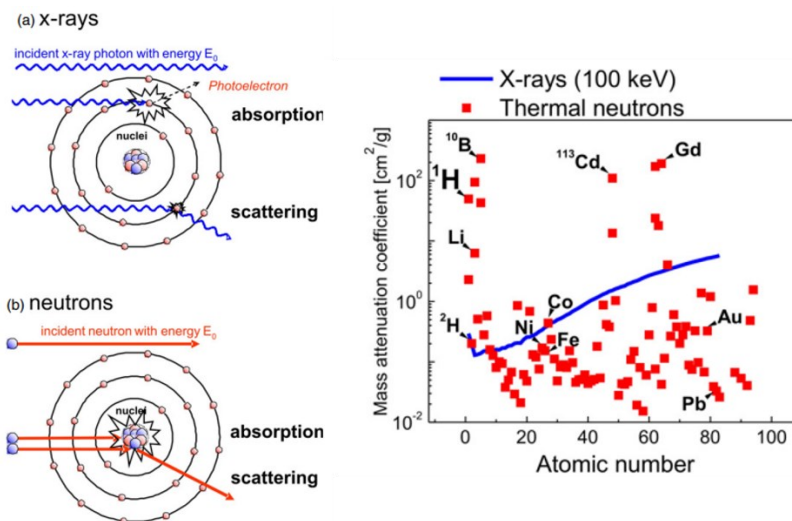


Figure 5.23: Interaction of matter with X-rays (top left) and neutrons (bottom left); mass attenuation coefficients for thermal neutrons and 100 keV x-rays for the different chemical elements (right) (Strobl et al., 2009).

Furthermore, neutron interactions depend also on its kinetic energy; as a matter of fact, neutrons can be divided into different categories (Alhussain, 2009):

- Cold: $E < 1$ meV;
- Thermal and Epithermal: $0,01$ eV $< E < 10$ keV;
- Fast: 10 keV $< E < 20$ MeV;
- Relativistic: $E > 20$ MeV.

For imaging analysis, thermal neutrons are typically used ($E \sim 25$ meV, $\lambda \sim 1.8$ Å), but also cold neutrons can be used based on the type of investigated material and analysis.

Therefore, based on the different type of interactions, it can be observed that the attenuation coefficient for X-rays increases with the atomic number of the elements, while neutrons don't follow a regular behaviour. The difference in tendency, shown in Figure 5.24. This aspect allows to easily discriminate materials with similar atomic number in some cases and allow to investigate samples that are difficult to analyse with X-ray radiation, e.g., metals (Figure 5.25).

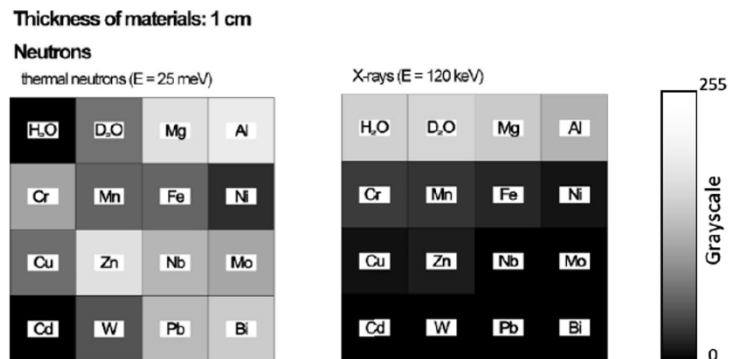


Figure 5.24: Greyscale attenuation maps the different interaction behaviour of thermal neutron (left) and X-Rays (right) with 1cm thickness of given materials. The darker the color, the stronger the attenuation, and vice versa (Oriol Sans Planell, 2022).



Figure 5.25: Differences in radiograph of an analog camera by X-rays (left) and neutrons (right) (from <https://www.psi.ch/en/science>)

To perform neutron imaging analysis, the basic concepts are the same of X-rays illustrated in section 2.2: the beam, produced by a source, interact with the sample and the transmitted signal is collected by a detector. However, other differences respect to X-rays are related to the instrumentation: for neutrons generation, a nuclear reactor or spallation source are required, thus experiments has to be conducted in large facilities (e.g., PSI in Swizerland and ISIS in UK); furthermore, neutron detectors consist generally of a scintillator layer ($ZnS/6LiF$ is one of the most widely used) that allow to convert neutrons in visible light photons, that bounces off a 45° angled mirror up to a digital camera that generate the image visible on a PC. The mirror allows to position the camera out of the neutron beam (and gamma radiation that could be generated) to avoid damages. Finally, if a CT scan is performed, generally neutron CT take longer time with respect to X-rays because of the different employed energies; moreover, different types of algorithms are used for CT reconstruction, since the beam geometry in case of neutron is a parallel beam geometry (as for synchrotron radiation), that differ from the most used ones for cone beam geometry (typical of X-rays).

5.3.2 NICHE facility development

In this framework, the Cultural Heritage Network (CHNet) of the Italian Nuclear Physics Institute (INFN) proposed and started a project called Neutron Imaging in Cultural HERitage (NICHE) devoted to the development and exercise of a neutron imaging station on the thermal port of the 250 kW TRIGA Mark-II reactor managed by the Laboratorio Energia Nucleare Applicata (LENA) in Pavia

(Figure 5.26 top). In the project five INFN sections were involved with different task (Firenze, Milano Bicocca, Pavia, Bologna and Torino) (Gelli et al., 2023).



Figure 5.26: The LENA reactor (PV) and the installed NICHE setup in the shielded room. Neutron channel with pinhole and custom-made camera box for imaging analysis is shown.

In April 2021 the setup was established and now NICHE works as a neutron imaging station, after the realization and the characterization of all the elements, that are easy to remove and install when necessary (technical specification of the components are summarized in Table 5.5). The setup is installed in an experimental hutch (main area is $1,25 \times w 0,6 \times h 2,1$ m), in which a custom-made sample holder and neutron camera box were installed, making possible to

adjust the distances of the components through collinear guide rails fixed on the ground (Figure 5.23 bottom-left). The neutron exit port is equipped with a shutter pneumatically controlled from outside, that allows the stop of the neutron beam and with some interchangeable pinholes with different diameters for the neutron beam collimation (Figure 5.23 bottom-right). The sample holder is equipped with two remotely controlled motorized linear stages along the vertical and the horizontal direction perpendicular to the beam and a rotating stage for sample rotation and potential tomographic projections acquisition. All the motors are controlled via a LabVIEW 2018 SP1 developed code, which also includes the acquisition control of the neutron camera. The neutron camera box for transmitted signal detection is composed by a scintillator screen coupled with a digital camera mounted on a remotely controlled translation stage to adjust the focus. The typical working distance between sample and the detector, taking into account the encumbrance of the various components, is of the order of 40 mm. Due to the shape and size of the experimental hutch and sample manipulation system, there are limitations in the relative distance of the camera and the sample holder with respect to the beam shutter and pin-hole system (distance value between the shutter and the scintillator ranges between 1100 and 1920 mm). In order to fully characterize all the setup components and the optimal analysis parameters, several measurements tests were performed (geometries, integration time, spatial resolution etc.); the obtained values are summarized in Table 5.6.

Table 5.5: Technical specification of the NICHE set-up

Pin-holes	10-20-30 cm, B ₄ C ceramix in Al holder
Motors controller	Arduino Mega and LD09 CNC driver
Rotatory stage controller	Physik Instrumente, PI
Detector scintillator	Ag doped 300 μ m ⁶ LiF/ZnS 2:1
Camera	ZWO ASI 2600 MM CMOS (16 bit)
Camera pixel	30 μ m \times 30 μ m
Voxel	min. 8 μ m, max. 24 μ m

Table 5.6: Instrumental parameters of the configuration of the NICHE set-up
(all values are reported considering the 10 mm pin-hole diameter)

Pin-hole to scintillator distance	1410 mm
L/D coefficient	140
Field of view (round, diameter)	65 mm
Best spatial resolution (0 mm ODD)	150 μm
Working-distance spatial resolution (40 mm ODD)	180 μm
Best signal to noise acquisition time	1200 s
Usual acquisition time	300/600 s
Tomography-mode acquisition time	150 s

In the framework of the project, some radiographic and tomographic tests were performed on ad-hoc realized samples, in order to evaluate the measurements feasibility and to obtain the different materials attenuation coefficients for the beamline characterization. In particular, several radiographs were conducted on different bronze alloys specimens realized specifically for this purpose (different percentage of the composed elements Cu, Sn, Pb). Some of them were also treated with different solution (CuSO_4 and NH_4Cl) in order to test the influence of the artificial corrosion patinas that wants to simulate the real corrosion of ancient bronze artefacts (Figure 5.24)

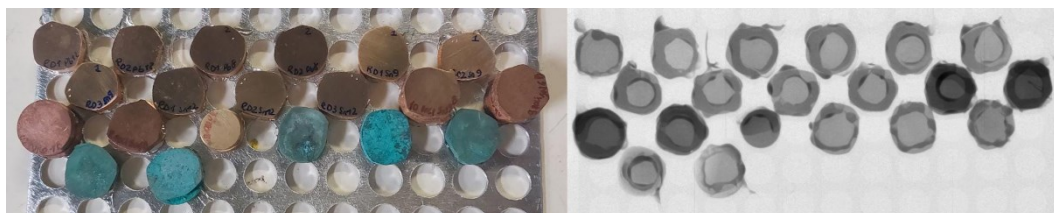


Figure 5.27: Some of the bronze testing samples analyzed and the corresponding neutron radiography. The green samples are the ones treated with different chemical solution to realized artificial corrosion patinas.

The analysis of raw data was performed by using the free software package ImageJ. For each sample, after correction and normalization of the neutron radiographs, the medium intensity and standard deviation was obtained from a ROI 50x50 pixel in the center of the object; applying so the Lambert-Beer law, we can calculate the mass attenuation coefficient Σ/ρ (g/cm^2) for all the sample, having measured the thickness and computed the density based on the known chemical composition. For every alloy, two samples were analyzed as they are (A and B) and then overlapped (A+B), in order to have a greater thickness and verify that the attenuation coefficient doesn't change.

As it is possible to observe from the reported graphs in Figure 5.25, there is a different behavior in function of the Cu-Pb% concentration in the different sample: for Cu-Sn sample there are no substantial changes in the attenuation coefficient as Cu Σ is predominant; however, for Cu-Sn-Pb samples a slight decrease of the coefficient as a function of the Pb concentration can be noticed. About the patinated samples (Figure 5.26), from the obtained radiography is not possible to highlight some changes of Σ/ρ respect to the non-corroded ones, probably because of the small thickness of the patinas (25 μm for sulphate-based and 150 μm for chloride-based, measured with SEM analysis). Furthermore, no considerations on the different compositions between the patina and the bulk could be made in this case (only tomography could provide this kind of information).

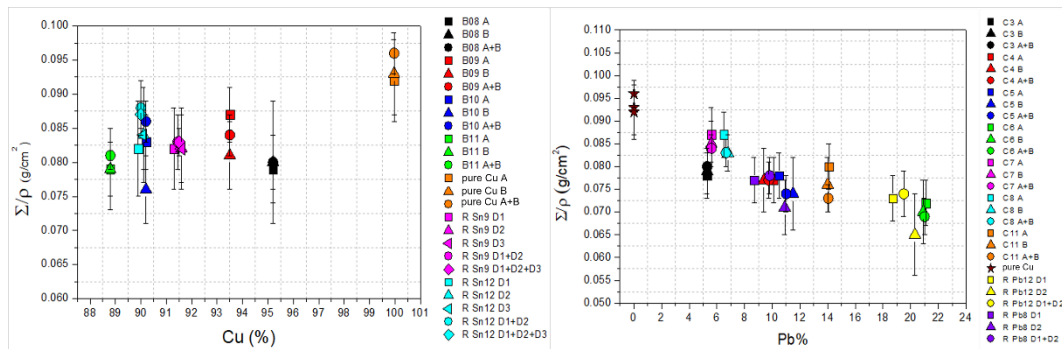


Figure 5.28: Mass attenuation coefficient results from the analyzed bronze samples; it is possible to notice the difference between the Cu-Sn alloys, where Sn% doesn't influence the results, and the Cu-Sn-Pb where if Pb% increase, Σ/ρ decrease.

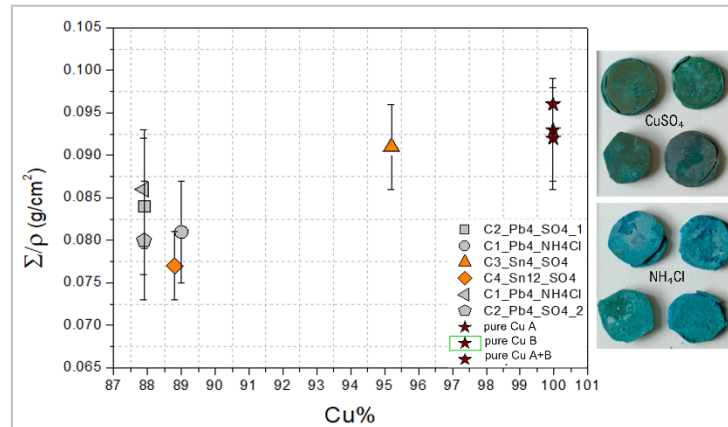


Figure 5.29: Mass attenuation coefficient results obtained for the patinated samples; in this case, no difference respect to the non-altered sample could be highlighted because of the low thickness of the corrosion layer.

Moreover, in the project framework, there was the possibility to study some ancient Egyptian animal bronze votive coffins that belong to the Museo Egizio of Torino 's collections with neutron tomography, for the study of the manufacturing of the objects and the animal mummified remains inside. Previously, an attempt to study these objects with X-ray CT was made at CCR laboratory (Venaria Reale) with the set-up described in section 5.1, but due to the high attenuation coefficient of the bronze and its thickness, little information could be obtained. Unfortunately, due to technical problems with NICHE beamline arose with recent changes in the radioprotection Italian law, the tomographic measurements on the Egyptian bronze artefacts were conducted at the FISH (First Imaging Station in Holland) beamline at the TU-Delft Reactor at Delft, Netherlands, that has similar characteristic in terms of neutron beam (energy and flux) respect to the LENA center (Zhou et al., 2018). The measurements were performed on 8 samples, for which ad-hoc aluminum housing were realized for the neutron CT (Al has a low attenuation coefficient, thus does not create problems in the reconstruction). Since the limited field of view (FOV), more than one CT acquisition was necessary for some of the artefacts due to the dimensions. Moreover, since generally neutron CT needs more acquisition time respect to X-ray CT because of the different beam flux rate, several days were required for the measurements. Previously to the reconstruction, the same images correction adopted for X-ray CT (using white and dark images) and the stitching among the different CT portion of the same object were performed. The CT reconstructions were then carried out with to different software (Muhrec and Octopus, (Dierick et al., 2004; Kaestner, 2011) by

INFN sections of Torino and Firenze. In Table 5.7 technical and acquisition parameters are summarized.

Table 5.7: Technical specification of TU-Delft reactor and neutron CT acquisition parameters

Reactor power	2298 - 2305 kW
Thermal flux	$3 \cdot 10^6 \text{ cm}^{-2}\text{s}^{-1}$
L/D	325 hor., 277 ver.
Camera pixel size	58 μm
FOV	7×15 cm
Integration time	30 s
ODD	8.7-11 cm
N° of projection	500-800

In general, it was possible to visualize the mummies inside the coffins, thanks to the lower attenuation of the bronze respect to the organic materials and the microstructure of the metal. For two objects with no faunal remains inside, neutron CT allowed to see the casting core and metal pins for the manufacturing. In the following, some of the results obtained will be described.

Sample C.0887 and C.2381, a cat-shape bronze coffin and a bronze box with a crowned hawk respectively (Figure 5.30 and 5.31), showed very well the faunal remains inside: in particular, bones inside the textile wrapping are clearly distinguishable. From a first analysis, their attribution to a little cat and a bird (especially for the long empty bones) effectively could be confirmed. Also, some textiles details could be seen in the CT slices. For the cat in particular, remain of the casting core in the head is visible and it could be appreciated how it follow the cat muzzle; also, some metal pins (probably iron-based) were found at the height of the breast and the nape of the neck, used for the manufacturing. In both the samples, bronze porosity in some areas (especially in the full-metal parts) is visible; this particular emerged also from the previous x-ray CT analysis.

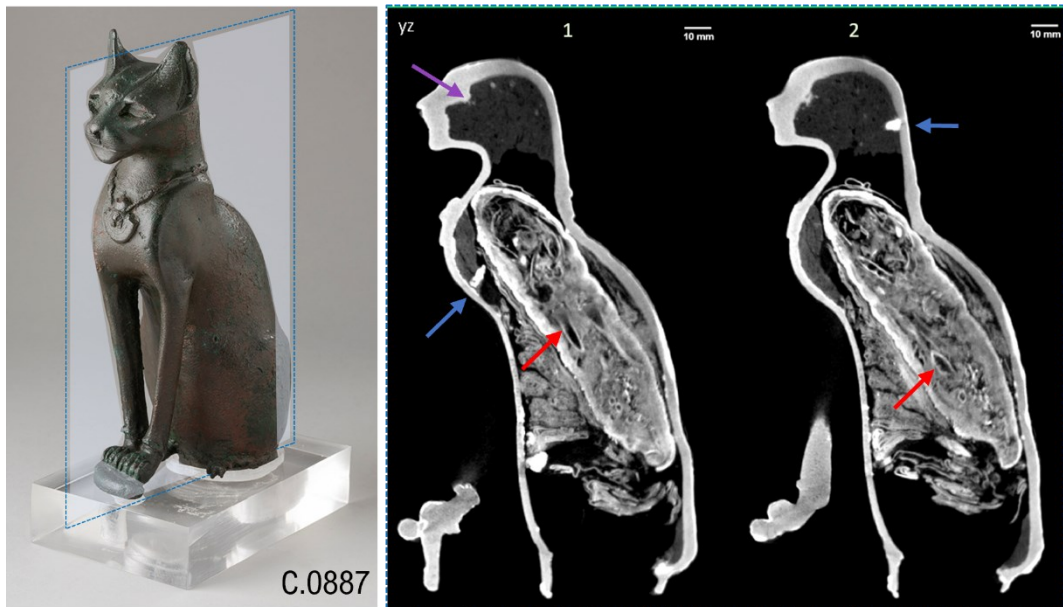


Figure 5.30: CT slice obtained for sample C.0887 (cat); the mummy is visible inside the coffin (red arrow: bones), together with filling bundles. Blue arrows indicate the metal pins, while purple arrow indicates the casting core in the whole head.

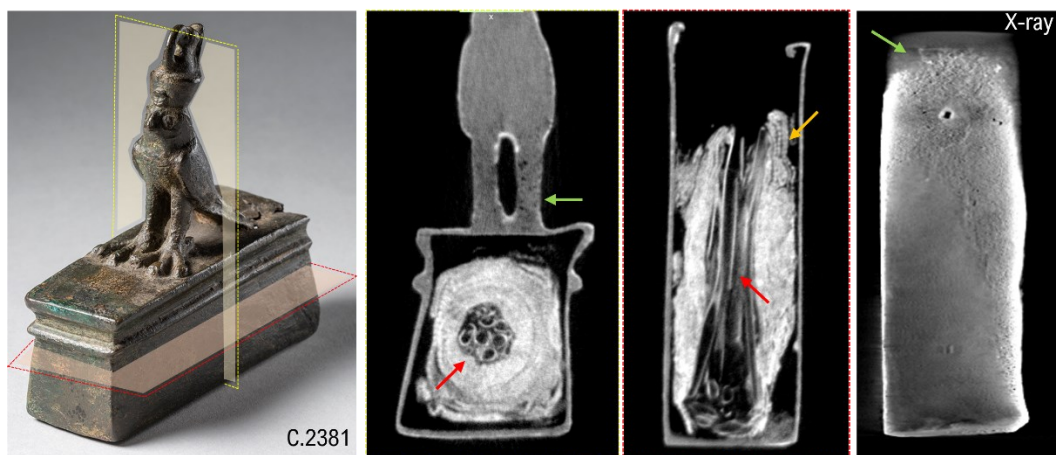


Figure 5.31: CT slice obtained for sample C.2381 (crowned hawk); the mummy is visible inside the bronze box, together with many bundles (red arrows: bones; orange arrow: detail of textile). Green arrows indicate bronze porosity, visible also in the X-ray CT.

Samples C.0893 and C.5220 are instead two examples of objects without mummified remains inside. For the first one, a bronze cat head, probably part of a votive coffin like sample C.0887 (Figure 5.32), neutron CT revealed the casting core filling in all the volume, together with some metals filtering in it (more

radiopaque areas), probably due to some melting problems during the manufacturing process. As for the previous cases, bronze porosity was identified for example in the left ear, while in the right one a particular brighter area is visible in correspondence of the hole, probably due to some gold residues derived from the earrings that were present in antiquity. In the second sample, a hawk whose paws are missing (Figure 5.33), casting core is clearly visible in the remaining part of the legs, while the head is filled with another type of material, presumably a lead compound based on the different attenuation between neutrons and X-rays (visible also at naked eye along a fracture on the head). Also in this case, a metal pin was found at the breast height, and bronze porosity is present, especially in the area between the legs. Moreover, in both samples, a more radiopaque layer on the surface could be noticed, probably due to the corrosion, even if also the presence of protective compounds applied in the past for conservation treatments.

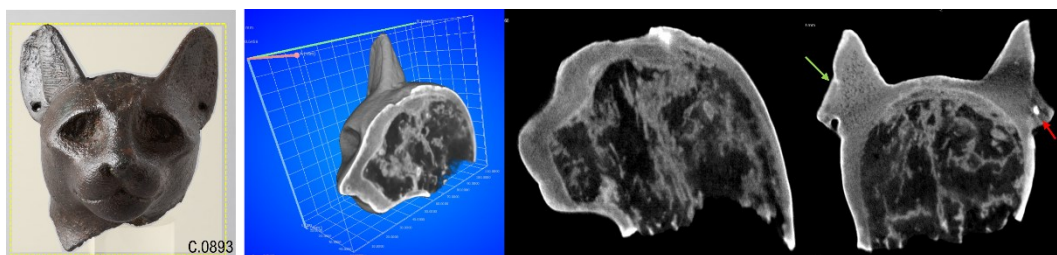


Figure 5.32: CT slice obtained for sample C.0893 (cat head); casting core with metals contaminants is visible inside. The green arrow indicates bronze porosity in the left ear, while the red arrow indicates the presumably gold material inside the right ear hole.

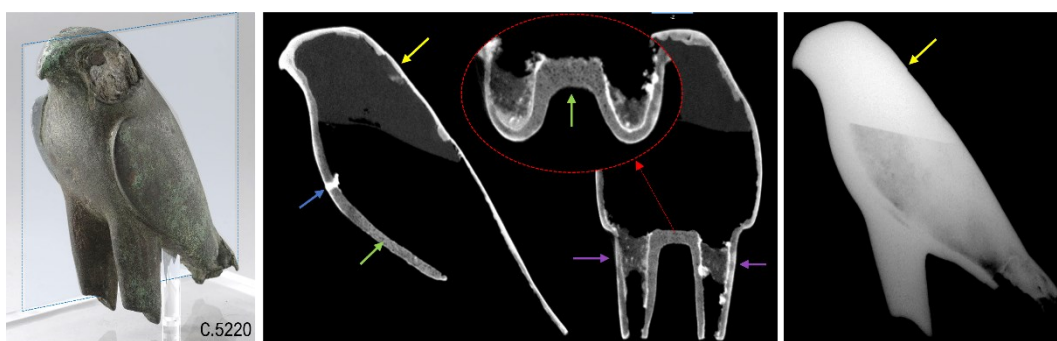


Figure 5.33: CT slice obtained for sample C.5220 (hawk); casting core remains are visible inside the two broken legs (purple arrows), together with bronze porosity (green arrows). Yellow arrows indicate lead filling, visible with different radiopacity in neutron CT (left) and x-ray radiography (right). Blue arrow indicates a metal pin.

Chapter 6

Conclusions

In this thesis, a general introduction to computed tomography (CT), a widely used technique in many fields of application with different aims, is given, followed by a description of the physical principles of X-rays and CT, including the individual steps of the CT process. The application of CT in the field of cultural heritage is currently very common for different purposes, such as the investigation of ancient manufacturing techniques through the visualization of inner structures and morphologies, and to assess the state of conservation of artworks. In this sense, CT is used mainly for qualitative analysis, but in some cases, a quantitative evaluation of sample features could be fundamental. In this study, a CT dimensional analysis of cultural heritage objects was performed to obtain quantitative data by applying the concept of industrial CT. This necessity arises for a particular category of objects, that is, historical woodwind musical instruments: due to conservative problems of wood, most of the time they could not be played by musicians, and this led to the loss of their ancient sound. A new approach using modern technologies to solve this issue consists of realising printed copies using additive manufacturing methods, starting from a digital model that can be obtained through CT analysis. The dimensional accuracy of the copies is important in the case of wind instruments because sound depends principally on the dimensions of the inner cavity and holes. In this sense, it is important to perform dimensional analysis of CT data.

To have a better knowledge of the topic, an overview of the principal concepts of industrial CT dimensional metrology, with indication of available

standards and guidelines, together with issues concerning measurements, was provided. In the same framework, the identification and description of different factors that could influence CT dimensional measurements were performed. Some of the most used CT reference objects were illustrated, and following suggestions given by some authors, two custom-made reference objects were developed for this work: a ball plate and a ball bar made of carbon fibre structures and calibrated alumina spheres. The use of spheres allows to consider as reference measurement the centre-to-centre distance between them; this is a reliable quantity because it does not depend on the chosen threshold for surface determination of the CT volume. These two samples were employed for the characterization of CT systems and for the evaluation of some factors influencing CT, which could be a source of errors; in particular, some X-ray tube parameters (voltage, focal spot size), sample orientation, and geometric features (magnification) were tested using the reference objects. In addition, a correction methodology already presented by some authors for CT voxel size scaling was used for the performed CT scans.

The reached results were illustrated in the second part of the thesis, through the evaluation of the SD parameter (deviation of the CT measurements respect to the reference ones) of the data before and after the application of voxel size correction. In general, it could be affirmed that the only parameter that influences dimensional analysis and showed the largest deviations is the geometric magnification; it depends on the CT scan geometry, so on distances between source, sample and detector. Among them, it is experimented that SOD (source to object distance) is subject to a larger error during initial measurements, and this is in line with the bigger SD values obtained. Since SOD is the most important error source in this case, it was decided to apply the correction methods to this parameter to obtain finally the corrected voxel size. In all the performed tests, the correction methodology effectiveness was verified for the used calibration objects.

In the last part of the thesis, analysis of the application of the correction method to different samples is presented. For this purpose, different strategies were tested using the developed calibration objects, which were both scanned before and after the sample and together it in the same CT acquisition, to identify the best methodology for a proper dimensional correction. A preliminary test conducted using two different CT datasets already acquired for other tests wanted to evaluate the two strategies using always the calibration objects (in the first case, a CT scan of the ball plate made before and after was used to correct the middle scan of the ball plate itself; in the second case, the ball plate and the ball bar were

scanned together and then used to correct the other), from which the correction using the ball plate seemed to work better.

Then, the first CT scan of a sample was performed on a LEGO brick, chosen because of its regular shape, and dimensions of length, knobs diameters and centre distance were evaluated. For this sample, beyond the two illustrated correction strategies, a third correction test was conducted using some calibrated features (in this case, c-c knobs distances), as suggested in the literature, and possible because the brick reference measures were obtained with the same machine used for the calibration objects (an ATOS Scanbox). The obtained results showed a different situation with respect to the already experimented ones, since the SD values do not follow a specific trend, but every measured distance has both positive and negative deviations. The applied correction in this case seems to have no influence on the data, except for the third one (using calibrated features), but since the starting SD values are not homogeneous, the same is true for the corrected dataset; in fact, some values improve and some worsen, based on the applied correction factor ($>$ or $<$ 1). The same situation occurred for CT tests performed on a musical instrument (Piccolo Flute), for which the lengths, terminal part diameters, and hole diameters were chosen as measured quantities. Some explanations could be found in the evaluated features, such as diameters, whose measurements are not independent of the threshold choice as the c-c distance, and thus larger errors could occur. Another possible reason is the software used, which was developed for image processing but not specifically for metrological aims like others used in the industry. Lastly, the highlighted variability in CT dimension analysis over time could also have an effect in this sense.

Some suggestions for the future development of this work are to investigate other CT influencing factors, which may be more dependent on the instrumentation, to provide some evidence on possible systematic errors. Another important aspect is to perform other measurements on different samples to better investigate the intrinsic variability of dimensional analysis on different measured features and CT over time, and some reconstruction and analysis tests with other software could be conducted to assess the different available measurement tools.

In the final chapter of this thesis, some of the parallel works and projects conducted on different types of artworks using the CT technique were illustrated, and the best measuring strategies were studied and applied to very wide object typologies, from constituent materials (ceramic, glass, wood, etc.) to shape and dimensions (from a few to tens of centimetres). The analyses were conducted both

at the Centro Conservazione e Restauro “la Venaria Reale” and at the Physics Department of the University of Torino, where equipped laboratory for CT is installed. All the analyses involved universities, research centres, museums, and other institutions in synergic and multidisciplinary collaboration.

In addition to X-rays, imaging analysis with other probes has been performed, particularly using neutrons. During collaboration with the research project NICHE of the INFN, it could be possible to develop and install a new neutron imaging beamline principally dedicated to artwork analysis at the L.E.N.A centre in Pavia, where a thermal neutron reactor is available. In the framework of the project, some bronze artefacts from the Museo Egizio of Torino were analysed using neutron tomography at the TU Delft reactor in the Netherlands because it was impossible to conduct the analysis in Italy. Neutron imaging demonstrated its potential in this case for the analysis of metallic materials, and it was useful for obtaining important information on these artefacts.

References

- Albertin, F., Bettuzzi, M., Brancaccio, R., Morigi, M. P., & Casali, F. (2019). X-ray computed tomography in situ: An opportunity for museums and restoration laboratories. *Heritage*, 2(3), 2028–2038.
- Alhussain, A. (2009). *Comparison study of reflected and transmitted thermal neutron flux in water and other moderators*. [PhD Thesis]. King Saud University
- Alloteau, F., Majérus, O., Valbi, V., Biron, I., Lehuédé, P., Caurant, D., Charpentier, T., & Seyeux, A. (2020). Evidence for different behaviors of atmospheric glass alteration as a function of glass composition. *Npj Materials Degradation*, 4(1), 36.
- Amiri, S., Muhammad Ali, P., Mohammed, S., Hanus, R., Abdulkareem, L., Alanezi, A., Eftekhari-Zadeh, E., Roshani, G. H., Nazemi, E., & Kalmoun, E. M. (2021). Proposing a Nondestructive and Intelligent System for Simultaneous Determining Flow Regime and Void Fraction Percentage of Gas–Liquid Two Phase Flows Using Polychromatic X-Ray Transmission Spectra. *Journal of Nondestructive Evaluation*, 40, 47.
- Badran, A., Marshall, D., Legault, Z., Makovetsky, R., Provencher, B., Piché, N., & Marsh, M. (2020). Automated segmentation of computed tomography images of fiber-reinforced composites by deep learning. *Journal of Materials Science*, 55, 16273–16289.
- Bär, F. P. (2018). *Recommendations For the Three-Dimensional Computed Tomography of Musical Instruments*. Germanisches National Museum. Musices. Available online: <https://www.gnm.de/en/research/research-projects/musices/>
- Barclay, R. L. (1996). The conservation of musical instruments. *Museum International*, 48(1), 9–14.

- Barrett, J. F., & Keat, N. (2004). Artifacts in CT: Recognition and avoidance. In *Radiographics* (Vol. 24, Issue 6). Radiological Society of North America Inc.
- Bartscher, M., Sato, O., Härtig, F., & Neuschaefer-Rube, U. (2014). Current state of standardization in the field of dimensional computed tomography. *Measurement Science and Technology*, 25(6), 064013.
- Bellia, A. (2019). Towards a new approach in the study of Ancient Greek music: Virtual reconstruction of an ancient musical instrument from Greek Sicily. In *Digital Scholarship in the Humanities*, Vol. 34, Issue 2, pp. 233–243. Oxford University Press.
- Berger, M., Yang, Q., & Maier, A. (2018). X-ray Imaging. In *Medical Imaging Systems: An Introductory Guide [Internet]* (pp. 119–145). Springer International Publishing.
- Bettuzzi, M., Brancaccio, R., Morigi, M. P., & Casali, F. (2007). Effective dynamic range measurement for a CCD in full-field industrial x-ray imaging applications. *Optical Measurement Systems for Industrial Inspection V*, 6616, 66161L.
- Blažek, P., Šrámek, J., Zikmund, T., Kalasová, D., Hortvík, V., Klapetek, P., & Kaiser, J. (2019). *Voxel size and calibration for CT measurements with a small field of view*. 9th Conference on Industrial Computed Tomography (iCT) 2019, 13-15 Feb, Padova, Italy. *e-Journal of Nondestructive Testing* Vol. 24 (3).
- Boutin, H., Le Conte, S., Vaiedelich, S., Fabre, B., & Le Carrou, J.-L. (2017). Acoustic dissipation in wooden pipes of different species used in wind instrument making: An experimental study. *The Journal of the Acoustical Society of America*, 141(4), 2840–2848.
- Brancaccio, R., Bettuzzi, M., Casali, F., Morigi, M. P., Levi, G., Gallo, A., Marchetti, G., & Schneberk, D. (2011). Real-time reconstruction for 3-D CT applied to large objects of cultural heritage. *IEEE Transactions on Nuclear Science*, 58 (4 PART 1), 1864–1871.

- Brunke, O., Santillan, J., & Suppes, A. (2010). Precise 3D dimensional metrology using high-resolution x-ray computed tomography (μ CT). *Developments in X-Ray Tomography VII*, 7804, 203–215.
- Carmignato, S., Dewulf, W., & Leach, R. (2017). Industrial X-ray computed tomography. In *Industrial X-Ray Computed Tomography*. Springer International Publishing.
- Carmignato, S., Dreossi, D., Mancini, L., Marinello, F., Tromba, G., & Savio, E. (2009). Testing of x-ray microtomography systems using a traceable geometrical standard. *Measurement Science and Technology*, 20(8), 084021.
- Casali, F. (2006). X-ray and Neutron Digital Radiography and Computed Tomography for Cultural Heritage. In *Physical Techniques in the study of Art Archaeology and Cultural Heritage*, Vol. 1 (pp. 1-221). Elsevier.
- Castellano, A., Quarta, S., & Donativi, M. (2007). Tecniche radiografiche per l'archeometria. In *Elementi di archeometria. Metodi fisici per i beni culturali* (pp. 177–229). Edizioni Egea.
- Chhem, R. K., & Brothwell, D. R. (2008). *Paleoradiology. Imaging Mummies and Fossils*. Springer Berlin, Heidelberg.
- Coltman, J. W. (2005). Effect of Material on Flute Tone Quality. *The Journal of the Acoustical Society of America*, 49 (2B), 520–523.
- Damodaran, A., Sugavaneswaran, M., & Lessard, L. (2021). An overview of additive manufacturing technologies for musical wind instruments. In *SN Applied Sciences* (Vol. 3, Issue 2). Springer Nature.
- Del Vesco, P., & Moiso, B. (2017). *Missione Egitto 1903-1920: l'avventura archeologica MAI raccontata: [exposition, Torino, Museo Egizio, 11 marzo-10 settembre 2017]*. Panini editore.
- Pierobon, A. (2012) *Accuracy of geometrical measurements using computed tomography* [PhD Thesis]. University of Padova.
- Dierick, M., Masschaele, B., & Van Hoorebeke, L. (2004). Octopus, a fast and user-friendly tomographic reconstruction package developed in LabView®. *Measurement Science and Technology*, 15(7), 1366.

- EN 16016-2. (2011). *EN 16016-2 - Non-Destructive Testing - Radiation method - Computed tomography - Part 2: Principle, equipment and samples.*
- Enríquez-León, A. J., de Souza, T. D., Aragão, F. T. S., Braz, D., Pereira, A. M. B., & Nogueira, L. P. (2022). Determination of the air void content of asphalt concrete mixtures using artificial intelligence techniques to segment micro-CT images. *International Journal of Pavement Engineering*, 23(11), 3973–3982.
- Erika Fissore. (2021). *Creazione di un protocollo ottimizzato per la ricostruzione tomografica. Studio e applicazione di metodi per la correzione di artefatti.* [Master's degree Thesis]. University of Torino.
- Feldkamp, L. A., Davis, L. C., & Kress, J. W. (1984). Practical cone-beam algorithm. *Journal of the Optical Society of America A*, 1(6), 612–619.
- Forrester, P., Bouterse, J., Pel, T., Paleo, L., & Goodwin, C. (2018). Communications. *FoMRHI Quarterly*, 142.
- Gelli, N., Giuntini, L., Cantini, F., Sans-Planell, O., Magalini, M., Manetti, M., Sodi, L., Massi, M., Castelli, L., Czelusniak, C., Taccetti, F., Bella, T. E., Marcucci, G., Clemenza, M., Di Martino, D., Morigi, M., Bettuzzi, M., Vigorelli, L., Re, A., ... Grazi, F. (2023). The new INFN-CHNet neutron imaging facility. *Nuclear Instruments and Methods in Physics Research Section A: Accelerators, Spectrometers, Detectors and Associated Equipment*, 168189.
- Ghani, M. U., Ren, L., Wong, M., Li, Y., Zheng, B., Rong, X. J., Yang, K., & Liu, H. (2017). Noise power characteristics of a micro-computed tomography system. *Journal of Computer Assisted Tomography*, 41(1), 82–89.
- Goldman, L. W. (2007). Principles of CT: Radiation Dose and Image Quality. *Journal of Nuclear Medicine Technology*, 35(4), 213.
- Greg Michael. (2001). X-ray computed tomography. *Physics Education*, 36(6), 442.
- Guntoro, P., Ghorbani, Y., Koch, P.-H., & Rosenkranz, J. (2019). X-ray Microcomputed Tomography (μ CT) for Mineral Characterization: A Review of Data Analysis Methods. *Minerals*, 9.

- Hatchfield, P., & Newman, R. (1991). Ancient Egyptian gilding methods. In *Gilded Wood: Conservation and History*, Sound View Press.
- Hiller, J., & Reindl, L. M. (2012). A computer simulation platform for the estimation of measurement uncertainties in dimensional X-ray computed tomography. *Measurement: Journal of the International Measurement Confederation*, 45(8), 2166–2182.
- Howe, R., Shahbazmohamadi, S., Bass, R., & Singh, P. (2014). Digital evaluation and replication of period wind instruments: the role of micro-computed tomography and additive manufacturing, *Early Music*, Volume 42, Issue 4, November 2014, Pages 529–536
- Hunt, D. (2012). Properties of wood in the conservation of historical wooden artifacts. *Journal of Cultural Heritage*, 13(3, Supplement), S10–S15.
- Ignesti, A. (2007). Il flauto traversiere e il suo procedimento costruttivo. *Philomusica On-line*, Vol. 6(1), Università degli Studi di Pavia.
- Kaestner, A. P. (2011). MuhRec—A new tomography reconstructor. *Nuclear Instruments and Methods in Physics Research Section A: Accelerators, Spectrometers, Detectors and Associated Equipment*, 651(1), 156–160.
- Kak, A. C., Slaney, M., & Wang, G. (2002). Principles of Computerized Tomographic Imaging. *Medical Physics*, 29(1), 107.
- Kardjilov, N., & Festa, G. (2017). *Neutron Scattering Applications and Techniques Neutron Methods for Archaeology and Cultural Heritage*. Springer International Publication.
- Karp, C. (1978). Woodwind Instrument Bore Measurement. In *Source: The Galpin Society Journal* (Vol. 31).
- Katz, J. (2017). Digitized Maya music: The creation of a 3D database of Maya musical artifacts. *Digital Applications in Archaeology and Cultural Heritage*, 6, 29–37.
- Kiekens, K., Welkenhuyzen, F., Tan, Y., Bleys, P., Voet, A., Kruth, J. P., & Dewulf, W. (2011). A test object with parallel grooves for calibration and accuracy assessment of industrial computed tomography (CT) metrology. *Measurement Science and Technology*, 22(11).

- Krauss, A., & Whymark, A. (2021). The Influence of Crack Propagation on Tektite Glass Corrosion Sculpture. *52nd Lunar and Planetary Science Conference*, 2548, 1489.
- Kruth, J. P., Bartscher, M., Carmignato, S., Schmitt, R., De Chiffre, L., & Weckenmann, A. (2011). Computed tomography for dimensional metrology. *CIRP Annals - Manufacturing Technology*, 60(2), 821–842.
- Lehmann, E. H., Lämmlein, S., & Mannes, D. (2018). Neutron imaging as tool for investigations on historical musical instruments. *Journal of Archaeological Science: Reports*, 20, 239–243.
- Lenting, C. (2019). *Glass Corrosion: Towards a Unifying Mechanistic Model*. [PhD Thesis]. University of Bonn.
- Lifton, J. J. (2015). *The Influence of Scatter and Beam Hardening in X-ray Computed Tomography for Dimensional Metrology*. [PhD Thesis]. University of Southampton.
- Lifton, J. J., Malcolm, A. A., McBride, J. W., & Cross, K. J. (n.d.). *The Application of Voxel Size Correction in X-ray Computed Tomography for Dimensional Metrology*. Singapore International NDT Conference & Exhibition, 19-20 July 2013. *e-Journal of Non-destructive Testing* Vol. 18(8).
- Lombardo, T., Gentaz, L., Verney-Carron, A., Chabas, A., Loisel, C., Neff, D., & Leroy, E. (2013). Characterisation of complex alteration layers in medieval glasses. *Corrosion Science*, 72, 10–19.
- Mallat, S. G. (1999). *A wavelet tour of signal processing*. Second Edition. Academic Press, Elsevier.
- Martz, H. E., Logan, C. M., Schneberk, D. J., & Shull, P. J. (2016). *X-ray Imaging: fundamentals, industrial techniques and applications*. CRC Press.
- Morigi, M. P., Casali, F., Bettuzzi, M., Brancaccio, R., & D'Errico, V. (2010). Application of X-ray Computed Tomography to Cultural Heritage diagnostics. *Applied Physics A: Materials Science and Processing*, 100(3), 653–661.
- Müller, P. (2010). Use of reference objects for correction of measuring errors in X-ray computed tomography. Kgs.Lyngby: DTU Mechanical Engineering.

- Müller, P. (2013). *Coordinate Metrology by Traceable Computed Tomography*. [PhD Thesis]. Technical University of Denmark.
- Müller, P.; Hiller, J.; Cantatore, A. ;, Bartscher, M. ;, & De Chiffre, L. (2017). Investigation on the influence of image quality in X-ray CT metrology. In *Citation*. APA.
- Müller, P., Hiller, J., & Tosello, G. (2012). New reference object for metrological performance testing of industrial CT systems. Proceedings of the 12th euspen International Conference, Stockholm, June 2012.
- Nervo, M. (2013). *Il progetto neu-ART: studi e applicazioni ; Neutron and X-ray tomography and imaging for cultural heritage*. Editris.
- Nico, J. S., & Snow, W. M. (2005). Fundamental Neutron Physics. *Annual Review of Nuclear and Particle Science*, 55(1), 27–69.
- Object Research Systems (ORS) Inc. (2022). *Dragonfly 2022.2 (Computer Software)*. Available online: <http://www.theobjects.com/dragonfly>.
- Oriol Sans Planell. (2022). *Development of a Novel Compact Neutron Collimator for Neutron Imaging Applications within the ANET Project* [PhD Thesis]. University of Torino.
- Otsu, N. (1979). A threshold selection method from gray-level histograms. *IEEE Transactions on Systems, Man, and Cybernetics*, 9(1), 62–66.
- Otte, A., Thieme, T., & Beck, A. (2013). Computed tomography alone reveals the secrets of ancient mummies in medical archaeology. *Hellenic Journal of Nuclear Medicine*, 16(2), 148–149.
- Pal, D., Sharma, K. Sen, & Hsieh, J. (2013). Metal artifact correction algorithm for CT. *IEEE Nuclear Science Symposium Conference Record*.
- Re, A., Lo Giudice, A., Nervo, M., Buscaglia, P., Luciani, P., Borla, M., & Greco, C. (2016). The importance of tomography studying wooden artefacts: A comparison with radiography in the case of a coffin lid from ancient Egypt. *International Journal of Conservation Science*, Volume 7, Special Issue 2, 2016: 935-944.

- Rossi, H. H., & Kellerer, A. M. (1995). Roentgen. *Radiation Research*, *144*(2), 124–128.
- Rueckel, J., Stockmar, M., Pfeiffer, F., & Herzen, J. (2014). Spatial resolution characterization of a X-ray microCT system. *Applied Radiation and Isotopes*, *94*, 230–234.
- Schäfers, K. P., Bolwin, K., Büther, F., Hermann, S., Jacobs, A. H., Kösters, T., Kuhlmann, M., Schäfers, M., & Viel, T. (2014). 1.10 - High-Resolution Small Animal Imaging. In A. Brahme (Ed.), *Comprehensive Biomedical Physics* (pp. 181–211). Elsevier.
- Schalm, O., Nuyts, G., & Janssens, K. (2021). Some critical observations about the degradation of glass: The formation of lamellae explained. *Journal of Non-Crystalline Solids*, *569*, 120984.
- Schmitt, R., & Niggemann, C. (2010). Uncertainty in measurement for x-ray-computed tomography using calibrated work pieces. *Measurement Science and Technology*, *21*(5), 054008.
- Seibert, J. A. (2004). X-ray imaging physics for nuclear medicine technologists. Part 1: Basic principles of x-ray production. *Journal of Nuclear Medicine Technology*, *32*(3), 139–147.
- Seibert, J. A., & Boone, J. M. (2005). X-ray imaging physics for nuclear medicine technologists. Part 2: X-ray interactions and image formation. *Journal of Nuclear Medicine Technology*, *33*(1), 3–18.
- Seibert, J. A., Boone, J. M., & Lindfors, K. K. (1998). Flat-field correction technique for digital detectors. *Proc.SPIE*, *3336*, 348–354.
- Singh, H. (2016). *Textbook of Radiology Physics*. JP Medical Ltd.
- Steele, A. G., & Douglas, R. J. (2006). Extending En for measurement science. *Metrologia*, *43*(4).
- Strobl, M., Manke, I., Kardjilov, N., Hilger, A., Dawson, M., & Banhart, J. (2009). Advances in neutron radiography and tomography. *Journal of Physics D: Applied Physics*, *42*(24).

- Tan, Y. (2015). *Scanning and Post-processing Parameter Optimization for CT Dimensional Metrology*. [PhD Thesis]. KU Leuven, Science, Engineering & Technology Group.
- Tansella, F., Vigorelli, L., Ricchiardi, G., Re, A., Bonizzoni, L., Grassini, S., Staropoli, M., & Lo Giudice, A. (2022). X-ray Computed Tomography Analysis of Historical Woodwind Instruments of the Late Eighteenth Century. *Journal of Imaging*, 8(10).
- Trent Neel, S., Gibson, R., Daniels, C. R., & Klosterman, E. L. (1998). Dimensional Accuracy in X-Ray Computed Tomography Imaging. In D. O. Thompson & D. E. Chimenti (Eds.), *Review of Progress in Quantitative Nondestructive Evaluation: Volume 17A* (pp. 411–412). Springer US.
- Triolo, R., Giambona, G., Lo Celso, F., Ruffo, I., Kardjilov, N., Hilger, A., Manke, I., & Paulke, A. (2010). Combined Application of X-Ray and Neutron Imaging Techniques to Wood Materials. *Conservation Science in Cultural Heritage*, 10(1), 143–158.
- Van den Bulcke, J., Van Loo, D., Dierick, M., Masschaele, B., Van Hoorebeke, L., & Van Acker, J. (2017). Nondestructive research on wooden musical instruments: From macro- to microscale imaging with lab-based X-ray CT systems. *Journal of Cultural Heritage*, 27, S78–S87.
- Vigorelli, L., Re, A., Buscaglia, P., Manfreda, N., Nervo, M., Cavaleri, T., Del Vesco, P., Borla, M., Grassini, S., Guidorzi, L., & Lo Giudice, A. (2022). Comparison of two ancient Egyptian Middle Kingdom statuettes from the Museo Egizio of Torino through computed tomographic measurements. *Journal of Archaeological Science: Reports*, 44.
- Vigorelli, L., Re, A., Guidorzi, L., Cavaleri, T., Buscaglia, P., Nervo, M., Facchetti, F., Borla, M., Grassini, S., & Lo Giudice, A. (2021). X-ray imaging investigation on the gilding technique of an Ancient Egyptian taweret wooden statuette. *Journal of Imaging*, 7(11).
- Villarraga-Gómez, H. (2016). X-ray computed tomography for dimensional measurements. *Digital Imaging 2016*, 44–57.

- Villarraga-Gómez, H., Herazo, E. L., & Smith, S. T. (2019). X-ray computed tomography: from medical imaging to dimensional metrology. In *Precision Engineering* (Vol. 60, pp. 544–569). Elsevier Inc.
- Villarraga-Gómez, H., Lee, C. B., & Smith, S. T. (2018). Dimensional metrology with X-ray CT: A comparison with CMM measurements on internal features and compliant structures. *Precision Engineering*, *51*, 291–307.
- Villarraga-Gómez, H., Morse, E. P., Hocken, R. J., & Smith, S. T. (2014). Dimensional metrology of internal features with X-ray computed tomography. *Proc. of 29th ASPE Annual Meeting*, 684–689.
- Watkins, T., & Payzant, E. A. (2013). Neutron Characterization for Additive Manufacturing. *Advanced Materials & Processes*. Vol. 171 (3).
- Weckenmann, A., & Krämer, P. (2009). Assessment of measurement uncertainty caused in the preparation of measurements using computed tomography. XIX IMEKO World Congress Fundamental and Applied Metrology September 6–11, 2009, Lisbon, Portugal.
- Wevers, M., Kerckhofs, G., Pyka, G., Herremans, E., Van Ende, A., Hendrickx, R., Verstrynghe, E., Mariën, A., Valcke, E., Pareyt, B., & Wilderjans, E. (2012). X-ray Computed Tomography for Non-Destructive Testing. Proceedings iCT 2012, 4th International Conference on Industrial Computed Tomography, Wels, Austria.
- Wilson, P., Williams, M. A., Warnett, J. M., Attridge, A., Ketchum, H., Hay, J., & Smith, M. P. (2017). Utilizing X-ray computed tomography for heritage conservation: The case of *Megalosaurus bucklandii*. 2017 IEEE International Instrumentation and Measurement Technology Conference (I2MTC), 1–5.
- Withers, P. J., Bouman, C., Carmignato, S., Cnudde, V., Grimaldi, D., Hagen, C. K., Maire, E., Manley, M., Du Plessis, A., & Stock, S. R. (2021). X-ray computed tomography. *Nature Reviews Methods Primers*, *1*(1), 18.
- X-RAY WorX GmbH. (2014). Internal target cooling improves results of high-resolution computed tomography. *E-Journal of Nondestructive Testing*, *19* (3).

- Xue, L., Suzuki, H., Ohtake, Y., Fujimoto, H., Abe, M., Sato, O., & Takatsuji, T. (2015). Numerical Analysis of the Feldkamp-Davis-Kress Effect on Industrial X-Ray Computed Tomography for Dimensional Metrology. *Journal of Computing and Information Science in Engineering*, 15(2).
- Zemek, M., Blažek, P., Šrámek, J., Šalplachta, J., Zikmund, T., Klapetek, P., Takeda, Y., Omote, K., & Kaiser, J. (2020). Voxel Size Calibration for High-resolution CT. 10th Conference on Industrial Computed Tomography (iCT) 2020, 4-7 Feb, Wels, Austria. *e-Journal of Nondestructive Testing* Vol. 25(2).
- Zhou, Z., Plomp, J., van Eijck, L., Vontobel, P., Harti, R. P., Lehmann, E., & Pappas, C. (2018). FISH: A thermal neutron imaging station at HOR Delft. *Journal of Archaeological Science: Reports*, 20, 369–373.

Appendix A: Instrumentation alignment

The aim in this operational phase is to make the projections of the same point of the sample fall, at each angle of rotation, always in the same pixel (with an accuracy of ± 1 pixel).

Once the CT geometry is determined (SDD and SOD), the first alignment of the instrumentation is performed using a laser pointer to position the various elements of the setup on a macro scale, aiming to obtain the source and the object in line with the centre of the detector (Figure A.1). In addition, the rotating platform is levelled manually to ensure that the plane on which the object is placed perpendicular to the plane of the detector. Then, a more precise procedure takes place with X-rays using a small sharp object (in this case, a tungsten needle) positioned with its point corresponding to the sample centre of gravity and with the detector central pixel (Figure A.1). The needle is placed slightly distant from the centre of rotation to ensure that during rotation, its projection covers the entire detector surface, going as externally as possible on the horizontal plane near the image edges, allowing a proper alignment of the whole area. The needle is then observed in different positions, and the coordinates of its uppermost central pixel are used to fix the alignment. It starts looking at the needle's radiographs, using the LabVIEW program in "live" mode, at 0° and 180° , to see if there is correspondence of needle position; if not, the platform is rotated to a certain degree until the two projections are aligned (the considered needle pixel has the same x-coordinate, Figure A.2). The reached angle is now used as the new 0° ; therefore, the other considered angles (90° , 180° , and 270°) will be increased or decreased with the same quantity for the subsequent alignment steps.

At the new 0° and 180° , the y-axis is then considered, and the coordinate with the higher value determines if the source centre is too high or too low with respect to the object, as can be seen in Figure 28. The source is then lowered or raised manually, acting on the support on which it is placed. This is done until the y-coordinate is the same in both positions. The needle is then radiographed at 90° and 270° to check the y coordinate in the two positions. If it is different, it means that the object plane is not levelled; this is fixed by tightening or loosening two of the rotating platform's screws, which raises or lowers the platform on the two opposite sides until the y-coordinates coincide (Figure A.2). After the last check of x and y coordinates on all four considered positions, the platform is returned to

position 0° (always the new one) and the detector is moved so that the reference pixel of the needle corresponds to the exact centre of the detector's area (in this case, the detector pixel centre has coordinates $x=1152$ and $y=1470$).

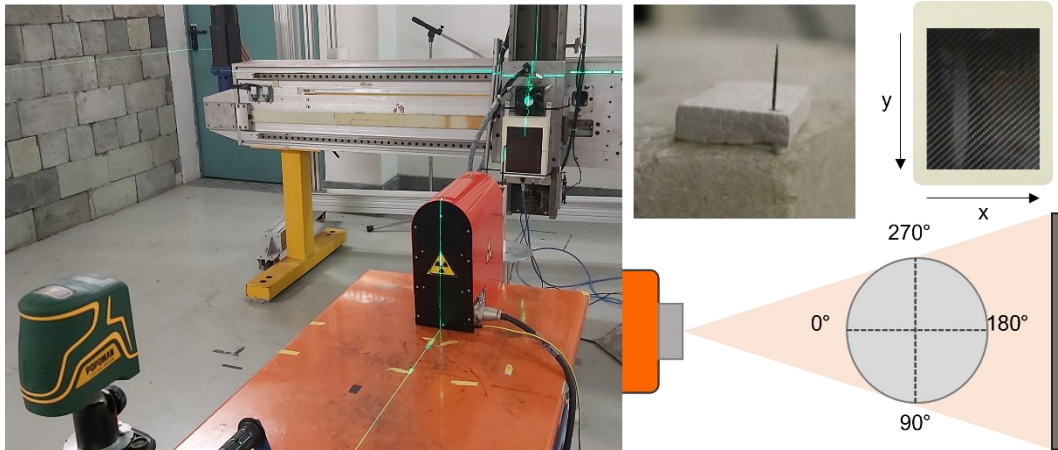


Figure A.1: First alignment with laser pointer, with positioning of tungsten needle and definition of degree to check.

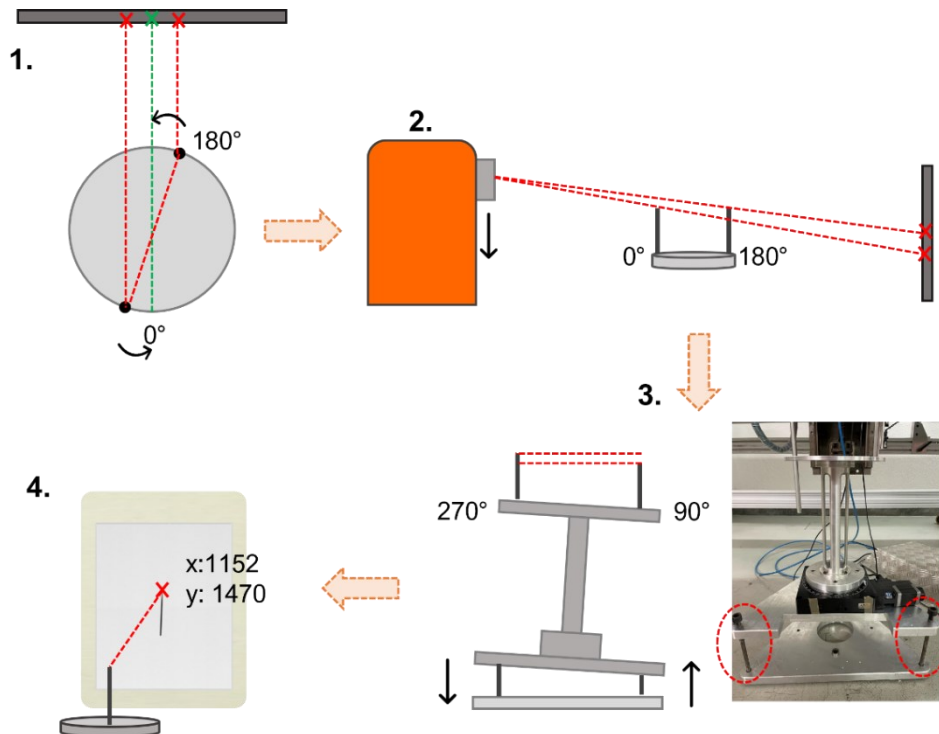


Figure A.2: Schematic workflow for the alignment procedure.

Once the alignment procedure is completed, the needle is substituted with the actual sample on the platform, and a test to verify that it remains within the active detector area is made by rotating it by 360° and it is possible to proceed with the CT acquisition.

Appendix B: CT reconstruction and data analysis on Dragonfly

The software used for CT reconstruction, visualisation, and analysis of the resulting 3D object is Dragonfly, distributed by Object Research Systems (ORS). Once raw projections are loaded together with the average white and dark images (see Section 2.2.3), the tool for CT reconstruction can be run. In the first window (geometry acquisition), besides specifying the X-ray beam type (Cone Beam or Parallel Beam, in our case the former), a series of input parameters is necessary for the voxel dimension calculation and the reconstruction itself (Figure B.1):

- Min. angle: starting angle of the tomography (0°).
- Angle step: determine the number of projections that the software have to read from the ones already loaded.
- Source to detector distance (mm).
- Source to object distance (mm).
- Detector spacing: detector pixel size (mm).

In addition, the clockwise steps could be flagged or not based on the rotation direction and in the “Advanced Acquisition Parameters” (red square in Figure B.1) menu, source voltage, current, and integration time could be added; the detector angle and source offset are set to 0, while the detector offset value is found in the subsequent step (rotation centre research).

After choosing the reconstruction algorithm, in our case the FDK algorithm, the rotation centre, expressed as pixel detector offset, could be found with the specific tool. It could be possible to perform the first automatic research using image metric parameters (in this case, the Shannon entropy or the image sharpness) in order to obtain the first idea of the offset, looking at the minimum of the curve that the software computes on the input data. Subsequently, manual

research can be performed by selecting an appropriate offset range. Looking at the preview reconstructed images of the chosen slice created by the tool based on different centres, one should select the one with the best reconstruction in terms of sharpness. The corresponding pixel offset is automatically added to the acquisition parameter window as the detector offset (green square in Figure B.1). Then, the input images for the flat field correction (white and dark) were loaded to compute the reconstruction (Figure B.1, blue square). In addition, several filters and artefact correction tools are present and can be used when necessary (for our study, no additional filters or corrections have been performed). Once all the required parameters are loaded, the reconstruction begins, and the resultant 32bit images are saved in a specific directory together with a log file containing reconstruction data and information.

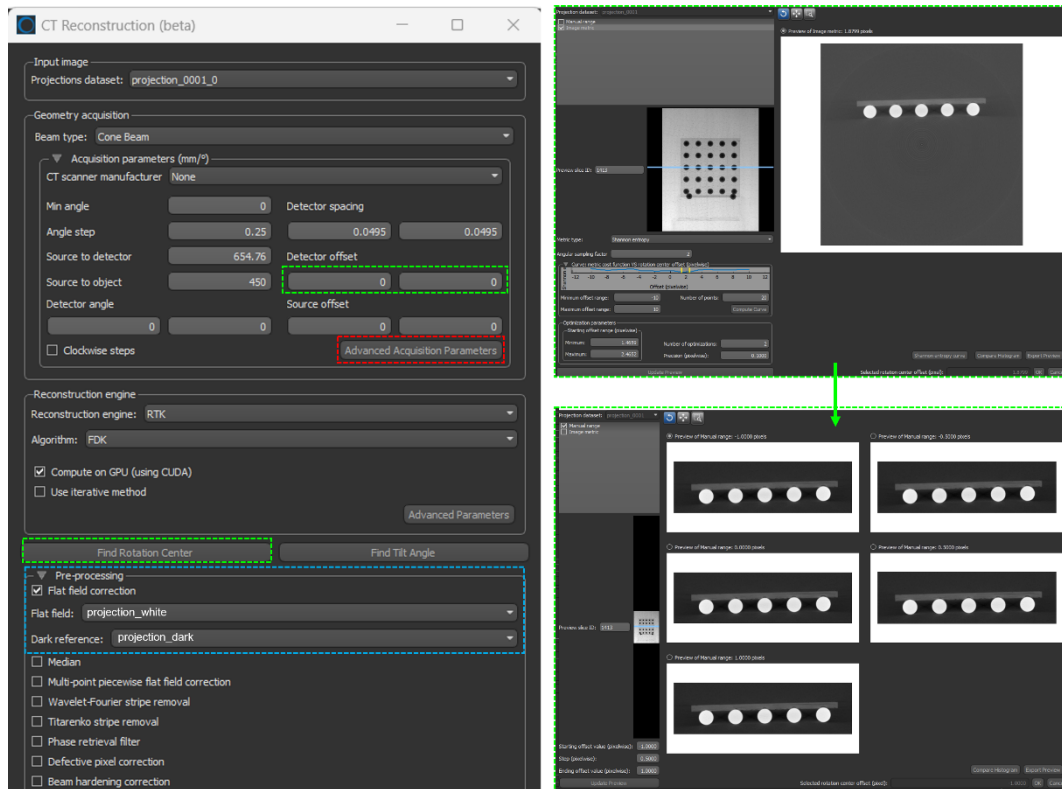


Figure B.1: Menus of the CT reconstruction tool in Dragonfly (left: principal window; right: rotation center definition window)

The reconstructed slices are then loaded in Dragonfly, that automatically read the image spacing (voxel dimension) from the saved log file. In this phase it could be possible to select and resize the slices (i.e., cutting off the useless empty volume, Figure B.2).

In Dragonfly, the reconstructed object is visualized in the three spatial direction and as a 3D volume; in the “Segment” menu, it can be possible to select a specific ROI based on histogram thresholding method, also using the Otsu algorithm, for the automatic segmentation of the spheres that have all the same gray level (Figure B.3).

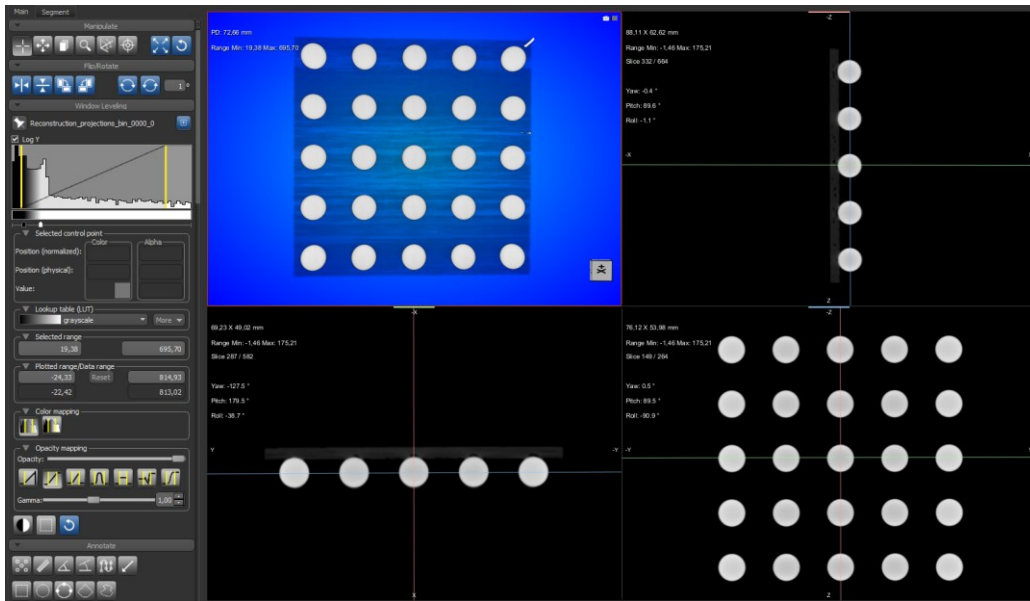


Figure B.2: Reconstructed slices visualization with 3D render model in Drgonfly.

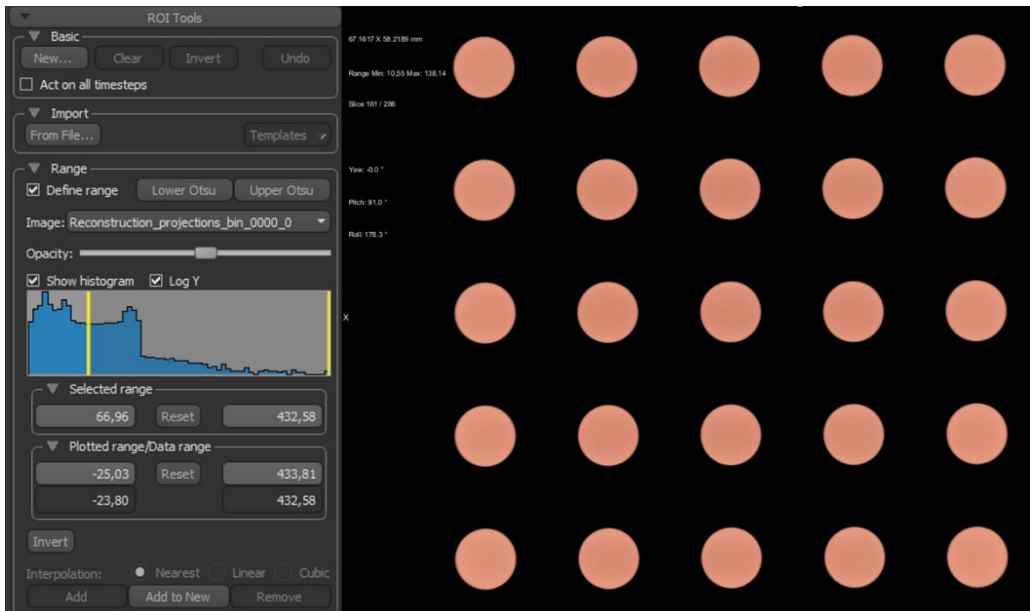


Figure B.3: Spheres segmentation using Otsu automatic algorithm in Dragonfly.

Subsequently, diving the created ROI in a Multi-ROI (Figure B.4), it can be possible to segment all the spheres separately (selecting the “Connected Components” option, where all the unconnected voxels of the ROI are considered distinct elements) and calculate the centroids, that results in 25 points with spatial coordinates (x, y, z), expressed in millimeters based on the voxel size, from which distances can be calculated through:

$$L_{CT} = \sqrt{(x_1 - x_2)^2 + (y_1 - y_2)^2 + (z_1 - z_2)^2}$$

If only one distance is needed (as in the case of ball bar), the two centroids' points can be selected and distance can be automatically calculated by the software (the used equation is the same).

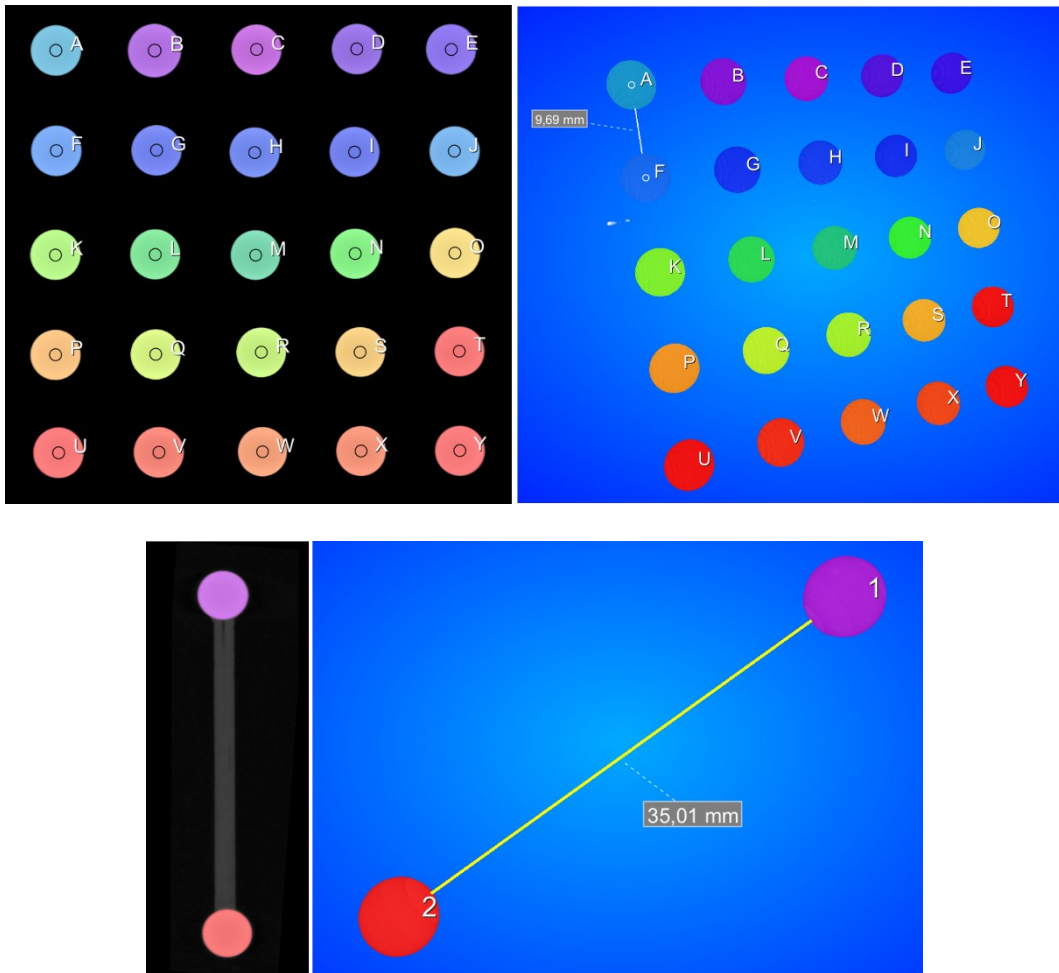


Figure B.4: Creation of the spheres multi-ROIs and examples of distance measurements in Dragonfly.

Since the voxel is the minimum unit of 3D objects, the uncertainty associated with L_{CT} is the equivalent of 1 voxel in millimeters. For the ball plates, the first test listed in section 4.2 results in the determination of a statistical error, which will be quadratically added to the voxel size to obtain the total error for each L_{CT} .

In addition, further analysis could be conducted both with Dragonfly and other image processing software, as Fiji, like the analysis of SNR and measurements with surface meshes.

Appendix C: Center-to-center spheres distances of the Ball plate

Table 1: Reference c-c spheres distances measured by ATOS Scanbox (± 0.002 mm)

L _{ref}	A	B	C	D	E	F	G	H	I	J	K	L	M	N	O	P	Q	R	S	T	U	V	W	X	
B	10.010																								
C	19.995	9.985																							
D	30.009	19.999	10.014																						
E	39.995	29.985	20.000	9.986																					
F	10.003	14.155	22.357	31.636	41.228																				
G	14.132	9.997	14.138	22.378	31.624	9.993																			
H	22.362	14.138	9.997	14.154	22.354	20.002	10.010																		
I	31.625	22.354	14.142	10.003	14.131	30.005	20.012	10.002																	
J	41.229	31.611	22.358	14.130	9.980	40.004	30.011	20.001	9.999																
K	20.003	22.361	28.265	36.051	44.698	10.000	14.127	22.344	31.608	41.218															
L	22.352	19.994	22.347	28.290	36.045	14.135	9.997	14.136	22.362	31.627	9.979														
M	28.291	22.362	19.995	22.366	28.271	22.370	14.159	9.999	14.139	22.360	19.989	10.011													
N	36.069	28.295	22.379	20.028	22.373	31.632	22.382	14.158	10.025	14.169	29.981	20.003	9.992												
O	44.717	36.044	28.280	22.357	19.991	41.229	31.629	22.356	14.137	10.011	39.977	29.998	19.988	9.996											
P	30.010	31.643	36.066	42.456	50.012	20.007	22.377	28.302	36.078	44.749	10.007	14.166	22.388	31.636	41.248										
Q	31.632	30.011	31.622	36.069	42.421	22.369	20.013	22.364	28.290	36.065	14.136	10.017	14.150	22.350	31.618	10.023									
R	36.043	31.614	29.994	31.637	36.059	28.268	22.359	19.997	22.373	28.310	22.322	14.134	9.999	14.141	22.378	19.996	9.973								
S	42.419	36.048	31.622	30.015	31.632	36.044	28.287	22.359	20.012	22.393	31.586	22.351	14.128	9.987	14.164	29.996	19.973	10.000							
T	50.012	42.432	36.064	31.632	29.998	44.735	36.079	28.294	22.370	20.017	41.224	31.640	22.365	14.137	10.006	40.030	30.007	20.034	10.034						
U	40.010	41.248	44.728	50.025	56.576	30.007	31.637	36.069	42.445	50.025	20.006	22.381	28.306	36.059	44.735	10.000	14.155	22.357	31.614	41.257					
V	41.248	40.018	41.239	44.742	50.001	31.638	30.021	31.634	36.068	42.444	22.366	20.025	22.376	28.275	36.058	14.163	10.008	14.134	22.338	31.633	10.019				
W	44.719	41.230	39.995	41.240	44.718	36.051	31.629	29.999	31.628	36.072	28.264	22.367	20.000	22.344	28.289	22.366	14.128	10.001	14.125	22.377	20.006	9.987			
X	50.014	44.729	41.233	40.006	41.220	42.442	36.078	31.629	30.003	31.630	36.056	28.308	22.367	19.978	22.353	31.657	22.372	14.174	9.991	14.134	30.034	20.015	10.029		
Y	56.579	50.010	44.738	41.257	40.022	50.007	42.447	36.070	31.646	30.041	44.704	36.066	28.288	22.359	20.030	41.240	31.612	22.381	14.161	10.024	40.000	29.981	19.994	9.966	

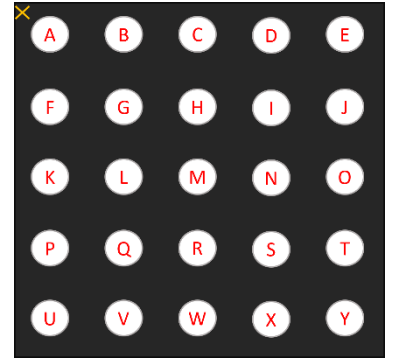


Table 2: CT c-c spheres distances of 150kV measurements, rep.1 **before and **after** correction (± 0.06 mm)**

L_{CT_1}	A	B	C	D	E	F	G	H	I	J	K	L	M	N	O	P	Q	R	S	T	U	V	W	X	Y
A		9.99	19.98	30.01	40.00	9.99	14.13	22.34	31.64	41.22	19.99	22.35	28.30	36.07	44.73	29.98	31.61	36.04	42.40	50.00	39.98	41.25	44.70	50.00	56.57
B	10.00		9.99	20.02	30.01	14.13	9.99	14.13	22.38	31.62	22.34	19.99	22.37	28.30	36.07	31.61	29.98	31.61	36.04	42.43	41.21	40.02	41.21	44.72	50.01
C	20.00	10.00		10.03	20.02	22.33	14.13	9.99	14.17	22.36	28.25	22.34	19.99	22.37	28.30	36.05	31.60	29.98	31.61	36.06	44.70	41.24	39.98	41.22	44.74
D	30.05	20.05	10.05		9.99	31.64	22.39	14.19	10.04	14.13	36.08	28.32	22.38	20.03	22.39	42.48	36.08	31.65	30.03	31.65	50.04	44.78	41.26	40.02	41.29
E	40.05	30.05	20.05	10.00		41.23	31.63	22.37	14.13	9.95	44.71	36.05	28.25	22.34	19.99	50.01	42.41	36.04	31.61	29.98	56.57	50.01	44.70	41.20	40.02
F	10.01	14.15	22.36	31.68	41.28		9.99	19.98	30.01	40.00	9.99	14.13	22.38	31.64	41.24	19.99	22.35	28.27	36.03	44.73	29.98	31.65	36.04	42.43	49.99
G	14.15	10.01	14.15	22.42	31.67	10.00		9.99	20.02	30.01	14.13	9.99	14.17	22.38	31.64	22.36	19.99	22.35	28.27	36.07	31.61	30.03	31.61	36.06	42.43
H	22.37	14.15	10.01	14.21	22.40	20.01	10.00		10.03	20.02	22.33	14.13	9.99	14.17	22.38	28.28	22.34	19.99	22.35	28.30	36.05	31.64	29.98	31.62	36.07
I	31.68	22.41	14.18	10.05	14.15	30.05	20.05	10.05		9.99	31.63	22.37	14.13	9.99	14.13	36.09	28.28	22.36	19.99	22.35	42.44	36.08	31.61	29.98	31.64
J	41.28	31.66	22.39	14.15	9.96	40.05	30.05	20.05	10.00		41.24	31.64	22.35	14.16	10.04	44.77	36.08	28.32	22.40	20.03	50.04	42.48	36.08	31.64	30.07
K	20.01	22.37	28.29	36.12	44.77	10.01	14.15	22.36	31.67	41.29		9.99	20.02	30.01	40.00	9.99	14.13	22.34	31.59	41.24	19.99	22.39	28.27	36.07	44.71
L	22.38	20.01	22.37	28.35	36.10	14.15	10.01	14.15	22.40	31.68	10.00		10.03	20.02	30.01	14.16	9.99	14.13	22.34	31.64	22.36	20.03	22.35	28.30	36.06
M	28.34	22.40	20.01	22.41	28.29	22.41	14.18	10.01	14.15	22.38	20.05	10.05		9.99	19.98	22.41	14.16	9.99	14.10	22.34	28.32	22.40	19.99	22.35	28.27
N	36.12	28.34	22.40	20.06	22.37	31.68	22.41	14.18	10.01	14.18	30.05	20.05	10.00		9.99	31.67	22.37	14.16	9.99	14.13	36.09	28.32	22.36	19.99	22.37
O	44.79	36.12	28.34	22.42	20.01	41.29	31.68	22.41	14.15	10.05	40.05	30.05	20.01	10.00		41.27	31.63	22.37	14.16	9.99	44.75	36.08	28.28	22.34	20.03
P	30.02	31.65	36.09	42.53	50.08	20.02	22.39	28.32	36.14	44.83	10.01	14.18	22.44	31.71	41.32		10.03	20.02	30.01	40.05	9.99	14.20	22.38	31.68	41.25
Q	31.65	30.02	31.64	36.13	42.47	22.38	20.02	22.37	28.32	36.12	14.15	10.01	14.18	22.40	31.67	10.05		9.99	19.98	30.01	14.16	10.04	14.13	22.38	31.61
R	36.08	31.65	30.02	31.70	36.09	28.31	22.38	20.01	22.39	28.35	22.37	14.15	10.01	14.18	22.40	20.05	10.00		9.99	20.02	22.37	14.16	9.99	14.17	22.36
S	42.46	36.08	31.65	30.07	31.65	36.08	28.31	22.38	20.01	22.43	31.64	22.37	14.12	10.01	14.18	30.05	20.00	10.00		10.03	31.63	22.35	14.13	10.00	14.17
T	50.07	42.49	36.11	31.69	30.02	44.79	36.12	28.34	22.38	20.06	41.29	31.68	22.37	14.15	10.01	40.10	30.05	20.05	10.05		41.27	31.64	22.37	14.13	10.04
U	40.03	41.27	44.76	50.11	56.65	30.02	31.66	36.09	42.50	50.11	20.02	22.39	28.36	36.14	44.81	10.01	14.18	22.40	31.67	41.32		10.03	20.02	30.06	40.00
V	41.31	40.07	41.30	44.84	50.08	31.69	30.07	31.68	36.13	42.53	22.42	20.06	22.43	28.35	36.12	14.22	10.05	14.18	22.38	31.68	10.05		9.99	20.02	29.97
W	44.76	41.27	40.03	41.31	44.76	36.09	31.65	30.02	31.65	36.13	28.31	22.38	20.02	22.39	28.32	22.41	14.15	10.01	14.15	22.40	20.05	10.00		10.03	19.98
X	50.07	44.78	41.28	40.07	41.25	42.49	36.11	31.66	30.02	31.68	36.12	28.34	22.38	20.01	22.37	31.72	22.41	14.18	10.01	14.15	30.10	20.05	10.05		9.94
Y	56.64	50.08	44.80	41.34	40.08	50.06	42.49	36.12	31.68	30.11	44.77	36.10	28.31	22.40	20.06	41.30	31.65	22.39	14.19	10.05	40.06	30.01	20.01	9.96	

Table 3: CT c-c spheres distances of 150kV measurements, rep.2 **before** and **after** correction (± 0.06 mm)

L _{CT_2}	A	B	C	D	E	F	G	H	I	J	K	L	M	N	O	P	Q	R	S	T	U	V	W	X	Y
A		10.03	20.01	30.04	40.02	9.99	14.15	22.39	31.63	41.26	20.02	22.37	28.31	36.09	44.71	30.00	31.62	36.04	42.43	50.02	39.99	41.26	44.70	50.03	56.61
B	10.05		9.98	20.01	29.99	14.15	10.03	14.15	22.35	31.63	22.38	20.01	22.37	28.31	36.03	31.64	30.00	31.61	36.05	42.43	41.23	40.03	41.20	44.74	50.04
C	20.05	10.00		10.03	20.01	22.34	14.15	9.99	14.12	22.37	28.27	22.34	19.97	22.37	28.24	36.05	31.59	29.96	31.61	36.04	44.69	41.22	39.94	41.21	44.74
D	30.10	20.05	10.05		9.98	31.64	22.40	14.15	9.98	14.12	36.07	28.30	22.34	20.01	22.31	42.45	36.04	31.60	30.00	31.61	50.00	44.73	41.19	39.98	41.25
E	40.10	30.05	20.05	10.00		41.24	31.65	22.36	14.15	9.99	44.72	36.07	28.27	22.38	19.97	50.02	42.42	36.05	31.64	30.00	56.57	50.01	44.69	41.22	40.03
F	10.00	14.18	22.38	31.70	41.31		9.98	20.01	29.99	40.02	10.03	14.15	22.39	31.64	41.22	20.01	22.37	28.27	36.05	44.73	30.00	31.66	36.04	42.46	50.04
G	14.18	10.05	14.18	22.44	31.71	10.00		10.03	20.01	30.04	14.12	9.99	14.15	22.39	31.62	22.34	19.97	22.33	28.27	36.06	31.59	30.00	31.58	36.07	42.46
H	22.43	14.18	10.00	14.18	22.40	20.05	10.05		9.98	20.01	22.36	14.15	9.99	14.15	22.33	28.30	22.34	19.97	22.35	28.27	36.05	31.63	29.96	31.62	36.08
I	31.69	22.39	14.15	10.00	14.18	30.05	20.05	10.00		10.03	31.61	22.36	14.12	10.03	14.12	36.07	28.27	22.34	20.01	22.37	42.42	36.06	31.59	30.00	31.66
J	41.34	31.69	22.41	14.15	10.00	40.10	30.10	20.05	10.05		41.25	31.65	22.36	14.18	9.98	44.76	36.07	28.30	22.40	20.01	50.02	42.45	36.05	31.63	30.05
K	20.05	22.43	28.32	36.14	44.81	10.05	14.15	22.40	31.67	41.33		9.98	20.01	29.99	39.98	9.98	14.12	22.33	31.59	41.22	19.97	22.37	28.24	36.06	44.73
L	22.41	20.05	22.39	28.35	36.14	14.18	10.00	14.18	22.40	31.71	10.00		10.03	20.01	30.00	14.15	9.99	14.12	22.35	31.63	22.34	20.02	22.33	28.31	36.09
M	28.36	22.41	20.01	22.39	28.32	22.43	14.18	10.00	14.15	22.40	20.05	10.05		9.98	19.97	22.40	14.15	9.98	14.12	22.35	28.30	22.38	19.97	22.37	28.31
N	36.16	28.36	22.41	20.05	22.43	31.70	22.43	14.18	10.05	14.21	30.05	20.05	10.00		9.98	31.64	22.34	14.12	9.98	14.12	36.04	28.27	22.30	19.97	22.37
O	44.80	36.09	28.30	22.35	20.01	41.30	31.68	22.37	14.15	10.00	40.05	30.05	20.00	10.00		41.25	31.61	22.36	14.18	10.03	44.72	36.06	28.27	22.36	20.06
P	30.06	31.70	36.11	42.53	50.12	20.05	22.39	28.35	36.14	44.85	10.00	14.18	22.44	31.70	41.33		10.03	20.01	29.99	40.02	9.99	14.18	22.37	31.67	41.27
Q	31.68	30.06	31.65	36.11	42.50	22.41	20.01	22.39	28.32	36.14	14.15	10.01	14.18	22.38	31.67	10.05		9.98	19.97	29.99	14.15	10.03	14.12	22.39	31.64
R	36.11	31.67	30.01	31.66	36.11	28.33	22.37	20.01	22.39	28.35	22.37	14.15	10.00	14.14	22.40	20.05	10.00		9.98	20.01	22.36	14.15	9.99	14.18	22.41
S	42.51	36.12	31.67	30.06	31.70	36.12	28.33	22.39	20.05	22.45	31.65	22.39	14.15	10.00	14.21	30.05	20.00	10.00		10.03	31.60	22.32	14.09	9.99	14.19
T	50.11	42.51	36.11	31.67	30.06	44.82	36.13	28.33	22.41	20.05	41.30	31.69	22.39	14.15	10.05	40.10	30.05	20.05	10.05		41.24	31.61	22.34	14.12	10.03
U	40.06	41.31	44.77	50.09	56.67	30.06	31.65	36.11	42.50	50.12	20.01	22.39	28.35	36.11	44.81	10.00	14.18	22.40	31.66	41.31		10.03	20.01	30.04	40.02
V	41.34	40.11	41.30	44.81	50.10	31.72	30.06	31.69	36.13	42.53	22.41	20.05	22.43	28.32	36.12	14.21	10.05	14.18	22.36	31.67	10.05		9.98	20.01	29.99
W	44.78	41.28	40.02	41.27	44.77	36.11	31.64	30.01	31.65	36.11	28.30	22.37	20.01	22.35	28.32	22.41	14.15	10.00	14.11	22.38	20.05	10.00		10.03	20.01
X	50.12	44.82	41.29	40.06	41.30	42.54	36.14	31.68	30.06	31.69	36.13	28.36	22.41	20.01	22.41	31.73	22.43	14.21	10.00	14.14	30.10	20.05	10.05		9.98
Y	56.72	50.13	44.82	41.33	40.11	50.14	42.54	36.15	31.72	30.10	44.82	36.16	28.36	22.41	20.10	41.35	31.70	22.45	14.21	10.05	40.10	30.05	20.05	10.00	

Table 4: CT c-c spheres distances of 150kV measurements, rep.3 **before** and **after** correction (± 0.06 mm)

L _{CT_3}	A	B	C	D	E	F	G	H	I	J	K	L	M	N	O	P	Q	R	S	T	U	V	W	X	Y
A		9.99	19.97	30.01	39.99	10.00	14.14	22.38	31.62	41.25	20.01	22.39	28.28	36.05	44.73	30.01	31.64	36.04	42.41	49.99	40.01	41.27	44.73	50.04	56.59
B	10.00		9.99	20.02	30.01	14.13	10.00	14.17	22.36	31.65	22.34	20.01	22.34	28.28	36.06	31.62	30.01	31.60	36.04	42.41	41.22	40.01	41.22	44.75	50.01
C	20.00	10.00		10.03	20.02	22.34	14.13	10.00	14.14	22.38	28.23	22.34	19.96	22.34	28.28	36.04	31.61	29.96	31.60	36.03	44.69	41.21	39.96	41.23	44.73
D	30.05	20.05	10.05		9.99	31.64	22.40	14.16	10.00	14.14	36.05	28.30	22.36	20.01	22.34	42.46	36.08	31.62	30.01	31.60	50.01	44.73	41.22	40.01	41.26
E	40.05	30.05	20.05	10.00		41.23	31.64	22.36	14.13	9.96	44.69	36.05	28.26	22.36	19.96	50.02	42.43	36.04	31.62	29.96	56.56	49.99	44.69	41.21	40.01
F	10.02	14.15	22.37	31.69	41.29		9.99	20.02	30.01	40.04	10.00	14.17	22.36	31.62	41.25	20.00	22.38	28.28	36.05	44.73	30.01	31.66	36.07	42.48	50.02
G	14.16	10.02	14.15	22.43	31.69	10.00		10.03	20.02	30.05	14.10	10.00	14.14	22.36	31.65	22.36	20.01	22.34	28.28	36.06	31.61	30.01	31.62	36.09	42.45
H	22.42	14.19	10.02	14.18	22.39	20.05	10.05		9.99	20.02	22.34	14.13	9.96	14.11	22.34	28.30	22.36	19.96	22.32	28.24	36.04	31.61	29.96	31.62	36.04
I	31.67	22.39	14.16	10.02	14.15	30.05	20.05	10.00		10.03	31.60	22.36	14.13	10.00	14.14	36.08	28.30	22.36	20.01	22.34	42.43	36.06	31.61	30.01	31.65
J	41.31	31.69	22.42	14.16	9.97	40.10	30.10	20.05	10.05		41.24	31.66	22.40	14.20	10.00	44.79	36.11	28.33	22.42	20.01	50.04	42.46	36.08	31.65	30.05
K	20.03	22.37	28.27	36.10	44.76	10.02	14.12	22.37	31.64	41.30		9.99	19.97	29.96	39.99	10.00	14.14	22.32	31.58	41.21	20.01	22.39	28.28	36.08	44.71
L	22.42	20.03	22.37	28.34	36.10	14.19	10.02	14.15	22.39	31.70	10.00		9.99	19.97	30.01	14.16	10.00	14.11	22.32	31.61	22.36	20.01	22.34	28.31	36.05
M	28.32	22.37	19.99	22.39	28.30	22.39	14.16	9.97	14.15	22.43	20.00	10.00		9.99	20.02	22.40	14.16	10.00	14.14	22.36	28.30	22.38	20.01	22.41	28.31
N	36.10	28.32	22.37	20.03	22.39	31.67	22.40	14.13	10.02	14.22	30.01	20.00	10.00		10.03	31.64	22.36	14.13	10.00	14.14	36.05	28.27	22.34	20.01	22.39
O	44.79	36.11	28.32	22.38	19.99	41.31	31.70	22.38	14.16	10.02	40.05	30.05	20.05	10.05		41.29	31.65	22.40	14.19	10.00	44.75	36.07	28.30	22.38	20.05
P	30.05	31.67	36.09	42.52	50.09	20.03	22.39	28.34	36.13	44.86	10.02	14.18	22.43	31.69	41.35		10.03	20.02	30.01	40.04	10.00	14.20	22.40	31.71	41.26
Q	31.69	30.05	31.65	36.13	42.49	22.41	20.03	22.39	28.34	36.16	14.16	10.02	14.18	22.39	31.70	10.05		9.99	19.97	30.01	14.13	10.00	14.14	22.40	31.62
R	36.10	31.65	30.01	31.67	36.09	28.32	22.38	19.99	22.39	28.37	22.36	14.13	10.02	14.15	22.43	20.05	10.00		9.99	20.02	22.36	14.13	10.00	14.20	22.38
S	42.47	36.09	31.65	30.05	31.67	36.10	28.32	22.35	20.03	22.45	31.62	22.35	14.16	10.02	14.21	30.05	20.00	10.00		10.03	31.60	22.32	14.10	10.00	14.17
T	50.07	42.48	36.08	31.65	30.01	44.79	36.11	28.29	22.38	20.03	41.27	31.65	22.40	14.16	10.02	40.10	30.05	20.05	10.05		41.24	31.61	22.36	14.13	10.05
U	40.07	41.28	44.76	50.08	56.64	30.05	31.65	36.09	42.49	50.12	20.03	22.39	28.34	36.10	44.82	10.02	14.15	22.39	31.64	41.30		10.03	20.02	30.05	39.99
V	41.33	40.07	41.27	44.80	50.06	31.70	30.05	31.65	36.11	42.52	22.42	20.03	22.41	28.31	36.12	14.22	10.02	14.15	22.35	31.66	10.05		9.99	20.02	29.96
W	44.79	41.28	40.02	41.28	44.76	36.12	31.66	30.01	31.65	36.13	28.32	22.37	20.03	22.37	28.34	22.44	14.16	10.02	14.12	22.39	20.05	10.00		10.03	19.97
X	50.11	44.81	41.29	40.07	41.27	42.54	36.15	31.66	30.05	31.70	36.14	28.35	22.44	20.04	22.41	31.75	22.44	14.22	10.02	14.15	30.10	20.05	10.05		9.94
Y	56.67	50.09	44.79	41.31	40.07	50.09	42.51	36.10	31.69	30.10	44.77	36.10	28.35	22.42	20.08	41.32	31.67	22.42	14.19	10.06	40.05	30.01	20.00	9.96	

Table 5: CT c-c spheres distances of orientation measurements, horizontal **before** and **after** correction (± 0.05 mm)

LCT_hor	A	B	C	D	E	F	G	H	I	J	K	L	M	N	O	P	Q	R	S	T	U	V	W	X	Y
A		10.03	19.99	30.02	40.02	10.00	14.14	22.37	31.63	41.23	19.99	22.34	28.28	36.08	44.72	29.99	31.63	36.07	42.42	50.02	40.02	41.24	44.73	50.01	56.58
B	10.04		9.96	19.99	29.99	14.16	10.00	14.12	22.34	31.59	22.35	19.96	22.33	28.28	36.03	31.61	29.99	31.62	36.02	42.42	41.25	39.99	41.22	44.70	49.99
C	20.01	9.97		10.03	20.03	22.36	14.16	10.00	14.16	22.37	28.27	22.34	20.00	22.40	28.30	36.05	31.63	30.03	31.63	36.09	44.75	41.23	40.02	41.24	44.76
D	30.04	20.01	10.04		10.00	31.65	22.39	14.14	10.00	14.12	36.06	28.27	22.35	20.03	22.36	42.43	36.07	31.64	29.99	31.63	50.03	44.72	41.25	39.99	41.25
E	40.05	30.01	20.04	10.00		41.25	31.65	22.35	14.14	9.96	44.71	36.04	28.27	22.38	20.00	50.00	42.43	36.07	31.61	29.99	56.59	49.98	44.73	41.21	40.02
F	10.00	14.17	22.38	31.67	41.28		10.00	20.03	30.02	40.02	10.00	14.14	22.37	31.65	41.24	20.00	22.37	28.30	36.06	44.76	30.03	31.64	36.07	42.44	50.02
G	14.15	10.00	14.17	22.41	31.67	10.00		10.03	20.03	30.02	14.11	9.96	14.14	22.38	31.63	22.34	19.99	22.37	28.28	36.08	31.63	29.99	31.63	36.06	42.44
H	22.39	14.13	10.01	14.15	22.37	20.04	10.04		10.00	19.99	22.36	14.14	10.00	14.16	22.36	28.29	22.38	20.03	22.36	28.30	36.10	31.63	30.03	31.63	36.08
I	31.66	22.36	14.18	10.00	14.15	30.04	20.04	10.00		10.00	31.62	22.35	14.14	10.03	14.14	36.06	28.29	22.38	19.99	22.37	42.45	36.05	31.64	29.99	31.65
J	41.26	31.61	22.39	14.13	9.97	40.05	30.04	20.01	10.00		41.23	31.62	22.36	14.18	10.03	44.73	36.08	28.32	22.38	20.03	50.04	42.43	36.10	31.63	30.06
K	20.01	22.37	28.29	36.08	44.75	10.01	14.12	22.38	31.64	41.26		10.00	19.99	29.99	39.98	10.00	14.14	22.35	31.60	41.24	20.03	22.37	28.28	36.06	44.71
L	22.36	19.98	22.35	28.29	36.06	14.15	9.97	14.15	22.37	31.64	10.00		10.00	19.99	29.99	14.16	10.03	14.16	22.36	31.64	22.41	20.03	22.39	28.30	36.06
M	28.30	22.34	20.01	22.37	28.29	22.39	14.15	10.00	14.15	22.38	20.01	10.00		10.00	19.99	22.36	14.16	10.03	14.14	22.38	28.32	22.37	20.03	22.37	28.30
N	36.10	28.30	22.42	20.04	22.40	31.67	22.40	14.17	10.04	14.19	30.01	20.01	10.00		10.00	31.61	22.35	14.14	9.96	14.14	36.06	28.25	22.35	19.96	22.36
O	44.76	36.05	28.32	22.37	20.01	41.27	31.66	22.37	14.15	10.04	40.01	30.01	20.01	10.00		41.22	31.62	22.36	14.14	10.00	44.73	36.03	28.29	22.34	20.03
P	30.01	31.63	36.08	42.46	50.03	20.01	22.35	28.32	36.08	44.76	10.00	14.17	22.38	31.63	41.25		10.00	19.99	29.99	40.02	10.03	14.16	22.35	31.63	41.22
Q	31.65	30.01	31.66	36.09	42.46	22.39	20.01	22.40	28.31	36.10	14.15	10.04	14.17	22.37	31.64	10.00		10.00	19.99	30.02	14.16	10.00	14.14	22.37	31.61
R	36.09	31.64	30.05	31.67	36.09	28.32	22.39	20.04	22.40	28.34	22.37	14.17	10.04	14.15	22.38	20.01	10.00		10.00	20.03	22.36	14.11	10.00	14.14	22.35
S	42.45	36.05	31.65	30.01	31.63	36.08	28.30	22.37	20.01	22.40	31.63	22.37	14.15	9.97	14.15	30.01	20.01	10.00		10.03	31.63	22.33	14.16	10.00	14.16
T	50.06	42.45	36.11	31.65	30.01	44.79	36.11	28.32	22.39	20.04	41.27	31.67	22.40	14.15	10.00	40.05	30.04	20.04	10.04		41.26	31.62	22.39	14.14	10.03
U	40.05	41.28	44.78	50.07	56.63	30.05	31.66	36.12	42.48	50.07	20.04	22.43	28.34	36.08	44.76	10.04	14.17	22.38	31.65	41.29		10.03	19.99	30.02	39.98
V	41.27	40.02	41.26	44.75	50.02	31.66	30.01	31.66	36.07	42.46	22.39	20.04	22.38	28.27	36.05	14.17	10.01	14.12	22.35	31.64	10.04		9.96	19.99	29.95
W	44.76	41.25	40.05	41.28	44.77	36.09	31.65	30.05	31.67	36.12	28.30	22.40	20.04	22.37	28.32	22.37	14.15	10.00	14.17	22.41	20.01	9.97		10.03	19.99
X	50.04	44.73	41.27	40.02	41.24	42.47	36.08	31.65	30.01	31.66	36.08	28.32	22.39	19.98	22.35	31.66	22.39	14.15	10.00	14.15	30.04	20.01	10.04		9.96
Y	56.62	50.03	44.79	41.28	40.05	50.05	42.47	36.10	31.67	30.08	44.74	36.09	28.32	22.37	20.04	41.25	31.64	22.37	14.17	10.04	40.01	29.97	20.01	9.97	

Table 6: CT c-c spheres distances of orientation measurements, vertical and spot S **before** and **after** correction (± 0.05 mm)

L _{CT_ver}	A	B	C	D	E	F	G	H	I	J	K	L	M	N	O	P	Q	R	S	T	U	V	W	X	Y
A		10.01	19.98	30.02	39.99	10.00	14.11	22.38	31.64	41.22	20.01	22.36	28.28	36.07	44.70	30.01	31.62	36.03	42.41	50.01	40.02	41.23	44.71	50.03	56.58
B	10.01		9.97	20.01	29.99	14.14	9.97	14.14	22.36	31.60	22.34	19.97	22.33	28.28	36.02	31.62	29.98	31.58	36.03	42.42	41.23	39.98	41.20	44.73	49.99
C	19.99	9.98		10.04	20.01	22.34	14.14	10.00	14.16	22.36	28.25	22.34	19.97	22.37	28.28	36.05	31.61	29.98	31.62	36.07	44.73	41.22	39.98	41.25	44.74
D	30.03	20.02	10.05		9.97	31.65	22.40	14.16	10.00	14.11	36.06	28.30	22.35	20.01	22.34	42.46	36.07	31.63	30.01	31.62	50.04	44.74	41.23	40.02	41.26
E	40.01	30.00	20.02	9.98		41.22	31.64	22.34	14.11	9.97	44.69	36.04	28.25	22.34	19.97	50.00	42.41	36.04	31.62	29.98	56.57	49.99	44.70	41.22	40.02
F	10.01	14.14	22.35	31.66	41.24		9.97	20.01	30.02	39.99	10.01	14.14	22.36	31.64	41.22	20.01	22.36	28.25	36.04	44.73	30.01	31.62	36.05	42.46	50.00
G	14.12	9.97	14.14	22.41	31.65	9.98		10.04	20.05	30.02	14.12	10.00	14.16	22.41	31.64	22.37	20.01	22.36	28.30	36.10	31.64	30.01	31.63	36.11	42.46
H	22.39	14.15	10.01	14.17	22.35	20.02	10.05		10.01	19.98	22.35	14.14	9.97	14.14	22.33	28.30	22.36	19.98	22.34	28.28	36.07	31.62	29.98	31.63	36.06
I	31.65	22.37	14.17	10.01	14.12	30.03	20.06	10.01		9.97	31.62	22.37	14.14	10.00	14.11	36.08	28.30	22.37	20.01	22.36	42.46	36.07	31.62	30.01	31.64
J	41.27	31.64	22.40	14.15	9.98	40.05	30.07	20.02	10.01		41.20	31.61	22.34	14.14	10.00	44.73	36.06	28.30	22.39	20.01	50.02	42.44	36.05	31.63	30.05
K	20.02	22.35	28.26	36.08	44.71	10.01	14.12	22.36	31.63	41.25		9.97	19.98	29.99	39.96	10.00	14.11	22.30	31.57	41.22	20.01	22.34	28.25	36.07	44.69
L	22.37	19.98	22.35	28.31	36.05	14.15	10.01	14.14	22.38	31.66	9.98		10.01	20.01	29.99	14.16	10.01	14.11	22.34	31.64	22.39	20.01	22.36	28.32	36.06
M	28.31	22.37	20.02	22.39	28.29	22.39	14.19	10.01	14.17	22.40	19.99	10.01		10.01	19.98	22.39	14.16	10.01	14.14	22.37	28.32	22.39	20.01	22.40	28.30
N	36.09	28.29	22.38	20.02	22.35	31.65	22.42	14.14	10.01	14.17	30.00	20.02	10.01		9.97	31.65	22.37	14.16	10.00	14.14	36.08	28.30	22.36	20.01	22.37
O	44.73	36.04	28.29	22.35	19.98	41.24	31.65	22.34	14.12	10.01	39.98	30.00	19.99	9.98		41.23	31.62	22.37	14.16	10.00	44.73	36.06	28.28	22.36	20.04
P	30.03	31.64	36.07	42.48	50.02	20.02	22.38	28.31	36.10	44.78	10.01	14.17	22.39	31.66	41.25		10.01	19.98	29.99	40.03	10.00	14.14	22.36	31.67	41.22
Q	31.64	29.99	31.62	36.09	42.43	22.37	20.02	22.37	28.31	36.10	14.12	10.01	14.15	22.39	31.63	10.01		9.97	19.98	30.02	14.16	10.00	14.14	22.41	31.62
R	36.04	31.59	29.99	31.65	36.06	28.27	22.37	19.99	22.38	28.34	22.31	14.12	9.98	14.17	22.39	19.99	9.98		10.01	20.05	22.36	14.14	10.00	14.21	22.39
S	42.43	36.04	31.64	30.03	31.64	36.06	28.31	22.35	20.02	22.41	31.59	22.35	14.12	10.01	14.17	30.00	19.99	10.01		10.04	31.61	22.34	14.11	10.00	14.16
T	50.03	42.44	36.08	31.64	29.99	44.76	36.11	28.29	22.37	20.02	41.24	31.65	22.37	14.15	10.01	40.05	30.04	20.06	10.05		41.27	31.65	22.37	14.14	10.04
U	40.04	41.25	44.75	50.06	56.60	30.03	31.66	36.09	42.48	50.07	20.02	22.40	28.31	36.10	44.76	10.01	14.17	22.37	31.63	41.29		10.01	20.01	30.05	39.99
V	41.25	40.00	41.24	44.76	50.01	31.64	30.03	31.64	36.09	42.48	22.35	20.02	22.37	28.31	36.08	14.14	10.01	14.14	22.35	31.66	10.01		10.01	20.05	29.99
W	44.73	41.22	40.00	41.25	44.72	36.06	31.65	29.99	31.64	36.09	28.27	22.37	19.99	22.37	28.29	22.37	14.15	10.01	14.12	22.39	20.02	10.01		10.04	19.98
X	50.06	44.75	41.27	40.04	41.24	42.48	36.13	31.65	30.03	31.66	36.09	28.34	22.38	20.02	22.37	31.69	22.42	14.22	10.01	14.14	30.07	20.06	10.05		9.94
Y	56.60	50.02	44.77	41.28	40.04	50.03	42.48	36.07	31.66	30.06	44.71	36.08	28.29	22.38	20.05	41.24	31.63	22.40	14.17	10.04	40.01	30.00	19.99	9.94	

Table 7: CT c-c spheres distances of orientation measurements, tilted **before** and **after** correction (± 0.05 mm)

L_{CT_til}	A	B	C	D	E	F	G	H	I	J	K	L	M	N	O	P	Q	R	S	T	U	V	W	X	Y
A		10.03	20.00	30.03	40.03	10.04	14.15	22.39	31.64	41.25	20.03	22.36	28.32	36.09	44.74	30.03	31.66	36.08	42.46	50.04	40.04	41.29	44.73	50.02	56.60
B	10.04		9.96	20.00	29.99	14.15	9.99	14.12	22.34	31.60	22.36	19.96	22.35	28.27	36.03	31.62	30.00	31.60	36.04	42.42	41.25	40.01	41.20	44.69	49.99
C	20.01	9.97		10.03	20.03	22.33	14.13	9.97	14.13	22.37	28.26	22.31	19.99	22.36	28.28	36.03	31.61	29.98	31.62	36.06	44.72	41.23	39.97	41.20	44.73
D	30.04	20.01	10.04		10.00	31.63	22.39	14.13	9.97	14.12	36.06	28.27	22.37	20.01	22.35	42.43	36.07	31.62	30.01	31.61	50.02	44.73	41.22	39.97	41.25
E	40.05	30.01	20.04	10.00		41.23	31.65	22.35	14.12	9.97	44.72	36.04	28.29	22.37	19.99	50.00	42.43	36.05	31.63	29.98	56.59	50.00	44.71	41.19	40.02
F	10.04	14.15	22.34	31.64	41.25		9.96	20.00	29.99	39.99	9.99	14.11	22.35	31.61	41.21	19.99	22.35	28.26	36.04	44.72	30.01	31.64	36.02	42.40	49.99
G	14.16	10.00	14.14	22.40	31.67	9.97		10.03	20.03	30.03	14.12	9.97	14.16	22.39	31.64	22.35	20.01	22.36	28.30	36.09	31.64	30.02	31.61	36.06	42.45
H	22.40	14.13	9.98	14.14	22.36	20.01	10.04		10.00	20.00	22.37	14.13	10.02	14.15	22.36	28.30	22.38	20.01	22.38	28.30	36.09	31.65	30.00	31.61	36.07
I	31.66	22.35	14.14	9.98	14.13	30.01	20.04	10.00		10.00	31.63	22.36	14.17	10.04	14.15	36.08	28.31	22.38	20.04	22.38	42.47	36.09	31.64	30.00	31.66
J	41.27	31.62	22.38	14.13	9.98	40.01	30.04	20.01	10.00		41.23	31.62	22.37	14.17	10.02	44.73	36.08	28.30	22.39	20.01	50.03	42.44	36.07	31.61	30.04
K	20.04	22.37	28.27	36.08	44.75	9.99	14.13	22.38	31.65	41.26		10.00	20.00	29.99	39.99	10.00	14.14	22.35	31.61	41.25	20.02	22.39	28.26	36.05	44.71
L	22.38	19.97	22.32	28.28	36.06	14.11	9.98	14.14	22.37	31.64	10.00		10.00	20.00	29.99	14.17	10.04	14.15	22.37	31.65	22.41	20.05	22.37	28.30	36.07
M	28.33	22.36	20.00	22.38	28.30	22.36	14.17	10.02	14.17	22.39	20.01	10.00		10.00	20.00	22.36	14.15	9.99	14.14	22.37	28.30	22.37	19.98	22.34	28.29
N	36.11	28.29	22.38	20.02	22.38	31.63	22.40	14.16	10.04	14.17	30.01	20.01	10.00		10.00	31.62	22.36	14.13	10.00	14.14	36.07	28.28	22.34	19.96	22.37
O	44.77	36.05	28.30	22.36	20.00	41.24	31.66	22.37	14.16	10.02	40.01	30.01	20.01	10.00		41.23	31.63	22.36	14.15	9.99	44.73	36.05	28.28	22.33	20.03
P	30.04	31.64	36.05	42.46	50.03	20.00	22.36	28.32	36.09	44.76	10.01	14.17	22.37	31.64	41.25		10.00	20.00	29.99	40.03	10.02	14.18	22.34	31.63	41.22
Q	31.67	30.01	31.63	36.09	42.46	22.36	20.02	22.40	28.33	36.09	14.15	10.04	14.15	22.37	31.64	10.00		10.00	20.00	30.03	14.15	10.02	14.12	22.37	31.62
R	36.10	31.62	29.99	31.64	36.07	28.28	22.38	20.02	22.40	28.32	22.36	14.16	9.99	14.14	22.37	20.01	10.00		10.00	20.03	22.37	14.14	9.99	14.14	22.37
S	42.48	36.06	31.64	30.02	31.65	36.06	28.32	22.39	20.05	22.40	31.63	22.38	14.15	10.01	14.16	30.01	20.01	10.00		10.03	31.63	22.34	14.13	9.96	14.15
T	50.07	42.44	36.08	31.63	29.99	44.75	36.11	28.31	22.39	20.02	41.27	31.67	22.39	14.15	9.99	40.05	30.04	20.04	10.04		41.27	31.63	22.39	14.13	10.04
U	40.06	41.27	44.74	50.05	56.62	30.02	31.65	36.11	42.49	50.06	20.03	22.42	28.32	36.08	44.76	10.02	14.16	22.39	31.64	41.29		10.03	20.00	30.03	39.99
V	41.31	40.04	41.25	44.76	50.03	31.66	30.04	31.67	36.11	42.46	22.40	20.06	22.38	28.29	36.07	14.18	10.02	14.15	22.35	31.65	10.04		9.96	20.00	29.96
W	44.75	41.22	39.99	41.24	44.73	36.04	31.63	30.01	31.65	36.09	28.28	22.38	19.99	22.35	28.30	22.36	14.13	9.99	14.13	22.40	20.01	9.97		10.03	20.00
X	50.04	44.71	41.22	39.99	41.21	42.43	36.08	31.63	30.01	31.63	36.07	28.31	22.35	19.97	22.34	31.65	22.38	14.15	9.97	14.14	30.04	20.01	10.04		9.96
Y	56.63	50.02	44.75	41.27	40.04	50.01	42.47	36.09	31.68	30.06	44.74	36.09	28.30	22.38	20.04	41.24	31.63	22.38	14.15	10.04	40.01	29.98	20.01	9.97	

Table 8: CT c-c spheres distances of focal spot size measurements, spot M **before** and **after** correction (± 0.05 mm)

s_M	A	B	C	D	E	F	G	H	I	J	K	L	M	N	O	P	Q	R	S	T	U	V	W	X	Y
A		10.01	19.98	30.02	39.99	10.00	14.14	22.36	31.64	41.25	19.97	22.35	28.27	36.07	44.70	30.01	31.62	36.02	42.41	50.01	40.01	41.23	44.71	50.00	56.57
B	10.01		9.97	20.01	29.98	14.16	10.00	14.14	22.37	31.64	22.34	20.01	22.35	28.30	36.04	31.65	30.01	31.61	36.05	42.44	41.26	40.02	41.23	44.73	50.02
C	19.99	9.98		10.04	20.01	22.34	14.11	9.97	14.16	22.39	28.23	22.34	19.97	22.37	28.27	36.05	31.61	29.98	31.62	36.06	44.72	41.22	39.98	41.21	44.74
D	30.03	20.02	10.05		9.97	31.64	22.37	14.13	10.00	14.14	36.04	28.30	22.35	20.01	22.34	42.46	36.07	31.63	30.01	31.62	50.03	44.74	41.23	39.98	41.26
E	40.01	30.00	20.02	9.98		41.23	31.61	22.34	14.14	10.00	44.69	36.05	28.27	22.37	20.01	50.02	42.43	36.07	31.65	30.01	56.59	50.01	44.72	41.21	40.05
F	10.01	14.17	22.35	31.66	41.25		10.01	20.01	30.02	40.02	9.97	14.14	22.36	31.64	41.21	20.01	22.36	28.25	36.04	44.73	30.01	31.62	36.04	42.44	50.00
G	14.15	10.01	14.12	22.38	31.63	10.01		10.01	20.01	30.02	14.11	10.00	14.14	22.37	31.60	22.38	20.01	22.34	28.27	36.07	31.65	30.01	31.62	36.06	42.44
H	22.37	14.15	9.97	14.14	22.35	20.02	10.01		10.00	20.01	22.34	14.16	10.00	14.16	22.34	28.32	22.39	20.01	22.37	28.30	36.10	31.65	30.01	31.63	36.08
I	31.65	22.39	14.17	10.01	14.14	30.03	20.02	10.01		10.01	31.60	22.37	14.13	10.00	14.11	36.08	28.30	22.37	20.01	22.35	42.46	36.07	31.62	29.98	31.64
J	41.27	31.65	22.40	14.15	10.01	40.05	30.03	20.02	10.01		41.22	31.64	22.37	14.16	10.00	44.76	36.08	28.32	22.40	20.01	50.04	42.46	36.07	31.61	30.05
K	19.99	22.35	28.24	36.06	44.71	9.98	14.12	22.36	31.62	41.25		9.97	19.98	29.98	39.96	10.04	14.14	22.31	31.58	41.22	20.04	22.37	28.27	36.07	44.70
L	22.37	20.02	22.35	28.31	36.07	14.15	10.01	14.17	22.38	31.66	9.98		10.01	20.01	29.98	14.16	10.00	14.11	22.34	31.64	22.38	20.01	22.36	28.30	36.06
M	28.29	22.37	19.98	22.36	28.29	22.37	14.15	10.01	14.14	22.38	19.99	10.01		10.00	19.98	22.39	14.16	10.00	14.14	22.37	28.32	22.39	20.01	22.37	28.30
N	36.09	28.31	22.38	20.02	22.38	31.65	22.39	14.17	10.01	14.17	30.00	20.02	10.01		9.97	31.64	22.37	14.16	10.00	14.14	36.08	28.30	22.35	19.97	22.37
O	44.73	36.06	28.29	22.35	20.02	41.24	31.62	22.35	14.12	10.01	39.98	30.00	19.99	9.98			31.61	22.37	14.16	10.00	44.73	36.06	28.27	22.32	20.04
P	30.03	31.67	36.07	42.48	50.04	20.02	22.40	28.34	36.10	44.78	10.04	14.17	22.40	31.66	41.25		10.00	19.98	29.98	40.02	10.00	14.14	22.36	31.66	41.22
Q	31.64	30.03	31.62	36.09	42.46	22.37	20.02	22.40	28.31	36.10	14.14	10.01	14.17	22.39	31.63	10.01		9.97	19.98	30.02	14.16	10.00	14.14	22.39	31.61
R	36.04	31.63	29.99	31.65	36.09	28.27	22.35	20.02	22.38	28.34	22.33	14.12	10.01	14.17	22.39	19.99	9.98		10.01	20.05	22.36	14.14	10.00	14.19	22.39
S	42.43	36.07	31.64	30.03	31.67	36.06	28.29	22.38	20.02	22.41	31.60	22.35	14.14	10.01	14.17	30.00	19.99	10.01		10.04	31.61	22.34	14.11	9.97	14.16
T	50.03	42.46	36.08	31.64	30.03	44.76	36.09	28.31	22.37	20.02	41.25	31.65	22.39	14.15	10.01	40.05	30.04	20.06	10.05		41.26	31.65	22.37	14.11	10.04
U	40.04	41.28	44.75	50.06	56.62	30.03	31.67	36.12	42.48	50.07	20.05	22.40	28.34	36.10	44.75	10.01	14.17	22.37	31.63	41.28		10.00	20.01	30.05	39.99
V	41.25	40.04	41.24	44.76	50.04	31.64	30.03	31.67	36.09	42.48	22.38	20.02	22.40	28.31	36.08	14.14	10.01	14.14	22.35	31.66	10.01		10.01	20.05	29.98
W	44.73	41.25	40.00	41.25	44.75	36.06	31.64	30.03	31.64	36.09	28.29	22.37	20.02	22.37	28.29	22.37	14.15	10.01	14.12	22.39	20.02	10.01		10.04	19.98
X	50.03	44.75	41.24	40.00	41.24	42.46	36.08	31.65	29.99	31.62	36.09	28.31	22.38	19.98	22.34	31.67	22.40	14.19	9.98	14.12	30.07	20.06	10.05		9.94
Y	56.60	50.04	44.77	41.28	40.07	50.03	42.46	36.10	31.66	30.06	44.73	36.08	28.31	22.38	20.05	41.24	31.63	22.40	14.17	10.04	40.01	30.00	19.99	9.94	

Table 9: CT c-c spheres distances of focal spot size measurements, spot L **before** and **after** correction (± 0.05 mm)

s_L	A	B	C	D	E	F	G	H	I	J	K	L	M	N	O	P	Q	R	S	T	U	V	W	X	Y
A		10.00	20.01	30.01	39.99	10.00	14.14	22.37	31.63	41.24	20.01	22.35	28.30	36.08	44.73	30.01	31.62	36.07	42.43	50.00	40.01	41.27	44.71	50.03	56.59
B	10.01		10.01	20.01	29.98	14.13	9.97	14.14	22.36	31.62	22.34	19.97	22.35	28.30	36.04	31.61	29.97	31.62	36.04	42.41	41.22	40.01	41.19	44.72	50.01
C	20.02	10.01		10.01	19.98	22.37	14.13	10.00	14.14	22.36	28.27	22.35	20.01	22.38	28.27	36.07	31.62	30.01	31.62	36.04	44.73	41.25	39.98	41.23	44.74
D	30.03	20.02	10.01		9.97	31.64	22.37	14.16	10.00	14.14	36.05	28.29	22.38	20.04	22.35	42.45	36.07	31.65	30.01	31.62	50.03	44.75	41.23	40.01	41.26
E	40.01	30.00	19.99	9.98		41.22	31.60	22.34	14.11	9.97	44.68	36.03	28.27	22.37	19.97	49.99	42.41	36.05	31.60	29.97	56.56	49.99	44.69	41.21	40.01
F	10.01	14.14	22.38	31.66	41.24		10.01	20.01	30.01	40.02	10.00	14.14	22.37	31.64	41.24	20.01	22.35	28.30	36.06	44.73	30.01	31.66	36.04	42.46	50.02
G	14.15	9.97	14.14	22.38	31.62	10.01		10.00	20.01	30.01	14.14	10.00	14.16	22.39	31.63	22.38	20.01	22.38	28.30	36.06	31.65	30.04	31.62	36.09	42.46
H	22.39	14.15	10.01	14.17	22.35	20.02	10.01		10.01	20.01	22.34	14.13	10.00	14.16	22.36	28.29	22.35	20.01	22.35	28.27	36.07	31.64	29.97	31.63	36.07
I	31.65	22.37	14.15	10.01	14.12	30.03	20.02	10.01		10.01	31.61	22.37	14.16	10.04	14.14	36.08	28.29	22.38	20.01	22.35	42.45	36.08	31.62	30.01	31.65
J	41.27	31.64	22.37	14.15	9.98	40.05	30.03	20.02	10.01		41.23	31.64	22.39	14.18	10.00	44.76	36.08	28.32	22.38	20.01	50.04	42.45	36.07	31.64	30.04
K	20.02	22.35	28.29	36.08	44.71	10.01	14.15	22.35	31.63	41.25		9.97	19.98	29.98	39.99	10.00	14.11	22.34	31.60	41.21	20.00	22.38	28.25	36.06	44.71
L	22.37	19.98	22.36	28.31	36.05	14.15	10.01	14.14	22.38	31.66	9.98		10.00	20.01	30.01	14.16	10.00	14.16	22.37	31.63	22.38	20.04	22.35	28.32	36.08
M	28.31	22.37	20.02	22.40	28.29	22.39	14.17	10.01	14.17	22.40	19.99	10.01		10.01	20.01	22.37	14.14	10.00	14.14	22.36	28.29	22.37	19.97	22.37	28.30
N	36.10	28.31	22.40	20.05	22.38	31.66	22.40	14.17	10.04	14.19	30.00	20.02	10.01		10.01	31.63	22.36	14.14	9.97	14.11	36.06	28.27	22.32	19.97	22.35
O	44.76	36.07	28.29	22.37	19.98	41.27	31.65	22.37	14.15	10.01	40.01	30.03	20.02	10.01		41.26	31.64	22.39	14.16	10.00	44.76	36.07	28.29	22.37	20.04
P	30.03	31.63	36.09	42.48	50.02	20.02	22.40	28.31	36.10	44.78	10.01	14.17	22.38	31.65	41.28		10.00	20.01	30.01	40.02	10.00	14.18	22.36	31.66	41.25
Q	31.64	29.99	31.64	36.09	42.43	22.37	20.02	22.37	28.31	36.10	14.12	10.01	14.14	22.37	31.66	10.01		10.01	20.01	30.02	14.16	10.04	14.14	22.40	31.64
R	36.09	31.64	30.03	31.67	36.07	28.31	22.40	20.02	22.40	28.34	22.36	14.17	10.01	14.14	22.40	20.02	10.01		10.01	20.01	22.37	14.14	9.97	14.16	22.37
S	42.46	36.06	31.64	30.03	31.62	36.09	28.31	22.37	20.02	22.40	31.62	22.39	14.15	9.97	14.17	30.03	20.02	10.01		10.01	31.64	22.36	14.14	10.00	14.16
T	50.03	42.44	36.06	31.64	29.99	44.76	36.09	28.29	22.37	20.02	41.24	31.65	22.37	14.12	10.01	40.05	30.04	20.02	10.01		41.26	31.62	22.37	14.14	10.04
U	40.04	41.25	44.76	50.06	56.60	30.03	31.67	36.09	42.48	50.07	20.02	22.40	28.31	36.08	44.78	10.01	14.17	22.38	31.66	41.28		10.04	20.01	30.05	40.02
V	41.29	40.04	41.28	44.78	50.02	31.68	30.06	31.66	36.10	42.48	22.40	20.05	22.38	28.29	36.09	14.19	10.04	14.14	22.37	31.64	10.04		9.97	20.01	29.98
W	44.73	41.22	40.00	41.25	44.72	36.06	31.64	29.99	31.64	36.09	28.27	22.37	19.98	22.34	28.31	22.37	14.15	9.97	14.14	22.39	20.02	9.98		10.04	20.01
X	50.06	44.75	41.26	40.04	41.24	42.48	36.11	31.65	30.03	31.66	36.09	28.34	22.38	19.98	22.38	31.69	22.42	14.17	10.01	14.14	30.07	20.02	10.05		9.97
Y	56.63	50.04	44.77	41.29	40.04	50.05	42.48	36.09	31.67	30.06	44.74	36.10	28.31	22.37	20.05	41.28	31.66	22.39	14.17	10.04	40.04	30.00	20.02	9.98	

Table 10: CT c-c spheres distances of n° of proj. measurements, no binning **before** and **after** correction (± 0.05 mm)

no bin	A	B	C	D	E	F	G	H	I	J	K	L	M	N	O	P	Q	R	S	T	U	V	W	X	Y
A		10.01	19.99	30.00	40.00	9.98	14.12	22.36	31.63	41.23	19.98	22.34	28.27	36.04	44.70	29.99	31.60	36.02	42.41	50.01	39.99	41.24	44.69	50.00	56.58
B	9.72		9.98	19.99	30.00	14.15	9.98	14.14	22.36	31.62	22.34	19.98	22.34	28.27	36.03	31.62	29.99	31.59	36.04	42.42	41.24	40.01	41.21	44.72	50.01
C	19.42	9.70		10.01	20.01	22.36	14.13	10.00	14.15	22.37	28.26	22.34	19.98	22.36	28.27	36.06	31.62	29.99	31.62	36.06	44.73	41.25	39.99	41.23	44.74
D	29.14	19.42	9.72		10.01	31.63	22.36	14.15	10.00	14.14	36.04	28.28	22.34	20.01	22.34	42.44	36.06	31.62	30.01	31.62	50.02	44.74	41.23	39.99	41.25
E	38.86	29.14	19.44	9.72		41.25	31.63	22.37	14.15	9.98	44.71	36.06	28.28	22.38	19.98	50.02	42.44	36.07	31.65	29.99	56.60	50.03	44.73	41.22	40.02
F	9.69	13.74	21.72	30.72	40.06		10.01	20.01	30.02	40.03	10.00	14.15	22.38	31.63	41.24	20.01	22.36	28.27	36.06	44.76	30.01	31.66	36.05	42.46	50.04
G	13.71	9.69	13.72	21.72	30.72	9.72		10.01	20.01	30.02	14.13	10.00	14.15	22.37	31.62	22.38	20.01	22.35	28.29	36.08	31.65	30.04	31.62	36.08	42.46
H	21.72	13.73	9.72	13.74	21.72	19.44	9.72		10.01	20.01	22.34	14.13	9.98	14.13	22.35	28.29	22.36	19.98	22.35	28.29	36.07	31.64	29.99	31.62	36.07
I	30.72	21.72	13.75	9.72	13.72	29.16	19.44	9.72		10.01	31.61	22.36	14.13	10.00	14.12	36.08	28.29	22.37	20.01	22.35	42.46	36.08	31.62	29.99	31.63
J	40.03	30.69	21.71	13.71	9.67	38.86	29.14	19.42	9.70		41.23	31.64	22.37	14.18	10.00	44.76	36.09	28.33	22.41	20.01	50.06	42.47	36.09	31.63	30.04
K	19.41	21.70	27.45	35.00	43.42	9.72	13.72	21.70	30.70	40.03		9.98	19.99	29.97	39.98	10.00	14.12	22.31	31.59	41.24	20.01	22.37	28.25	36.06	44.73
L	21.70	19.41	21.70	27.47	35.01	13.75	9.72	13.72	21.72	30.71	9.70		10.01	19.99	30.00	14.16	10.00	14.12	22.35	31.65	22.39	20.03	22.35	28.31	36.08
M	27.46	21.70	19.41	21.70	27.45	21.74	13.75	9.69	13.72	21.71	19.42	9.72		9.98	19.99	22.39	14.16	10.00	14.14	22.38	28.33	22.40	20.01	22.37	28.31
N	35.01	27.46	21.72	19.43	21.71	30.73	21.73	13.73	9.72	13.76	29.11	19.42	9.70		10.01	31.63	22.36	14.15	10.00	14.15	36.08	28.29	22.36	19.98	22.38
O	43.42	35.00	27.46	21.70	19.39	40.06	30.72	21.71	13.71	9.72	38.83	29.14	19.42	9.72		41.26	31.64	22.39	14.18	10.00	44.76	36.08	28.31	22.36	20.03
P	29.13	30.72	35.02	41.22	48.58	19.43	21.74	27.48	35.04	43.46	9.72	13.76	21.75	30.72	40.07		10.01	19.99	30.00	40.05	10.00	14.17	22.36	31.67	41.27
Q	30.70	29.13	30.71	35.02	41.21	21.72	19.43	21.71	27.48	35.04	13.71	9.72	13.76	21.72	30.73	9.72		9.98	19.99	30.05	14.16	10.03	14.14	22.40	31.66
R	34.99	30.69	29.13	30.72	35.02	27.46	21.71	19.41	21.73	27.50	21.67	13.71	9.72	13.74	21.75	19.42	9.70		10.01	20.06	22.37	14.15	10.00	14.19	22.41
S	41.19	35.01	30.72	29.15	30.72	35.02	27.48	21.71	19.43	21.76	30.68	21.71	13.73	9.72	13.78	29.14	19.42	9.72		10.06	31.63	22.35	14.13	9.98	14.17
T	48.55	41.19	35.01	30.70	29.10	43.45	35.03	27.46	21.70	19.43	40.04	30.72	21.72	13.73	9.72	38.88	29.16	19.46	9.74		41.30	31.67	22.42	14.15	10.03
U	38.84	40.06	43.45	48.59	54.96	29.15	30.74	35.04	41.24	48.60	19.43	21.75	27.52	35.04	43.48	9.72	13.76	21.73	30.73	40.10		10.03	20.01	30.07	40.05
V	40.06	38.87	40.07	43.46	48.58	30.75	29.18	30.73	35.05	41.24	21.73	19.46	21.76	27.48	35.05	13.76	9.74	13.74	21.71	30.74	9.74		9.98	20.04	30.02
W	43.41	40.03	38.84	40.05	43.43	35.02	30.72	29.13	30.72	35.05	27.44	21.71	19.43	21.71	27.50	21.72	13.73	9.72	13.72	21.75	19.44	9.70		10.06	20.04
X	48.57	43.43	40.05	38.84	40.01	41.24	35.05	30.71	29.13	30.72	35.03	27.49	21.73	19.41	21.71	30.76	21.76	13.78	9.69	13.72	29.21	19.47	9.77		9.98
Y	54.96	48.57	43.46	40.06	38.84	48.60	41.24	35.03	30.73	29.18	43.44	35.04	27.49	21.73	19.46	40.09	30.75	21.77	13.76	9.74	38.91	29.16	19.46	9.70	

Table 11: CT c-c spheres distances of n° of proj. measurements, binning 2x and 90 kV **before** and **after** correction (± 0.05 mm)

bin 2x	A	B	C	D	E	F	G	H	I	J	K	L	M	N	O	P	Q	R	S	T	U	V	W	X	Y
A		10.01	19.99	29.99	40.00	9.98	14.12	22.36	31.62	41.23	19.98	22.34	28.27	36.06	44.70	29.99	31.61	36.03	42.42	50.00	39.99	41.24	44.70	50.00	56.57
B	9.72		9.98	19.99	29.99	14.13	9.98	14.13	22.36	31.61	22.34	19.98	22.34	28.29	36.03	31.62	29.99	31.60	36.05	42.42	41.24	40.01	41.21	44.71	50.00
C	19.42	9.70		10.01	20.01	22.34	14.13	10.00	14.15	22.37	28.26	22.34	19.98	22.37	28.27	36.06	31.61	29.99	31.63	36.06	44.73	41.25	39.99	41.23	44.74
D	29.13	19.42	9.72		10.01	31.61	22.36	14.15	10.00	14.13	36.03	28.27	22.34	20.01	22.34	42.44	36.04	31.62	30.01	31.62	50.02	44.74	41.22	39.99	41.24
E	38.85	29.13	19.44	9.72		41.22	31.62	22.36	14.13	9.95	44.70	36.04	28.26	22.34	19.96	50.01	42.40	36.04	31.62	29.96	56.58	50.01	44.70	41.19	39.99
F	9.69	13.72	21.70	30.70	40.04		9.98	19.99	29.99	40.00	10.00	14.14	22.36	31.63	41.21	20.01	22.36	28.27	36.06	44.73	30.01	31.65	36.05	42.44	50.01
G	13.71	9.69	13.72	21.72	30.72	9.70		10.01	20.01	30.02	14.13	10.00	14.15	22.39	31.62	22.38	20.01	22.36	28.30	36.08	31.65	30.04	31.63	36.08	42.46
H	21.71	13.73	9.72	13.74	21.72	19.41	9.72		10.01	20.01	22.34	14.13	9.98	14.15	22.34	28.29	22.34	19.98	22.36	28.29	36.07	31.64	29.99	31.62	36.06
I	30.72	21.71	13.75	9.72	13.72	29.13	19.44	9.72		10.01	31.61	22.36	14.13	10.00	14.12	36.08	28.27	22.36	20.01	22.35	42.46	36.08	31.62	29.99	31.63
J	40.05	30.71	21.73	13.73	9.67	38.85	29.16	19.44	9.72		41.23	31.64	22.37	14.16	10.00	44.76	36.07	28.31	22.40	20.01	50.06	42.47	36.08	31.63	30.04
K	19.41	21.70	27.45	35.00	43.41	9.72	13.72	21.70	30.70	40.05		9.98	19.99	29.99	39.98	10.00	14.14	22.33	31.61	41.24	20.01	22.37	28.27	36.06	44.72
L	21.70	19.41	21.70	27.46	35.01	13.73	9.72	13.72	21.72	30.73	9.70		10.01	20.01	29.99	14.16	10.00	14.13	22.37	31.65	22.39	20.03	22.36	28.30	36.07
M	27.46	21.70	19.41	21.70	27.45	21.72	13.75	9.69	13.72	21.73	19.42	9.72		10.01	19.99	22.39	14.15	10.00	14.15	22.38	28.33	22.40	20.01	22.37	28.30
N	35.03	27.48	21.73	19.43	21.70	30.72	21.75	13.75	9.72	13.76	29.13	19.44	9.72		9.98	31.65	22.36	14.15	10.00	14.13	36.10	28.31	22.36	19.98	22.36
O	43.42	34.99	27.46	21.70	19.39	40.03	30.72	21.70	13.71	9.72	38.83	29.13	19.41	9.70		41.25	31.61	22.37	14.16	10.00	44.76	36.08	28.29	22.36	20.03
P	29.13	30.72	35.02	41.22	48.57	19.43	21.74	27.48	35.04	43.48	9.72	13.76	21.75	30.75	40.07		10.03	20.01	30.02	40.05	10.00	14.17	22.38	31.67	41.27
Q	30.70	29.13	30.70	35.01	41.19	21.72	19.43	21.70	27.46	35.03	13.73	9.72	13.74	21.72	30.71	9.74		9.98	19.99	30.02	14.18	10.03	14.13	22.38	31.63
R	35.00	30.69	29.13	30.71	35.00	27.46	21.72	19.41	21.71	27.50	21.69	13.73	9.72	13.74	21.73	19.44	9.69		10.01	20.04	22.39	14.16	10.00	14.17	22.39
S	41.21	35.02	30.73	29.15	30.71	35.02	27.49	21.72	19.43	21.76	30.70	21.73	13.75	9.72	13.76	29.16	19.41	9.72		10.03	31.65	22.37	14.13	9.98	14.15
T	48.57	41.21	35.02	30.71	29.10	43.45	35.05	27.48	21.71	19.43	40.05	30.74	21.74	13.73	9.72	38.90	29.16	19.46	9.74		41.30	31.67	22.39	14.15	10.03
U	38.84	40.06	43.45	48.59	54.96	29.15	30.74	35.04	41.24	48.62	19.43	21.75	27.52	35.06	43.48	9.72	13.78	21.75	30.75	40.12		10.03	20.04	30.07	40.05
V	40.06	38.87	40.07	43.46	48.58	30.74	29.18	30.73	35.04	41.26	21.73	19.46	21.76	27.50	35.05	13.76	9.74	13.76	21.73	30.76	9.74		10.01	20.04	30.02
W	43.42	40.03	38.84	40.04	43.42	35.02	30.72	29.13	30.71	35.04	27.46	21.72	19.43	21.71	27.48	21.74	13.73	9.72	13.72	21.75	19.46	9.72		10.03	20.01
X	48.57	43.43	40.05	38.84	40.01	41.22	35.04	30.71	29.13	30.73	35.03	27.49	21.73	19.41	21.71	30.76	21.74	13.76	9.69	13.74	29.21	19.46	9.74		9.98
Y	54.95	48.57	43.45	40.06	38.84	48.58	41.24	35.03	30.72	29.18	43.44	35.04	27.49	21.72	19.46	40.08	30.72	21.75	13.75	9.74	38.90	29.16	19.44	9.70	

Table 12: CT c-c spheres distances of n° of proj. measurements, binning 3x **before** and **after** correction (± 0.05 mm)

bin 3x	A	B	C	D	E	F	G	H	I	J	K	L	M	N	O	P	Q	R	S	T	U	V	W	X	Y
A		10.01	19.99	30.00	39.98	9.98	14.10	22.34	31.60	41.21	19.98	22.33	28.25	36.04	44.68	29.99	31.60	36.02	42.41	49.99	39.99	41.23	44.69	49.99	56.58
B	9.72		9.98	19.99	29.97	14.15	9.98	14.12	22.34	31.59	22.36	19.98	22.33	28.27	36.01	31.63	29.99	31.59	36.04	42.41	41.24	40.02	41.21	44.71	50.01
C	19.42	9.70		10.01	19.99	22.36	14.15	10.00	14.14	22.35	28.28	22.36	19.98	22.36	28.25	36.07	31.62	29.99	31.63	36.05	44.73	41.26	39.99	41.22	44.74
D	29.14	19.42	9.72		9.98	31.63	22.38	14.16	10.00	14.12	36.06	28.29	22.36	20.01	22.33	42.46	36.06	31.62	30.01	31.61	50.03	44.76	41.23	39.99	41.25
E	38.83	29.11	19.42	9.70		41.22	31.62	22.36	14.13	9.95	44.70	36.04	28.26	22.34	19.96	50.01	42.41	36.04	31.62	29.96	56.57	50.01	44.70	41.20	39.99
F	9.69	13.74	21.72	30.73	40.04		9.98	19.99	30.00	40.00	10.00	14.14	22.36	31.63	41.22	20.01	22.36	28.27	36.06	44.74	30.01	31.65	36.05	42.44	50.04
G	13.70	9.69	13.74	21.74	30.72	9.70		10.01	20.01	30.02	14.13	10.00	14.15	22.39	31.62	22.38	20.01	22.36	28.31	36.09	31.64	30.04	31.63	36.08	42.48
H	21.69	13.71	9.72	13.76	21.72	19.42	9.72		10.01	20.01	22.34	14.13	9.98	14.15	22.35	28.29	22.34	19.98	22.36	28.29	36.06	31.64	29.99	31.62	36.08
I	30.70	21.69	13.73	9.72	13.72	29.14	19.44	9.72		10.01	31.61	22.36	14.13	10.00	14.12	36.08	28.28	22.36	20.01	22.35	42.44	36.08	31.62	29.99	31.64
J	40.03	30.69	21.71	13.71	9.67	38.86	29.16	19.44	9.72		41.23	31.64	22.37	14.16	10.00	44.77	36.07	28.31	22.40	20.01	50.04	42.48	36.08	31.63	30.04
K	19.41	21.71	27.47	35.02	43.42	9.72	13.72	21.70	30.70	40.05		9.98	19.99	30.00	39.98	10.00	14.14	22.34	31.61	41.24	20.01	22.38	28.27	36.07	44.75
L	21.69	19.41	21.71	27.48	35.01	13.73	9.72	13.72	21.72	30.73	9.70		10.01	20.01	30.00	14.16	10.00	14.13	22.37	31.65	22.38	20.03	22.36	28.31	36.10
M	27.44	21.69	19.41	21.71	27.45	21.72	13.75	9.69	13.72	21.73	19.42	9.72		10.01	19.99	22.39	14.15	10.00	14.15	22.38	28.31	22.40	20.01	22.37	28.32
N	35.01	27.46	21.72	19.43	21.70	30.73	21.75	13.75	9.72	13.76	29.14	19.44	9.72		9.98	31.66	22.36	14.15	10.00	14.14	36.08	28.31	22.36	19.98	22.38
O	43.40	34.98	27.44	21.69	19.39	40.03	30.72	21.71	13.71	9.72	38.83	29.14	19.42	9.70		41.26	31.62	22.37	14.16	10.00	44.74	36.08	28.29	22.36	20.03
P	29.13	30.72	35.04	41.24	48.58	19.43	21.74	27.48	35.04	43.48	9.72	13.76	21.75	30.75	40.07		10.03	20.01	30.02	40.05	10.00	14.17	22.38	31.67	41.30
Q	30.69	29.13	30.71	35.02	41.19	21.72	19.43	21.70	27.47	35.04	13.73	9.72	13.74	21.72	30.71	9.74		9.98	19.99	30.02	14.16	10.03	14.14	22.38	31.66
R	34.99	30.69	29.13	30.72	35.00	27.46	21.72	19.41	21.71	27.50	21.69	13.73	9.72	13.74	21.73	19.44	9.70		10.01	20.04	22.37	14.16	10.00	14.17	22.41
S	41.19	35.01	30.72	29.15	30.71	35.02	27.49	21.72	19.43	21.76	30.70	21.73	13.75	9.72	13.76	29.16	19.42	9.72		10.03	31.63	22.37	14.13	9.98	14.17
T	48.55	41.19	35.01	30.70	29.10	43.45	35.05	27.48	21.71	19.43	40.06	30.74	21.74	13.73	9.72	38.90	29.16	19.46	9.74		41.28	31.67	22.39	14.15	10.03
U	38.84	40.06	43.45	48.59	54.95	29.15	30.73	35.02	41.22	48.60	19.43	21.74	27.50	35.04	43.46	9.72	13.76	21.73	30.73	40.10		10.01	20.01	30.05	40.05
V	40.05	38.87	40.07	43.47	48.58	30.74	29.18	30.73	35.05	41.26	21.73	19.46	21.76	27.50	35.05	13.76	9.74	13.76	21.73	30.76	9.72		10.01	20.04	30.05
W	43.41	40.03	38.84	40.05	43.42	35.02	30.72	29.13	30.71	35.05	27.46	21.72	19.43	21.71	27.48	21.74	13.73	9.72	13.72	21.75	19.44	9.72		10.03	20.04
X	48.55	43.42	40.04	38.84	40.01	41.23	35.05	30.71	29.13	30.73	35.03	27.49	21.73	19.41	21.71	30.76	21.74	13.76	9.69	13.74	29.18	19.46	9.74		10.01
Y	54.96	48.57	43.46	40.06	38.84	48.60	41.26	35.05	30.73	29.18	43.47	35.06	27.51	21.73	19.46	40.11	30.75	21.77	13.76	9.74	38.91	29.19	19.47	9.72	

Table 13: CT c-c spheres distances of voltages measurements, 150 kV before and after correction (± 0.05 mm/ ± 0.04)

150kV	A	B	C	D	E	F	G	H	I	J	K	L	M	N	O	P	Q	R	S	T	U	V	W	X	Y
A		10.01	19.99	30.00	39.99	9.98	14.10	22.34	31.61	41.23	19.98	22.33	28.27	36.04	44.70	29.99	31.59	36.03	42.39	49.99	39.99	41.23	44.71	49.99	56.58
B	9.72		9.98	19.99	29.98	14.15	9.98	14.12	22.34	31.62	22.36	19.98	22.35	28.27	36.03	31.63	29.99	31.61	36.03	42.41	41.24	40.02	41.23	44.72	50.02
C	19.42	9.70		10.01	19.99	22.35	14.13	9.98	14.12	22.36	28.26	22.33	19.98	22.35	28.26	36.05	31.60	29.99	31.59	36.03	44.72	41.23	39.99	41.22	44.74
D	29.14	19.42	9.72		9.98	31.63	22.38	14.15	9.98	14.14	36.05	28.28	22.36	20.01	22.33	42.45	36.05	31.63	29.99	31.60	50.02	44.74	41.24	39.99	41.26
E	38.84	29.12	19.42	9.70		41.22	31.62	22.35	14.11	9.98	44.70	36.03	28.26	22.36	19.96	50.00	42.41	36.05	31.60	29.96	56.58	49.99	44.71	41.20	40.02
F	9.69	13.74	21.71	30.72	40.04		9.98	19.99	30.00	40.01	10.00	14.14	22.37	31.62	41.23	20.01	22.35	28.27	36.04	44.73	30.01	31.65	36.06	42.45	50.03
G	13.70	9.69	13.73	21.73	30.71	9.70		10.01	20.02	30.03	14.13	10.00	14.17	22.38	31.64	22.38	20.01	22.38	28.29	36.08	31.65	30.04	31.65	36.09	42.48
H	21.70	13.71	9.69	13.74	21.71	19.42	9.72		10.01	20.02	22.34	14.13	10.00	14.15	22.36	28.30	22.36	20.01	22.35	28.29	36.08	31.64	30.01	31.63	36.10
I	30.70	21.70	13.71	9.69	13.71	29.14	19.44	9.72		10.01	31.62	22.36	14.15	10.03	14.14	36.08	28.30	22.39	20.01	22.36	42.46	36.08	31.65	30.01	31.67
J	40.05	30.71	21.72	13.73	9.69	38.86	29.17	19.44	9.72		41.23	31.63	22.36	14.17	9.98	44.75	36.07	28.31	22.37	19.98	50.04	42.45	36.08	31.62	30.04
K	19.41	21.72	27.45	35.01	43.41	9.72	13.73	21.70	30.71	40.04		9.99	19.99	29.98	39.99	10.00	14.12	22.33	31.59	41.23	20.01	22.38	28.27	36.06	44.73
L	21.69	19.41	21.69	27.47	35.00	13.73	9.72	13.73	21.72	30.72	9.70		10.01	19.99	30.00	14.17	10.00	14.14	22.35	31.64	22.39	20.03	22.38	28.31	36.09
M	27.46	21.71	19.41	21.72	27.45	21.73	13.77	9.72	13.74	21.72	19.42	9.72		9.98	19.99	22.39	14.15	10.00	14.12	22.36	28.31	22.38	20.01	22.36	28.31
N	35.01	27.46	21.71	19.43	21.72	30.72	21.74	13.75	9.74	13.76	29.12	19.42	9.70		10.01	31.63	22.35	14.15	9.98	14.14	36.07	28.28	22.36	19.98	22.39
O	43.42	34.99	27.45	21.69	19.39	40.05	30.73	21.72	13.73	9.69	38.84	29.14	19.42	9.72		41.26	31.64	22.40	14.17	10.00	44.76	36.08	28.31	22.37	20.06
P	29.13	30.72	35.02	41.23	48.57	19.43	21.74	27.48	35.05	43.47	9.72	13.76	21.74	30.72	40.07		10.01	19.99	30.00	40.04	10.00	14.17	22.37	31.66	41.27
Q	30.69	29.13	30.69	35.02	41.19	21.71	19.43	21.72	27.48	35.03	13.71	9.72	13.74	21.71	30.73	9.72		9.98	19.99	30.03	14.17	10.03	14.15	22.39	31.65
R	34.99	30.70	29.13	30.72	35.02	27.46	21.73	19.43	21.75	27.50	21.69	13.73	9.72	13.74	21.75	19.42	9.70		10.01	20.04	22.36	14.13	10.00	14.17	22.41
S	41.18	34.99	30.69	29.13	30.69	35.01	27.48	21.71	19.43	21.73	30.69	21.71	13.71	9.69	13.76	29.14	19.42	9.72		10.03	31.64	22.35	14.15	10.00	14.19
T	48.55	41.19	35.00	30.69	29.10	43.45	35.05	27.48	21.72	19.41	40.05	30.73	21.72	13.73	9.72	38.89	29.17	19.47	9.75		41.28	31.65	22.40	14.15	10.05
U	38.84	40.06	43.44	48.59	54.95	29.15	30.74	35.04	41.24	48.60	19.43	21.75	27.50	35.03	43.48	9.72	13.76	21.72	30.73	40.10		10.03	20.02	30.05	40.04
V	40.05	38.87	40.05	43.45	48.56	30.74	29.17	30.73	35.05	41.23	21.73	19.46	21.74	27.47	35.04	13.76	9.74	13.73	21.71	30.74	9.75		9.98	20.02	30.00
W	43.42	40.04	38.84	40.05	43.43	35.03	30.74	29.15	30.74	35.04	27.46	21.73	19.43	21.72	27.50	21.73	13.75	9.72	13.74	21.76	19.44	9.70		10.03	20.02
X	48.56	43.43	40.03	38.84	40.02	41.23	35.05	30.72	29.15	30.71	35.03	27.50	21.72	19.41	21.73	30.75	21.75	13.76	9.72	13.74	29.19	19.44	9.75		9.99
Y	54.96	48.58	43.46	40.07	38.87	48.60	41.26	35.06	30.76	29.17	43.45	35.05	27.50	21.74	19.48	40.08	30.75	21.76	13.78	9.77	38.89	29.14	19.44	9.70	

Table 14: CT c-c spheres distances of magnification measurements, M1 **before** and **after** correction (± 0.06 mm)

M1	G	H	I	L	M	N	Q	R	S
G		10.02	20.00	9.99	14.15	22.40	20.02	22.36	28.31
H	10.04		9.98	14.11	9.99	14.15	22.36	19.98	22.36
I	20.03	10.00		22.32	14.14	10.03	28.28	22.36	20.02
L	10.01	14.13	22.36		9.97	19.99	10.03	14.12	22.36
M	14.18	10.01	14.17	9.99			14.14	9.99	14.15
N	22.44	14.18	10.05	20.03	10.04		22.36	14.14	9.99
Q	20.06	22.40	28.33	10.05	14.16	22.40		9.97	19.99
R	22.40	20.01	22.40	14.15	10.01	14.16	9.99		10.02
S	28.36	22.40	20.06	22.40	14.18	10.01	20.03	10.04	

Table 15: CT c-c spheres distances of magnification measurements, M2 **before** and **after** correction (± 0.06 mm)

M2	G	H	I	L	M	N	Q	R	S
G		10.01	20.01	10.00	14.15	22.39	20.01	22.36	28.30
H	9.72		10.01	14.13	9.98	14.15	22.34	19.98	22.36
I	19.44	9.72		22.36	14.13	10.00	28.27	22.36	20.01
L	9.72	13.72	21.72		10.01	20.01	10.00	14.13	22.37
M	13.75	9.69	13.72	9.72		10.01	14.15	10.00	14.15
N	21.75	13.75	9.72	19.44	9.72		22.36	14.15	10.00
Q	19.43	21.70	27.46	9.72	13.74	21.72		9.98	19.99
R	21.72	19.41	21.71	13.73	9.72	13.74	9.69		10.01
S	27.49	21.72	19.43	21.73	13.75	9.72	19.41	9.72	

Table 16: CT c-c spheres distances of magnification measurements, M4 **before** and **after** correction (± 0.04 mm)

M4	G	H	I	L	M	N	Q	R	S
G		10.01	20.01	10.00	14.16	22.37	20.02	22.38	28.29
H	10.32		10.01	14.13	10.00	14.13	22.37	20.00	22.35
I	20.64	10.32		22.35	14.14	9.97	28.29	22.34	19.97
L	10.32	14.58	23.05		9.99	20.00	10.02	14.16	22.36
M	14.60	10.32	14.58	10.31		10.00	14.15	9.99	14.13
N	23.07	14.58	10.28	20.63	10.32		22.38	14.14	10.00
Q	20.65	23.07	29.18	10.33	14.59	23.09		10.03	20.01
R	23.08	20.62	23.04	14.60	10.31	14.58	10.34		9.98
S	29.18	23.05	20.60	23.06	14.58	10.32	20.64	10.30	

Table 17: CT c-c spheres distances of measurements at different time, time 0 **before and **after** correction (± 0.06 mm)**

time 0	A	B	C	D	E	F	G	H	I	J	K	L	M	N	O	P	Q	R	S	T	U	V	W	X	Y
A		10.01	20.01	30.02	39.98	10.01	14.12	22.35	31.61	41.22	20.01	22.35	28.30	36.06	44.72	30.01	31.62	36.06	42.41	50.01	40.02	41.24	44.70	50.03	56.62
B	10.00		10.01	20.01	29.97	14.12	9.96	14.12	22.33	31.60	22.33	19.96	22.35	28.26	36.03	31.61	29.97	31.61	36.02	42.41	41.23	39.97	41.18	44.72	50.03
C	20.00	10.00		10.01	19.97	22.35	14.15	10.00	14.12	22.33	28.27	22.35	20.01	22.35	28.26	36.06	31.61	30.01	31.61	36.05	44.75	41.22	39.97	41.24	44.76
D	30.01	20.01	10.00		9.96	31.63	22.39	14.18	10.00	14.12	36.05	28.30	22.39	20.01	22.35	42.45	36.06	31.67	30.01	31.62	50.05	44.73	41.23	40.02	41.28
E	39.97	29.96	19.96	9.96		41.19	31.61	22.35	14.12	9.96	44.67	36.03	28.27	22.33	19.96	49.97	42.39	36.06	31.61	29.97	56.57	49.96	44.69	41.21	40.02
F	10.00	14.12	22.35	31.62	41.18		9.96	19.97	29.97	39.98	10.00	14.12	22.35	31.61	41.22	20.01	22.35	28.26	36.02	44.72	30.01	31.62	36.02	42.44	50.04
G	14.11	9.96	14.15	22.39	31.60	9.96		10.01	20.01	30.02	14.12	10.00	14.18	22.39	31.65	22.37	20.01	22.39	28.30	36.10	31.65	30.01	31.62	36.11	42.51
H	22.34	14.11	10.00	14.18	22.35	19.96	10.00		10.01	20.01	22.31	14.12	10.00	14.15	22.37	28.27	22.33	20.01	22.35	28.30	36.06	31.60	29.97	31.64	36.11
I	31.60	22.32	14.11	10.00	14.11	29.96	20.01	10.00		10.01	31.58	22.35	14.15	10.01	14.15	36.05	28.27	22.39	20.01	22.37	42.45	36.04	31.61	30.01	31.68
J	41.21	31.59	22.32	14.11	9.96	39.97	30.01	20.01	10.00		41.20	31.63	22.37	14.15	10.00	44.73	36.05	28.33	22.39	20.01	50.04	42.42	36.06	31.64	30.06
K	20.00	22.33	28.26	36.04	44.65	10.00	14.11	22.31	31.58	41.19		9.96	19.97	29.97	39.98	10.00	14.12	22.31	31.57	41.22	20.01	22.35	28.23	36.06	44.74
L	22.34	19.96	22.35	28.29	36.02	14.11	10.00	14.11	22.35	31.62	9.96		10.01	20.01	30.02	14.15	10.01	14.15	22.35	31.65	22.39	20.01	22.35	28.33	36.12
M	28.29	22.34	20.00	22.39	28.26	22.35	14.18	10.00	14.15	22.37	19.96	10.00		10.01	20.01	22.35	14.12	10.00	14.12	22.37	28.30	22.33	19.96	22.37	28.33
N	36.05	28.26	22.34	20.00	22.33	31.60	22.38	14.14	10.00	14.15	29.96	20.00	10.00		10.01	31.63	22.35	14.18	10.00	14.15	36.09	28.27	22.35	20.01	22.41
O	44.71	36.02	28.26	22.34	19.96	41.21	31.64	22.36	14.14	10.00	39.97	30.01	20.01	10.00		41.24	31.63	22.41	14.18	10.01	44.77	36.05	28.30	22.37	20.05
P	30.01	31.60	36.05	42.44	49.96	20.00	22.37	28.26	36.04	44.72	10.00	14.15	22.35	31.62	41.23		10.01	19.97	29.97	40.02	10.01	14.15	22.33	31.65	41.27
Q	31.61	29.96	31.60	36.05	42.38	22.34	20.00	22.33	28.26	36.04	14.11	10.00	14.12	22.35	31.62	10.00		9.96	19.97	30.02	14.18	10.00	14.12	22.39	31.67
R	36.05	31.60	30.01	31.66	36.05	28.26	22.38	20.00	22.39	28.32	22.31	14.14	10.00	14.18	22.41	19.96	9.96		10.01	20.06	22.35	14.09	9.96	14.18	22.43
S	42.40	36.01	31.60	30.01	31.60	36.01	28.29	22.34	20.00	22.39	31.56	22.34	14.11	10.00	14.18	29.96	19.96	10.00		10.05	31.63	22.31	14.12	10.00	14.21
T	50.00	42.40	36.04	31.61	29.96	44.71	36.09	28.29	22.36	20.00	41.21	31.64	22.36	14.14	10.00	40.01	30.01	20.05	10.05		41.29	31.63	22.39	14.15	10.05
U	40.01	41.22	44.73	50.03	56.55	30.01	31.65	36.05	42.44	50.03	20.00	22.39	28.29	36.08	44.76	10.00	14.18	22.35	31.62	41.28		10.05	20.01	30.06	40.07
V	41.23	39.96	41.21	44.71	49.94	31.61	30.01	31.59	36.03	42.41	22.34	20.00	22.33	28.26	36.04	14.14	10.00	14.08	22.31	31.62	10.05		9.96	20.01	30.02
W	44.69	41.17	39.96	41.22	44.67	36.01	31.61	29.96	31.60	36.05	28.23	22.34	19.96	22.35	28.29	22.32	14.11	9.96	14.12	22.39	20.01	9.96		10.05	20.06
X	50.02	44.71	41.23	40.01	41.20	42.43	36.10	31.63	30.01	31.63	36.05	28.32	22.36	20.00	22.37	31.64	22.38	14.18	10.00	14.15	30.05	20.00	10.05		10.01
Y	56.61	50.02	44.75	41.27	40.01	50.03	42.50	36.10	31.67	30.05	44.73	36.11	28.32	22.40	20.05	41.26	31.66	22.43	14.21	10.05	40.06	30.01	20.05	10.00	

Table 18: CT c-c spheres distances of measurements at different time, after 3 months **before** and **after** correction (± 0.06 mm)

3 months	A	B	C	D	E	F	G	H	I	J	K	L	M	N	O	P	Q	R	S	T	U	V	W	X	Y
A		10.02	19.99	30.02	40.03	9.99	14.12	22.38	31.62	41.24	19.98	22.34	28.28	36.08	44.72	29.96	31.62	36.02	42.43	50.01	40.00	41.22	44.69	50.01	56.58
B	10.04		9.97	20.00	30.02	14.14	9.99	14.15	22.34	31.62	22.34	19.98	22.36	28.31	36.05	31.62	30.01	31.60	36.06	42.43	41.26	40.00	41.21	44.73	50.02
C	20.03	9.99		10.02	20.04	22.32	14.11	9.99	14.13	22.36	28.22	22.30	19.98	22.38	28.28	36.02	31.60	29.96	31.62	36.05	44.72	41.19	39.95	41.22	44.73
D	30.07	20.03	10.04		10.02	31.61	22.36	14.14	9.99	14.12	36.02	28.25	22.36	20.02	22.36	42.43	36.06	31.62	30.01	31.62	50.03	44.70	41.20	40.00	41.25
E	40.11	30.07	20.08	10.04		41.24	31.65	22.38	14.17	9.99	44.71	36.05	28.31	22.40	20.02	50.03	42.45	36.08	31.66	30.01	56.63	50.00	44.72	41.25	40.04
F	10.01	14.16	22.36	31.67	41.31		9.97	19.99	29.97	39.99	9.99	14.12	22.34	31.62	41.21	19.98	22.36	28.24	36.04	44.72	30.01	31.62	36.02	42.43	50.00
G	14.15	10.01	14.13	22.40	31.71	9.99		10.02	20.00	30.02	14.11	9.99	14.15	22.40	31.63	22.36	20.02	22.36	28.31	36.08	31.66	30.01	31.62	36.09	42.46
H	22.42	14.18	10.01	14.17	22.42	20.03	10.04		9.98	20.00	22.32	14.11	9.99	14.15	22.34	28.28	22.36	19.98	22.36	28.28	36.08	31.60	29.96	31.62	36.06
I	31.67	22.38	14.15	10.01	14.20	30.02	20.03	10.00		10.02	31.57	22.32	14.14	10.03	14.15	36.06	28.28	22.36	20.02	22.38	42.46	36.03	31.60	30.01	31.66
J	41.31	31.67	22.40	14.15	10.01	40.06	30.07	20.03	10.04		41.20	31.61	22.38	14.18	10.03	44.75	36.08	28.31	22.40	20.02	50.06	42.42	36.06	31.64	30.05
K	20.01	22.38	28.27	36.08	44.79	10.01	14.14	22.36	31.63	41.28		9.98	19.95	29.97	39.95	9.99	14.12	22.30	31.59	41.21	20.02	22.36	28.25	36.05	44.70
L	22.38	20.01	22.34	28.30	36.12	14.15	10.01	14.13	22.36	31.67	10.00		9.97	19.99	29.97	14.18	10.03	14.12	22.36	31.63	22.42	20.02	22.36	28.31	36.07
M	28.33	22.40	20.01	22.40	28.37	22.38	14.18	10.01	14.17	22.42	19.99	9.99			20.00	22.36	14.14	9.99	14.15	22.38	28.31	22.34	19.98	22.38	28.31
N	36.14	28.36	22.42	20.06	22.44	31.68	22.44	14.18	10.05	14.20	30.02	20.03	10.04		9.98	31.64	22.36	14.14	9.99	14.13	36.09	28.25	22.32	19.98	22.36
O	44.80	36.11	28.33	22.40	20.06	41.28	31.69	22.38	14.18	10.05	40.02	30.02	20.03	10.00		41.24	31.61	22.36	14.14	9.99	44.75	36.01	28.25	22.34	20.02
P	30.02	31.67	36.08	42.50	50.12	20.01	22.40	28.33	36.12	44.83	10.01	14.20	22.40	31.69	41.31		10.02	20.00	30.02	40.04	10.03	14.19	22.38	31.67	41.26
Q	31.67	30.06	31.65	36.12	42.53	22.40	20.06	22.40	28.33	36.14	14.15	10.05	14.16	22.40	31.67	10.04		9.97	19.99	30.02	14.18	9.99	14.12	22.38	31.62
R	36.09	31.66	30.02	31.67	36.15	28.29	22.40	20.01	22.40	28.37	22.34	14.15	10.01	14.16	22.40	20.03	9.99		10.02	20.04	22.38	14.11	9.99	14.19	22.40
S	42.50	36.13	31.67	30.06	31.71	36.11	28.36	22.40	20.06	22.44	31.64	22.40	14.18	10.01	14.17	30.07	20.03	10.04		10.02	31.65	22.32	14.11	9.99	14.15
T	50.10	42.51	36.12	31.67	30.06	44.80	36.15	28.33	22.42	20.06	41.28	31.69	22.42	14.15	10.01	40.11	30.07	20.08	10.04		41.29	31.61	22.36	14.14	10.03
U	40.07	41.33	44.80	50.12	56.73	30.06	31.71	36.15	42.53	50.15	20.06	22.46	28.37	36.15	44.83	10.05	14.20	22.42	31.71	41.36		10.07	20.04	30.06	40.03
V	41.29	40.07	41.26	44.78	50.09	31.67	30.06	31.65	36.10	42.50	22.40	20.06	22.38	28.30	36.08	14.21	10.01	14.13	22.36	31.67	10.09		9.97	19.99	29.97
W	44.77	41.28	40.02	41.28	44.80	36.09	31.67	30.02	31.66	36.12	28.30	22.40	20.01	22.36	28.30	22.42	14.15	10.01	14.13	22.40	20.08	9.99		10.02	19.99
X	50.10	44.81	41.29	40.07	41.32	42.50	36.15	31.67	30.06	31.70	36.11	28.36	22.42	20.01	22.38	31.73	22.42	14.21	10.01	14.17	30.11	20.03	10.04		9.97
Y	56.68	50.11	44.81	41.33	40.11	50.09	42.54	36.13	31.72	30.11	44.78	36.13	28.36	22.40	20.06	41.33	31.68	22.44	14.18	10.05	40.11	30.02	20.03	9.99	

Table 19: CT c-c spheres distances of measurements at different time, after 4 months **before** and **after** correction (± 0.06 mm)

4 months	A	B	C	D	E	F	G	H	I	J	K	L	M	N	O	P	Q	R	S	T	U	V	W	X	Y
A		10.01	19.99	30.00	39.98	9.98	14.10	22.34	31.60	41.21	19.98	22.33	28.25	36.04	44.68	29.99	31.60	36.02	42.41	49.99	39.99	41.23	44.69	49.99	56.58
B	10.10		9.98	19.99	29.97	14.15	9.98	14.12	22.34	31.59	22.36	19.98	22.33	28.27	36.01	31.63	29.99	31.59	36.04	42.41	41.24	40.02	41.21	44.71	50.01
C	20.15	10.05		10.01	19.99	22.36	14.15	10.00	14.14	22.35	28.28	22.36	19.98	22.36	28.25	36.07	31.62	29.99	31.63	36.05	44.73	41.26	39.99	41.22	44.74
D	30.24	20.15	10.09		9.98	31.63	22.38	14.16	10.00	14.12	36.06	28.29	22.36	20.01	22.33	42.46	36.06	31.62	30.01	31.61	50.03	44.76	41.23	39.99	41.25
E	40.29	30.20	20.15	10.05		41.22	31.62	22.36	14.13	9.95	44.70	36.04	28.26	22.34	19.96	50.01	42.41	36.04	31.62	29.96	56.57	50.01	44.70	41.20	39.99
F	10.10	14.25	22.52	31.87	41.52		9.98	19.99	30.00	40.00	10.00	14.14	22.36	31.63	41.22	20.01	22.36	28.27	36.06	44.74	30.01	31.65	36.05	42.44	50.04
G	14.24	10.05	14.25	22.56	31.86	10.05		10.01	20.01	30.02	14.13	10.00	14.15	22.39	31.62	22.38	20.01	22.36	28.31	36.09	31.64	30.04	31.63	36.08	42.48
H	22.55	14.24	10.09	14.28	22.52	20.15	10.10		10.01	20.01	22.34	14.13	9.98	14.15	22.35	28.29	22.34	19.98	22.36	28.29	36.06	31.64	29.99	31.62	36.08
I	31.85	22.49	14.24	10.10	14.25	30.20	20.15	10.05		10.01	31.61	22.36	14.13	10.00	14.12	36.08	28.28	22.36	20.01	22.35	42.44	36.08	31.62	29.99	31.64
J	41.54	31.84	22.53	14.24	10.05	40.29	30.24	20.15	10.10		41.23	31.64	22.37	14.16	10.00	44.77	36.07	28.31	22.40	20.01	50.04	42.48	36.08	31.63	30.04
K	20.15	22.50	28.46	36.32	45.01	10.05	14.22	22.50	31.81	41.52		9.98	19.99	30.00	39.98	10.00	14.14	22.34	31.61	41.24	20.01	22.38	28.27	36.07	44.75
L	22.51	20.10	22.50	28.49	36.29	14.21	10.05	14.22	22.50	31.86	10.05		10.01	20.01	30.00	14.16	10.00	14.13	22.37	31.65	22.38	20.03	22.36	28.31	36.10
M	28.52	22.51	20.15	22.54	28.46	22.53	14.27	10.05	14.22	22.52	20.15	10.10		10.01	19.99	22.39	14.15	10.00	14.15	22.38	28.31	22.40	20.01	22.37	28.32
N	36.34	28.48	22.55	20.19	22.54	31.85	22.55	14.24	10.09	14.28	30.20	20.15	10.05		9.98	31.66	22.36	14.15	10.00	14.14	36.08	28.31	22.36	19.98	22.38
O	45.04	36.28	28.48	22.53	20.15	41.50	31.85	22.49	14.24	10.10	40.25	30.20	20.10	10.05		41.26	31.62	22.37	14.16	10.00	44.74	36.08	28.29	22.36	20.03
P	30.24	31.86	36.33	42.77	50.37	20.14	22.54	28.50	36.32	45.07	10.10	14.28	22.56	31.86	41.52		10.03	20.01	30.02	40.05	10.00	14.17	22.38	31.67	41.30
Q	31.86	30.20	31.84	36.33	42.71	22.51	20.15	22.50	28.46	36.32	14.24	10.10	14.25	22.50	31.81	10.09		9.98	19.99	30.02	14.16	10.03	14.14	22.38	31.66
R	36.30	31.81	30.20	31.86	36.29	28.45	22.51	20.10	22.50	28.50	22.49	14.24	10.05	14.22	22.50	20.15	10.05		10.01	20.04	22.37	14.16	10.00	14.17	22.41
S	42.73	36.28	31.85	30.24	31.86	36.28	28.48	22.49	20.14	22.56	31.81	22.51	14.21	10.05	14.25	30.20	20.10	10.05		10.03	31.63	22.37	14.13	9.98	14.17
T	50.36	42.69	36.30	31.85	30.20	45.02	36.32	28.45	22.51	20.15	41.50	31.85	22.49	14.21	10.05	40.29	30.20	20.15	10.09		41.28	31.67	22.39	14.15	10.03
U	40.29	41.51	45.03	50.38	56.96	30.20	31.84	36.29	42.71	50.37	20.15	22.54	28.50	36.29	45.01	10.05	14.25	22.52	31.82	41.52		10.01	20.01	30.05	40.05
V	41.55	40.29	41.55	45.09	50.38	31.85	30.24	31.86	36.33	42.78	22.53	20.19	22.56	28.50	36.32	14.24	10.10	14.28	22.52	31.87	10.05		10.01	20.04	30.05
W	45.06	41.51	40.29	41.55	45.03	36.30	31.86	30.20	31.84	36.33	28.48	22.55	20.15	22.50	28.46	22.53	14.24	10.10	14.22	22.52	20.15	10.09		10.03	20.04
X	50.38	45.02	41.52	40.29	41.50	42.73	36.33	31.82	30.20	31.84	36.32	28.52	22.51	20.10	22.48	31.88	22.53	14.27	10.05	14.22	30.24	20.19	10.10		10.01
Y	56.97	50.32	45.04	41.54	40.29	50.32	42.73	36.28	31.85	30.24	45.00	36.31	28.45	22.49	20.15	41.50	31.81	22.51	14.24	10.10	40.25	30.20	20.10	10.00	

Appendix D: Lego brick and Piccolo Flute measures

Table 20: Lego brick reference measures of lengths (A,B, and C), knobs diameter and knobs' center distances obtained with ATOS Scanbox (mm).

Lenghts, (± 0.005)		Knobs diameters (± 0.01)	
A	31.910	Ø 1	4.68
		Ø 2	4.37
		Ø 3	4.71
B	15.935	Ø 4	4.78
		Ø 5	4.79
		Ø 6	4.91
C	9.669	Ø 7	4.78
		Ø 8	4.73
Knobs center-to center distances (± 0.002)			
c-c 1-2	8.010	c-c 3-5	8.130
c-c 1-3	8.010	c-c 3-6	11.291
c-c 1-4	11.349	c-c 3-7	15.975
c-c 1-5	16.139	c-c 3-8	17.850
c-c 1-6	17.887	c-c 4-5	11.530
c-c 1-7	23.985	c-c 4-6	7.988
c-c 1-8	25.277	c-c 4-7	17.878
c-c 2-3	11.609	c-c 4-8	15.965
c-c 2-4	8.435	c-c 5-6	8.141
c-c 2-5	18.454	c-c 5-7	7.848
c-c 2-6	16.422	c-c 5-8	11.303
c-c 2-7	25.683	c-c 6-7	11.298
c-c 2-8	24.400	c-c 6-8	7.977
c-c 3-4	8.017	c-c 7-8	7.995

Table 21: Piccolo Flute reference measures of diameters, lengths and holes obtained with a centesimal caliper (instrumental error ± 0.01 mm). Diameters uncertainty = ± 0.03 mm; lengths uncertainty = ± 0.07 mm; holes diameters uncertainty = ± 0.04 mm

HEAD	L_{ref}	BODY	L_{ref}	FOOT	L_{ref}
A int	10.84	A' int	10.22	A'' int	8.97
A ext	17.05	A' ext	13.83	A'' ext	15.84
B int	14.43	B' int	8.04	B'' int	12.25
B ext	18.78	B' ext	11.33	B'' ext	20.11
C	126.60	C'	72.66	C''	113.36
D	75.68	D'	99.23	D''	19.65
hole 1	8.43	E'	8.14	E''	37.53
hole 1 ---	8.16	F'	24.54	F''	54.68
		G'	39.83	hole 1	4.40
		hole 1	3.83	hole 1 ---	4.40
		hole 1 ---	3.84	hole 2	4.49
		hole 2	4.56	hole 2 ---	4.30
		hole 2 ---	4.55	hole 3	3.65
		hole 3	4.71	hole 3 ---	3.56
		hole 3 ---	4.81		

Appendix E: Visible light and radiographic images of *BeArchaeo* pottery samples

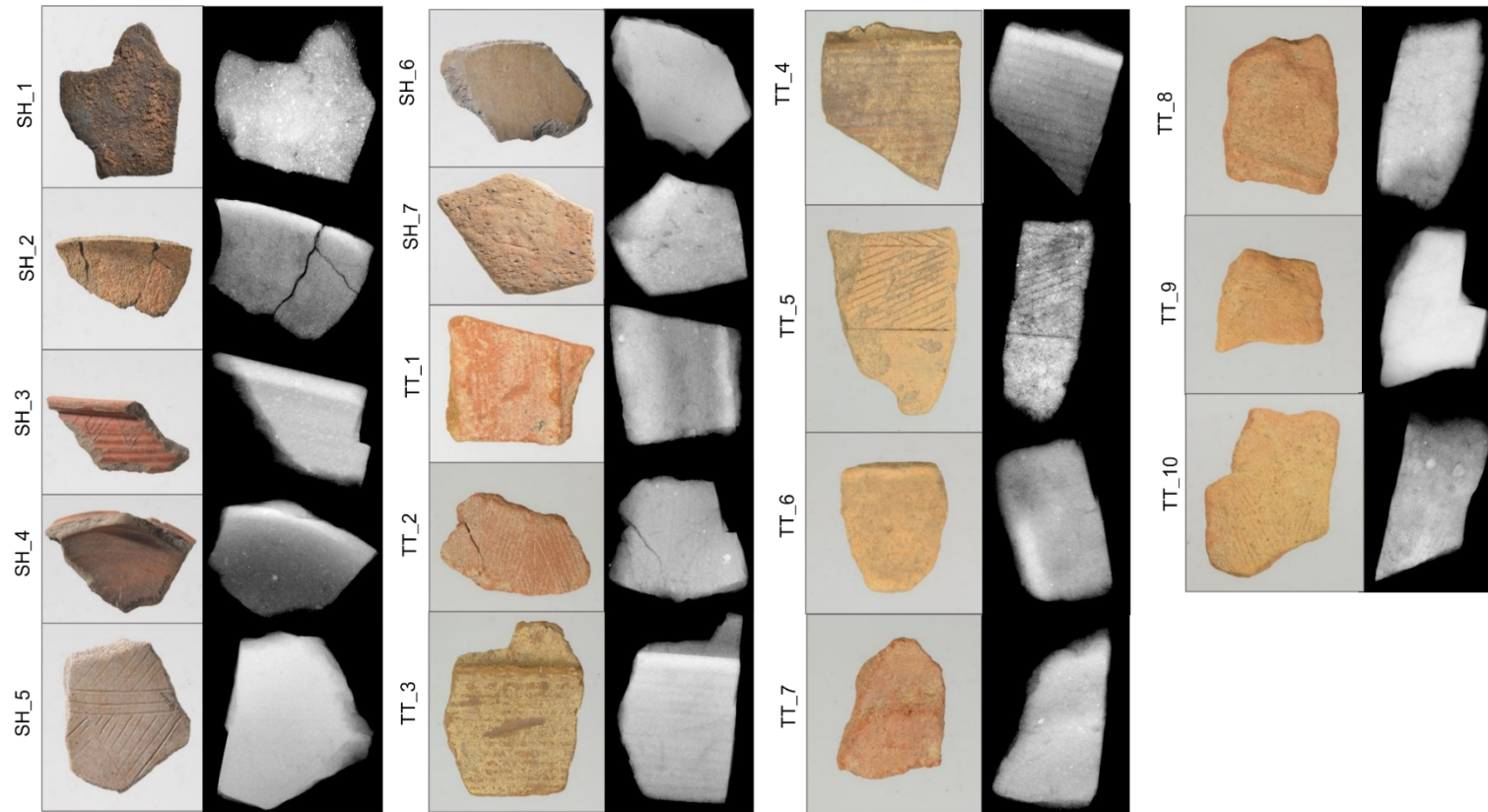


Figure E.1: Visible light and radiographic images of *BeArchaeo* pottery samples